

COMENIUS UNIVERSITY IN BRATISLAVA
FACULTY OF MATHEMATICS, PHYSICS & INFORMATICS



**COMPUTATIONAL MODEL OF SYNAPTIC PLASTICITY IN
CA1 REGION OF HIPPOCAMPUS**

Dissertation thesis

2021

Mgr. Matúš TOMKO

COMENIUS UNIVERSITY IN BRATISLAVA
FACULTY OF MATHEMATICS, PHYSICS & INFORMATICS

**COMPUTATIONAL MODEL OF SYNAPTIC PLASTICITY IN
CA1 REGION OF HIPPOCAMPUS**

Dissertation thesis

Study program: 9.2.1 - Informatics

Department: Department of Applied Informatics

Supervisor: prof. RNDr. Ľubica Beňušková, PhD.

Supervisor (specialist): prof. MUDr. Peter Jedlička, PhD.

2021

Mgr. Matúš TOMKO



19475348

Comenius University in Bratislava
Faculty of Mathematics, Physics and Informatics

THESIS ASSIGNMENT

Name and Surname:

Mgr. Matúš Tomko

Study programme:

Computer Science (Single degree study, Ph.D. III. deg., full time form)

Field of Study:

Computer Science

Type of Thesis:

Dissertation thesis

Language of Thesis:

English

Secondary language:

Slovak

Title: Computational model of synaptic plasticity in CA1 region of hippocampus

Annotation: Synaptic plasticity, that is, the ability of a neuron's synapses to vary in strength in response to a stimulus, is considered a mechanism by which the brain stores information such as declarative and procedural memory. Although several models of synaptic plasticity have been proposed, anything close to a wide consensus is lacking. A valuable way of determining if a proposed model of the synaptic plasticity is accurate is to conduct computational simulation of a neuron subject to the given model and apply identical protocols to those within a physical experiment, and to check for concordance under a variety of conditions.

Aim: Design and implement (in NEURON environment) a compartmental model of CA1 pyramidal cell using STDP meta-plasticity based on existing models, and compare their properties. Reproduce experimental results with regard to synaptic plasticity in the CA1 area.

Literature: Cutsuridis V, Graham B, Cobb S, Vida I (Eds.) (2010) Hippocampal Microcircuits: A Computational Modeler's Resource Book, Springer.
Jedlicka P, Benuskova L, Abraham WC (2015) A voltage-based STDP rule combined with fast BCM-like metaplasticity accounts for LTP and concurrent "heterosynaptic" LTD in the dentate gyrus in vivo. PLoS Computational Biology, 11(11): e1004588.
Carnevale, N.T. and Hines, M.L. The NEURON Book. Cambridge University Press, 2006.

Tutor: prof. RNDr. Ľubica Beňušková, PhD.

Department: FMFI.KAI - Department of Applied Informatics

Head of department: prof. Ing. Igor Farkaš, Dr.

Assigned: 19.01.2017

Approved: 14.06.2017

prof. RNDr. Rastislav Kráľovič, PhD.

Guarantor of Study Programme

.....
Student

.....
Tutor



ZADANIE ZÁVEREČNEJ PRÁCE

Meno a priezvisko študenta: Mgr. Matúš Tomko

Študijný program: informatika (Jednooborové štúdium, doktorandské III. st., denná forma)

Študijný odbor: informatika

Typ záverečnej práce: dizertačná

Jazyk záverečnej práce: anglický

Sekundárny jazyk: slovenský

Názov: Computational model of synaptic plasticity in CA1 region of hippocampus
Výpočtový model synapatickej plasticity v hipokampálnej oblasti CA1

Anotácia: Synaptická plasticita, teda schopnosť neurónových synáps meniť svoju silu ako odpoveď na stimulus, je považovaná za mechanizmus, pomocou ktorého mozog ukladá spomienky. Hoci bolo navrhnutých mnoho modelov synapatickej plasticity, zatiaľ ku všeobecnému konsenzu nedošlo. Cenným spôsobom ako overiť hodnovernosť modelu sú počítačové simulácie biofyzikálne realistického modelu neurónu s aplikáciou rovnakých protokolov stimulácie ako vo fyzickom experimente a overiť či výsledky pri rozličných podmienkach súhlasia.

Cieľ: Navrhnite a implementujte kompartmentový model CA1 pyramidálnej bunky s využitím STDP meta-plasticity na základe existujúcich modelov, a porovnajte ich vlastnosti. Zreprodukujte experimentálne výsledky ohľadom synapatickej plasticity v oblasti CA1.

Literatúra: Cutsuridis V, Graham B, Cobb S, Vida I (Eds.) (2010) Hippocampal Microcircuits: A Computational Modeler's Resource Book, Springer.

Jedlicka P, Benuskova L, Abraham WC (2015) A voltage-based STDP rule combined with fast BCM-like metaplasticity accounts for LTP and concurrent "heterosynaptic" LTD in the dentate gyrus *in vivo*. PLoS Computational Biology, 11(11): e1004588.

Carnevale, N.T. and Hines, M.L. The NEURON Book. Cambridge Univ. Press, 2006.

Školiteľ: prof. RNDr. Ľubica Beňušková, PhD.

Katedra: FMFI.KAI - Katedra aplikovanej informatiky

Vedúci katedry: prof. Ing. Igor Farkaš, Dr.

Spôsob sprístupnenia elektronickej verzie práce:

bez obmedzenia

Dátum zadania: 19.01.2017

Dátum schválenia: 14.06.2017

prof. RNDr. Rastislav Kráľovič, PhD.
garant študijného programu

.....
študent

.....
školiteľ

Acknowledgements

First and foremost, I would like to express my special thanks to my supervisor Lubica Beňušková, whose support, patience, insightful discussions and academic experiences help me to finish this PhD journey.

I would also like to thank my co-advisor Peter Jedlička, who gave me the opportunity to be part of his lab. Thank you for the advice, discussions and the possibility of professional growth during my internship at your lab and during summer schools.

I would like to express my most sincere appreciation to our head department, Igor Farkaš, for all help and support.

My colleagues, Alexander Šimko and Ivor Uhliarik, whose friendship and discussions really made this doctoral study more enjoyable.

I am eternally grateful to my parents Zlatica and Peter, sister Lucia and brother Jakub. You have been a constant source of love, emotional and moral support.

To my wonderful and incredibly supportive partner Mirka – thank you for always helping me keep things in perspective.

I hereby declare that I have worked independently based on professional scientific literature and based on consultations with the supervisors of my dissertation thesis.

.....

Abstrakt

Vo všeobecnosti je známe, že mozgové procesy súvisiace s učením a pamäťou sa odohrávajú na úrovni synáps. V závislosti od prebiehajúcej aktivity sú jednotlivé synaptické spojenia posilňované, respektíve oslabované. V neurobiológií sa tento jav nazýva synaptická plasticita. Medzi najznámejšie pravidlá synaptickej plasticity patrí Spike-Timing Dependent Plasticity (STDP) pravidlo, ktoré určuje smer a veľkosť zmeny synaptických váh na základe precízneho časovania pre- a post-synaptických udalostí (spajkov). V našej práci sme využili upravené STDP pravidlo, ktoré za postsynaptickú udalosť považuje prekročenie prahovej hodnoty lokálnym excitačným postsynaptickým potenciálom. Súčasne zahŕňa aj metaplasticitu, homeostatický mechanizmus na úrovni neurónu, ktorá reguluje veľkosť synaptických zmien v závislosti od aktivity neurónu. Našim cieľom bolo za použitia meta-STDP pravidla synaptickej plasticity modelovať experimentálne dátá namerané na hipokampálnych CA1 pyramidálnych neurónoch. V tejto práci sme využili metódy výpočtového modelovania: (1) vytvorili sme nový kompartmentálny model CA1 pyramidálneho neurónu s redukovanou morfológiou, ktorý sme validovali a porovnali s ostatnými modelmi pomocou nástroja HippoUnit, (2) na dendritický strom modelu sme podľa experimentálnych dát rozmiestnili excitačné synapsy rozšírené o meta-STDP pravidlo synaptickej plasticity, (3) stabilizovali sme synaptické váhy počas prebiehajúcej spontánnej aktivity, (4) aplikovali sme rôzne stimulačné protokoly za účelom reprodukowania experimentálnych dát a predikovania správania sa modelu pri zmenených parametroch a (5) ukázali sme význam aktívnych iónových kanálov a dendritických spajkov pri synaptickej plasticite. Naše simulácie vedú k predikcii výskytu heterosynaptickej plasticity na nestimulovaných synapsách v závislosti od ich polohy na dendritickom strome, použitom stimulačnom protokole a úrovni spontánnej aktivity. Súhrnné povedané, náš výskum *in silico* ukázal, že náš model je dostatočne biologicky presný a je vhodný na simulácie komplexných experimentálne pozorovaných vzorov homosynaptickej a heterosynaptickej plasticity.

Kľúčové slová: synaptická plasticita, metaplasticita, meta-STDP, výpočtové modelovanie, CA1 pyramidálne neuróny

Abstract

It is widely accepted that the brain processes related to learning and memory occur at the level of synapses. Individual synaptic connections are strengthened or weakened depending on the ongoing brain activity. In neurobiology, this is called synaptic plasticity. One of the best studied rules of synaptic plasticity is the Spike-Timing Dependent Plasticity (STDP) rule which defines the direction and magnitude of synaptic changes based on the precision timing of pre- and postsynaptic events (spikes). In our work, we implemented a modified STDP rule which considers reaching the threshold value by local excitatory postsynaptic potential as a postsynaptic event. The synaptic plasticity rule also includes metaplasticity, a homeostatic mechanism at the cellular level, that regulates the magnitude of synaptic changes according to previous neuronal activity. Our goal was to use our meta-STDP synaptic plasticity rule for modeling experimental data on synaptic plasticity measured in hippocampal CA1 pyramidal cells. In this work, we used computational modeling methods to: (1) develop a new compartmental model of CA1 pyramidal cell with reduced morphology and validate and compare it with other models using HippoUnit tests, (2) introduce excitatory synapses distributed along the dendritic tree according to experimental data and endow them with the meta-STDP plasticity, (3) stabilize synaptic weights during ongoing spontaneous activity, (4) apply synaptic plasticity induction protocols and reproduce experimental data and make predictions, (5) confirm the role of active ion channels in dendritic spike initiation and synaptic plasticity. Our simulations predicted the induction of heterosynaptic plasticity at unstimulated synapses, the magnitude of which depended on the level of spontaneous activity, the stimulation protocol used, and the dendritic compartment where it was observed. In summary, we conclude that our model is biologically accurate and is suitable for taking into account the complex experimentally observed patterns of homosynaptic and heterosynaptic plasticity.

Key words: synaptic plasticity, metaplasticity, meta-STDP, computational modeling, CA1 pyramidal cells

Table of Contents

1 Introduction	1
1.1 Outline.....	2
2 Neurobiology background.....	4
2.1 Learning and memory	4
2.2 Electrical activity in the neuron	5
2.2.1 The neuronal membrane	5
2.2.2 The movement of ions through the membrane	7
2.2.3 Nernst equation and the resting membrane potential.....	8
2.2.4 Action potential.....	10
2.3 Hippocampus.....	12
2.4 CA1 pyramidal neurons	13
2.4.1 Morphology.....	15
2.4.2 Sodium channels	15
2.4.3 Potassium channels	17
2.4.4 Calcium channels	18
2.4.5 Hyperpolarization-Activated Current (I_h)	19
2.5 Synaptic integration.....	19
2.5.1 Biochemistry of excitatory synaptic inputs.....	20
2.5.2 Distribution of excitatory synapses.....	21
2.5.3 Dendritic spikes	24
2.6 Synaptic plasticity	25
2.6.1 Mechanisms of long-term synaptic plasticity	26
2.6.2 Homeostatic mechanisms of synaptic plasticity	29
2.7 Summary	33
3 Mathematical and computational modeling.....	35
3.1 Computational neuroscience	35
3.2 Ordinary differential equations	36
3.2.1 Analytical solution	36
3.2.2 Numerical methods	37
3.3 Partial differential equations	39
3.4 Realistic neuron models	39
3.4.1 Passive electrical properties	40
3.4.2 Neuronal membrane dynamics	41

3.4.3	Multicompartmental model and the cable equation.....	43
3.4.4	Hodgkin-Huxley model	44
3.5	Models of synaptic plasticity.....	47
3.5.1	BCM model.....	48
3.5.2	STDP model.....	50
3.5.3	Meta-STDP model	53
3.6	Implementation.....	54
3.6.1	NEURON simulation environment.....	54
3.6.2	Code organization	57
3.6.3	Typical workflow	59
3.7	Summary	61
4	Computational model of CA1 pyramidal cell with meta-STDP stabilizes under ongoing spontaneous activity as <i>in vivo</i> (Tomko et al. 2019).....	62
4.1	Introduction	62
4.2	Methods.....	62
4.2.1	Compartmental model of the CA1 pyramidal cell	62
4.2.2	Model inputs	63
4.2.3	Synaptic plasticity	64
4.3	Results	65
5	A new reduced-morphology model for CA1 pyramidal cells and its validation and comparison with other models using HippoUnit (Tomko et al. 2021)	69
5.1	Introduction	69
5.2	Methods.....	71
5.2.1	Computational models of CA1 pyramidal cell	73
5.2.2	Tests of modified reduced-morphology models (labeled as "vTo21" at the end of the model's name; see Figure 6.6, Figure 6.7).....	76
5.2.3	Model validation by HippoUnit tests.....	76
5.2.4	Code availability	79
5.3	Results	79
5.3.1	Somatic features of tested models.....	79
5.3.2	Depolarization block test	81
5.3.3	Postsynaptic attenuation test.....	82
5.3.4	Backpropagating action potential test.....	84
5.3.5	Oblique integration test.....	87
5.3.6	Model runtimes and the importance of biophysical mechanisms for the performance of reduced-morphology models	89

6 Meta-STDP rule stabilizes synaptic weights under <i>in vivo</i> -like ongoing spontaneous activity in a computational model of CA1 pyramidal cell (Tomko et al. 2020).....	92
6.1 Introduction	92
6.2 Methods.....	92
6.2.1 Computational model of CA1 pyramidal cell	92
6.2.2 Model synaptic inputs.....	94
6.2.3 Synaptic plasticity rule.....	94
6.3 Results	95
6.3.1 Number of synapses, distribution of synapses and initial weights	95
6.3.2 Synaptic plasticity parameters	97
6.3.3 Results of simulations	97
7 Coincident activity of Schaffer and commissural pathways enables simultaneous LTP and LTD.....	100
7.1 Introduction	100
7.2 Methods.....	103
7.3 Results	105
8 Long-Term Potentiation and Depression in CA1 synapses	108
8.1 Introduction	108
8.2 Methods.....	110
8.3 Results	111
8.3.1 LTP and LTD are induced at apical and basal synapses.....	111
8.3.2 Effect of α and τ on the magnitude and direction of synaptic plasticity	114
9 Dendritic sodium spikes are required for long-term potentiation at distal synapses on hippocampal pyramidal neurons	117
9.1 Introduction	117
9.2 Methods.....	120
9.3 Results	121
9.3.1 Setting the synaptic weights.....	121
9.3.2 Effect of TTX on dendritic spikes	123
9.3.3 Effect of AP5 and nimodipine on dendritic spikes	124
9.3.4 The role of dSpikes in LTP induction at PP synapses	125
10 Discussion	128
10.1 Validation of our model using HippoUnit.....	128
10.1.1 Somatic voltage response.....	129
10.1.2 Depolarization block.....	129

10.1.3	Postsynaptic potential attenuation.....	130
10.1.4	Backpropagation of action potentials.....	131
10.1.5	Synaptic integration in dendrites	131
10.1.6	Limitation of the model	132
10.2	Stabilization of synaptic weights during ongoing spontaneous activity.....	133
10.3	Simulations of synaptic plasticity.....	134
10.3.1	Sequential stimulation protocol	134
10.3.2	High-frequency stimulation and paired-pulses stimulation protocols	136
10.3.3	Theta-burst stimulation	137
10.4	Synaptic plasticity rule	139
11	References	140
Appendix A	171
Appendix B	180

List of Tables

Table 2.1: The concentrations of various ions in the squid giant axon and outside the axon.	9
Table 5.1: Morphological structure of the To21 model.	75
Table 9.1: Dependence of EPSP amplitude on stimulus intensity.	122
Table B.1: Uniformly distributed passive parameters, active ionic conductances and reversal potentials of channels for each section of our model.	180
Table B.2: K_A, I_h conductances and reversal potential of passive current in individual sections of the model	180

List of Figures

Figure 2.1: The neuronal cell membrane.....	6
Figure 2.2: Action potential.	10
Figure 2.3: Hippocampus.	12
Figure 2.4: Dendritic structure of a CA1 pyramidal cell.	14
Figure 2.5: Sodium channels.	16
Figure 2.6: Chemical synapse.	20
Figure 2.7: Dendritic spine.	22
Figure 2.8: Schematic of the synapse strength distribution for the CA1 apical dendritic tree.	23
Figure 2.9: Action potential and dendritic spikes.	25
Figure 2.10: NMDAR-dependent LTP and LTD at hippocampal CA1 synapses.....	27
Figure 2.11: Various types of homo- and heterosynaptic plasticity.	32
Figure 3.1: The equivalent electrical circuit of a patch of membrane.	40
Figure 3.2: The behavior of the membrane potential in a RC circuit in response to an injected current.	42
Figure 3.3: A length of passive membrane described by a compartmental model (Inspired by Sterratt et al. 2011).	44
Figure 3.4: The Hodgkin-Huxley equivalent circuit (<i>HH circuit</i> 2011).	45
Figure 3.6: The BCM rule of synaptic plasticity.	49
Figure 3.7: Spike-Timing-Dependent Plasticity.	51
Figure 3.8: The UML Class diagram of the project.	58
Figure 3.9: The UML Activity diagram.	60
Figure 4.1:Compartmental model of CA1 pyramidal cell with position and number of synapses (schematic).	63
Figure 4.2: Ongoing input spontaneous activity over the period of 5s.	64
Figure 4.3: The CA1 pyramidal cell model firing at a frequency 2.56 Hz without synaptic plasticity over 10s.	66
Figure 4.4: The CA1 pyramidal cell model weights were stabilized with employed meta-STDP rule after a short transitory period.	67
Figure 4.5: The CA1 pyramidal cell model average weights in all the layers were stabilized with employed meta-STDP rule.	67
Figure 4.6: The CA1 pyramidal cell model depression and potentiation amplitudes were stabilized with employed meta-STDP rule.	67
Figure 4.7: The CA1 pyramidal cell model integrated spike count was stabilized with employed meta-STDP rule.	68
Figure 5.1: Validation of somatic voltage features, spike time features, and spike shape features using the Somatic Features Test.	73
Figure 5.2: The Depolarization Block Test expressed the ability of models to enter depolarization block under sustained input current.	82
Figure 5.3: The Postsynaptic Potential Attenuation Test evaluated the rate of attenuation of excitatory postsynaptic potentials (EPSPs) during their propagation along the apical trunk of the tested models.	83
Figure 5.4: The Backpropagating Action Potential (bAP) Test evaluates the models' ability to reproduce experimentally determined bAP attenuation.....	85

Figure 5.5: The Oblique Integration Test evaluated nonlinear dendritic integration of asynchronous and synchronous synaptic inputs in the oblique dendrites of the tested models.....	88
Figure 5.6: The final error score of all models achieved for each test.....	90
Figure 5.7: The runtimes of all models for each test.	91
Figure 6.1: Morphology and typical somatic responses of the model.	93
Figure 6.2: The CA1 pyramidal cell model depression and potentiation amplitudes were stabilized after a short transitory period with employed meta-STDP rule.	96
Figure 6.3: Evolution of the integrated spike count scaled by alpha with employed meta-STDP rule applied to the synapses of the CA1 pyramidal cell model.	98
Figure 6.4: Evolution of synaptic weights in the distal SO (left) and the proximal SO (right) of the CA1 pyramidal cell model.	98
Figure 6.5: Evolution of synaptic weights in the proximal SR (left) and the medial SR (right) of the CA1 pyramidal cell model.	98
Figure 6.6: Evolution of synaptic weights in the distal SR (left) and the SLM (right) of the CA1 pyramidal cell model.	99
Figure 6.7: Evolution of synaptic weights average in the stratum oriens, radiatum, and lacunosum-moleculare of the CA1 pyramidal cell model.	99
Figure 7.1: Position of stimulation and recording electrodes.	100
Figure 7.2: Coincident Schaffer/commissural activity induces LTP in both pathways in pentobarbital-anesthetized rats.	101
Figure 7.3: Coincident Schaffer/commissural activity induces LTP and LTD in urethane-anesthetized or freely-moving rats.	102
Figure 7.4: Coincident Schaffer/commissural activity induces LTD at both pathways at the 3 Hz level of spontaneous activity.	106
Figure 7.5: Coincident Schaffer/commissural activity induces LTP at both pathways at the1 Hz level of spontaneous activity.	107
Figure 8.1: Expression of strong and weak forms of LTP and LTD in the basal and apical dendrites of CA1 pyramidal neurons.	109
Figure 8.2: HFS induces LTP, and PP induces LTD at synapses in the basal and apical dendritic compartments of the CA1 pyramidal cell model.	112
Figure 8.3: HFS stimulation of synapses in SR results in LTP.	113
Figure 8.4: PP stimulation of synapses in SR results in LTD.	115
Figure 9.1: Application of 20 nM TTX blocks LTP induction at PP synapses (Adapted from Kim et al. 2015 with permission).	118
Figure 9.2: Proposed conceptual model for the critical role of Na-dSpikes in the induction of PP → CA1tuft LTP.	119
Figure 9.3: Model configuration.	121
Figure 9.4: Voltage recordings in response to different TBS intensities.	122
Figure 9.5: The effect of simulated TTX application on dendritic spikes.	124
Figure 9.6: The effect of simulated nimodipine application on dendritic spikes.	125
Figure 9.7: The effect of simulated AP5 application on dendritic spikes.	126
Figure 9.8: TBS stimulation protocol induces LTP at PP synapses in the presence of dendritic spikes.	127

List of Shortcuts

bAP	<i>backpropagating action potential</i>
AMPA	<i>α-amino-3-hydroxy-5-methyl-4-isoxazolepropionic acid</i>
AP	<i>action potential</i>
ATP	<i>adenosine triphosphate</i>
BCM	<i>Bienenstock-Cooper-Munro</i>
BK	<i>big conductance</i>
CA	<i>Cornus ammonis</i>
CaMKII	<i>Ca²⁺/CaM-dependent protein kinase II</i>
DG	<i>Dentate gyrus</i>
dSpike	<i>dendritic spike</i>
EC	<i>Entorhinal cortex</i>
EPSC	<i>excitatory postsynaptic current</i>
EPSP	<i>excitatory postsynaptic potential</i>
fEPSP	<i>field excitatory postsynaptic potential</i>
HVA	<i>high-voltage-activated</i>
IK	<i>intermediate conductance</i>
LEC	<i>lateral entorhinal cortex</i>
LTD	<i>long-term potentiation</i>
LTP	<i>long-term depression</i>
LVA	<i>low-voltage-activated</i>
MEC	<i>medial entorhinal cortex</i>
NMDA	<i>N-methyl-D-aspartate</i>
NO	<i>nitric oxide</i>
PSD	<i>postsynaptic density</i>
RPM	<i>resting membrane potential</i>
SK	<i>small conductance</i>
SLM	<i>stratum lacunosum-moleculare</i>
SO	<i>stratum oriens</i>
SR	<i>stratum radiatum</i>

SSt *sequential stimulation*

STDP *spike-timing dependent plasticity*

Chapter 1

1 Introduction

It is widely accepted that changes at the synaptic level, referred to as synaptic plasticity, are the mechanism underlying learning and memory. Therefore, it is important to study this phenomenon and learn more about functional consequences of different forms of synaptic plasticity including its homeostatic regulation. One way is to use computational neuroscience methods. Using biophysically realistic compartment models of neurons, researchers can explain, verify, and predict the plastic processes and behavior of different types of neurons. One of the best studied neurons is a CA1 pyramidal cell, the major excitatory neuron of the CA1 region of the hippocampus. The hippocampal network plays key roles in spatial navigation and episodic memory. However, details of plastic changes at stimulated and nonstimulated synapses and their dependence on local voltage changes have not yet been fully elucidated in the dendrites of CA1 neurons. Therefore, we decided to investigate synaptic plasticity in anatomically distinct regions in a biophysically realistic compartment model of the CA1 pyramidal cell.

The beginnings of the study of synaptic plasticity date back to the end of the 19th century. Since then, much has been found about synaptic plasticity in both the experimental and computational fields. Research by experimenters and theorists goes hand in hand. Experimenters discover the mechanisms and functions of synaptic plasticity, while theorists try to explain them using mathematical models. Hippocampus is a brain structure that is most subjected to the study of synaptic plasticity. Especially synaptic plasticity in the dentate gyrus and the CA3 and CA1 regions, which are also the primary sites of neurodegenerative diseases such as Alzheimer's disease, has been intensely studied.

The aim of this thesis is to employ the meta-STDP synaptic plasticity rule for modelling synaptic plasticity in the computational model of the CA1 pyramidal cell. The meta-STDP rule has previously been successfully used to model a phenomenon called heterosynaptic plasticity in the hippocampal granule cell (Jedlicka et al. 2015). Heterosynaptic plasticity is an important homeostatic mechanism which counteracts the changes induced by homosynaptic plasticity and balances synaptic weights. Heterosynaptic plasticity has been observed in many experimental studies in the CA1 region of hippocampus. Moreover, physiological and computational studies

showed that spike timing and state of the hippocampus play important roles in synaptic plasticity.

In this thesis, we seek to address three important goals related to the computational modelling of synaptic plasticity, namely: (1) to develop a novel well validated reduced-morphology computational model of the CA1 pyramidal neurons, (2) to test whether the reduced-morphology model endowed with the meta-STDP rule is able to keep synaptic weights stable during ongoing spontaneous activity as it happens in the hippocampus *in vivo*, and (3) to assess whether the reduced-morphology model endowed with the meta-STDP rule is able to account for complex experimentally observed patterns of homosynaptic and heterosynaptic plasticity induced by different stimulation protocols.

1.1 Outline

This thesis is organized into 10 chapters.

Neurobiology background. Chapter 2 gives a brief description of learning and memory and their relationship to the hippocampus. The hippocampus is described with a detailed focus on the neurophysiology of the CA1 pyramidal cell. The basics of the electrical activity of neurons, such as the cell membrane and ion flux through the membrane, the Nernst equation, the resting membrane potential, the action potential, and synaptic transmission, are introduced. At the end of Chapter 2, synaptic plasticity in terms of function, induction, mechanisms, and homeostasis is summarized.

Mathematical and computational modeling. In Chapter 3, basic concepts of computational modeling are discussed. Differential equations and partial differential equations are briefly explained. Mathematical background of synaptic plasticity and synaptic plasticity rules are presented. Compartmental modeling of neurons is introduced and the implementation of simulations is described.

Computational model of CA1 pyramidal cell with meta-STDP stabilizes under ongoing spontaneous activity as *in vivo*. Chapter 4 provides the results of synaptic weight stabilization in a compartment model of the CA1 pyramidal cell with the meta-STDP rule of synaptic plasticity. The model is described and the importance of stabilization weights during ongoing spontaneous activity is discussed.

A new reduced-morphology model for CA1 pyramidal cells and its validation and comparison with other models using HippoUnit. Chapter 5 introduces a new-reduced morphology model for CA1 pyramidal cells. Results of systematical testing of the model using HippoUnit are provided and discussed. Comparison of the model with other models is presented.

Meta-STDP rule stabilizes synaptic weights under in vivo-like ongoing spontaneous activity in a computational model of CA1 pyramidal cell. Chapter 6 provides the results of weight stabilization using the model presented in Chapter 5. In contrast to Chapter 4, synapses were distributed more realistically, and synaptic weights were generated from the normal distribution. The key parameters of meta-STDP and their influence on the stabilization of the whole system are discussed.

Coincident activity of Schaffer and commissural pathways enables simultaneous LTP and LTD. Chapter 7 presents the results of the first simulation of synaptic plasticity using the model from Chapter 5 and the synapse distribution from Chapter 6. A brief summary of the experimental data that were modeled are presented. The influence of the level of spontaneous activity on the direction of induced synaptic plasticity and heterosynaptic plasticity is discussed.

Long-Term Potentiation and Depression in CA1 synapses. Chapter 8 presents the results of the second simulation of synaptic plasticity using the model from Chapter 5 and the synapse distribution from Chapter 6. A brief summary of the experimental data that were modeled are presented. Finally, the explanation of the observed heterosynaptic plasticity and limitations of the model are discussed.

Dendritic sodium spikes are required for long-term potentiation at distal synapses on hippocampal pyramidal neurons. In Chapter 9, the role of dendritic sodium spikes for synaptic plasticity is discussed. Chapter 9 provides further validation of the model described in Chapter 5. The effect of dendritic sodium spikes on calcium influx through NMDAR channels and subsequent synaptic plasticity was demonstrated.

Discussion. Chapter 10 summarizes the main results of the thesis. Chapter 10 contains the main discussion of the thesis. The limitations of the thesis are also mentioned and directions and suggestions for possible future research are provided.

Chapter 2

2 Neurobiology background

In this chapter, we summarize the neurobiological background necessary for this work. We summarize some basic concepts of learning and memory and their relationship to brain structures, especially the hippocampus. We describe the structure of the hippocampus, its inputs / outputs and connectivity. We characterize the properties of the CA1 pyramidal cell in the CA1 region of the hippocampus, in which all the computational and experimental work in this thesis takes place.

We also briefly describe the basis of electrical activity in a neuron. We focus on the cell membrane, which separates the intracellular space of the neuron from the extracellular space and plays a key role in the electrical properties of a neuron. We describe the mechanisms of ion flux through the membrane, including ion diffusion and electrical drift, that are related to ion concentrations and the potential difference between the inner and outer membrane. We also briefly explain the Nernst equation, the resting membrane potential, and the generation of an action potential. Finally, we describe the principles of synaptic transmission.

In the last part of this chapter, we summarize the phenomenon of synaptic plasticity, which is the main mechanism of learning and memory. We focus on the long-term forms of synaptic plasticity, i.e., long-term potentiation (LTP) and long-term depression (LTD). We describe the mechanisms of induction and maintenance of plasticity and the homeostatic mechanism of synaptic plasticity.

2.1 Learning and memory

Learning and memory are cognitive functions. Learning can be defined as the acquisition of information and skills while subsequent retention of the information is called memory. Typically, learning and memory have three phases: encoding, storage, and retrieval (Melton 1963). Encoding refers to the acquisition and initial processing of information; storage refers to maintenance of the encoded information over time; and retrieval refers to the process by which the stored information is accessed and used.

There are several ways how to classify memory. Two main types of memory are declarative (explicit) memory and nondeclarative (implicit) memory. The declarative system of memory

has a conscious component and incorporates semantic and episodic memory. Declarative memory is thought to rely primarily on medial temporal lobe structures, including hippocampus. Nondeclarative memory, on the other hand, includes various subcomponents, of which procedural memory or formation of motor memories is the prominent. Nondeclarative memory is thought to depend mostly on striatum, cerebellum, and cortical association areas. Nondeclarative memory also includes a phenomenon called priming, simple forms of associative learning and simple forms of nonassociative learning such as habituation and sensitization (Cohen, Squire 1980; Brem et al. 2013).

Based on a temporal dimension, memory is classified into short-term memory and long-term memory. Short-term memory is essential component of cognition and is defined as the maintenance of information over a short period of time (seconds/minutes) (Brem et al. 2013). During short-term memory processing, certain parts of the brain are activated, including the prefrontal lobe and areas within the medial temporal gyrus (Coon, Mitterer 2008). Long-term memory refers to mechanisms by which acquired memories gain stability or are strengthened over time and become resistant to interference. Successful long-term storage includes several steps starting with the encoding the information, followed by short-term storage and consolidation from short-term memory to long-term memory, as well as repeated reconsolidation (Brem et al. 2013).

2.2 Electrical activity in the neuron

2.2.1 The neuronal membrane

The intracellular space of a neuron is separated from the extracellular space by the cell membrane. The intracellular space, cytoplasm, and the extracellular medium contain different concentrations of various ions. The principal ions include sodium (Na^+), potassium (K^+), calcium (Ca^{2+}), magnesium (Mg^{2+}) cations and chloride (Cl^-) anions. The charge carried by anions and cations is almost balanced on both sides of the cell membrane. Typically, the extracellular concentration of sodium is greater than its intracellular concentration. Conversely, the intracellular concentration of potassium is greater than its extracellular concentration. The distribution of ions and ion channels is heterogenous within a single neuron and across different cell types (Migliore, Shepherd 2002). They play important role in the generation of an action potential (Magee, Carruth 1999), its backpropagation into the dendritic tree (Jung et al. 1997), integration of synaptic inputs (Magee 1998) and synaptic plasticity (Jung et al. 1997). Taken together, ion channels crucially affect the electrical properties of neurons at different levels.

The neuronal membrane (**Figure 2.1**) is composed of an about 5 nm thick lipid bilayer. The lipid bilayer is made up of two layers of lipids. The hydrophobic ends of lipids point inside the membrane and the hydrophilic ends point outwards. This makes the membrane virtually impermeable to water and ions. Due to the impermeability of the membrane, a net of positively charged ions are kept on one side of the membrane and a net of negatively charged ions on the other side. This causes an electric field across the membrane (Sterratt et al. 2011).

The flow of ions through the membrane is allowed via ion channels and ionic pumps. Ion channels are macromolecular protein pores in the cell membrane providing ion transport across the membrane. They influence excitability of neuron and its physiological behavior. In general, two types of ion channels are presented in the membrane, active and passive. Active ion channels can be in two main states, open and closed. When a channel is opened, restricted class of ions can flow passively down their electrochemical gradient. This property is called selective permeability. In general, two types of ion channels are recognized by their gating mechanism. In voltage-gated channels, a change in membrane potential leads to a change in the conformation of the channel proteins and to the opening or closing of the channels. Ligand-gated channels change their state due to the binding of the ligand molecule to the extracellular receptor. Conversely, the permeability of passive ion channels is not affected by the membrane potential or any other element (Hille 2001). As part of this thesis is devoted to the optimization of the CA1 pyramidal cell model, we later discuss the individual channels in the CA1 pyramidal cell.

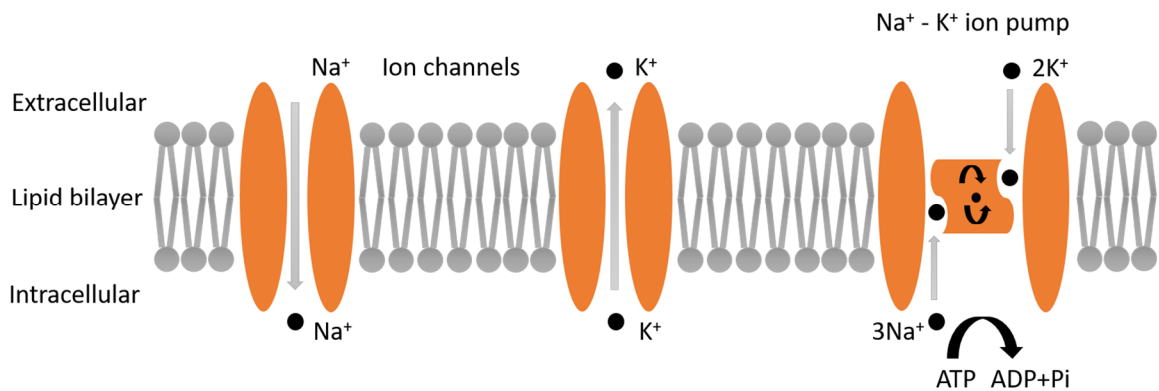


Figure 2.1: The neuronal cell membrane. The cell membrane consists of a lipid bilayer in which ion channels and ion pumps are incorporated to allow the movement of ions through the membrane (Inspired by Sterratt et al. 2011).

The ionic pumps are membrane-spanning proteins which actively push ions in and out of the cell. The transport of ions across the membrane through ion channels is in the direction of

the concentration gradient. Ions flow from higher concentration side of the membrane to lower concentration side to diminish the concentration gradient. Ion pumps counteract this process and push the ions against their concentration gradient. Each ion pump is specific for different ions. For example, the sodium-potassium exchanger pushes K^+ ions inside the cell and Na^+ ions out of the cell. For every two K^+ ions pumped into the cell, three Na^+ ions are pumped out of the cell. This requires the energy, which is provided by the hydrolysis of one molecule of adenosine triphosphate (ATP), which is a store of chemical energy in cells (Sterratt et al. 2011).

2.2.2 The movement of ions through the membrane

The net movement of particles from a region of higher concentration to a region of lower concentration is called diffusion. Diffusion is caused by the random motion of particles in liquids and gases, called the Brownian motion. The driving force of diffusion is the concentration gradient. The concentration of an arbitrary molecule or ion X is denoted $[X]$. When $[X]$ is higher on one side of the membrane than on the other side, the particles will diffuse from the higher concentration side to the lower concentration side due to the concentration gradient. The amount of X that flows through a cross-section of unit area per unit time is called flux. Units of flux are $cm^{-2}s^{-2}$, and the sign depends on the direction in which particles are flowing. By convention, flux is positive when the flow of particles is out of the cell and negative when the flow of particles is into the cell. The molar flux, $J_{X,diff}$, arising from the diffusion of molecule X , to its concentration gradient $d[X]/dx$ is:

$$J_{X,diff} = -D_X \frac{d[X]}{dx} \quad (2.1)$$

where D_X is diffusion coefficient of particle X . The negative sign indicates that the flux is in the opposite direction to that in which the concentration gradient increases (Sterratt et al. 2011).

Another type of movement of particles in the cytoplasm is the electrical drift, which is caused by an electric field. To explain this, suppose that the cytoplasm containing cations and anions is a cylindrical tube. The concentration of positive and negative ions is assumed to be uniform and therefore no ion movement along the tube occurs due to diffusion. If we place the electrodes connected to the battery at both ends of the tube so that one end has a higher electrical potential than the other end, the electric force will push the cations to the negative side of the battery and the anions will be pushed to the positive side. Since there are other particles in the cytoplasm, the individual particles will collide with each other, which prevents the acceleration of ions to the ends of the neurite. The flux of the electrical drift is:

$$J_{X,drift} = -\frac{D_X F}{RT} z_X [X] \frac{dV}{dx} \quad (2.2)$$

where z_X is ion's signed valency, R is the gas constant, T is the temperature in Kelvins, and F is the Faraday constant (Sterratt et al. 2011).

Diffusion describes the movement of ions due to a concentration gradient alone, whereas electrical drift describes the movement of ions in response to a potential gradient alone. Electrodiffusion describes the movement of ions related to the voltage and concentration. The total flux of ion X is the sum of diffusion flux and drift flux:

$$J_X = J_{X,diff} + J_{X,drift} \quad (2.3)$$

This is called Nernst-Planck equation and describe how charged ions move in solution in electric field (Sterratt et al. 2011).

The flux quantifies the number of moles of an ion flowing through a cross-section of unit area. The amount of positive charge flowing per unit of time past a point conductor, such as ion channel or neurite, is called current and is measured in amperes (A). The current density is the amount of charge flowing per unit of time per unit of cross-sectional area. The current density is denoted with the symbol I , the units are μAcm^{-2} , and is expressed as:

$$I_X = F z_X J_X \quad (2.4)$$

where I_X is the molar flux the ion X , z_X is ion's signed valency, and F is the Faraday's constant. The sign of the current depends on the direction in which the charged particles flowing. Thus, the current will be positive for cations when they are flowing outside the cell and negative when they flow inside the cell. The total current density flowing in a neurite or through a channel is the sum of the contribution from the individual ions (Sterratt et al. 2011).

2.2.3 Nernst equation and the resting membrane potential

The neuron membrane is at equilibrium when there is no net moving of ions through the membrane. The number of positive ions flowing from the extracellular space to the intracellular space due the electrical drift is equal to the number of positive ions flowing out of the cell because of the electrical drift. At equilibrium, a stable potential difference across the membrane, called the equilibrium potential, can be measured. The equilibrium potential for a single ion (E_X) can be calculated by the Nernst equation (1888):

$$E_X = \frac{RT}{z_X F} \ln \frac{[X]_{out}}{[X]_{in}} \quad (2.5)$$

where X is the membrane permeable ion, $[X]_{out}$ and $[X]_{in}$ are extracellular and intracellular concentrations of X , R is the gas constant, T is the temperature, and F is the Faraday constant (Sterratt et al. 2011).

As an example, consider the equilibrium potential for K^+ in the giant squid axon. Substituting the values from **Table 2.1** into the Nernst equation:

$$E_K = \frac{RT}{z_K F} \ln \frac{[K]_{out}}{[K]_{in}} = \frac{(8.314)(279.3)}{(+1)(9.648 \times 10^4)} \ln \frac{20}{400} = -72.1 \text{ mV} \quad (2.6)$$

we calculated the equilibrium potential for K^+ at the recording temperature 6.3°C (279.3 K).

Table 2.1: The concentrations of various ions in the squid giant axon and outside the axon. The equilibrium potentials are calculated using the Nernst equation, assuming the temperature of 6.3°C .

ion	K^+	Na^+	Ca^{2+}	Cl^-
Concentration inside (mM)	400	50	10^{-4}	40
Concentration outside (mM)	20	440	10	560
Equilibrium potential (mV)	-72	57	139	-64

The resting membrane potential is defined as the electrical potential difference across the membrane when the cell is in a non-excitatory state. This means, there is a balance between the concentration of the ions and permeability of the ions at both outside and inside of the cell. The Nernst equation describes situation when a membrane is permeable for one ion. However, the neuronal membrane is permeable for more than one type of ions. Thus, the resting membrane potential must lie between the equilibrium potentials of the individual ions. A quantitative prediction of the resting membrane potential describes the Golding-Hodgkin-Katz voltage equation:

$$E_m = \frac{RT}{F} \ln \frac{\left(\sum_{i=1}^{N^+} P_{i+} [i^+]_{out} + \sum_{i=1}^{N^-} P_{i-} [i^-]_{in} \right)}{\left(\sum_{i=1}^{N^+} P_{i+} [i^+]_{in} + \sum_{i=1}^{N^-} P_{i-} [i^-]_{out} \right)} \quad (2.7)$$

where P_{i+} is the permeability of i th positive charged ion, P_{i-} is the permeability of i th negative charged ion, $[i^{+(-)}]_{out(in)}$ is the intracellular (extracellular) concentration of i th ion, R is the gas constant, T is the temperature, and F is the Faraday constant. The resting membrane potential of the squid giant axon is around -65 mV (Sterratt et al. 2011).

2.2.4 Action potential

The primary function of neurons is to integrate synaptic inputs and convert them to an action potential (AP). Thus, the most of neurons communicate via action potentials which are mediated by voltage-gated Na^+ and voltage-gated K^+ channels. The simplest view is that the excitation and inhibition inputs sum up, and when the resulting depolarization exceeds a threshold level (about -55 mV), the action potential is initiated (Spruston et al. 2016). This can be also caused by a brief pulse of injected current.

Action potentials are typically initiated in the axon hillock. There are several reasons why. The density of sodium channels in the axon initial segment is significantly higher than in the soma (Hu et al. 2009), which contributes to a lower threshold for action potential in the axon. Simultaneous recording from axon and soma provided direct evidence that the action potential occurs first in the axon and later in the soma (Colbert, Johnston 1996).

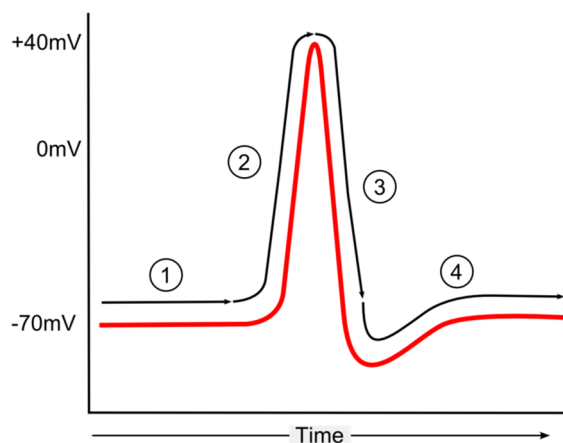


Figure 2.2: Action potential. (1) The resting membrane potential. (2) Stimulus starts the rapid change in membrane voltage or action potential. Opening of Na^+ channels cause depolarization. (3) When the membrane potential reaches the peak value, the sodium channels are closed, the potassium channels are opened, and the potassium efflux leads to repolarization of the membrane. (4) Hyperpolarization is a lowered membrane potential than the resting membrane potential. This is because more potassium channels open during the repolarization phase than during the resting membrane's state. The return to the steady state continues as additional potassium channels close (*Action potential schematic* 2017).

When the threshold is reached, a large number of voltage-gated Na^+ channels are opened allowing sodium ions to diffuse into the axon. This causes massive depolarization of the neuron as the membrane potential reaches 0 mV and then become positive. This phase is called the rising phase of action potential or the depolarization phase (**Figure 2.2**).

When the action potential reaches the peak, which is equal to the Na^+ equilibrium potential, sodium channels close and potassium channels open. This allows potassium flow out of the cell which returns the membrane potential back to the resting state. This phase is called the falling phase of action potential or repolarization (**Figure 2.2**). The potassium efflux can cause an overshooting of the resting state of membrane potential and cell becomes hyperpolarized. This phase is called hyperpolarization or after hyperpolarization potential (AHP). Potassium channels close and the membrane potential returns to a resting state. During this phase, known as the refractory period, subsequent action potential is impossible or difficult to generate (**Figure 2.2**). Once the membrane potential returns to a resting state, a new action potential can be generated.

The refractory period can be divided into an absolute refractory period and a relative refractory period. During the absolute refractory period, the sodium channels are in an inactivated state, and no action potential can be triggered. However, in the next relative refractory period, a sufficient number of sodium channels transition into their resting state and a stronger-than-usual stimulus can trigger a new action potential. The mathematical description of the Hodgkin-Huxley model of action potential will be introduced in Chapter 3 (see Hodgkin-Huxley model).

This description of an action potential applies to a small patch of membrane. Then, the self-amplifying depolarization of the patch membrane is sufficient to depolarize neighboring regions of the membrane. This causes the same cycle, and the action potential can propagate as a wave from the initial site of depolarization until it reaches the axon terminal to initiate synaptic transmission. Due to inactivation of sodium channels during the refractory period, action potentials spread in the axon only in one direction (Alberts et al. 2008).

Since the action potential is generated also in the soma, it can propagate back to the dendrites as a backpropagating action potential (bAP) (**Figure 2.9**) (Spruston et al. 2016). In pyramidal neurons, bAP spreads in apical, basal, and radial oblique dendrites (Frick et al. 2003; Nevian et al. 2007). Several factors affect the spread of bAP in the dendritic tree. The high density of potassium channels promotes back-propagation (Hoffman et al. 1997), while prolonged inactivation of dendritic sodium channels attenuates bAP (Colbert et al. 1997). It is similar with synaptic inputs, where excitatory synaptic inputs support the spread of bAPs into dendrites (Hoffman et al. 1997) and inhibitory ones weaken it (Tsubokawa, Ross 1996). An important factor is also the morphology of the dendritic tree, more precisely the branching

points at which bAP propagation may fail (Spruston et al. 1995; Golding et al. 2001). During the propagation of bAP in the apical trunk, its amplitude is attenuated. CA1 pyramidal cells show a dichotomy in the propagation of bAP, where one type of neuron shows a strong attenuation in the region of about 300 mm from the soma and the other type a weak attenuation. These types are classified as weakly-propagating or strongly-propagating neurons, respectively (Golding et al. 2001).

2.3 Hippocampus

The hippocampus is a brain structure located in the medial temporal lobe of the brain. It plays important roles in multiple cognitive functions, especially the long-term memory. It is involved in episodic memory, formation of new memories, their consolidation, storage, and recall of old memories (Moscovitch et al. 2016). Spatial memory and navigation are provided by the hippocampal place cells and their entorhinal counterparts (Moser et al. 2017).

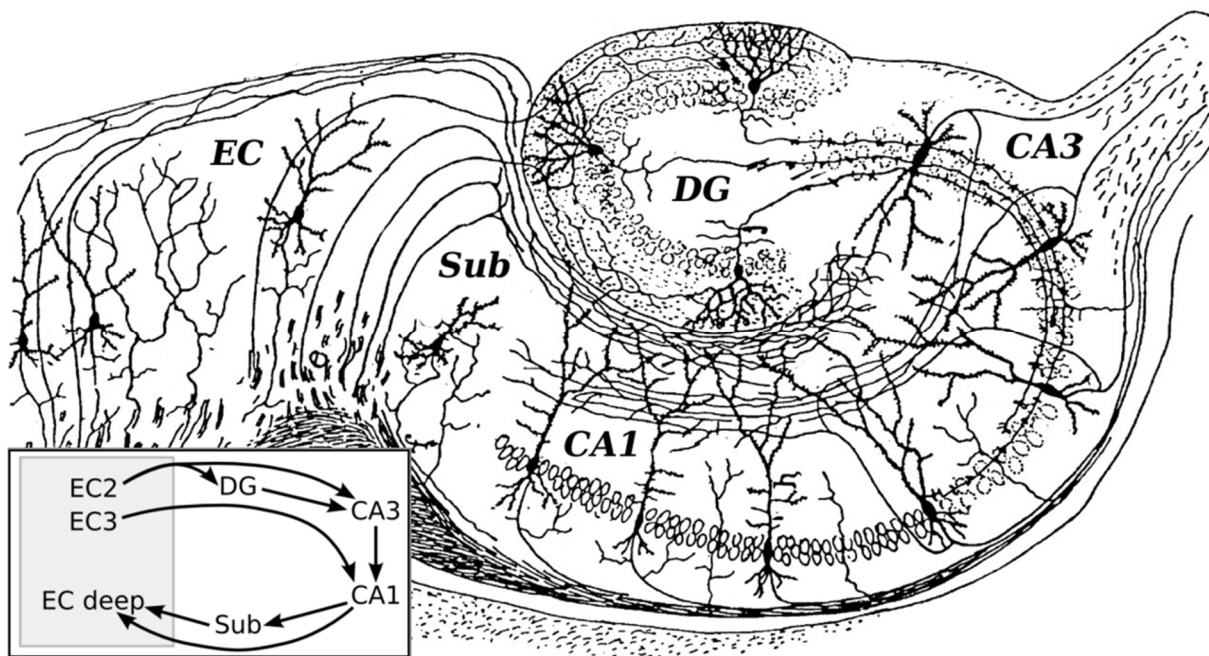


Figure 2.3: Hippocampus. Anatomy and the main pathways in the hippocampus (*Hippocampal formation* 2008). EC = entorhinal cortex, DG = dentate gyrus, CA3 = CA3 region, CA1 = CA1 region, Sub = subiculum.

The hippocampal formation is a compound structure and consists of three main areas: the dentate gyrus (DG), the hippocampus proper (Cornus Ammonis, CA) and the subiculum. The hippocampus proper is divided into the CA1 (close to the subiculum), the CA2 and the CA3 regions (**Figure 2.3**). The hilus forms interface between the dentate gyrus and the CA3 region. The entorhinal cortex (EC) is an adjacent structure to the hippocampus and plays the role of an input / output gateway for the flow of information to and from the hippocampal formation. The

EC is subdivided into a medial (MEC) and a lateral (LEC) part. The MEC receives visuospatial sensory inputs originated in the sensory cortices. Information from the amygdala, prefrontal cortex and hypothalamus are received by the LEC (Cutsuridis, Graham, et al. 2010).

The EC is the source of the perforant pathway, which projects to all sub-regions of the hippocampal formation. Entorhinal layer II projects to the dentate gyrus and CA3, whereas layer III projects to CA1 and the subiculum. The polysynaptic pathway, an extended version of the traditional tri-synaptic pathway, describes a unidirectional route that connects all sub-regions of the hippocampal formation sequentially. The dentate granule cells give rise to the mossy fiber pathway which targets the CA3 region. The CA3 axons called Schaffer collaterals project to CA1 and lastly CA1 pyramidal cells project to the subiculum. Output from the hippocampal formation arises in CA1 area and the subiculum and is directed to the parahippocampal region, in particular to the deep layers of the EC (**Figure 2.3**). (Cutsuridis, Graham, et al. 2010).

2.4 CA1 pyramidal neurons

Pyramidal neurons are one of the best studied classes of neurons. They were first discovered by Santiago Ramón y Cajal. Pyramidal cells are multipolar neurons that are found in various parts of the brain, including the cerebral cortex, hippocampus and amygdala. In the CA1 region of the hippocampus, the CA1 pyramidal cells are the major excitatory cells. They receive excitatory inputs from two main sources: (1) the CA3 pyramidal cells send their axons from the same hemisphere as the Schaffer collateral and from other hemisphere as the commissural pathway to the CA1 pyramidal cells and process an indirect information from the entorhinal cortex via the trisynaptic loop; (2) the temporoammonic (perforant) pathway which provides a direct information from the entorhinal cortex. CA1 pyramidal cells next project their axons to the subiculum (Ramon y Cajal 1995; Amaral, Witter 1989; Amaral et al. 1991).

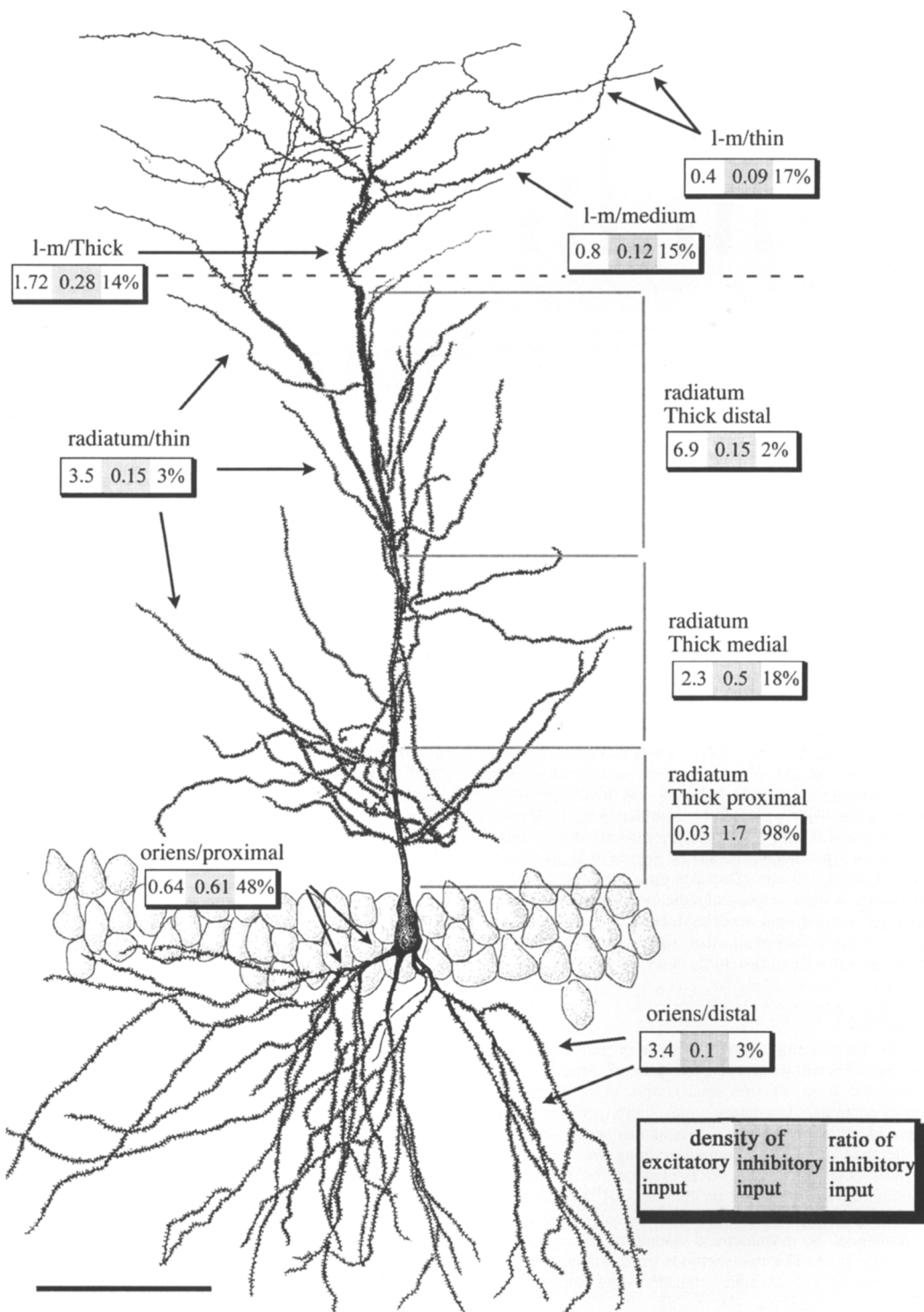


Figure 2.4: Dendritic structure of a CA1 pyramidal cell. The drawing illustrates the subclasses of dendrites. For every dendritic subclass, the density of excitatory, inhibitory (left and middle numbers, respectively, number/l μm) and the ratio of inhibitory synapses (right number) are shown. Scale bar= 100 μm (Adapted from Megías et al. 2001. Copyright 2021, Elsevier. With permission from Elsevier.).

2.4.1 Morphology

CA1 pyramidal cells are the principal excitatory cells of the CA1 region of the hippocampus. Characteristic triangular cell bodies with a diameter of $\sim 15 \mu\text{m}$ and a surface area of $465 \pm 50 \mu\text{m}^2$ are located in the stratum pyramidale. The basal dendritic tree in the stratum oriens is formed from two to eight dendrites which originate from the base of the soma. The diameter of the basal dendrites decreases with increasing distance from the soma. The apical dendritic tree of the CA1 pyramidal cells typically consists of one thick apical trunk. In the stratum radiatum, nine to thirty oblique dendrites emerge from the apical trunk. They have a similar branching pattern as the basal dendrites, while the most of branching points occur close to the origin of the dendrite. The apical trunk usually ends in several bifurcations that form the apical tuft in the stratum lacunosum-moleculare (**Figure 2.4**) (Bannister, Larkman 1995; Megías et al. 2001).

The axon typically originates from the base of the soma. The axon is directed downwards and can give off several collaterals. Axon provides excitatory inputs to the subiculum and entorhinal cortex. In addition, the axon targets inhibitory cells, specifically somatostatin-immunopositive, O-LM interneurons, providing a feedback inhibition (Katona et al. 1999; Maccaferri et al. 2000).

2.4.2 Sodium channels

Voltage-gated sodium currents were first recorded and mathematically described by Hodgkin and Huxley (Hodgkin, Huxley 1952). Sodium channels play a major role in the action potential initiation and propagation in the CA1 pyramidal cells. They are expressed in all three functional compartments of CA1 pyramidal cell compartments i.e., axon, soma and dendrites (Stuart et al. 1997). Voltage-gated sodium channels are formed by one large pseudotetrameric α subunit that is associated with one or two β subunits. In the CA1 pyramidal cells membrane, Nav1.1, Nav1.2, Nav1.6 subtypes are present (Lorincz, Nusser 2010; de Lera Ruiz, Kraus 2015).

Voltage-gated sodium channels have three conformational states: closed, open and inactivated (**Figure 2.5**). At the resting membrane potential, sodium channels are in the closed state. Sufficient membrane depolarization causes the activation gates open, and channels are permeable for sodium ions. The influx of Na^+ ions results in strong membrane depolarization, which is associated with a rising phase of the action potential. At the peak of the action potential, the membrane is strongly depolarized, which causes the closing of the inactivation gates thereby transforming the sodium channels into the inactivated state. In this state, the ion

channels are impermeable. The membrane potential stops rising and decreases to its resting value thanks to opening of potassium ion channels. During this phase no new action potential can be initiated. All ion channels are in the closed state and after the refractory period are ready to participate in a new action potential (Hodgkin, Huxley 1952).

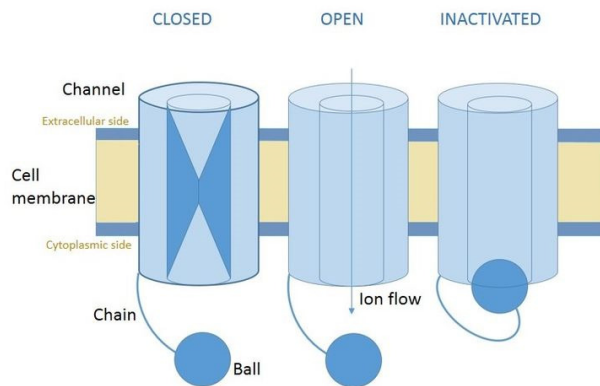


Figure 2.5: Sodium channels. The figure shows three conformational states of sodium channels: close, open, and inactivated (Inactivation diagram 2015).

Two major types of sodium currents mediated by voltage-gated sodium channels are known in CA1 pyramidal cells. The transient Na^+ current (I_{NaT}) is activated rapidly and inactivated within 1-2 ms and mediates the fast upstroke of action potentials in the action potential initiation segment(Hodgkin, Huxley 1952; Royeck et al. 2008; Uebachs et al. 2010). The density of sodium channels mediating I_{NaT} is in the action potential initiation segment ~50 more times that in the proximal dendrites (Kole et al. 2008). In dendrites, the density gradually decreases as function of distance from the soma (Lorincz, Nusser 2010).

The persistent Na^+ current (I_{NaP}) has slowly inactivating (or noninactivating) characteristics and more negative activation voltage than I_{NaT} (Crill 1996). The density of sodium channels mediating I_{NaP} gradually increases along the proximodistal axis (Mickus et al. 1999). The persistent sodium current modulates axonal excitability (Müller et al. 2018) and plays critical role in hippocampal gamma oscillations (Kang et al. 2020). It also contributes to the voltage dependence of spatial coding in CA1 pyramidal cells (Hsu et al. 2018).

Sodium channels are also involved in the initiation of dendritic spike. Dendritic sodium spikes are elicited by excitatory synapses and spread forward and backward from the site of initiation. By depolarizing the membrane, they are facilitating the opening of Ca^{2+} channels and the influx of Ca^{2+} and play important role in associative synaptic plasticity. Moreover,

some of dendritic spikes are initiated without occurrence of somatic spike (Colbert et al. 1997; Golding, Spruston 1998; Kim et al. 2015).

2.4.3 Potassium channels

The main function of potassium channels is to conduct potassium ions down their electrochemical gradient. They have a negative reversal potential, so they are active at the peak of action potential and act during the repolarization phase of an action potential. They set the membrane resting potential and modulate neuronal firing (Hille 2001). Four main types of potassium channels are known: voltage-gated, leak, inward-rectifying and voltage-dependent calcium-activated. In the following section, we briefly characterize the most important of them.

Multiple types of voltage-gated potassium channel are expressed in CA1 pyramidal cells which include an A-type potassium channel, a D-type potassium channel, an M-type potassium channel and a delayed-rectifier potassium channel (Storm 1990; Hoffman et al. 1997; Martina et al. 1998). The A-type potassium channels are characterized by a rapid time-dependent inactivation, and contribute to the majority of the total somatic K^+ current (Chen, Johnston 2004). In the somatodendritic compartment, their density progressively increases with the distance from the soma (Hoffman et al. 1997). The A-type potassium channels have impact on action potential shape, back-propagation of action potential (Hoffman et al. 1997; Kim et al. 2005), synaptic integration (Cai et al. 2004) and long-term potentiation (Watanabe et al. 2002).

The D-type potassium current is slowly-inactivating outward current. It is very little known about the distribution of D-type potassium channels, except that they have low-density distribution in the dendrites (Chen, Johnston 2004). They play a role in the regulation of dendritic calcium spike initiation (Golding et al. 1999) and inhibition of the spike afterhyperpolarization (Metz et al. 2007).

The M-type current is a true non-inactivating current because it is not inactivated with prolonged membrane depolarization. The M-type currents deactivate with a slow kinetics. These channels are expressed at very low density in the somatodendritic compartment in the CA1 pyramidal cells (Chen, Johnston 2004). The M-type potassium currents contribute to somatic bursting (Golomb et al. 2006; Gu et al. 2007) and to switching between persistent firing and depolarization block (Knauer, Yoshida 2019).

The delayed-rectifier potassium channels represent the majority of the sustained K⁺ current uniformly distributed along the apical dendrites. The delayed rectifier K⁺ current has very slow inactivation kinetics and therefore it does not appear to inactivate during several hundred milliseconds (Chen, Johnston 2004). They regulate action potential repolarization, the action potential properties, and firing patterns in CA1 pyramidal neurons (Liu, Bean 2014; Palacio et al. 2017).

The calcium-dependent potassium channels are widely expressed in the central nervous system. They are dually activated by voltage and by an increase in intracellular calcium concentration. The family of Ca²⁺-dependent K⁺ channels is divided into three subtypes based on their single channel conductance: small (SK), intermediate (IK) and big conductance potassium (BK) channels. They mediate afterhyperpolarization as well as action potential repolarization (Johnston et al. 2000; Faber, Sah 2003; Kshatri et al. 2018). SK channels are highly expressed in dendritic spines of CA1 pyramidal cells, where they become activated by the Ca²⁺ influx through N-methyl-D-aspartate (NMDA) receptors (Ngo-Anh et al. 2005; Wang et al. 2014). In dendrites, they can be activated also by the back-propagating action potential and thus play a key role in regulating both excitatory postsynaptic potential (EPSP) amplitude and STDP induction (Jones et al. 2017). SK channels are also presented in the soma and proximal dendrites of CA1 pyramidal neurons where they regulate their intrinsic excitability (Chen et al. 2014). Like SK channels, BK channels are expressed in the somatic region and in the pre- and post-synaptic compartments. They play an important role in the repolarization of an action potential, high-frequency firing and modulation of excitatory synaptic transmission (Sailer et al. 2006; Gu et al. 2007; Zhang et al. 2018; Gutzmann et al. 2019). BK channels facilitate high-frequency firing via fast spike repolarization, fAHP generation and by affecting Na⁺ channel inactivation and activation of other K⁺ channels (Gu et al. 2007).

2.4.4 Calcium channels

Two subgroups of voltage-gated calcium channels are known. The low-voltage-activated (LVA) calcium channels are activated after small membrane depolarization while the high voltage activated (HVA) calcium channels are activated by larger membrane depolarization (Lacinová 2005). The L-type calcium channels are present throughout the CA1 pyramidal cell dendrites, with the highest density in the proximal dendrites (Magee et al. 1996; Leitch et al. 2009). These channels, together with NMDA receptors, are involved in the induction of long-term potentiation in the CA1 region (Freir, Herron 2003; Wiera et al. 2017) as well as in the

long-term depression (Udagawa et al. 2006). The N-type calcium channels are located on the soma, dendrites, and spines (Mills et al. 1994). Like the L-type calcium channels, they are involved in long-term synaptic changes, both potentiation (Ali, Nelson 2006) and depression (Normann et al. 2000). Other substantial voltage-gated calcium channels are R-type and T-type channels. They play an important role in the generation of somatic afterdepolarization and action potential burst firing (Magee, Carruth 1999) as well as in synaptic plasticity (Takahashi, Magee 2009; Chen et al. 2012).

2.4.5 Hyperpolarization-Activated Current (I_h)

The hyperpolarization-activated current is an inward current activated by hyperpolarization more negative than ~ 60 mV (Maccaferri et al. 1993). The density of I_h increases over six-fold from soma to distal dendrites. The activation and deactivation kinetics of I_h are voltage- and temperature-dependent, with the time constants of activation and deactivation decreasing with hyperpolarization and depolarization, respectively. The regional differences in R_{in} and membrane time constant across the somatodendritic axis are attributable to the spatial gradient of I_h . The increased I_h density decreases EPSP amplitude and duration, thus it damps dendritic excitability (Magee 1998; Surges et al. 2004). Together with the sodium current, they regulate the subthreshold behavior of CA1 neurons, where I_h acts to decrease R_{in} and the membrane time constant, and sodium current, on the other hand, increases both (Yamada-Hanff, Bean 2015). Endogenous and exogenous activation of cannabinoid receptors modulates I_h current in CA1 neurons. Activation of this pathway decreases integration of excitatory synaptic inputs as well as LTP and limits spatial memory formation whereas its inhibition enhances dendritic integration and LTP (Maroso et al. 2016).

2.5 Synaptic integration

Synaptic integration is the biochemical and biophysical process by which individual neuron processes its synaptic inputs and converts them into an output signal (Etherington et al. 2010). There are many factors involved in this process such as membrane conductances, morphology of dendritic tree, size and relative timing of synaptic inputs, summation of inhibitory and excitatory inputs and location of synaptic inputs. In this section, we describe the biochemistry of excitation inputs, their distribution along the dendritic tree, and the role of dendritic spikes in synaptic integration.

2.5.1 Biochemistry of excitatory synaptic inputs

Chemical synapses are divided into excitatory or inhibitory, depending on how the release of neurotransmitters affects the induction of an action potential. When the action potential arrives at the presynaptic boutons, a cascade of biochemical reactions is triggered, resulting in the release of the neurotransmitter into the synaptic cleft. Binding of the transmitter to receptors at the postsynaptic membrane causes opening of ion channels (mixed Na^+/K^+ / Ca^{2+} channels in the excitatory synapse). The influx of positive ions through the membrane depolarizes the membrane and generates an excitatory postsynaptic potential (**Figure 2.6**) (Hille 2001; Chua et al. 2010).

The main excitatory transmitter in the hippocampus is glutamate which plays a primary role in synaptic plasticity. Two main classes of glutamate receptors mediate the action of glutamate: ionotropic and metabotropic receptors. For the purpose of this thesis, I focus on two ionotropic glutamate receptors: AMPA (α -amino-3-hydroxy-5-methyl-4-isoxazolepropionic acid) and NMDA (N-methyl-D-aspartate) receptors (Dingledine et al. 1999).

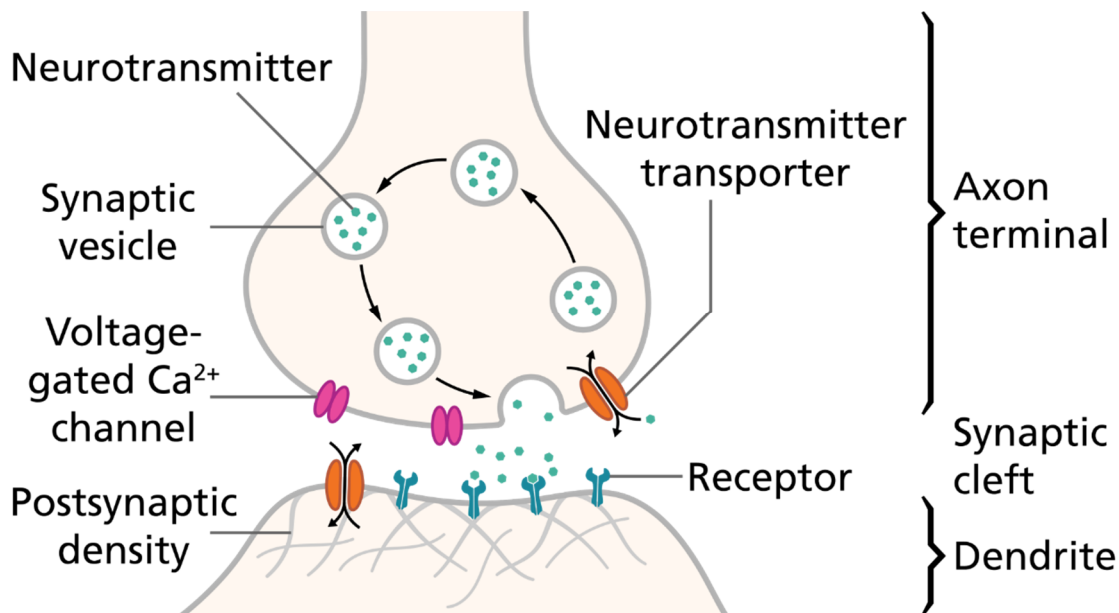


Figure 2.6: Chemical synapse. The presynaptic axonal ending (top) releases a neurotransmitter, which activates receptors on the nearby postsynaptic cell (bottom) (*Chemical synapse* 2015).

AMPA receptors are ligand-gated ion channels composed of various combinations of GluR1 – GluR4 subunits. In hippocampus, most of AMPA receptors are heterooligomers composed of GluR1/GluR2 or GluR2/GluR3 subunits. The subunit composition plays important role in the ion permeability and receptor trafficking dynamics (Wenthold et al. 1996; Shi et al. 2001). The presence or absence of the GluR2 subunit in the receptor complex

determines the permeability to calcium. The presence of the GluR2 subunit results in low conductance and calcium impermeability. On the other hand, GluR2-lacking AMPA receptors have higher conductance and are calcium permeable. However, the subunit composition of AMPA receptors can be dynamically altered by synaptic activity thereby contributing to synaptic plasticity (Derkach et al. 2007).

NMDA receptors are heteromultimers of NR1 and NR2A – D subunits. They have slower kinetics compared to the AMPA receptors. NMDA receptors act as coincidence detectors because they require both presynaptic and postsynaptic activity to open the ion channel. Presynaptic activity results in the release of glutamate, which then binds to and activates the receptor. Postsynaptic activity mediated by the AMPA receptors causes membrane depolarization and removal of the magnesium block from the NMDA receptors. The open NMDA receptor allows the flow of calcium, sodium, and potassium ions (McBain, Mayer 1994). NMDA receptors play a crucial role in some forms of synaptic plasticity (see below) (Malenka, Nicoll 1993; Tsien et al. 1996; Volianskis et al. 2015).

2.5.2 Distribution of excitatory synapses

The CA1 pyramidal cells receive synaptic excitatory synaptic inputs from three main sources. The Schaffer collaterals originate in the CA3 pyramidal cells of the same hemisphere and the commissural pathway in the CA3 pyramidal cells of different hemisphere terminate in dendrites in the stratum radiatum and stratum oriens. Distal apical dendrites in the apical tuft receive synaptic inputs predominantly from the entorhinal cortex (Amaral, Witter 1989).

A single CA1 pyramidal cell receives ~30,000 excitatory and 1,700 inhibitory inputs. Excitatory inputs target primarily dendritic spines, small mushroom-like membrane extensions that play important role in synaptic transmission and information storage (**Figure 2.7Figure 2.4**). The spine coverage of the dendrites increases with increasing distance from the soma. In contrast, the inhibitory inputs target dendritic shafts, and they are predominantly located in the proximal parts of basal and apical dendrites. Inhibitory inputs also target the soma. However, a situation in the stratum lacunosum-moleculare is slightly different. The dendritic tuft is less covered by the spines than distal dendrites in the stratum radiatum, and the coverage decreases with dendritic thickness. Excitatory inputs contacts not only dendritic spines but also dendritic shafts. In addition, the ratio of inhibitory inputs is higher than in the stratum radiatum or oriens (Megías et al. 2001).

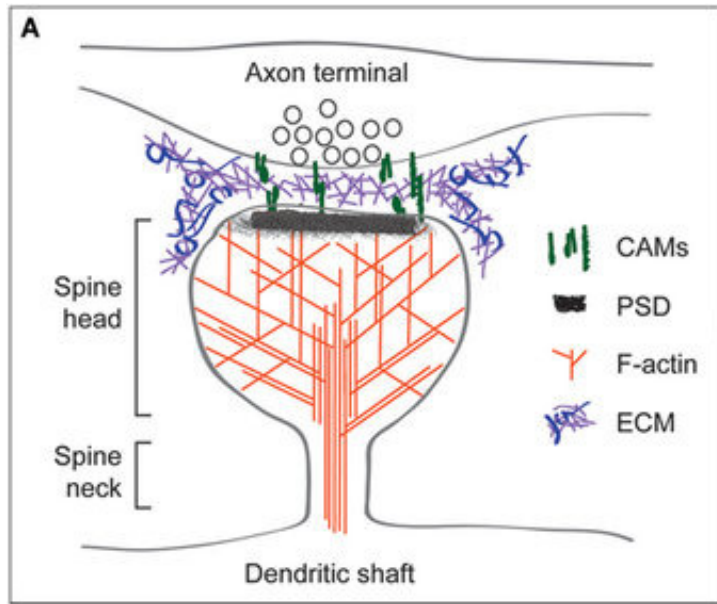


Figure 2.7: Dendritic spine. The spine head and neck are supported by a network of filamentous (F)-actin. Postsynaptic cell adhesion molecules (CAMs) connect to the postsynaptic density (PSD) and F-actin in the spine and extend from the spine to associate with CAMs on the presynaptic terminal. Perisynaptic and putative synaptic cleft extracellular matrix (ECM) may interact with multiple CAMs and other cell surface receptors (Adapted from Levy et al. 2014 with permission).

Dendrites receive majority of synaptic inputs. Evoked synaptic potentials spread towards the soma and contribute to neuronal output. Dendrites behave as leaky electrical cable and filter electrical signal passing through them (Häusser 2001). The voltage attenuation along the CA1 pyramidal cell is large. Steady-state potential attenuates to 50% at a distance of 280 μm from the soma. On the other hand, synaptic potentials induced on small distal dendrites were more than 100-fold attenuated during spread into the soma. Several factors contributing to the voltage attenuation were identified; including high axial resistivity, low membrane resistivity, and the I_h conductance which is higher in dendrites than the soma (Golding et al. 2005). In this case, the proximal synapses will be more effective in generating action potential than their distal counterparts, and the system will be "undemocratic." However, neurons have compensatory mechanisms for dendritic filtering (see also below), and each synapse may contribute equally to neuronal output (Häusser 2001).

Distribution of synapses and their strength are factors that seem to be finely regulated to compensate dendritic filtering. In the apical dendrites of CA1 pyramidal cells, the expression of AMPA receptors increases with distance from the soma, which is connected with increased number of strong synapses in distal dendrites. Synapses with a higher number of AMPA receptors are stronger, thereby reducing the localization dependence of unitary somatic

excitation potentials (Magee, Cook 2000; Andrásfalvy, Magee 2001; Smith et al. 2003; Nicholson et al. 2006). In an individual oblique dendrite, which radiates from the apical trunk, the spine density (which corresponds to the number of synapses) is approximately 50% greater in near-branch-origin segments compared to those near branch ends. Concurrently, the near-branch-origin synapses are about half as strong as the near-branch-end synapses. This scaling normalizes the contribution of individual synapse to the generation of dendritic spike and reduces the location-dependence of the synapses (**Figure 2.8**) (Katz et al. 2009). The situation in the basal dendrites is similar. The number of synapses decreases with a distance from the soma. However, the number of AMPA receptors (which is proportional to synaptic strength) increases and the number of NMDA receptors decreases with a distance from the soma. The higher number of AMPA receptors in the distal parts of dendrites compensates dendritic filtering and results in location-dependent somatic EPSPs (Magee, Cook 2000; Menon et al. 2013).

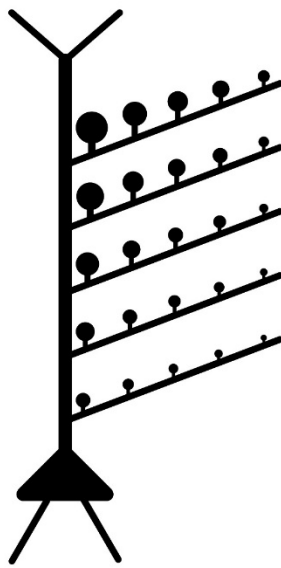


Figure 2.8: Schematic of the synapse strength distribution for the CA1 apical dendritic tree. The strength of synapses (depicted as the spine head size) increases with distance from the soma. In an individual branch, the near-branch-origin synapses are about half as strong as the near-branch-end synapses (Adapted from Katz et al. 2009. Copyright 2021, Elsevier. With permission from Elsevier.)

The distance of distal apical synapses in the apical tuft from the soma is more than 300 μm and therefore the activation of somatic spikes in the CA1 neurons by these synapses is limited. The number of synapses in the apical tuft is maintained at the same level as in the distal part of stratum radiatum dendrites. In contrast to stratum radiatum synapses, the number of AMPA receptors is the lowest in the stratum lacunosum-moleculare synapses and therefore

these synapses are weaker (**Figure 2.8**). These results suggest that this type of conductance scaling does not appear to extend to the stratum lacunosum-moleculare. NMDA receptors do not scale with distance from the soma. (Nicholson et al. 2006). However, the NMDA/AMPA ratio is highest in the stratum lacunosum-moleculare (Otmakhova et al. 2002). These observations imply another, dendritic spike-related compensatory mechanism for distal synapses in the apical tuft. Dendritic spikes act as a boosting mechanism for this synapse. Dendritic spikes can be triggered easily by brief burst of synaptic activity. The forward propagation of dendritic spikes along the apical tuft can be facilitated by modest activation of synapses in the stratum radiatum and they may contribute to neuronal output (Jarsky et al. 2005; Nicholson et al. 2006).

2.5.3 Dendritic spikes

Dendritic spikes (dSpikes) can be generated on the dendrites of the pyramidal neurons under similar conditions as the action potentials in the axon (**Figure 2.9**). The threshold for dSpikes initiation is approximately 10 mV more depolarized than for the soma (Gasparini et al. 2004). Dendritic spikes are mediated by the activation of voltage-gated Na^+ , Ca^{2+} channels, or NMDA-receptors, which results in sodium spikes, calcium spikes, or NMDA spikes, respectively (Figure 2.9) (Spruston et al. 2016). An important role here is also played by the K^+ channels, which together with the Na^+ channels set the threshold and determine the shape and propagation of the dSpikes (Gasparini et al. 2004). Exceeding the dSpikes initiation threshold can also occur by strong excitation by synapses that are highly synchronously activated (Losonczy, Magee 2006).

Dendritic spikes can remain localized to a particular part of the dendritic tree and thus have minimal effect on the somatic membrane potential. In this case, they occur without somatic action potential. The main reason why dSpikes propagation fails is that they are generated predominantly on thin dendrites that have a high impedance. The forward propagation toward thicker dendrites with a low impedance requires more current to depolarize and therefore the propagation of dSpikes fails. However, activation of neighboring dendrites can help to bridge this barrier, resulting in sufficient depolarization. If dSpikes are successfully propagated to the soma, depolarization of the soma may be sufficient to exceed the threshold and generate an action potential (Gasparini et al. 2004; Jarsky et al. 2005; Spruston et al. 2016).

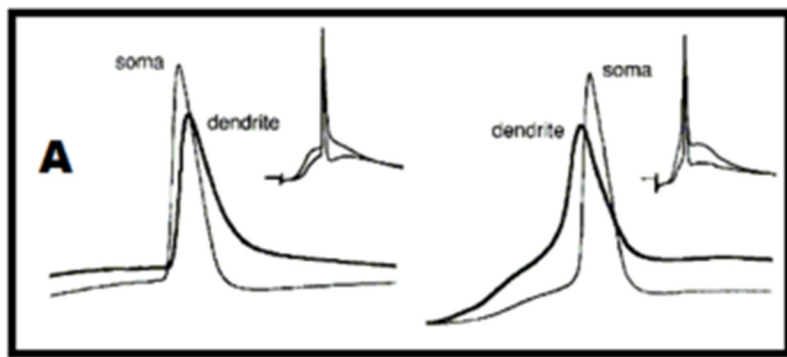


Figure 2.9: Action potential and dendritic spikes. Left: The action potential occurs before the dendritic spike. Right: The dendritic spike occurs before the action potential (Adapted from *Dendritic spike* 2013).

The excitability of dendrites has consequences in several ways. Dendritic spikes play an important role in inducing synaptic plasticity. For example, sodium spikes are required to induce long-term potentiation at distal apical dendrites (Kim et al. 2015). Another important function is to look at how dendritic excitability affects the integration of dendritic inputs. In this case, the neuron can be considered as a two-stage model. Individual dendrites serve as subunits that integrate synaptic inputs, resulting in dSpikes. Soma then integrates the dendritic inputs, leading to the action potential initiation (Polsky et al. 2004; Poirazi et al. 2003a; Gasparini, Magee 2006; Katz et al. 2009; Kastellakis, Poirazi 2019). Another function is that by activating the dendritic voltage channels, it is possible to increase the amplitude of dendritic EPSPs (Spruston et al. 2016).

2.6 Synaptic plasticity

Physical changes in our brain represent the basis of any adaptation, learning, and memory. Experience, events, remembering new facts, etc. or ingestion of psychotropic substances influence brain activity and result in modification of brain activity and/or organization. A major mechanism of these processes is synaptic plasticity. Specifically, the activity-dependent modification of the strength or efficacy of synaptic transmission at preexisting synapses and/or modification in the numbers of synapses. In addition, synaptic plasticity plays a key role in neuronal development and is associated with several major neuropsychiatric disorders.(Citri, Malenka 2008; Ramirez, Arbuckle 2016).

The idea of synaptic plasticity dates back to 1894. At that time, it was believed that the number of neurons in the brain remained stable throughout life. The Spanish neurologist

Santiago Ramon y Cajal therefore hypothesized that memories must be formed by strengthening existing neural connections (Ramon y Cajal 1894; Ramirez, Arbuckle 2016). This idea was extended in 1949 by the Canadian psychologist Donald Hebb. His postulate “When an axon of cell A is near enough to excite cell B or repeatedly or consistently takes part in firing it, some growth or metabolic change takes place in one or both cells such that A’s efficiency, as one of the cells firing B, is increased” describes the general principle of synaptic plasticity, also called *Hebbian learning*. In other words, coincident firing of inputs onto a neuron or coincident firing of the presynaptic and postsynaptic neurons leads to strengthening of synaptic connections (Hebb 1949). His “fire together wire together” theory was extended and supported by experiments in the following years (see below).

As mentioned above, synaptic plasticity plays an important role in a wide range of brain processes. It is therefore not surprising that various forms and mechanisms of synaptic plasticity have been discovered. Synaptic transmission can be enhanced or suppressed. Changes in synaptic transmission due to synaptic plasticity can last from milliseconds to hours, days, and longer. In addition, all excitatory synapses can virtually exhibit different forms of synaptic plasticity simultaneously (Citri, Malenka 2008). For the purposes of this dissertation, we will focus and describe in more detail the long-term forms of synaptic plasticity known as long-term potentiation (LTP) and long-term depression (LTD).

2.6.1 Mechanisms of long-term synaptic plasticity

It is widely accepted that the brain encodes external and internal events as complex, spatiotemporal patterns of activity in neural circuits. Then the new information is stored (i.e., memories are generated) when activity in neuronal circuits causes a long-lasting change in the pattern of synaptic weights (Citri, Malenka 2008). The first experimental evidence for this idea dates back to the early 1970s. Bliss and colleagues reported that repetitive activation of hippocampal excitatory synapses caused a long-lasting potentiation of synaptic strengths (Bliss, Lømo 1973).

The next important milestone in the study of long-lasting synaptic plasticity was the research of Levy and Steward (1983). They demonstrated the temporal contiguity requirements for long-term associative potentiation/depression in the hippocampus. They studied associative induction of LTP/LTD on ipsilateral and crossed projections from the entorhinal cortex to the dentate gyrus. The induction of long-term synaptic plasticity required precise timing of converging pathways rather than their synchronization. Long-term potentiation of the crossed

projection could be induced when the ipsilateral input was activated concurrently with, or following the activation of, the crossed input by as much as 20 ms. In the reversed order, LTD was induced (Levy, Steward 1983; Bi, Poo 2001). This temporal specificity agrees with the Hebb's postulate and is relevant for physiological functions, such as learning and memory, which are known to be temporally specific (Bi, Poo 2001).

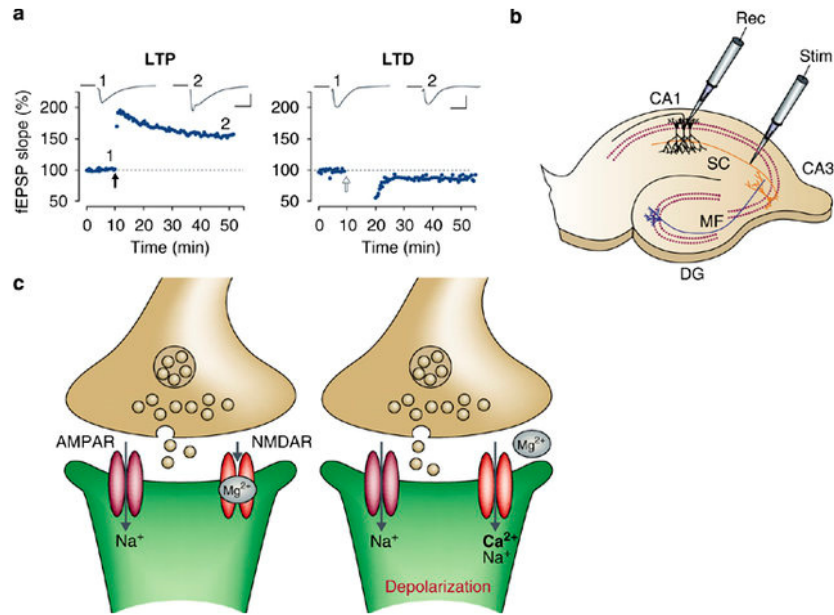


Figure 2.10: NMDAR-dependent LTP and LTD at hippocampal CA1 synapses. (a) Experiments illustrating LTP and LTD in the CA1 region of the hippocampus. Synaptic strength, defined as the initial slope of the field excitatory postsynaptic potential (fEPSP; normalized to baseline) is plotted as a function of time. Left panel demonstrates LTP elicited by high-frequency tetanic stimulation (black arrowhead). Right panel illustrates LTD elicited by low-frequency stimulation (open arrow). (b) A schematic diagram of the rodent hippocampal slice preparation. Typical electrode placements for studying synaptic plasticity at Schaffer collateral synapses onto CA1 neurons are indicated (Stim=stimulating electrode; Rec=recording electrode). (c) Model of synaptic transmission at excitatory synapses. During basal synaptic transmission (left panel), synaptically released glutamate binds to both the NMDARs and AMPARs. Na⁺ flows through the AMPAR channel but not through the NMDAR channel because of the Mg²⁺ block of this channel. Depolarization of the postsynaptic cell (right) relieves the Mg²⁺ block of the NMDAR channel and allows both Na⁺ and Ca²⁺ to flow into the dendritic spine. The resultant increase in Ca²⁺ in the dendritic spine is necessary for triggering the subsequent events that drive synaptic plasticity (Adapted from Citri, Malenka 2008. Copyright 2021, Springer Nature. With permission from Springer Nature.).

2.6.1.1 NMDAR-dependent LTP

The most studied form of synaptic plasticity in the CA1 region of hippocampus is NMDAR-dependent LTP (**Figure 2.10**). LTP plays important functional role in learning and memory (Martin et al. 2000; Takeuchi et al. 2013) and has several properties supporting this idea.

Similar to memory, LTP can be induced rapidly and is strengthened and prolonged by repetition. LTP shows cooperativity, it can be induced by the coincident activation of a critical number of synapses. Associativity of LTP means, that weak input (a small number of synapses) can be co-activated with a strong input (a larger number of synapses). Finally, LTP shows input specificity because it is triggered only on stimulated synapses and not on unstimulated counterparts (Citri, Malenka 2008).

LTP has two phases. An early phase (E-LTP) is protein synthesis independent, is induced by a single brief tetanus, and lasts up to 1-3 hours. A late phase (L-LTP) is protein dependent, requires *de novo* protein synthetization which involves activation of transcription factors, and there are visible structural changes. Repetitive applications of tetanus or one strong tetanus leads to L-LTP that lasts at least 24 hours (Baltaci et al. 2019).

Typical E-LTP induction protocols include a high-frequency stimulation (100 Hz, 1 s), a theta-burst stimulation, and STDP protocol (Citri, Malenka 2008; Baltaci et al. 2019). Theta-burst protocol typically consists of several repetitions of high-frequency bursts at 5 Hz. This pattern of firing also occurs spontaneously during behavior. Single burst is not sufficient to trigger LTP. However, repeated bursts at 5 Hz can induce maximal LTP due to disinhibition of feed-forward inhibition which is referred as priming (Larson, Munkácsy 2015). The STDP protocol is based on the matching of action potentials of presynaptic and postsynaptic neurons with a precise timing. LTP occurs when the presynaptic cell fires shortly before the postsynaptic one (Bi, Poo 2001; Baltaci et al. 2019).

The induction of LTP requires activation of NMDA receptors. During the strong stimulation, AMPA receptors are activated, and postsynaptic cell is depolarized. Depolarization causes NMDAR magnesium block dissociation and activation of NMDARs. Opening of NMDARs leads to strong calcium influx and increases in intracellular calcium concentration. This in turn leads to activation of $\text{Ca}^{2+}/\text{CaM}$ -dependent protein kinase II (CaMKII) that is sufficient and necessary for LTP induction. Activated CaMKII binds to the NR2B subunit of NMDA receptors and phosphorylates target proteins in postsynaptic density (PSD), which results in increased single-channel conductance, increased AMPAR insertion in PSD, and spine enlargement. The maintenance of these changes for longer time depends on *de novo* transcription as well as local dendritic protein synthesis (Citri, Malenka 2008; Baltaci et al. 2019).

2.6.1.2 NMDAR-dependent LTD

The opposite form of NMDAR-dependent LTP is NMDA-dependent LTD (**Figure 2.10**). The experimental evidence of LTD is dated in 1992. Dudek and Bear used low-frequency stimulation to induce LTD at excitatory synapses of CA1 pyramidal cell. One of the conclusions of their work was that the effects of conditioning stimulation could be prevented by application of NMDAR antagonist. Thus, they suggested that NMDA receptors are involved in the LTD triggering (Dudek, Bear 1992).

Similar to NMDAR-dependent LTP, NMDAR-dependent LTD is input- or synapse-specific. This is because NMDA receptors on synapses must be activated by presynaptic glutamate release during the induction protocol. In contrast to LTP, NMDAR-dependent LTD is typically triggered by a low-frequency stimulation (1 – 3 Hz for 5 – 15 min). This causes modest postsynaptic depolarization, which leads to a modest but prolonged increase in the intracellular calcium concentration due to modest and repeated activation of NMDAR (Citri, Malenka 2008; Lüscher, Malenka 2012). NMDAR-dependent LTD can be also induced by the STDP stimulation protocol. LTD occurs when the postsynaptic neuron fires slightly before (~5 ms) the presynaptic cell (Bi, Poo 2001; Lüscher, Malenka 2012).

Changes in the number of AMPA receptors are also crucial for induction of LTD. LTD requires the reduction of AMPA receptors in the postsynaptic density (PSD) (Anggono, Huganir 2012). Calcium-dependent protein phosphatase cascade consisting of calcium/calmodulin-dependent protein phosphatase calcineurin and protein phosphatase 1 (PP1) plays important role in the induction of LTD. The modest calcium increase preferentially activates phosphatases, which in turn leads to dissociation of AMPA receptors from the PSD. AMPA receptors are then moved to endocytic zones, where they are endocytosed and potentially degraded (Citri, Malenka 2008; Lüscher, Malenka 2012). Autophagy plays an important role in AMPAR trafficking, too. During the induction of LTD, the autophagy flux in the CA1 pyramidal cell is decreased, which causes reduction of endocytic recycling and is required for AMPA receptor internalization and synaptic depression (Shen et al. 2020).

2.6.2 Homeostatic mechanisms of synaptic plasticity

The previously described forms of synaptic plasticity are referred to as homosynaptic plasticity. Homosynaptic plasticity occurs at synapses that were involved in the activation of a neuron during stimulation protocol. This form of plasticity is known as input-specific or associative, and it is governed by Hebbian-type learning rules. Only purely homosynaptic plasticity could

potentially lead to pathological effect, such as synapses being strongly potentiated causing excitotoxicity, or strong depression causing their non-function. To prevent these conditions, there are mechanisms that ensure balance across various neural and synaptic features and thus contribute to the normal operation of neural systems with plastic synapses (Hulme et al. 2013; Chistiakova et al. 2014; 2015; Zenke, Gerstner 2017).

2.6.2.1 Synaptic scaling

A form of plasticity called synaptic scaling is a mechanism of homeostatic synaptic plasticity that occurs both *in vivo* and *in vitro* (Turrigiano 2008). The homeostatic synaptic scaling is defined as compensatory up- or down- scaling of synaptic weights triggered by prolonged severe change of neuronal activity (Chistiakova et al. 2015). The homeostatic synaptic scaling was first described in cultured neocortical neurons. Chronic blockade of cortical culture activity increased synaptic strength of all synapses and returned average firing rates back to control values. Similarly, blockade of GABA-mediated inhibition caused a reduction in the synaptic strength of all synapses and set the average firing rate close to control values (Turrigiano et al. 1998).

Originally, synaptic scaling was described as a global form of homeostatic plasticity. However, synaptic scaling can also work on local or neural network level. Local changes in synaptic signaling could induce local homeostatic changes in synaptic transmission. On the other hand, changes in network activity could be induced through activity-dependent release of soluble factor by many neurons or glia (Turrigiano 2008).

The molecular mechanisms underlying synaptic scaling are usually associated with the regulation of synaptic AMPA receptors in terms of number or subunit composition or both. They include several processes such as phosphorylation of GluA1 subunit of AMPARs, role of calcium-permeable or impermeable AMPA receptors, or different signaling molecules. Although these processes appear to be independent, they have a common target which is the regulation of trafficking or synaptic stabilization of AMPA receptors (Chowdhury, Hell 2018).

Homeostatic synaptic scaling operates on timescales of hours or days. These timescales are typical for developmental processes or recovery from pathological states (Chistiakova et al. 2015). Synaptic scaling can work in the extreme range of activity to function as a failsafe measure. For example, at extremely low activity, synaptic scaling may be appropriate to adjust synaptic strength. On the other hand, when neural activity is extremely high, input-independent global synaptic scaling may be an effective way to reduce activity (Lee, Kirkwood 2019).

Because homeostatic synaptic scaling works on time scales that are longer than the time scales at which associative synaptic plasticity is induced, additional mechanisms need to be considered to stabilize the system during the fast Hebbian learning (Chistiakova et al. 2015).

2.6.2.2 Heterosynaptic plasticity

Heterosynaptic plasticity is another form of plasticity that can maintain homeostasis. Heterosynaptic plasticity can be induced at synapses that were not involved in induction of homosynaptic plasticity (**Figure 2.11**). For this reason, all synapses can undergo heterosynaptic changes and therefore heterosynaptic plasticity usually affects a larger population of synapses than homosynaptic plasticity. Both forms of synaptic plasticity can be induced by typical protocols used for plasticity triggering and operate on the same time scale. However, they have different computational properties and play different roles in learning and memory. Homosynaptic plasticity is involved in Hebbian-type learning, while heterosynaptic plasticity counteracts the changes induced by homosynaptic plasticity and balances synaptic weights (Chistiakova et al. 2014; 2015). In addition, heterosynaptic plasticity plays important role in the developing brain where it shapes synaptic clustering. In turn in the adult brain, stimulation of synaptic clusters leads to potentiation of nearby asynchronously active synapses (Magó et al. 2020; Chater, Goda 2021). A key feature of each cortical dynamics is the balance between excitatory and inhibitory inputs. Heterosynaptic interactions between excitatory and inhibitory synapses are critical factors in synaptic organization. Heterosynaptic plasticity can induce a dendrite-specific temporally precise excitatory/inhibitory balance. Although this balance on individual dendrites has small effect on the somatic membrane dynamics, collective effect from all the dendrites has a significant effect on the postsynaptic activity (Hiratani, Fukai 2017).

What are the mechanisms or signaling pathways involved in the expression of heterosynaptic plasticity? A current review from Chater and Goda (2021) summarized molecular mechanisms underlying heterosynaptic signaling. They include voltage and calcium signals, diffusible molecules such as nitric oxide (NO), and extracellular communication via astrocytes and exosomes (Chater, Goda 2021). Another important signaling molecules are calcineurin and CaMKII. Spatially clustered stimulation leads to calcineurin activation which in turn causes the shrinkage of spines close to stimulation site and their heterosynaptic depression (Oh et al. 2015). CaMKII has more efficient propagation and therefore can activate distal spines, which could promote their heterosynaptic potentiation (Tong et al. 2021).

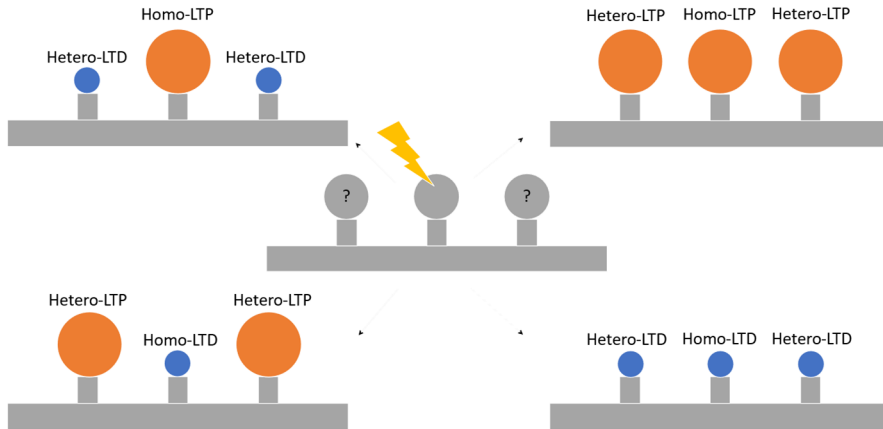


Figure 2.11: Various types of homo- and heterosynaptic plasticity. Stimulation of central synapse leads to homosynaptic LTP (up) or LTD (down). At neighboring unstimulated synapses is induced heterosynaptic plasticity (Inspired by Chater, Goda 2021).

During various forms of synaptic plasticity, the number of AMPA receptors in PSD plays an important role. Long-term potentiation is associated with higher number AMPA receptors, while long-term depression with their lower number (Chater, Goda 2014). The mechanisms of AMPA receptor trafficking involved in LTP/LTD can promote heterosynaptic plasticity at unstimulated synapses (Antunes, Simoes-de-Souza 2018). Furthermore, the competition of synapses for limited number of receptors can produce transient heterosynaptic LTD and the amount of heterosynaptic plasticity is inversely related to the size of the local receptor pool (Triesch et al. 2018).

2.6.2.3 Metaplasticity

Metaplasticity represents a higher-order form of synaptic plasticity, or plasticity of synaptic plasticity. Metaplasticity refers to activity-dependent and persistent changes in the state of synapses or neurons that alter magnitude and/or duration of subsequent synaptic plasticity. In other words, prior activity of neuron regulates the outcome of the subsequent activity-dependent synaptic plasticity (Abraham, Bear 1996; Abraham 2008; Hulme et al. 2013). Metaplasticity as a regulatory mechanism was observed in regulation of experience-dependent changes in visual and somatosensory cortical synapses (Benuskova et al. 1994; Kirkwood et al. 1996; Philpot et al. 2007), synaptic plasticity in the dentate gyrus (Benuskova, Abraham 2007; Jedlicka et al. 2015), as well as in the hippocampus (Wang, Wagner 1999; Abraham et al. 2001; Hulme et al. 2012).

There are several intracellular and extracellular mechanism of metaplasticity regulation (Hulme et al. 2013). At the intracellular level, G-protein signaling can trigger metaplastic changes favoring LTP or LTD (Huang et al. 2012). In the case of extracellular mechanisms, calcium signaling and endocannabinoid signaling are involved. For example, metaplasticity is dependent on a calcium signal arising from intracellular stores. This type of metaplasticity can regulate subsequent synaptic plasticity not only in the same dendritic compartment but can also spread in dendritic tree and regulate synaptic plasticity in more distant dendrites (Hulme et al. 2012). Retrograde endocannabinoid signals can trigger long-term depression at inhibitory synapses. Silencing of inhibitory synapses in a restricted area of a dendritic tree, endocannabinoid can facilitate induction of subsequent LTP on nearby excitatory synapses (Chevaleyre, Castillo 2004).

Metaplasticity has functional roles in both developmental and adult brain. During the developmental process, three forms of metaplasticity were observed at hippocampal synapses. Firstly, metaplasticity regulates multiple developmental phases of presynaptic transmitter release. Secondly, metaplasticity regulates developmental switch to GluR3-AMPA receptors. The third form of metaplasticity during development is that low-frequency stimulation does not induce LTD but raises the threshold for the subsequent induction of LTP (Vose, Stanton 2017). In the adult brain, metaplasticity has other important roles in addition to the functions already mentioned. For example, hippocampal metaplasticity is required for the formation of temporal associative memory (Xu et al. 2014). On the other hand, dysfunction of metaplasticity could have consequences in illnesses characterized by cognitive, memory, and affective impairments (Vose, Stanton 2017).

2.7 Summary

The aim of this chapter was to provide a brief biological view of the brain structures involved in learning and memory. We started with a general description of electrical activity in a neuron. It is important to understand the process of ion flux through the cell membrane. Therefore, we explained diffusion, electrical drift and electrodiffusion. We also presented the Nernst equilibrium potential and the resting membrane potential. Because neurons communicate primarily through action potentials, we have explained the mechanism of the action potential and its spreading. In this section, we described the hippocampus as a key structure of the brain that is involved in learning and memory.

The main purpose of this work is to model synaptic plasticity in the CA1 pyramidal cell model. Therefore, we focused on a detailed description of the CA1 pyramidal cell. We mentioned the morphology, the main ionic content, the mechanism and distribution of synapses, and a phenomenon called dendritic spikes. Finally, we discussed different types and mechanisms of synaptic plasticity, with the main focus on long-term forms of synaptic plasticity, LTP and LTD.

Chapter 3

3 Mathematical and computational modeling

In this chapter, we discuss basic concepts of computational modeling in neuroscience. The chapter can be divided into three parts. In the first part, we summarize mathematical methods required by computational modeling, such as differential equations and partial differential equation. In the second part we focus on computational modeling itself. We will explain a membrane representation as an equivalent electrical circuit. We introduce the Hodgkin-Huxley model of the action potential and the principle of compartmental modeling. we focus on mathematical models of synaptic plasticity. We describe the BCM rule, the STDP rule and the STDP rule extended by metaplasticity - the meta-STDP rule. In the third part, we describe the NEURON simulation environment, which we use to simulate our experiments. We also describe the organization of the code and the typical workflow.

3.1 Computational neuroscience

Computational neuroscience is the field of study in which mathematical tools and theories are used to investigate brain function. It can incorporate diverse approaches from electrical engineering, computer science, and physics in order to understand how the nervous system process information.

The brain is the most complex structure composed of a vast number of neurons and characterized by ultra-high complexity of structural connectivity. Theory and computational modeling play an important role in understanding the functioning of the neural system. First, massive data from brain connectomics, transcriptome and neurophysiology increasingly demand novel analysis tools being developed by theorists. Second, the brain systems are too complex to comprehend by experiments and intuition alone. Third, theory and modeling, in concert with experimentation, are needed to advance our understanding of how the brain works across spatiotemporal scales, from molecules to neural circuits, and to functions and behavior (Wang et al. 2020).

There are three types of modeling approaches. First, descriptive models are designed to quantitatively characterize experimental data. Signal processing algorithms and stochastic process models for neuronal spike trains belong to this category. Second, normative theories aim at explaining brain processes at the functional level. For instance, statistical Bayesian

inference theory argues that neural coding and processing of sensory stimuli depends on the organism's prior knowledge about the environment, hence can be optimized based on the prior probability distribution of the sensory input. Third, mechanistic models, also called biologically-realistic models, are constructed based on the two pillars of neuroscience: neuroanatomy (cell types, connectivity) and neurophysiology (from biophysics of neurons and synapses to neural population activity during behavior) (Wang et al. 2020).

In this thesis we focus on the third approach. We have developed a biologically realistic model of the CA1 pyramidal cell. We confirmed the biological accuracy of the model by systematic testing of selected physiological features. We implemented the meta-STDP rule of synaptic plasticity in the model and reproduced typical stimulation protocols used to induce synaptic plasticity.

3.2 Ordinary differential equations

Differential equations allow us to describe the evolution in time and space of quantities such as membrane potential or calcium concentration. Therefore, we briefly describe methods for solving differential equations.

We assume on ordinary differential equation for the rate of change of membrane voltage:

$$\frac{dV}{dt} = f(V, t) \quad (3.1)$$

where f is a given function of t and V , and V contained in R^m is a vector. In this equation, t is the independent variable and $V = V(t)$ is the dependent variable. The equation is the first order ordinary differential equation because the order of derivative is one with a single independent variable (t).

3.2.1 Analytical solution

Let the function $f(V, t)$ be defined on an area $\Omega = (t_0 - a, t_0 + a) \times (V_0 - b, V_0 + b)$, where a, b are positive real numbers with properties on the whole Ω :

- is continuous,
- is bounded by the constant K ,
- satisfies the Lipschitz condition with respect to solution y .

Then the differential equation (3.1) has exactly one solution $V = \varphi(t)$, which passes through the point $A = (t_0, V_0)$, i.e., $V_0 = \varphi(t_0)$ on the interval $(t_0 - c, t_0 + c)$, where $c = \min \left\{ a, \frac{b}{K} \right\}$.

We get the solution $y = \varphi(t)$ as the limit of the sequence of functions $\{V_n(t)\}_{n=1}^{\infty}$, where:

$$V_n(t) = V_0 + \int_{t_0}^t f(t, V_{n-1}(t)) dt \quad n = 1, 2, \dots \quad (3.2)$$

Equation (3.2) has an analytic solution if there is an exact solution for the integration of y .

3.2.2 Numerical methods

The numerical integration methods provide approximation of differential equations that cannot be solved analytically. They enable to calculate value of quantity e.g., voltage at any particular time point or spatial position. We present three fundamental methods: the forward Euler method, the backward Euler method, and the central difference.

The forward Euler method estimates the time derivative at time t as the slope of the straight line passing through the points $(t, V(t))$ and $(t + \Delta t, V(t + \Delta t))$, for a small time-step Δt :

$$\frac{dV}{dt} \approx \frac{V(t + \Delta t) - V(t)}{\Delta t}. \quad (3.3)$$

This is known as a finite difference method, because it is estimating a quantity, the rate of change of voltage, that changes continually with time, using a measured change over a small but finite time interval Δt . How accurate this estimation is, depends on how fast the rate of change of V is at that time. It becomes more accurate the smaller Δt is. Substituting this expression into (3.1) gives:

$$\frac{V(t + \Delta t) - V(t)}{\Delta t} = f(V(t), t). \quad (3.4)$$

To calculate the voltage at time point $(t + \Delta t)$, we rearrange this equation:

$$V(t + \Delta t) = V(t) + f(V(t), t)\Delta t. \quad (3.5)$$

Suppose we start at time 0 with a known voltage $V(0) \equiv V^0$. We can use this formula to calculate iteratively the voltage at future time points Δt , $2\Delta t$, $3\Delta t$ and so on. If $t = n\Delta t$ and we use the notation $V^n \equiv V(t)$ and $V^{n+1} \equiv V(t + \Delta t)$, then:

$$V^{n+1} = V^n + f(V^n, n\Delta t)\Delta t. \quad (3.6)$$

This approximation has the first order accuracy in time due to the local error between the calculated value of V and its true value is proportional to the size of the time-step Δt (Sterratt et al. 2011).

The backward Euler method calculates the value of quantity using the past value. This method has also the first order accuracy, moreover, is more stable because the local error increases but remains within finite bounds as the time-step is increased. The approximation of the time derivative is:

$$\frac{dV}{dt} \approx \frac{V(t) - V(t - \Delta t)}{\Delta t}. \quad (3.7)$$

Substituting into (3.1) we get:

$$\frac{V(t) - V(t - \Delta t)}{\Delta t} = f(V(t), t). \quad (3.8)$$

Shifting this to the same time points as the forward Euler method yields:

$$\frac{V(t - \Delta t) - V(t)}{\Delta t} = f(V(t + \Delta t), t + \Delta t). \quad (3.9)$$

For the same time-step, the forward Euler method could overestimate the rate of change in voltage and the backward Euler method could underestimate it. However, for larger time-steps, the backward Euler method never overshoots the final steady state value of V (Sterratt et al. 2011).

The central difference method uses past and future points to estimate the time derivative of quantity value. This method is more accurate and stable than two previous. The approximation of time derivative is the average of both Euler's methods:

$$\frac{dV}{dt} \approx \frac{V(t + \Delta t) - V(t - \Delta t)}{2\Delta t}. \quad (3.10)$$

If we use the expression for the backward Euler method involving the future voltage, $V(t + \Delta t)$, then the equation (3.1) is approximated by:

$$\frac{V(t + \Delta t) - V(t)}{\Delta t} = \frac{1}{2}[f(V(t + \Delta t), t + \Delta t) + f(V(t), t)]. \quad (3.11)$$

The central difference method is second order accurate in time because the error is proportional to the square of the time-step Δt (Sterratt et al. 2011).

3.3 Partial differential equations

In the partial differential equations, the function of dependent variable might be dependent on more than one independent variable. An example is the cable equation which involves the first derivative of V with respect to time and the second derivative of V with respect to space. For the temporal discretisation, we can use the same methods as for ordinary differential equations. To discretize a spatial dimension, the central difference method can be used:

$$\frac{dV}{dt} \approx \frac{V(x + \Delta x) - 2V(x) - V(x - \Delta x)}{(\Delta x)^2} \quad (3.12)$$

for a small spatial step Δx . The position x corresponds to a midpoint of compartment j , $x + \Delta x$ corresponds to compartment $j + 1$, $x - \Delta x$ corresponds to compartment $j - 1$, and the length of each compartment is $l = \Delta x$ (Stewart et al. 2011).

The Crank-Nicholson method (Crank, Nicolson 1947) uses the central difference method for both the temporal and spatial discretizations. This method is more stable and accurate for this type of partial differential equations. The solution is the average of the forward and backward Euler approximations. It involves a system of equations involving values for voltage at the new time point in all compartments, which must be solved simultaneously (Stewart et al. 2011).

3.4 Realistic neuron models

The electrical properties of neuron can be described in terms of an equivalent electrical RC circuit comprising of a battery, resistors, and capacitor (**Figure 3.1**). A potential difference resulted from a difference of extracellular and intracellular ion concentrations is stored at a battery. Resistors are used to model different ion channels. The phospholipid bilayer acts as an insulator that separates the ionic charge and therefore is modeled as a capacitor (Stewart et al. 2011).

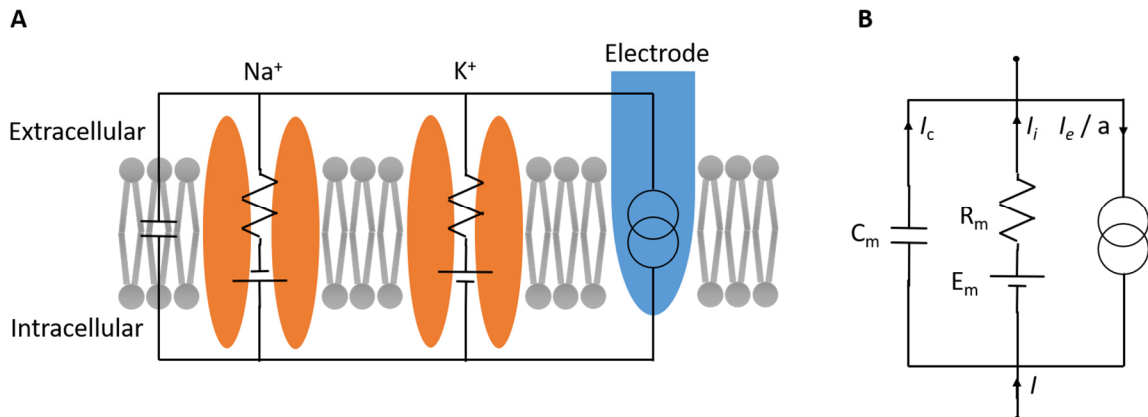


Figure 3.1: The equivalent electrical circuit of a patch of membrane. The equivalent RC circuit comprises the membrane capacitance in parallel with one resistor and battery in series for each type of ion channel. There is also a current source that represents an electrode that is delivering a constant amount of current (Inspired by Sterratt et al. 2011).

3.4.1 Passive electrical properties

The specific membrane capacitance (C_m) refers to the capacitance per unit area of membrane. It is considered as a constant across many classes of neuron. A typical value of C_m is $0.9 \mu\text{F}/\text{cm}^2$. It influences synaptic efficacy and determines a speed of spreading of electrical signals along dendrites and unmyelinated axons (Rall 1962; Gentet et al. 2000). For CA1 pyramidal cells, the specific membrane capacitance was experimentally and computationally estimated to value of $1.0 \mu\text{F}/\text{cm}^2$ (Golding et al. 2001). The total membrane capacitance of neuron (c_m) is proportional to the membrane surface area ($a = \pi dl$) with the specific membrane capacitance, $c_m = C_m a$ which means that increasing of the membrane surface area increases the total membrane capacitance.

The specific membrane resistance (R_m) is defined by the density of open ion channels at resting potentials. It is inverse related to the specific membrane conductance. The membrane resistance is also related to the membrane surface area. The total membrane resistance (r_m) is defined as $r_m = R_m/a$. The specific membrane resistance in the CA1 pyramidal cells has a non-uniform distribution. It drastically decreases from the soma to the apical distal dendrites which can be described by a sigmoidal function. At the proximal apical dendrites, the value of R_m is greater than $\sim 10^4 \Omega\text{cm}^2$, whereas at the distal dendrites is the value of R_m less than $\sim 10^3 \Omega\text{cm}^2$. As the membrane capacitance, the membrane resistance plays important role in a synaptic integration and voltage attenuation along dendrites (Golding et al. 2005; Omori et al. 2006; 2009).

3.4.2 Neuronal membrane dynamics

Goldman–Hodgkin–Katz (GHK) current equation predicts the current I_X mediated by a single ionic species X flowing across a membrane when the membrane potential is V . This can be approximated by the equation:

$$I_X = g_X(V - E_X) \quad (3.13)$$

where X is the ion of interest, E_X its equilibrium potential, and g_X is the gradient of the line with the units of conductance per unit area, often mS cm^{-2} . The term in brackets $(V - E_X)$ is called the driving force. Using Thévenin's theorem, we can calculate the equivalent electromotive force (E_m) and membrane resistance for channels X, Y, Z :

$$\begin{aligned} E_m &= \frac{g_X E_X + g_Y E_Y + g_Z E_Z}{g_X + g_Y + g_Z} \\ \frac{1}{R_m} &= g_m = g_X + g_Y + g_Z. \end{aligned} \quad (3.14)$$

By Kirchhoff's current law, the sum of the current I_a flowing through the membrane and the injected current I_e is equal to the sum of the capacitive current $I_c a$ and the ionic current $I_i a$:

$$\begin{aligned} I_a + I_e &= I_c a + I_i a \\ I + I_e/a &= I_c + I_i. \end{aligned} \quad (3.15)$$

The ionic current flowing through the resistor and battery is given by:

$$I_i = \frac{(V - E_m)}{R_m}. \quad (3.16)$$

Finally, the capacitive current is calculated as:

$$I_c = C_m \frac{dV}{dt}. \quad (3.17)$$

where C_m is the specific membrane capacitance and dV/dt is the rate of change of voltage. The rate of the change of the membrane potential is proportional to the net flow of the current through the membrane and is inversely proportional to the capacitance:

$$\frac{dV}{dt} = \frac{I}{C} \quad (3.18)$$

(Sterratt et al. 2011).

In current clamp mode, the circuit contains a current source represents an electrode that is delivering a constant amount of current. The change of the membrane potential when the current is injected, and the circuit is isolated is described in the formula:

$$C_m \frac{dV}{dt} = \frac{E_m - V}{R_m} + \frac{I_e}{a}, \quad (3.19)$$

where C_m is the specific membrane capacitance, V is the membrane potential, E_m is the resting membrane potential, R_m is the specific membrane resistance, I_e is injected current, and a is an area. This relationship represents the first order ordinary differential equation for the membrane potential V . It described how is the change in the membrane potential related to itself and the injected current at every instant in time (Sterratt et al. 2011).

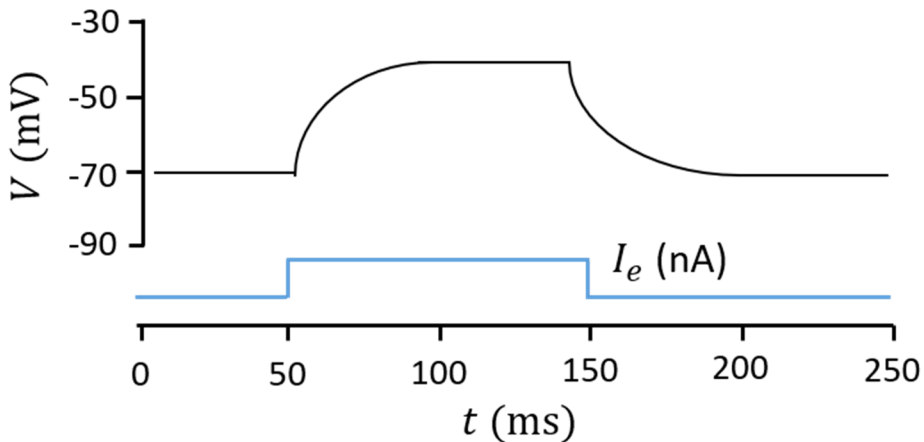


Figure 3.2: The behavior of the membrane potential in a RC circuit in response to an injected current.
When the current is injected, the increase in the membrane potential occurs and lasts as long as the current is injecting. As soon as the current injection is stopped, the membrane potential rapidly falls down to the resting value (Inspired by Sterratt et al. 2011).

When the injected current is a square pulse of magnitude I_e with a duration t_e , the behavior of the membrane potential in the RC circuit is shown in **Figure 3.2**. Two phases are distinguished: depolarization and repolarization. The depolarization phase begins with current injection and lasts as long as the current is injecting. The membrane potential rises from the resting value to the limit value. The course of changing the membrane potential can be described by an inverted decaying exponential function. As soon as the current injection is stopped, the membrane potential rapidly falls down to the resting value as a decaying exponential function. After the injection of the negative current, the membrane potential decreases below the resting value, which is referred to as hyperpolarization (Sterratt et al. 2011).

Analytical solution of (3.19) gives exponentials mentioned above. When we assume that the initial membrane potential is at the rest value, $V = E_m$ and $t = 0$, then the inverted decaying exponential function has a form:

$$V = E_m + \frac{R_m I_e}{a} \left(1 - \exp \left(-\frac{t}{R_m C_m} \right) \right). \quad (3.20)$$

In the case of repolarization, we define V_0 as the value of the membrane potential reached at the end of the current injection at $t = t_e$, the response of the membrane potential is given by:

$$V = E_m + (V_0 - E_m) \exp \left(\frac{t - t_e}{R_m C_m} \right), \quad (3.21)$$

which is the decaying exponential function (Sterratt et al. 2011).

The term $R_m C_m$ in a denominator of both equations is called the membrane time constant, τ . This is a product of the membrane capacitance and membrane resistance. The membrane time constant expresses the time scale of cell's membrane response to input. In addition, the membrane response to input also characterizes the input resistance, R_{in} . It is defined as the change in the steady state membrane potential divided by the injected current causing it (Koch 1999):

$$R_{in} = \frac{V_\infty - E_m}{I_e}. \quad (3.22)$$

3.4.3 Multicompartmental model and the cable equation

The previous explanation assumed an area of membrane over which the membrane potential is effectively constant, isopotential. However, in a real neuron, the axial current flows along the neurite, therefore it cannot be considered as isopotential. For this reason, the dendrite is splitted up into cylindrical compartments with a length l , a diameter d with a surface area $a = \pi dl$. The current can flow longitudinally through cytoplasm and the extracellular media which is modeled by axial resistances (R_a) that connect compartments (Figure 3.3). The axial resistance is proportional to the length of a compartment and inversely proportional to cylinder's cross-section area: $4R_a l / \pi d^2$. The membrane current is now equal to the sum of leftwards and rightwards axial currents:

$$I_j a = \frac{V_{j+1} - V_j}{4R_a l / \pi d^2} + \frac{V_{j-1} - V_j}{4R_a l / \pi d^2}, \quad (3.23)$$

where V_j denotes the membrane potential of j th compartment. The change of the membrane potential of j th compartment when current is injected is now expressed as:

$$C_m \frac{dV_j}{dt} = \frac{E_m - V_j}{R_m} + \frac{d}{4R_a} \left(\frac{V_{j+1} - V_j}{l^2} + \frac{V_{j-1} - V_j}{l^2} \right) + \frac{I_{e,j}}{\pi dl}. \quad (3.24)$$

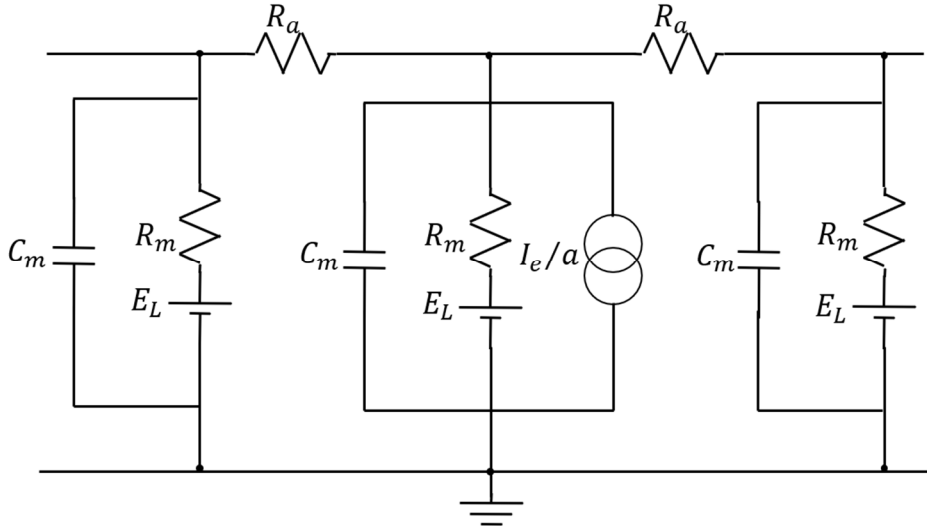


Figure 3.3: A length of passive membrane described by a compartmental model (Inspired by Sterratt et al. 2011).

The spatiotemporal evolution of the membrane potential describes the cable equation:

$$C_m \frac{\partial V}{\partial t} = \frac{E_m - V_j}{R_m} + \frac{d}{4R_a} \frac{\partial^2 V}{\partial^2 x^2} \frac{I_e}{\pi d l} \quad (3.25)$$

where the membrane potential is a function of distance x along the continuous cable, and time $V(x, t)$, and $I_e(x, t)$ is the current injected per unit length at position x (Sterratt et al. 2011).

3.4.4 Hodgkin-Huxley model

The Hodgkin-Huxley model (HH model) of neuron was developed by Hodgkin and Huxley (partly in collaboration with Katz) in 1952. The model mathematically describes the form of the action potential in the squid giant axon. They used the voltage clamp to produce the experimental data required to construct mathematical descriptions of how the sodium, potassium, and leaks currents depend on the membrane potential. Simulations of the model produce action potentials similar to experimentally recorded. The HH model is capable of reproducing significant features of the membrane potential (Sterratt et al. 2011).

Figure 3.4 show the Hodgkin-Huxley equivalent circuit of a compartment. The HH model contains three types of ionic currents: a sodium current, I_{Na} , a potassium current, I_K , and a leak current, I_L . The sodium and potassium currents are active and depend on voltage. The equation corresponds to the equivalent circuit is:

$$I = I_c + I_i = C_m \frac{dV}{dt} + I_i. \quad (3.26)$$

The total ionic current I_i is the sum of sodium, potassium, and leak currents:

$$I_i = I_{Na} + I_K + I_L \quad (3.27)$$

The magnitude of each type of current is calculated using the equation (3.13). As example, for the sodium current it is:

$$I_{Na} = g_{Na}(V - E_{Na}) \quad (3.28)$$

where g_{Na} is the sodium conductance and E_{Na} is the sodium equilibrium potential.

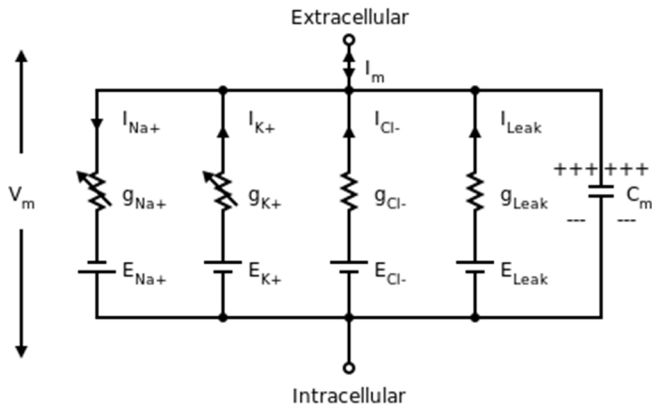


Figure 3.4: The Hodgkin-Huxley equivalent circuit (HH circuit 2011).

In order to fit the parameters, Hodgkin-Huxley used the ion substitution method. They isolated the currents carried by each type of ion. To describe the voltage dependence of ionic conductivities, they used the idea that the membrane contains a number of gates which control the ionic flow through the membrane. Each gate is controlled by a number of independent gating particles, each of which can be in either an open or closed position. The movement of gating particles between open and closed positions is controlled by the membrane voltage. The gating variable n is the probability of a single gating particle being in the open position. The gating variables act independently of each other. Therefore, the probability of the entire gate being open is equal to n^x , where x is the number of gating particles (Sterratt et al. 2011).

In the case of potassium current, the conductance rises to a constant value upon depolarization. This rise in conductance is called activation. The conductance stays at this peak value until the voltage falls to the resting value. The fall in conductance is referred to as deactivation and shows an exponential course (Sterratt et al. 2011).

The relation between the potassium conductance g_K and gating particle open probability n is:

$$g_K = \overline{g_K} n^4 \quad (3.29)$$

where $\overline{g_K}$ is the maximum potassium current conductance and n^4 refers to four gating particles.

The movement of a gating particle between its closed (C) and open (O) position can be described by a reversible chemical reaction:



The fraction of gating particles in the O state is n and the fraction of gating particles in the C state is $n - 1$. The α_n and β_n are the rate coefficients which depend on the membrane potential. The change of gating variable n over time is:

$$\frac{dn}{dt} = \alpha_n(V)(1 - n) - \beta_n(V)n. \quad (3.31)$$

The rate functions for the gating variables obey these equations (Sterratt et al. 2011):

$$\alpha_n = 0.01 \frac{V + 55}{1 - \exp(-(V + 55)/10)} \quad (3.32)$$

$$\beta_n = 0.125 \exp(-(V + 65)/80). \quad (3.33)$$

The sodium conductance is activated and rises from its the rest value when the membrane is depolarized. Upon reaching the maximal conductance, the sodium current is inactivated and decays back to the rest, even while the clamped voltage remains in a sustained depolarising step. Hodgkin and Huxley used gating type variable h to represent the level of inactivation. The h variable is either in the ‘not inactivated’ state or the ‘inactivated’ state. The rate of transition between these states is voltage dependent and is expressed as:

$$\frac{dh}{dt} = \alpha_h(1 - h) - \beta_h h \quad (3.34)$$

where α_h and β_h are voltage-dependent rate coefficients.

The sodium gating particle m determines sodium conductance activation and is defined as:

$$\frac{dm}{dt} = \alpha_m(1 - m) - \beta_m m \quad (3.35)$$

where α_m and β_m are the voltage-dependent rate coefficients. The rate functions for the gating variables obey these equations (Sterratt et al. 2011):

$$\alpha_m = 0.1 \frac{V + 40}{1 - \exp(-(V + 40)/10)} \quad (3.36)$$

$$\beta_m = 4 \exp(-(V + 65)/18) \quad (3.37)$$

$$\alpha_h = 0.07 \exp(-(V + 65)/20). \quad (3.38)$$

$$\beta_h = \frac{1}{\exp(-(V + 35)/10) + 1}. \quad (3.39)$$

The sodium current conductance is expressed as:

$$g_{Na} = \overline{g_{Na}} m^3 h \quad (3.40)$$

which indicates, there are used three gating particles (Sterratt et al. 2011).

The third component of HH models is the leak current, I_L . This current is a voltage-independent and is assumed as a resting background current consisting of mixture of ions. The leak current is denoted as:

$$I_L = \overline{g_L} (V - E_L) \quad (3.41)$$

where $\overline{g_L}$ is the leak current conductance and E_L is the leak current equilibrium potential (Sterratt et al. 2011).

The change of membrane potential over time in a small patch of squid giant axon is given by the equation:

$$C_m \frac{dV}{dt} = -\overline{g_L}(V - E_L) - \overline{g_{Na}} m^3 h (V - E_{Na}) \\ - \overline{g_K} n^4 (V - E_K) + I \quad (3.42)$$

where I is the local circuit current, the net contribution of the axial current from neighboring regions of the axon (Sterratt et al. 2011).

The HH model can be used to explain the absolute and relative refractory period of the axon. The gating variables take a long time, relative to the duration of an action potential, to recover to their resting values. It should be harder to generate an action potential during this period for two reasons. Firstly, the inactivation of the sodium conductance (low value of h) means that any increase in m due to increasing voltage will not increase the sodium conductance as much as it would when h is at its higher resting value. Secondly, the prolonged activation of the potassium conductance means that any inward sodium current has to counteract a more considerable outward potassium current than in the resting state (Sterratt et al. 2011).

3.5 Models of synaptic plasticity

The principle of synaptic plasticity was formulated by Donald Hebb in 1949. His theory can be simply formulated as “neurons that fire together, wire together”. This is mathematically described in a network of neurons as a simple equation:

$$\frac{dw_{i,j}}{dt} = x_{i,j} \quad (3.43)$$

where $w_{i,j}$ is the weight from i th neuron to j th neuron and $x_{i,j}$ is the input from i th neuron to j th neuron (Hebb 1949). The problem of Hebbian learning is obvious. The synapses following this rule would increase in strength without bound and the whole system would be unstable. The key question was how such learning could be stabilized (Cooper, Bear 2012).

3.5.1 BCM model

One successful synaptic plasticity rule that allowed network stability is Bienenstock-Cooper-Munro (BCM) rule (Bienenstock et al. 1982). It was based on experimental data from developing visual cortex. The key feature of BCM rule that a neuron possesses a sliding synaptic modification threshold θ_M , which is defined as the time average of the square of neuronal activity. The modification threshold determines the direction of synaptic weights change. The BCM rule expresses synaptic change as a Hebb-like product of the presynaptic activity x and a nonlinear function $\phi(c, \theta_M)$ of postsynaptic activity c (Bienenstock et al. 1982) Although the firing rate of a neuron y depends in a complex and nonlinear fashion on the postsynaptic potentials, the BCM rule considers that the region between the excitation threshold and saturation may be reasonably approximated by a linear input-output relationship of the neuron (Benuskova et al. 2001). The postsynaptic activity c is defined as the product between presynaptic activity x and synaptic weight w :

$$c(t) = \sum_i w_i(t)x_i(t). \quad (3.44)$$

The modification of i th synaptic weight at time t is proportional to the product of input activity at the i th synapse, $x_i(t)$, and the function ϕ :

$$\frac{dw_i(t)}{dt} = \eta\phi(c(t), \theta_M(t))x_i(t) = \eta c(t)[c(t) - \theta_M(t)], \quad (3.45)$$

where η is modification rate.

When $c > \theta_M$, $\phi(c)$ is positive and all active synapses are potentiated. On the other hand, when the postsynaptic activity is weaker, $0 < c < \theta_M$, $\phi(y)$ is negative and all active synapses are weakened. The sliding threshold θ_M is a whole cell parameter and is calculated over some recent past time τ :

$$\theta_M(t) = \alpha \langle c^2(t) \rangle_\tau = \alpha \frac{1}{\tau} \int_{-\infty}^t c^2(t') e^{-(t-t')/\tau} dt'. \quad (3.46)$$

The positive constant α determines how far to the right on the activity axis we can place the actual or effective threshold for synaptic potentiation (Bienenstock et al. 1982; Benuskova et al. 2001).

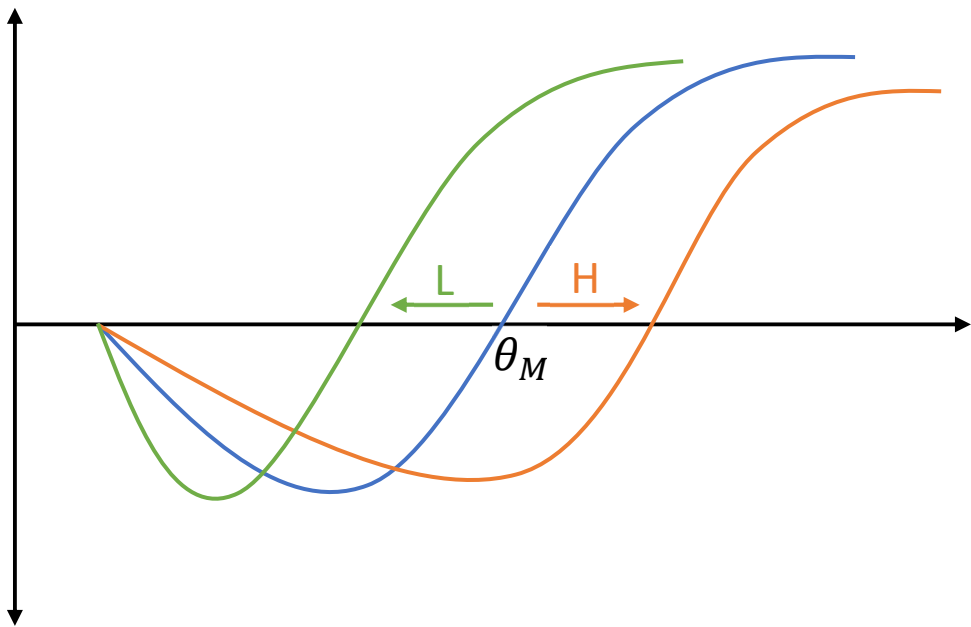


Figure 3.5: The BCM rule of synaptic plasticity. The x-axis represents the postsynaptic activity and the y-axis the function of postsynaptic activity as the magnitude of weight change. The sliding modification threshold θ_M defines the direction of synaptic weight change. Higher (H) / lower (L) postsynaptic activity increases (decreases) the LTP threshold, making LTP (LTD) more difficult to induce (Inspired by Wang, Tao 2009).

The sliding modification threshold θ_M is a homeostatic mechanism which keeps the modifiable synapses within useful dynamic range. The Hebbian positive-feedback process increases efficiency of effective synapses which make them even more effective. On the other hand, weak synapses are even more weakened by this process. The modification threshold stabilizes Hebbian plasticity by negative-feedback. The LTP threshold increases if the postsynaptic activity is increased, making LTP more difficult and LTD easier to induce. The process is inverted if the postsynaptic activity is reduced (**Figure 3.5**). The sliding modification threshold corresponds to metaplasticity (Jedlicka 2002; Lee, Kirkwood 2019).

Recent experiments have demonstrated the sliding threshold both *in vivo* and *in vitro* (Cooper, Bear 2012; Lee, Kirkwood 2019). Studies in sensory cortices showed that sensory

deprivation alters the synaptic modification threshold favor LTP (Kirkwood et al. 1996; Hardingham et al. 2008). Abraham et al. (2001) showed that LTP threshold can be modified heterosynaptically and cell firing is critical to sliding the LTP threshold (Abraham et al. 2001). The similar results were observed in CA1 area of hippocampus (Dudek, Bear 1992; Wang, Wagner 1999).

3.5.2 STDP model

In contrast to the BCM model, the Spike-Timing-Dependent Plasticity (STDP) synaptic plasticity rule is based on precise timing of pre- and post-synaptic spikes (Markram et al. 1997). STDP is a form of Hebbian synaptic plasticity rule which has been demonstrated in various neural circuits over a wide spectrum of species, from insects to humans and is now widely considered a biologically plausible model for synaptic modification occurring *in vivo* (Caporale, Dan 2008).

In Hebb's learning rule, repeated activation of a presynaptic cell immediately before spikes in a postsynaptic cell, induces synaptic strengthening (Hebb 1949). A typical experimental STDP protocol consists in pairing pre- and post-synaptic stimulations with a fixed $\Delta t = t_{post} - t_{pre}$, where t_{post} is a time of occurring a postsynaptic spike and t_{pre} is a time of occurring a presynaptic spike. In the case of $\Delta t < 0$, the postsynaptic spike occurs before the presynaptic spike which leads to weakening of synaptic strength. Conversely, when the postsynaptic spike occurs after the presynaptic one ($\Delta t > 0$), the synaptic strength is increased. When the presynaptic and postsynaptic spike occurs at the same time ($\Delta t = 0$), the effect is ignored. These pairings are then repeated between 15 and 200 times (between 0.1 and 15 Hz) with the spike timing and spike interval between successive pairing being kept constant (Cui et al. 2018).

The modification of weight can be formalized:

$$\Delta w_+ = A_+ \exp\left(-\frac{\Delta t}{\tau_+}\right) \quad (3.47)$$

$$\Delta w_- = A_- \exp\left(\frac{\Delta t}{\tau_-}\right), \quad (3.48)$$

where A_+ and A_- are constants depending on the nature of neuron and τ_+ and τ_- are decay constants. The critical window for modification is about 40 ms in width and is temporally asymmetric. It is obvious when the percentage change in the excitatory postsynaptic current (EPSC) is plotted against spike timing (

Figure 3.6). The length of the spike-timing window can be variable within the cell types which reflects the diversity of synaptic machinery and may serve for specific functions of information processing at different stages of neural pathways (Bi, Poo 2001).

There are several ways how to implement spike pairing. The two basic pairing schemes are all-to-all and the nearest neighbors. In all-to-all scheme, for each presynaptic spike are consider all previous postsynaptic spikes to effect of depression, and for each postsynaptic spike are consider all previous presynaptic spikes to effect of potentiation. Symmetrical nearest neighbors scheme means that each presynaptic spike is paired with the last postsynaptic spike and each postsynaptic spike is paired with the last presynaptic spike. In the case of a presynaptic centered paired scheme, for each presynaptic spike is considered a nearest postsynaptic spike occurred before the presynaptic one and a nearest postsynaptic spike occurred after the presynaptic one (Morrison et al. 2008).

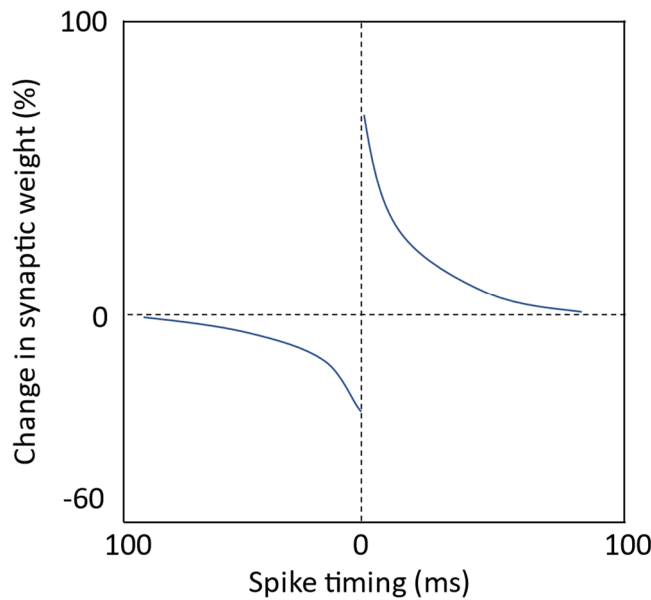


Figure 3.6: Spike-Timing-Dependent Plasticity. The figure shows a critical window for synaptic plasticity. LTD occurs when a postsynaptic spike precedes a presynaptic spike. When a presynaptic spike occurs before a postsynaptic spike, LTP is induced (Inspired by Bi, Poo 2001).

What is the cellular mechanism that controls the detection of the temporal order of pre- and post-synaptic spiking? NMDA receptors play a central role in this machinery since they are activated during correlated spiking activity and cause the induction both LTP and LTD. For correlated spiking with positive intervals, spiking following synaptic inputs apparently helps to open NMDARs, allowing high-level Ca^{2+} influx, thus LTP. With negative intervals, spiking

allows low-level Ca^{2+} influx through voltage-gated Ca^{2+} channels, which was followed immediately by additional low level Ca^{2+} influx due to NMDARs, resulting in LTD (Bi, Poo 2001).

Multiple mechanisms contribute to the control of STDP by neuromodulation. First, at the network level, neuromodulation alters the excitability and spiking dynamics of neural circuits, thus determining whether the pre- and postsynaptic spiking requirements for inducing STDP are met or not. Second, at the synaptic level, neuromodulation gates the synaptic activation of glutamate receptors, including NMDA receptors, which are crucial for both timing-dependent potentiation and depression. Third, at the intracellular signaling level, neuromodulation directly activates, inhibits, or regulates intracellular signaling cascades involved in synaptic plasticity. The neuromodulatory influence on STDP can be associated with an equally extensive range of behavioral processes, including attention, reward-based learning, and fear-conditioning, as well as pathological states, such as addictive behaviors (Brzosko et al. 2019).

What is the relationship between BCM and STDP? Izhikevich and Desai (2003) asked this question and came up with the answer that the nearest-neighbor STDP implementation is compatible with BCM with a fixed modification threshold. One reason is that postsynaptic spikes backpropagate into the dendritic tree and reset the membrane voltage in dendritic spines. Consequently, the most recent postsynaptic spike overrides the effect of all the earlier spikes, so that the membrane voltage is really only a function of time since the latest postsynaptic spike. Similarly, the first succeeding postsynaptic spike may override the effect of subsequent spikes due to calcium saturation or glutamate receptor desensitization. Making this assumption, one finds that when the postsynaptic spike train is a Poisson process with firing rate x , the postsynaptic probability density (the probability of observing a spike with a certain delay t) becomes exponential in time, xe^{-xt} . High (low) firing rates x result in predominantly small (large) intervals and hence in potentiation (depression). The expected magnitude of synaptic modification per one presynaptic spike has the form:

$$c(x) = \frac{\overbrace{\int_0^\infty A_+ e^{-t/\tau_+} xe^{-xt} dt}^{\text{average potentiation}} + \overbrace{\int_0^\infty A_- e^{t/\tau_-} xe^{xt} dt}^{\text{average depression}}}{x} \\ = x \left(\frac{A_+}{\tau_+^{-1} + x} + \frac{A_-}{\tau_-^{-1} + x} \right). \quad (3.49)$$

This is in agreement with the BCM synapse in the sense that low activity results in depression and large activity results in potentiation. The threshold between potentiation and depression (the zero crossing of $c(x)$),

$$\vartheta = -\frac{A_+/\tau_- + A_-/\tau_+}{A_+A_-}, \quad (3.50)$$

has positive values when $A_+ > |A_-|$ (potentiation dominates depression for short intervals) and negative values when $|A_-|\tau_- > A_+\tau_+$ (depression area is greater than potentiation area) (Izhikevich, Desai 2003). The sliding modification threshold can be ensured by metaplasticity (see below).

3.5.3 Meta-STDP model

The meta-STDP synaptic plasticity rule (Benuskova, Abraham 2007; Jedlicka et al. 2015) combines the BCM model (Bienenstock et al. 1982), STDP model (Markram et al. 1997), and metaplasticity (Abraham, Bear 1996) in one unified theoretical framework. The meta-STDP rule used in the simple spiking neuron model (Benuskova, Abraham 2007; Benuskova, Jedlicka 2012) as well as in the compartmental neuron model (Jedlicka et al. 2015) has successfully reproduced *in vivo* experimental data from dentate gyrus (Abraham et al. 2001).

In the study of Benuskova et al. (2007), the authors used a simple solely spike-based model. Inputs spikes along the medial perforant path (MPP) and the lateral perforant path (LPP) were generated with specific frequencies either at random (during spontaneous activity) or periodically (during testing and HFS). To simulate synaptic plasticity, they employed the STDP rule modified to incorporate the BCM sliding LTP/LTD threshold. For the STDP rule, they used the nearest-neighbor additive implementation, that for each presynaptic spike, only two postsynaptic spikes are considered. The positive and negative weight changes respected formulas (3.47) and (3.48). The BCM sliding threshold was incorporated in the STDP rule through the amplitudes of synaptic changes, such as:

$$A_+(t) = A_+(0) \left(\frac{1}{\theta_M(t)} \right) \quad (3.51)$$

$$A_-(t) = A_-(0)\theta_M(t), \quad (3.52)$$

where the current value of the modification threshold θ_M was calculate as in (3.46). Using this model, they have shown that homosynaptic LTP occurred as a consequence of tetanization delivered to the MPP, and LTD occurred simultaneously at LPP, as experiments, but only if the model include ongoing spontaneous activity. The blocked spontaneous activity also

blocked the LTD (Benuskova, Abraham 2007). Using the same model, they have been able to induce LTP using the low-frequency stimulation protocol (Benuskova, Jedlicka 2012).

In the more recent study of Jedlicka et al (2015), the authors used a more complex, conductance-based compartmental model of a dentate gyrus granule cell. The model contained two dendrites representing the MPP and LPP which were connected to the soma. The model was endowed with a synaptic plasticity mechanism containing a presynaptically centered nearest-neighbor implementation of the STDP rule with fast homeostasis (metaplasticity), respecting the equations (3.46), (3.47), (3.48), (3.51), and (3.52). The model included biophysics of the main ion channels in the dendrites and soma. They employed a realistic simulation of the granule cell spontaneous activity as *in vivo* with a significant peak around 8 Hz. The dendritic voltage threshold for the postsynaptic event detection at a synapse for local STDP implementation was -37 mV. The somatic voltage threshold for action potential detection for BCM homeostasis calculations was 0 mV (Jedlicka et al. 2015).

Using the combined STDP and BCM rules and compartmental modeling, they have been able to induce homosynaptic LTP and concurrent heterosynaptic LTD, as observed *in vivo*, as long as spontaneous activity continues in the input pathways. In addition, they have shown that the degree of LTD depends on the degree of LTP, due to the implemented homeostatic BCM rule that stabilizes cell firing. Their simulations have shown that ongoing background activity is a key determinant of the degree of long-term potentiation and especially long-term depression. A critical parameter of the model that affects BCM calculations is the length of the cell-firing integration period. They have shown that their model was stable and robust when using a relatively fast integration period (Jedlicka et al. 2015).

3.6 Implementation

In this section, we briefly describe the NEURON simulation environment, the organization of the code and the typical workflow.

3.6.1 NEURON simulation environment

NEURON (Hines, Carnevale 1997) provides a powerful and flexible environment for implementing biologically realistic models of electrical and chemical signaling in neurons and networks of neurons. It was developed at Yale University by Hines and colleagues. Total of 2304 research reports that have used NEURON was verified as of February 2, 2020 (<https://www.neuron.yale.edu/neuron/publications/neuron-bibliography>). NEURON is an

effective tool for biologically realistic compartmental modeling. Experimentalists can use its tools for cross-validating data, fitting a model data and experimental data, manipulating with experimentally inaccessible parameters. Theoreticians can use NEURON for testing hypothesis (Hines, Carnevale 1997). In our work, we used NEURON to develop, validate and simulate the CA1 pyramidal cell model.

Every nerve simulation program solves for the longitudinal spread of voltage and current by approximating the cable equation as a series of compartments connected by resistors. The sum of all the compartment areas is the total membrane area of the whole nerve. Using trial and error approach one can determine how many compartments and what time step should be used. Both the accuracy of the approximation and the computation time increase as the number of compartments used to represent the cable increases and the time step decreases. When the cable is “short,” a single compartment can be made to adequately represent the entire cable. For long cables or highly branched structures, it may be necessary to use a large number of compartments (Hines, Carnevale 1997).

The building block of NEURON compartmental models is **section**, which is a continuous length of unbranched cable. Sections are connected together to form any kind of branched tree structure. Each section is ultimately discretized into one or more compartments (**segments**) of equal length. The number of segments is specified by the parameter **nseg**, which can have a different value for each section. At the center of each segment is a **node**, the location where the internal voltage of the segment is defined. The transmembrane currents over the entire surface area of a segment are associated with its node. Based on the position of the nodes, NEURON calculates the values of internal model parameters such as the average diameter, axial resistance, and compartment area that are assigned to each segment. Distance along the length of a section is discussed in terms of the normalized position parameter x . One end of the section corresponds to $x = 0$ and the other end to $x = 1$. A section has **nseg** segments that are demarcated by evenly spaced boundaries at intervals of $1/nseg$. The nodes at the centers of these segments are located at $x = (2i - 1)/2nseg$, where i is an integer in the range [1, **nseg**] (Hines, Carnevale 1997).

Here are some important consequences from this. The only nodes whose locations are not affected by **nseg** are the nodes at the 0 and 1 ends. If **nseg** is an odd number, the section will have a node at its midpoint (0.5). Therefore, it is generally best for **nseg** to be an odd number. If the **nseg** is increased by an odd factor (e.g., multiply by 3), none of the existing

nodes will be destroyed. Instead, new nodes will be added between existing nodes. If the nseg is divided by an odd factor, some nodes will be destroyed, but those that remain will stay in their previous locations (Hines, Carnevale 1997).

NEURON incorporates a programming language based on Hoc, a floating point calculator with C-like syntax (Kernighan, Pike 1983; Hines, Carnevale 1997). NMODL language is used for adding additional mechanisms, ion channels, and signaling pathway (Hines, Carnevale 2000). Hoc is not exactly an interpreted language. Hoc statements are first dynamically compiled to an internal stack machine representation using a *yacc* parser and then the stack machine statements are executed. A key feature for neuroscientists is that Hoc syntax was extended in order to represent the notion of continuous cables, called sections. Sections are connected to form a tree shaped structure. User can specify the physical properties of a neuron without regard for the purely numerical issue of how many compartments are used to represent each of the cable sections. Hoc syntax provides some limited support for classes, objects, data encapsulation, polymorphism, but not inheritance (Hines et al. 2009).

NEURON includes option to use Python as a secondary scripting language. There are three distinct ways to use NEURON with Python. One is to run the NEURON program with Python as the interpreter accepting interactive commands in the terminal window. Another is to run NEURON with Hoc as the interactive interpreter and access Python functionality through Hoc objects and function calls. These first two cases are referred to as embedded Python. The third way is to dynamically import NEURON in a running Python or IPython instance, which is referred to as using NEURON as an extension module for Python. The Python interface to NEURON goes through the *neuron* module, especially the *neuron.h* submodule. The *neuron.h* submodule allows loading files, executing code, and calling functions written in Hoc (Hines et al. 2009). We used a binary installer which provides Python embedded in NEURON.

There are several benefits to using Python as a secondary scripting language. Python is a fully object-oriented language, supporting encapsulation, polymorphism and inheritance. Python provides expressive syntax, powerful debugging capabilities, and support for modularity, facilitating the construction and maintenance of complex programs. Useful tools can be easily plug-in to the user's code (Oliphant 2007; Hines et al. 2009). For example, Numpy (Harris et al. 2020) and Scipy (Virtanen et al. 2020) provide core scientific functionality, while Matplotlib (Hunter 2007) is useful for 2-D plotting.

NEURON supports parallel simulations at the single cell level (Hines et al. 2008) as well as at the network level (Migliore et al. 2006). In the case of parallel network simulations, NEURON uses *ParallelContext* class, built on the standard and widely available Message Passing Interface (MPI). The simple spike distribution mechanism (*MPI_Allgather*) distributes all spike times to all processors. Each processor integrates the equations for its subnet over an interval equal to the minimum (interprocessor) presynaptic spike generation to postsynaptic spike delivery connection delay (Migliore et al. 2006). At the single cell level, a multi-compartment neuron model is divided into subtrees such that no subtree has more than two connection points to other subtrees. The subtrees can be simulated on different processors and the entire system remains amenable to direct Gaussian elimination with only a modest increase in complexity. Accuracy is the same as with standard Gaussian elimination on a single processor (Hines et al. 2008).

NEURON runs under MacOS, MS Windows, and UNIX/Linux. Published models are accessible from public databases such as ModelDB or NeuronDB (Hines, Carnevale 1997).

3.6.2 Code organization

All scripts are written in Python, version 3.7. Source codes are available in the GitHub repository, https://github.com/tomko-neuron/CA1_plasticity. Source code is organized in following directories.

CA1_plasticity.experiments

This directory contains user-defined experiments. Each experiment has a defined directory that contains all the necessary files and scripts. A typical experiment directory structure is illustrated for our “experiment1”.

CA1_plasticity.experiments.experiment1

This directory contains the files and scripts need for the simulations mentioned in Chapter 7. The directory contains the `main.py` script that is used to run a simulation. The script is described in Typical workflow. The `figures` subdirectory contains saved figures, the `recordings` subdirectory contains saved recordings, the `settings` subdirectory contains all settings. This subdirectory contains `setting.json` and `synapses.json` files needed for the simulation configuration and add synapses to the model.

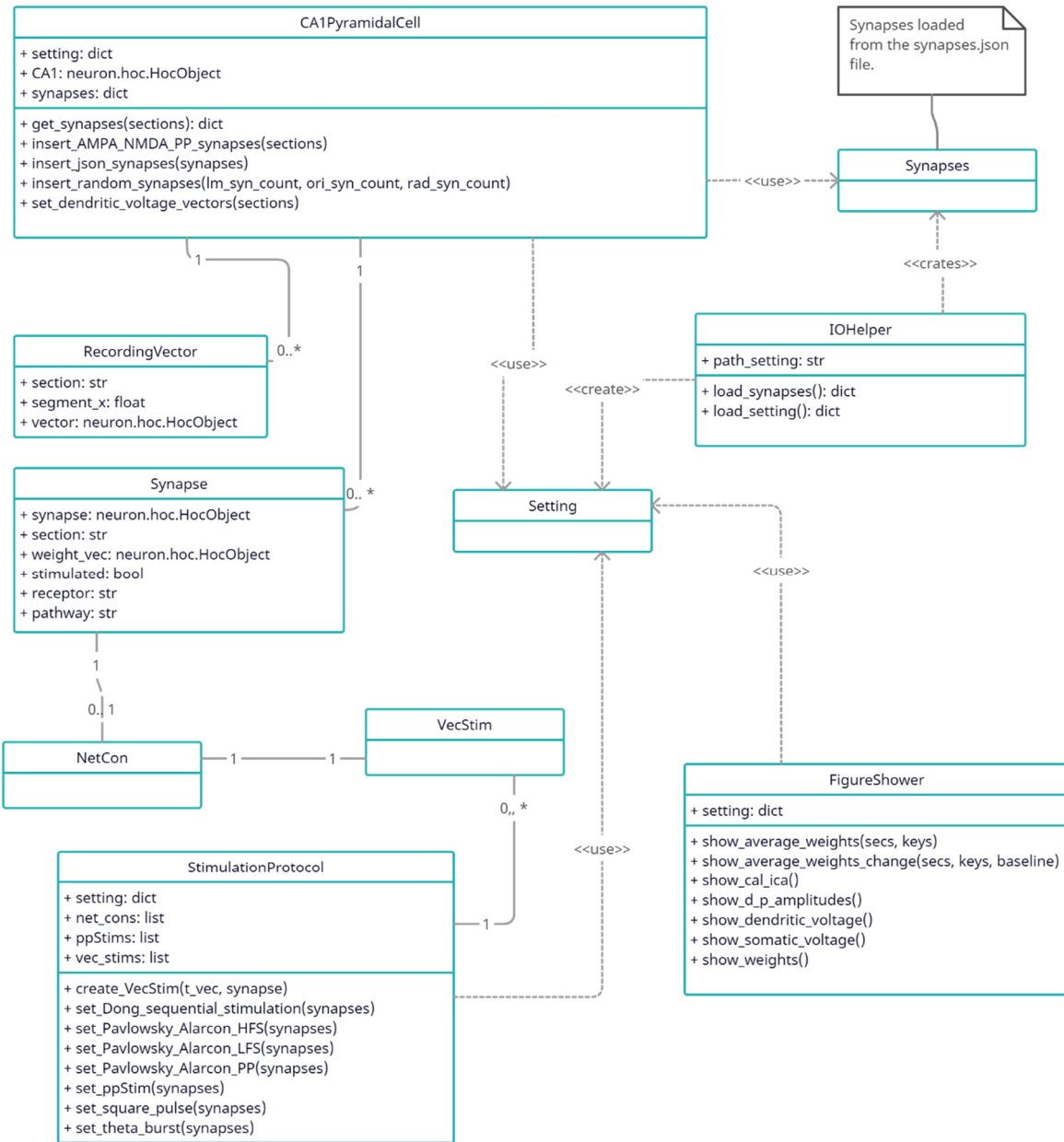


Figure 3.7: The UML Class diagram of the project. The diagram shows classes, their main attributes and methods and relationships between objects.

CA1_plasticity.io

This directory contains two classes used for data processing. The `IOHelper` class is used to load and save the settings and recordings. The `FigureShower` class is used to visualize the recorded data. Several methods are defined in the `FigureShower` class to plot the evolution of voltages, synaptic weights and ionic currents over time.

CA1_plasticity.model

This directory contains the classes and files needed to work with the model. The `CA1PyramidalCell` class represents a model of the CA1 pyramidal cell. The constructor loads the model from a `.hoc` file. The class defines methods for adding synapses, setting recording vectors and setting spontaneous activity. The `StimulationProtocol` class is used to set a stimulation protocol. Each stimulation protocol is defined by its own method and the parameters are defined in the `setting.json` file in the experiment directory (see above). The `mods` directory contains additional `.mod` files that must be precompiled. They are loaded when the model is loaded. The `hoc_models` directory contains the models defined in HOC.

3.6.3 Typical workflow

A typical workflow consists of four main stages: (1) configuration, (2) model instantiation, (3) simulation and (4) saving and analysis (**Figure 3.8**). Here we describe details about each stage.

Configuration

At this stage, the user defines the `setting.json` and `synapses.json` files. The `setting.json` file contains a nested settings dictionary. The individual parameters are defined in the following dictionaries: *BCM* for BCM parameters, *netstim* for spontaneous activity parameters, *simulation* for simulation parameters, *synapses* for synapse parameters, *initial_weights* for initial synaptic weights, *section_lists* for section lists and *protocol* for stimulation protocol parameters. For each stimulation protocol is a dictionary of parameters.

The `synapses.json` file contains a nested dictionary of synapses that are added to the model. The file contains a directory of sections. Each section contains a list of synapses. The parameters of each synapse are defined as a dictionary.

Model instantiation

At this stage, the model is being prepared. Settings and additional `.mod` files are loaded. The model is loaded from a template written in HOC. The template defines the morphology and biophysics of the model. Next, the user can configure the model. The user can insert predefined synapses from the `synapses.json` file or insert synapses randomly, set spontaneous activity and set recording vectors.

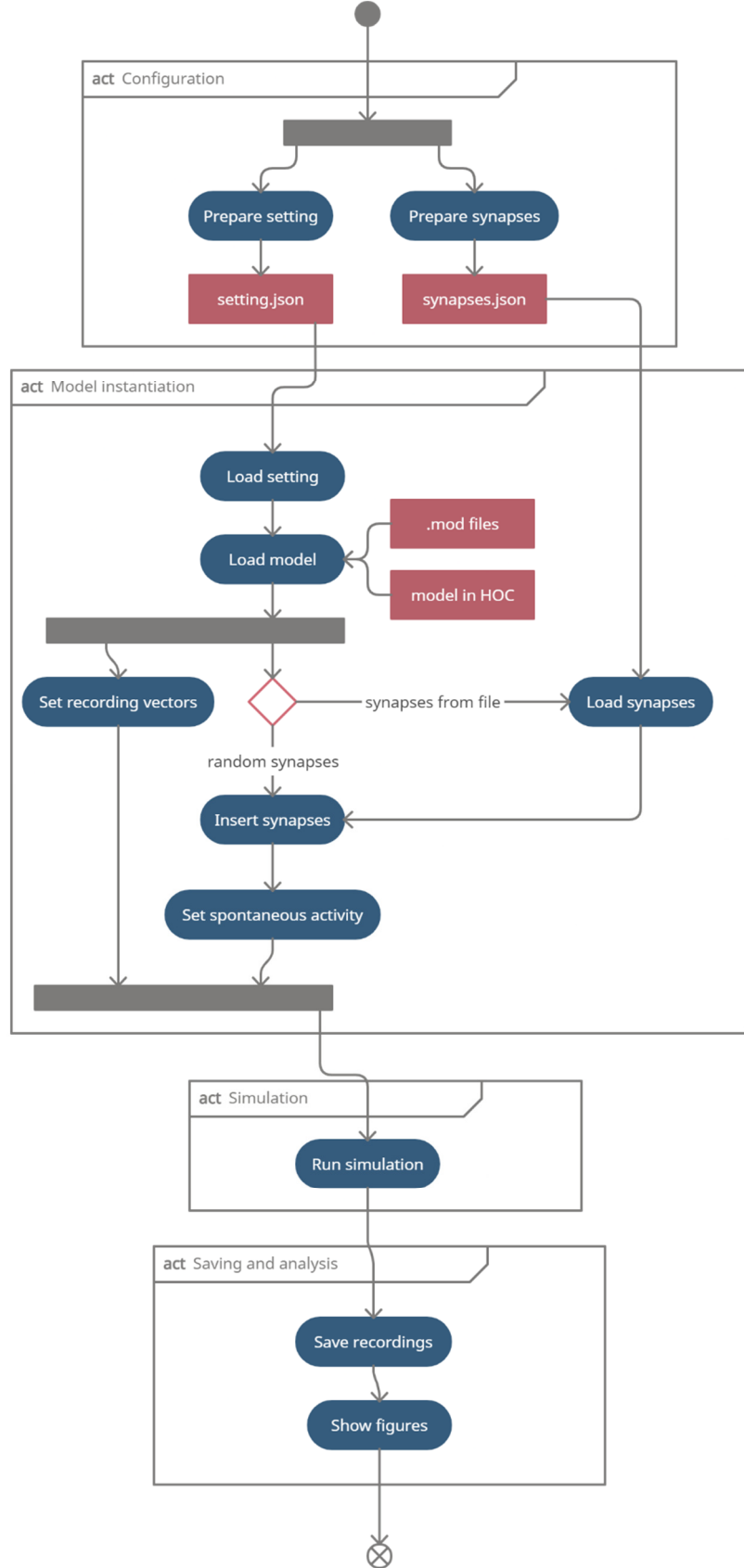


Figure 3.8: The UML Activity diagram. The diagram shows four stages of the typical workflow: (1) configuration, (2) model instantiation, (3) simulation and (4) saving and analysis.

Simulation

When the model is ready, the simulation can begin. Simulation parameters are set from the `setting.json` file. NEURON is used as a back-end simulator.

Saving and analysis

When the simulation is complete, the data is saved. The recorded voltages are saved in the `voltages.p` file. The evolution of BCM parameters over time is saved in the `bcm.p` file. The recorded ion currents are saved in the `currents.p` file. Synapses are stored in two files: `synapses.json` contains a nested dictionary of synapses that can be re-used in next simulation, `synapses.p` also contains the evolution of synaptic weights over time. The settings are saved in the `setting.json` file. All `.p` files are binary files with a nested dictionary structure.

The user can use several methods defined in the `FigureShower` class to analyze the data. When creating an instance of a class, the user must define the path to the directory containing the recordings, the path to the directory where the figures will be saved, the dictionary containing the settings, and set whether the figures will be saved automatically. Each method can have additional parameters.

3.7 Summary

In this chapter, we described mathematical basics of computational neuroscience. We briefly introduced differential equations and analytical and numerical methods for solving differential equations. Our simulations are based on a compartmental model of CA1 pyramidal cell. Thus, we introduced a compartmental model of neuron and a cable theory which is a mathematical basis of the multicompartmental model. We also described passive and active properties of neuron model. In Chapter 2 we described the theory of action potential from biological view. In this chapter, we introduced the Hodgkin-Huxley model which is a quantitative model of action potential. We presented synaptic plasticity in terms of computational modeling. We introduced two fundamental models of synaptic plasticity, the BCM model and the STDP model, and their combination in the meta-STDP model. The aim of introducing these models was to demonstrate their use in various experimental studies of synaptic plasticity. Secondly, we employed the meta-STDP rule to model synaptic plasticity in this thesis. As all of our simulations run in the NEURON environment, we briefly described its properties. Finally, we described the organization of the code and the typical workflow.

Chapter 4

4 Computational model of CA1 pyramidal cell with meta-STDP stabilizes under ongoing spontaneous activity as *in vivo* (Tomko et al. 2019)

4.1 Introduction

Synaptic plasticity is the basic mechanism of learning and memory. It is the ability of neurons to change efficacies of synaptic weights in response to stimuli. There is no general agreement on which synaptic plasticity rule(s) hold in the brain, although some general principles have been agreed upon. Thus, we implemented the Spike-Timing Dependent Plasticity rule with metaplasticity (meta-STDP) in a biophysically realistic computational model of hippocampal CA1 pyramidal cell in order to model synaptic plasticity in alive hippocampus. Characteristic feature of the brain *in vivo* is an ongoing spontaneous or background activity in neural circuits. Neurons should not change their weights as a result of this background activity, only when a statistically different pattern of input activity appears. As a first step in our research, we subjected our CA1 model to realistically simulated input activity and we have achieved realistic output spontaneous activity and stabilization of synaptic weights after a short time.

4.2 Methods

4.2.1 Compartmental model of the CA1 pyramidal cell

NEURON simulation environment (Hines, Carnevale 1997), version 7.6.5, and Python, version 3.6, running on PC under Windows 7 or Windows 10 were used to create and simulate the model. The model was previously published by Cutsuridis et al. (2009). Source code of the model is available from the ModelDB database at <https://senselab.med.yale.edu/modedb/>, accession No. 123815. The CA1 pyramidal cell compartmental model is comprised 15 distinct sections, i.e. soma, axon, 4 stratum oriens (SO) dendritic sections, 3 stratum radiatum (SR) dendritic sections, and 6 stratum lacunosum-moleculare (SLM) dendritic sections (Cutsuridis, Cobb, et al. 2010).

Each section contains a calcium pump and buffering mechanism, a calcium activated slow afterhyperpolarization (AHP) potassium current, a medium AHP potassium current, a high

voltage activated (HVA) L-type calcium current, an HVA R-type calcium current, a low voltage activated (LVA) T-type calcium current, an h current, a fast sodium current, a delayed rectifier potassium current, a slowly inactivating M-type potassium current and a fast-inactivating A-type potassium current. Active and passive properties were taken from (Poirazi et al. 2003a; 2003b).

4.2.2 Model inputs

The NEURON built-in class *Exp2Syn* is used to model all excitatory synapses. This class models synaptic conductivity g as a two-state kinetic scheme described by two exponential functions:

$$g(t) = w(e^{t/\tau_2} - e^{t/\tau_1}) \quad (4.1)$$

where w is synaptic weight, $\tau_1 = 0.5$ ms is the rise time constant, and $\tau_2 = 3$ ms is the decay time constant. The peak conductance represents synaptic weight and is modified according to the plasticity rule (see below).

A total number of excitatory synapses was set at 98 (see **Figure 4.1**). The distribution of synapses on the dendritic tree was determined according to experimental data (Megías et al. 2001). The number of synapses in the stratum oriens distal sections was 40, representing 40.81% of all model synapses. Apical branches in the stratum radiatum were modelled by tree connected sections with total number of 52 excitatory synapses, representing 53.06% of all model synapses. The total number of excitatory synapses in the stratum lacunosum-moleculare sections was 6, representing 6.12% of all model synapses.

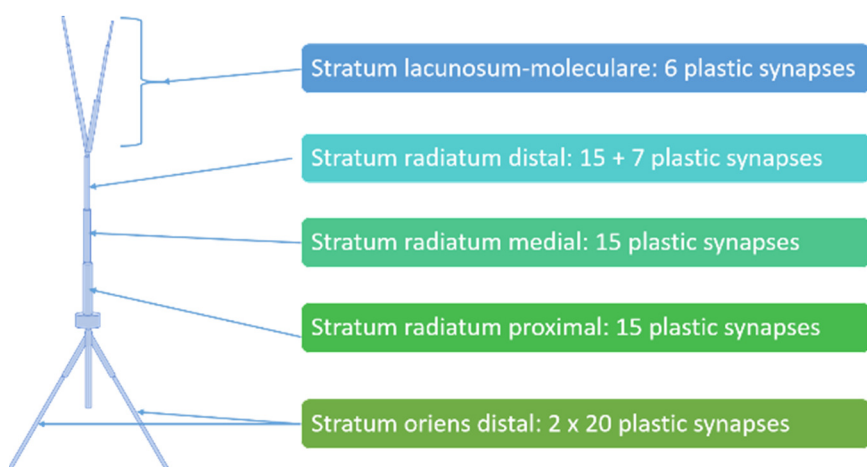


Figure 4.1: Compartmental model of CA1 pyramidal cell with position and number of synapses (schematic).

There are two main excitatory synaptic inputs into the CA1 cell i.e., Schaffer and commissural pathways, which make synapses in all layers except soma and stratum lacunosum-moleculare. In the latter, synapses originate from the perforant path. Based on experimental data (Shinohara et al. 2012), we divided synapses as follows: for stratum oriens 2 x 20 synapses (12 commissural and 8 Schaffer) and for stratum radiatum 17 commissural and 35 Schaffer synapses.

Each synapse received a train of presynaptic spikes that were generated by independent spikes generators. In NEURON it is taken care of by the built- in process *NetStim*. Presynaptic spikes sequence delivered to one synapse consisted of a combination of random and periodic spike trains. We have chosen this strategy because we can thus simulate the theta activity that is a prominent state of the hippocampal network (Buzsáki 2002), plus the background random spikes.

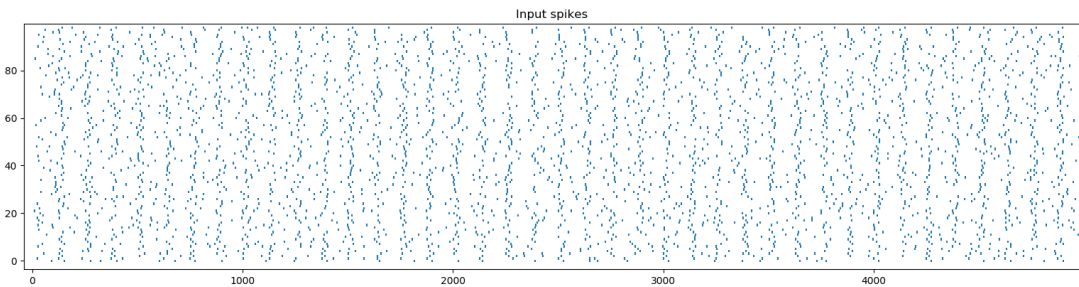


Figure 4.2: Ongoing input spontaneous activity over the period of 5s. In this graph the x-axis is the time in ms, and y-axis is the order number of a synapse.

4.2.3 Synaptic plasticity

Meta-STDP rule was employed to model synaptic plasticity. Implementation of the rule was the same as for the granule cell (Jedlicka et al. 2015). We too have used the presynaptic centered pairing scheme because it is biologically relevant and compatible with the BCM theory. In this scheme, for each presynaptic spike, only one last and one next postsynaptic spike is considered. The weight change is calculated as:

$$w(t + \Delta t) = w(t)(1 + \Delta w_p - \Delta w_d) \quad (4.2)$$

where Δw_p is positive weight change and Δw_d is negative weight change.

On the one hand, the positive weight change (potentiation) occurs when presynaptic spike precedes postsynaptic spike. On the other hand, weakening of the weight (depression) occurs when postsynaptic spike precedes presynaptic spike. It is formulated using equations (3.47)

and (3.48). Parameter t_{post} in our case represents the instant of time at which the voltage on the postsynaptic dendrite, where a synapse is located, exceeds the threshold of -37 mV. It is experimentally estimated threshold for induction of LTP/LTD (Lisman, Spruston 2005).

Amplitudes of LTP / LTD in the meta-STDP are dynamically changed as a function of a previous temporal average of soma spiking which is calculated using equations (3.46), (3.51), and (3.52).

In our simulations, we used already existing .mod files (<https://senselab.med.yale.edu/modeldb>ShowModel.cshtml?model=185350>) (Jedlicka et al. 2015) to model plastic synapses according to the meta-STDP synaptic plasticity rule. We joined these files with the files of the compartmental CA1 model into a one synaptically plastic CA1 model.

4.3 Results

The first step was to optimize our model parameters to mimic firing as in *in vivo* conditions. We performed it in two phases: the model with fixed weights (without synaptic plasticity rule) and the model with plastic weights (with the synaptic plasticity rule described above).

In experiments with the model with fixed weights we manipulated the values of initial weights and parameter *start* of *NetStim*. The model output firing frequency corresponded to *in vivo* CA1 pyramidal cell behavior when the weights were randomly initiated to values from interval [0.0002, 0.0003) and parameter *start* of *NetStim* to random values from interval [0, 46]. Average input frequency from 10 runs was 7.27 (standard deviation 0.03) and average output frequency was 2.56 (standard deviation 0.76), see **Figure 4.3**.

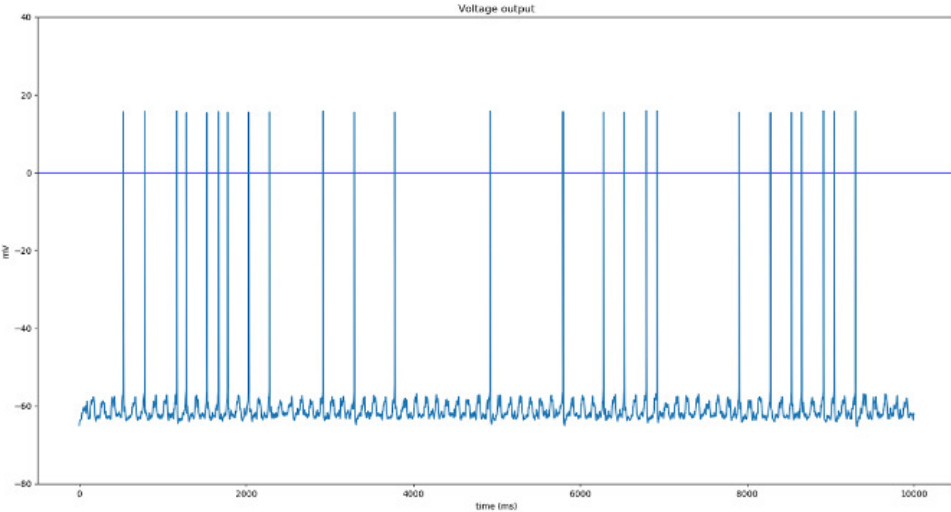


Figure 4.3: The CA1 pyramidal cell model firing at a frequency 2.56 Hz without synaptic plasticity over 10s. The x-axis is the time in ms, and y-axis is the somatic voltage in mV.

The model with plastic synapses had more parameters that were optimized. Each simulation run covered about 5 minutes of real time. Parameters were considered as optimal when the model output firing frequency was about 2.0 Hz, and weights, average weights, and amplitudes A_p and A_d were dynamically stable. This has been accomplished using the following parameter values: *NetStim* parameter *start* from interval [0, 40), initial random weights from interval [0.0002, 0.0006). Initial amplitudes were set to $A_p(0) = 0.004$ for potentiation and $A_d(0) = 0.002$ for depression. Scaling constant α was set to 3000. Decay time constant for potentiation and depression was $\tau_p = \tau_d = 15$ ms, and averaging time constant τ for the postsynaptic spike count was set to 50000 ms.

The following figures show the results of individual weights (**Figure 4.4**), average weights (**Figure 4.5**), potentiation and depression amplitudes (**Figure 4.6**) and integrated spike count θ_M (**Figure 4.7**) for one typical simulation. The next figure shows the evolution of individual synaptic weights in all the layers i.e., oriens distal, radiatum proximal, radiatum medial, radiatum distal and lacunosum-moleculare, over the first 5 minutes of time.

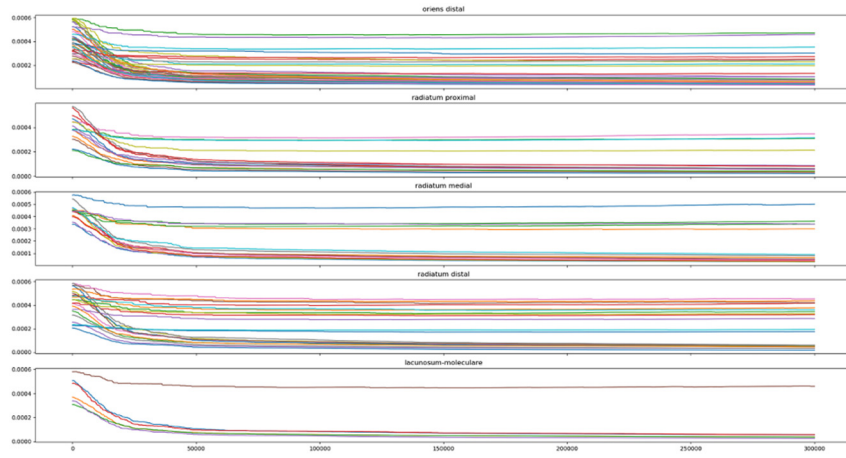


Figure 4.4: The CA1 pyramidal cell model weights were stabilized with employed meta-STDP rule after a short transitory period. The x-axis denotes time in ms and the y-axis denotes values of synaptic weights. Output firing frequency 1.78 Hz.

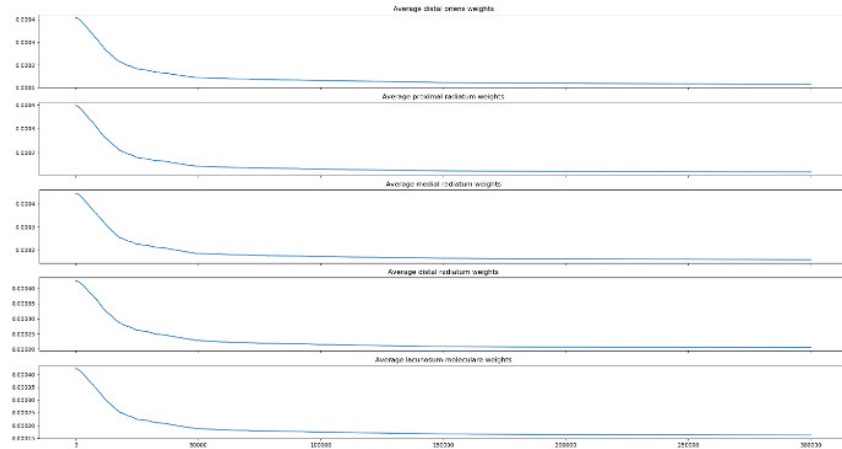


Figure 4.5: The CA1 pyramidal cell model average weights in all the layers were stabilized with employed meta-STDP rule. Output firing frequency 1.78 Hz.

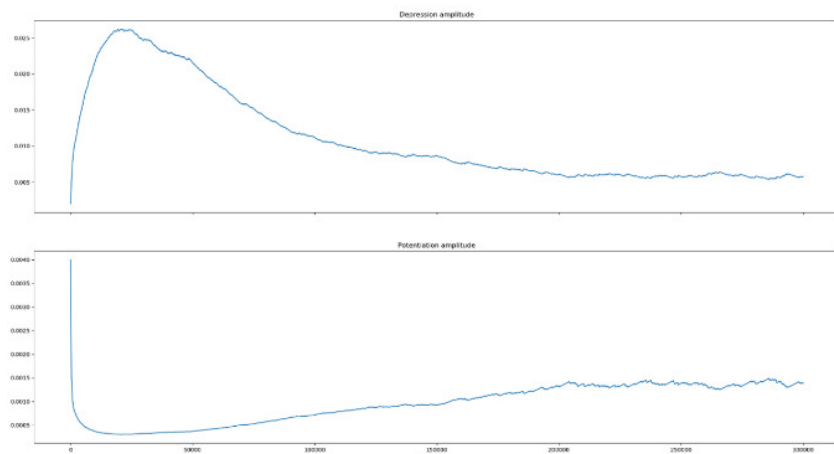


Figure 4.6: The CA1 pyramidal cell model depression and potentiation amplitudes were stabilized with employed meta-STDP rule. Output firing frequency 1.78 Hz.

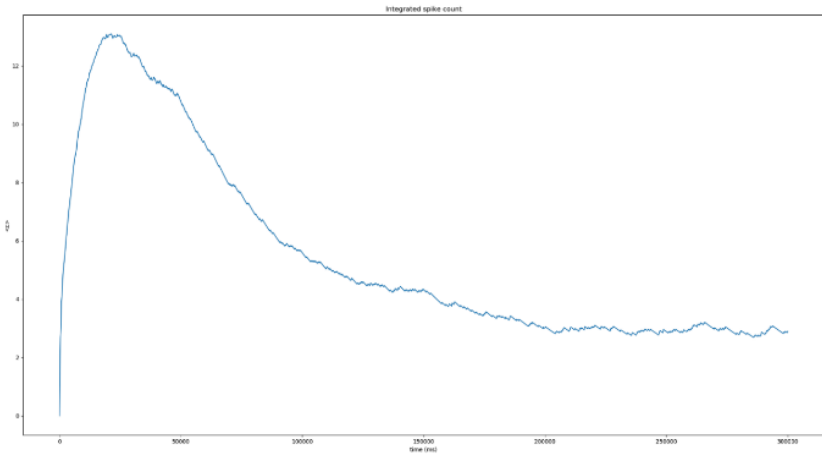


Figure 4.7: The CA1 pyramidal cell model integrated spike count was stabilized with employed meta-STDP rule. Output firing frequency 1.78 Hz.

Chapter 5

5 A new reduced-morphology model for CA1 pyramidal cells and its validation and comparison with other models using HippoUnit (Tomko et al. 2021)

Modeling long-term neuronal dynamics may require running long-lasting simulations. Such simulations are computationally expensive, and therefore it is advantageous to use simplified models that sufficiently reproduce the real neuronal properties. Reducing the complexity of the neuronal dendritic tree is one option. Therefore, we have developed a new reduced-morphology model of the rat CA1 pyramidal cell which retains major dendritic branch classes. To validate our model with experimental data, we used HippoUnit, a recently established standardized test suite for CA1 pyramidal cell models. The HippoUnit allowed us to systematically evaluate the somatic and dendritic properties of the model and compare them to models publicly available in the ModelDB database. Our model reproduced (1) somatic spiking properties, (2) somatic depolarization block, (3) EPSP attenuation, (4) action potential backpropagation, and (5) synaptic integration at oblique dendrites of CA1 neurons. The overall performance of the model in these tests achieved higher biological accuracy compared to other tested models. We conclude that, due to its realistic biophysics and low morphological complexity, our model captures key physiological features of CA1 pyramidal neurons and shortens computational time, respectively. Thus, the validated reduced-morphology model can be used for computationally demanding simulations as a substitute for more complex models.

5.1 Introduction

Biologically realistic compartmental modeling has become a standard and widely used method in neuroscience (Herz et al. 2006; Einevoll et al. 2019). In combination with experiments, it represents a powerful tool for predicting and better understanding the complex electrophysiological behavior of neurons under physiological (Billeh et al. 2020) as well as pathological conditions (Mäki-Marttunen et al. 2019). However, despite considerable progress, a major challenge in the field has been that most published models have been tuned ad hoc for a limited set of experiments and therefore fail at generalizing the results to other experimental conditions (Almog, Korngreen 2016). We have recently developed a toolbox that supports the

generalization of simulation results from one neuronal morphology to others (Beining et al. 2017). Nevertheless, standardized tests for capturing a canonical set of experimental features are urgently needed for all nerve cell types. Accordingly, the HippoUnit test battery has recently been developed to address this problem for CA1 pyramidal cells (Sáray et al. 2021). So far it has been successfully applied to full-morphology models. However, simulations of long-lasting neuronal dynamics, occurring on the time scale of tens of minutes, hours, or days (e.g., long-term synaptic plasticity or homeostatic synaptic and intrinsic plasticity), are often not feasible in models with full morphology and detailed biophysics. Therefore, here we aimed to develop a new reduced-morphology model that would decrease computational times as compared to full-morphology models while preserving their biophysical realism.

CA1 pyramidal neurons are one of the most studied cell types in the brain. Many computational models of CA1 pyramidal cells have provided insights into their electrophysiological behavior and function. On ModelDB8, more than 130 model entries can be found (<https://senselab.med.yale.edu/ModelDB/ModelList?id=258>) including several biophysically and morphologically detailed models (Poirazi et al. 2003a; 2003b; Gasparini et al. 2004; Katz et al. 2009; Narayanan, Johnston 2010; Uebachs et al. 2010; Kim et al. 2015). These models were created for simulations of selected experimental tests but some of them have been recently evaluated by using the standardized set of HippoUnit tests (Sáray et al. 2021). However, no reduced-morphology CA1 pyramidal neuron models have yet been exposed to such systematic testing.

Thus, in this work, we have used the battery of standardized HippoUnit tests to validate our CA1 pyramidal cell model with reduced morphology. For a comparison, we used a previously validated full-morphology model (Migliore et al. 2018) as a reference model and three published reduced-morphology models that have not been tuned before for any of the HippoUnit features as controls. The three reduced-morphology models have been tuned previously for the following specific purposes. The models by Cutsuridis et al. (2010) and Cutsuridis and Poirazi (2015) have been used in circuit models with realistic spike timing of several hippocampal neuron types with respect to theta rhythm (see details in Methods). These models simulated input pattern recall and storage in the CA1 (Cutsuridis, Cobb, et al. 2010), and long latencies of hippocampal cell activities in the entorhinal-hippocampal network due to theta modulated inhibition (Cutsuridis, Poirazi 2015), respectively. The model from Turi et al. (2019) has been used within a hippocampal circuit model that has predicted the role of disinhibition in goal-directed spatial learning (Turi et al. 2019).

Here, we employ the HippoUnit tests to compare these published models to a new compartmental model with reduced morphology. We show that our model is able to account for the following six well-established characteristic anatomical and physiological properties of CA1 pyramidal cells (see Methods for details): (1) The reduced dendritic morphology contains all major dendritic branch classes. In addition to anatomy, the model reproduces also 5 key physiological features, including (2) somatic electrophysiological responses, (3) depolarization block, (4) EPSP attenuation (5) action potential (AP) backpropagation, and (6) synaptic integration at oblique dendrites. By measuring the runtimes of the models, we show that the reduced-morphology models shorten the computational times as compared to the full-morphology model. By comparing the runtimes among the reduced models, we confirm that differences in the numbers of compartments and in the ion channel content primarily dictate the length of the simulations.

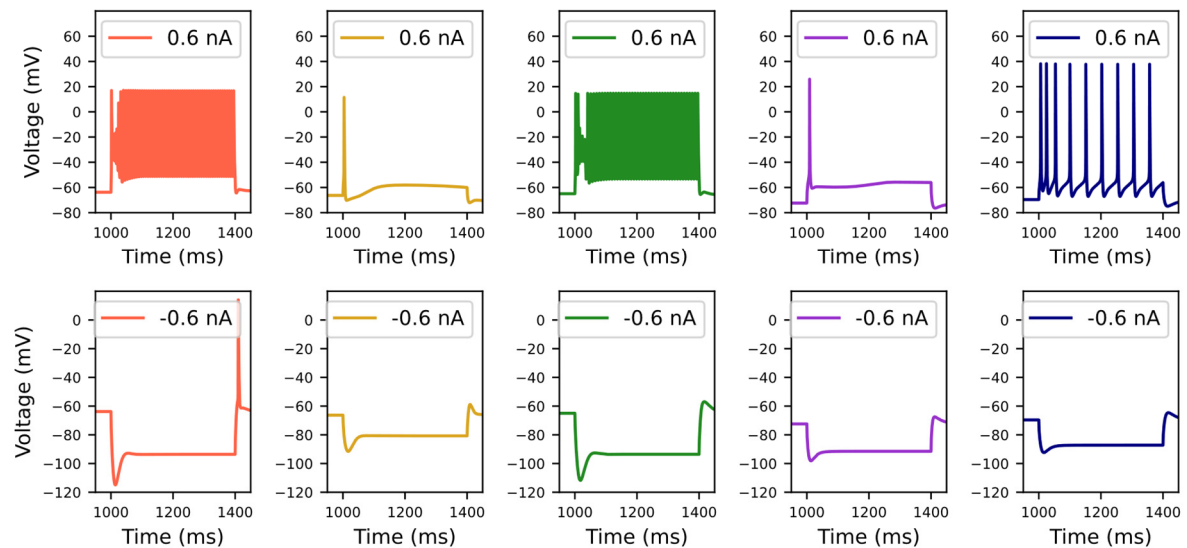
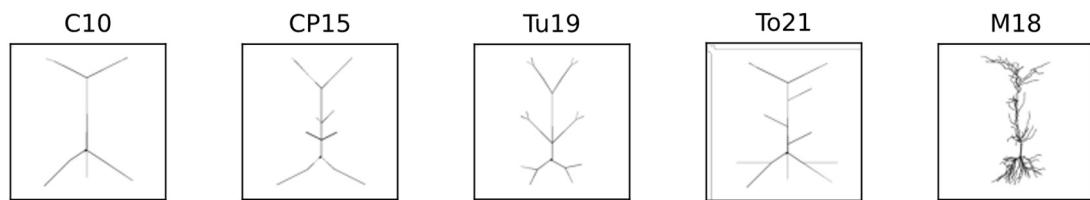
5.2 Methods

We used HippoUnit (Sáray et al. 2021), a Python test suite, for automatic and quantitative validation of compartmental models of neurons built in NEURON (Hines, Carnevale 1997). HippoUnit is based on NeuronUnit, an extensible SciUnit-driven library designed for the testing of neuron models (Gerkin et al. 2019). HippoUnit implements standard experimental protocols that are run on hippocampal neuronal models, thus providing a systematic evaluation of model performance. We used the following tests that are available in HippoUnit: Somatic Features Test, Depolarization Block Test, Postsynaptic Potential Attenuation Test, Backpropagating Action Potential Test and Oblique Integration Test (Sáray et al. 2021).

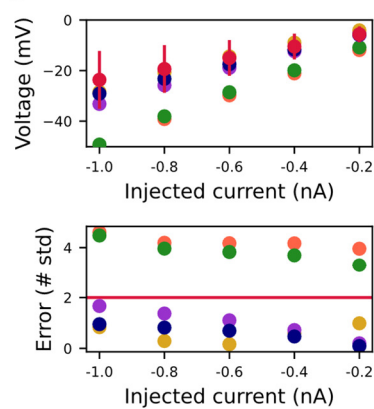
In the HippoUnit, a set of target features is specified for each test expressed as the mean and standard deviation. The output of a model is compared to the experimental data via feature-based error functions. Error is expressed as the absolute difference between the model output and a mean value of a feature, divided by the standard deviation (Z-score) (Druckmann et al. 2007). The overall model score for a given test is the average of the errors of all tested features (Sáray et al. 2021). All simulations in our study were performed under MS Windows 10, Python version 3.7 and NEURON version 7.7.2. Device specification was: 2.60 GHz CPU and 16 GB RAM.



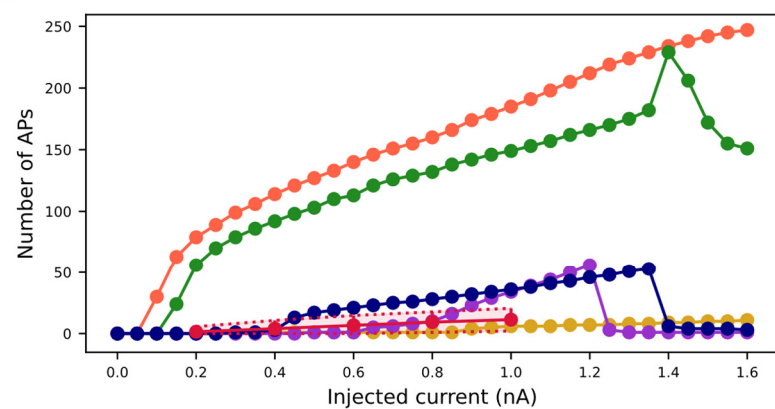
a



b



c



d

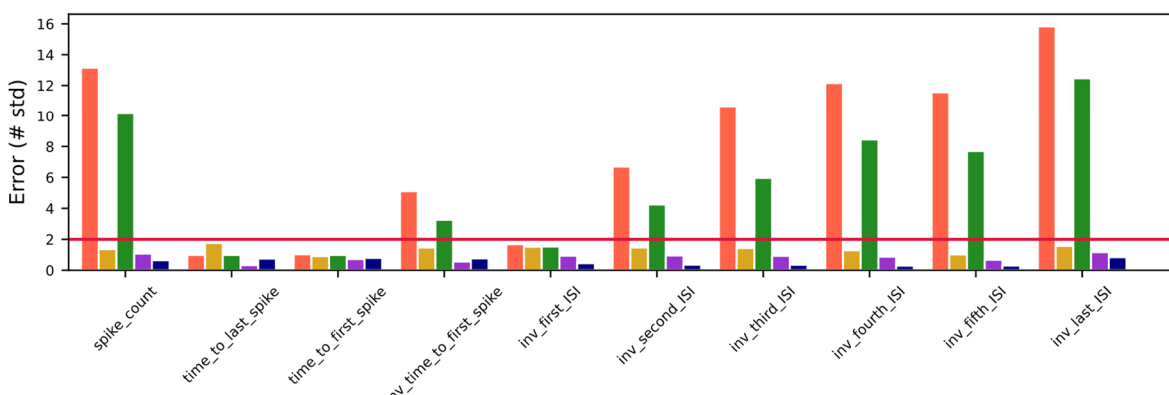


Figure 5.1: Validation of somatic voltage features, spike time features, and spike shape features using the Somatic Features Test **(a)** The first row shows the morphology of tested models. Reduced-morphology models are based on the simplified anatomy of the C10 model. For comparison, one well-tuned full-morphology M18 model was included. The second and third rows show the typical somatic response of the tested models to the positive and negative somatic current injections. **(b)** Voltage deflection of models across the different somatic current injections (top) and corresponding errors (bottom). The red horizontal line represents $sd = 2$ and determines the maximum error accepted. **(c)** Number of fired APs as a function of injected current. The red line marked as experiment represents experimental values obtained from the Migliore et al. paper (Migliore et al. 2018). The red shaded area corresponds to twice the experimental standard deviation. **(d)** Model errors in selected spike event features expressed by the number of standard deviations. The red horizontal line represents $sd = 2$ and determines the maximum error accepted.

5.2.1 Computational models of CA1 pyramidal cell

Five compartmental models of the CA1 pyramidal cell were used for testing. Four models (Cutsuridis, Cobb, et al. 2010; Cutsuridis, Poirazi 2015; Migliore et al. 2018; Turi et al. 2019) are available in the ModelDB repository (<https://senselab.med.yale.edu/ModelDB/>). Our new model has been optimized based on HippoUnit tests, the others were not and hence served as controls. The model of Migliore et al. (Migliore et al. 2018) has been previously tuned for selected features of the somatic feature test and was therefore included as a reference (benchmark) model. A further description of the models is given below. Their schematic architectures are shown in **Figure 5.1**.

5.2.1.1 Model of Cutsuridis et al. (2010) – C10 model

This is a reduced-morphology model of the CA1 pyramidal cell that was used to model pattern encoding and retrieval in a small CA1 microcircuit. The model is available from ModelDB under accession number 123815. The model is composed of 15 sections, i.e., one for the soma, one for the axon, four for the basal dendrites, three for the apical dendritic trunk in the stratum radiatum and six for the dendritic tuft in the stratum lacunosum-moleculare (**Figure 5.1**). The model contains the following ion channels: Hodgkin-Huxley-like channel including both a sodium and a delayed rectifier potassium channel, a non-specific I_h channel, two additional types of potassium channels (K_A , K_M), three types of calcium channels (Ca_L , Ca_R , Ca_T), two types of calcium activated potassium channels (K_{Ca} , K_{Cagk}), and a calcium pump / buffering mechanism. Biophysical properties were adapted from the Poirazi model (Poirazi et al. 2003a; 2003b). For more details, see original paper (Cutsuridis, Cobb, et al. 2010).

5.2.1.2 Model of Cutsuridis and Poirazi (2015) – CP15 model

This is a similar reduced-morphology model of the CA1 pyramidal cell that was used in a computational study on how theta modulated inhibition can account for the long temporal

windows in entorhinal-hippocampal loop. The model has the same morphology (**Figure 5.1**) as the C10 model described above, with one exception. Four sections connected to the apical trunk have been added to the model representing oblique dendrites. The model contains the same biophysical properties as the previous described model that were adapted from the Poirazi model (Poirazi et al. 2003a; 2003b; Cutsuridis, Poirazi 2015). Accession number in ModelDB is 181967.

5.2.1.3 Full-morphology model of Migliore et al. (2018) – M18 model

To compare reduced-morphology models to a previously tuned realistic full-morphology model (**Figure 5.1**), we included the M18 model in our tests. This full-morphology model of the CA1 pyramidal cell is the result of a recent study that analyzed variability in the peak specific conductance of ion channels in individual CA1 neurons. A set of morphologically and biophysically accurate models was generated. The models are accessible from ModelDB under accession number 244688. The source code of the selected model is in a file named “cell_seed3_0-pyr-08.hoc”¹⁷. The model contains the following ion channels: a sodium channel, three types of potassium channels (K_{DR} , K_A , K_M), a non-specific I_h channel, three types of calcium channels (Ca_L , Ca_N , Ca_T), two types of calcium activated potassium channels (K_{Ca} , K_{Cagk}), and a calcium accumulation mechanism. The peak conductance of I_{KA} and I_h and the equilibrium potential of the passive current (e_{pas}) are calculated separately for each section according to its distance from the soma. The assignment of these values based on the distance from the soma is described by a linear function whose parameter values were fitted during the M18 model optimization process. The remaining conductances are distributed uniformly (Migliore et al. 2018).

5.2.1.4 Model of Turi et al. (2019) – Tu19 model

This reduced-morphology model of CA1 pyramidal cell was used in a biophysical model of CA1 hippocampal region that simulates the place cells/fields dynamics. The active and passive properties are the same as in C10 model, however they were adjusted to achieve a more realistic attenuation of the AP backpropagation. The morphology (**Figure 5.1**) of the model is based on that of the C10 model. The model has two basal dendrites, each consisting of three sections. Oblique dendrites are modeled by two dendrites that are connected to the apical trunk in its proximal part. Each consists of four sections. Two dendrites of four sections together represent

dendrites in the stratum lacunosum-moleculare (Turi et al. 2019). Accession number in ModelDB is 246546.

5.2.1.5 Our new reduced-morphology model – To21

The reduced-morphology of our CA1 pyramidal cell model was inspired mainly by the C10 model. However, since the apical dendritic tree of this model consists only of the apical trunk (radTprox, radTmed, radTdist sections) and has no oblique branches, we extended the model by three thin oblique dendrites. With this improvement, we were able to better model synaptic integration on these branches (see Oblique integration test). In our model, the apical trunk of total length 400 μm consists of three interconnected sections that originate from the apical end of the somatic section. At the end of the apical trunk, two dendrites are attached. Each consists of three interconnected sections and together represents dendrites in the stratum lacunosum-moleculare (apical tuft). In addition, we added two branches to the basal dendritic tree. Furthermore, our model contains one section representing the soma and one section representing the axon. Basal dendrites are modeled by six sections, two for proximal stratum oriens (SO) dendrites and four for distal SO dendrites. The structure of the model is shown in **Figure 5.1** and in **Table 5.1**. Passive and active properties were adapted from the M18 model. Kinetics of inserted ionic channels are described in **Appendix A** and used parameters are in **Table 0.1** and **Table 0.2**.

Table 5.1: Morphological structure of the To21 model.

Section	Section Lists	Num. of Segments	Diameter (μm)	Length (μm)
Soma	all, somatic	1	10	10
Axon	all, axonal	7	1	150
Proximal SO dendrite	all, basal	3	2	100
Distal SO dendrite	all, basal	7	1.5	200
Thick proximal SR dendrite	all, apical, trunk	3	4	100
Thick medium SR dendrite	all, apical, trunk	3	3	100
Thick distal SR dendrite	all, apical, trunk	7	2	200
Thin SR dendrites	all, apical, oblique	7	1	150
Thick SLM dendrite	all, apical	3	2	100
Medium SLM dendrite	all, apical	5	1.5	100
Thin SLM dendrite	all, apical	3	1	50

The model optimization

We used a trial-and-error approach to manually optimize our model. Instead of tuning the individual parameters randomly, we adapted the active and passive properties from the established full-morphology M18 model. With this strategy, we created a realistic hybrid model with reduced morphology. The goal of the optimization process was to achieve a final score of less than 2 in each HippoUnit test. During the optimization process, we manually adjusted the values of selected conductances. After each modification, we tested the model for the modified property. For the Depolarization Block Test, we adjusted the following conductances in the somatic section: g_{Kap} , g_{Kmb} , g_{Kdr} , g_{Nax} , g_{Cal} , g_{Cat} , g_{KCa} . We used as initial values those listed in Table 1 in Bianchi et al. (Bianchi et al. 2012). For the Backpropagating Action Potential Test, we adjusted the potassium and sodium conductances, specifically g_{Kdr} , g_{Kad} , g_{Nax} , for the sections forming the apical trunk and the oblique dendrites. We modified the conductances on the basis of figure 7 in the paper of Golding et al. (Golding et al. 2001) featuring bAP-tuned ion channel parameters.

5.2.2 Tests of modified reduced-morphology models (labeled as "vTo21" at the end of the model's name; see Figure 6.6, Figure 6.7)

To test the hypothesis that changing the content of ion channels in reduced models can improve their physiological properties, we replaced the original set of channels in the C10, CP15 and Tu19 models with those from our To21 model (which were based on ion channels from the full-morphology M18 model). Subsequently, we tested the modified models using HippoUnit tests.

5.2.3 Model validation by HippoUnit tests

The battery of HippoUnit tests has been described in detail before (Sáray et al. 2021). The Postsynaptic potential attenuation test and the Backpropagating action potential test required an explicitly defined list of sections forming an apical trunk. The apical trunk section list was defined as a continuous sequence of interconnected sections, the first section being connected to the soma and the last section being at the stratum radiatum / stratum lacunosum-moleculare boundary (about 350 μ m from the soma). Similarly, the Oblique Integration Test required an explicitly defined oblique dendrites list. We created these lists for each tested model by hand.

Here, we describe the details of tests used to validate the computational models in the current study.

5.2.3.1 Somatic features test

A total of 73 different somatic electrophysiological features are implemented in the Somatic Features Test. These include spike event features, spike shape features, and voltage features. In the first step of testing, the somatic membrane potential responses to somatic current injection of amplitudes from -1.0 nA to 1.0 nA with a step size of 0.2 nA are obtained. Then, the Electrophys Feature Extraction Library (eFEL) of the Blue Brain Project (Geit et al. 2016) is used for feature extraction from the voltage traces. The extracted somatic features are compared to experimental data obtained from sharp electrode recordings in adult rat CA1 pyramidal cells (Migliore et al. 2018). For each tested feature, the model error in the feature is expressed as multiple of the standard deviation. The mean feature error is calculated by averaging of errors over the different input step amplitudes. Finally, the resulting model score is computed by averaging of all errors (Sáray et al. 2021).

For closer comparison we selected 12 features based on which the M18 model was optimized (Migliore et al. 2018). They included voltage base, voltage deflection, spike count, time to last spike, time to first spike, 1.0 over time to first spike (`inv_time_to_first_spike`), 1.0 over the first interspike interval (`inv_first_ISI`), 1.0 over the second interspike interval (`inv_second_ISI`), 1.0 over the third interspike interval (`inv_third_ISI`), 1.0 over the fourth interspike interval (`inv_fourth_ISI`), 1.0 over the fifth interspike interval (`inv_fifth_ISI`), and 1.0 over the last interspike interval (`inv_last_ISI`).

5.2.3.2 Depolarization block test

HippoUnit implements the Depolarization Block Test as a series of somatic current stimulations. NEURON's built-in single pulse current clamp point process is used for current injection. The current intensity is in the range of 0 nA to 1.6 nA with a step of 0.05 nA . Target features are the current threshold for the depolarization block (I_{th}) and the membrane potential during the depolarization block (V_{eq}). In addition, the test displays the I/O curve (Sáray et al. 2021).

5.2.3.3 Postsynaptic potential attenuation test

The EPSP is evoked by EPSC-shaped current stimuli on the apical trunk at different distances from the soma. NEURON's built-in synapse model *Exp2Syn* ($\tau_{rise} = 0.1\text{ ms}$, $\tau_{decay} = 0.1\text{ ms}$,

$EPSC_amp = 0.03$ nA) is used to stimulate the dendrite. To set the synaptic weights, a stimulus with a weight of 0 is first used for each location. The last 10% of the evoked trace is averaged and the resting membrane potential (V_m) is determined. The synaptic weight required to induce EPSC with the experimentally determined amplitude ($EPSC_amp$) is calculated as:

$$weight = \frac{-EPSC_amp}{V_m}. \quad (5.1)$$

For each selected location, the peak amplitude of local EPSP and somatic EPSP is measured, and the postsynaptic potential attenuation is calculated as:

$$attenuation = \frac{EPSP_{soma}}{EPSP_{dend}} \quad (5.2)$$

To calculate the error scores, the average values of the attenuation in the regions 100 μ m, 200 μ m, and 300 μ m from the soma are first calculated. Feature Z-scores are calculated by comparing the average attenuation values and the observed data. The total score represents the average of the feature Z-scores (Sáray et al. 2021).

5.2.3.4 Backpropagating action potential test

In the HippoUnit, the Backpropagating Action Potential Test is implemented in two steps. In the first step, the amplitude of the somatically injected current at which the cell fires at a frequency of around 15 Hz is found. In the next step, a current of this amplitude is injected into the soma. The amplitudes of the first and last AP of a train are measured at the distances of 50 μ m, 150 μ m, 250 μ m and 350 μ m from the soma (Sáray et al. 2021).

5.2.3.5 Oblique integration test

The Oblique Integration Test is implemented in the HippoUnit package in two steps. In the first step, appropriate dendrites are found. They must meet two conditions: (1) they must be near to the soma (distance < 200 μ m), and (2) the synaptic input must not evoke a somatic AP. Then each selected dendrite is tested with an increasing number of synchronized and asynchronized inputs at the proximal and distal locations. One synaptic input is modeled as two components (AMPA and NMDA) with the same time of stimulus delivery. NEURON's built-in synapse model Exp2Syn is used as an AMPA component. HippoUnit's built-in synapse model with Jahr & Stevens voltage dependence is used as an NMDA component (Jahr, Stevens 1990; Sáray et al. 2021). The synaptic weight of NMDA synapse is half the magnitude of the AMPA synapse. In the scenario of synchronous activity, 10 synaptic input activations are

delivered to the tested dendrite. The interval between inputs is 0.1 ms. The asynchronous scenario is modeled with 10 synaptic inputs and 2 ms interval between inputs. Dendritic EPSPs at the place of stimuli and EPSPs at the soma are recorded during the test. The target features tested are mean threshold for dendritic spike initiation measured at the soma, proximal and distal threshold for dendritic spike initiation measured at the soma, degree of nonlinearity at the threshold, suprathreshold degree of nonlinearity, peak derivative of somatic voltage at the threshold, peak amplitude of somatic EPSP, time to peak of somatic EPSP and degree of nonlinearity in the case of asynchronous inputs (Sáray et al. 2021).

5.2.3.6 Run time measurement

We implemented a measurement of runtime of each test for each model. We started measuring time just before calling the main procedure that triggers the test. We ended the time measurement after the end of the given method. Thus, timing involves preparing the model for testing, testing itself, calculating scores, and saving the results. We ran each test on each model ten times and calculated the average test runtime. HippoUnit tests use the Pool class from the Python multiprocessing module for parallel simulations in one neuronal model, for example for stimuli of different intensities or stimuli at different locations on dendrites. The pool size was set to 10.

5.2.4 Code availability

The models source code and Python scripts needed to run HippoUnit tests are available in the GitHub repository, <https://github.com/tomko-neuron/HippoUnit/tree/master/paper>. The source code of the CA1 model can be found in ModelDB, <http://modeldb.yale.edu/266901>.

5.3 Results

5.3.1 Somatic features of tested models

First, we assessed the ability of the five tested CA1 pyramidal cell models to simulate somatic electrophysiological features (one full-morphology M18 model and four reduced-morphology models: our To21 and published C10, CP15, Tu19 models, see Methods). For this purpose, ten 400 ms current injections with amplitudes in the range from -1.0 nA to 1.0 nA were applied to each tested model. In CA1 pyramidal neurons, injection of hyperpolarizing current induces an I_h -mediated voltage sag whereas injection of depolarizing current elicits firing with accommodation of the AP frequency (Metz et al. 2005). The resting membrane potential (RMP) of a single CA1 pyramidal cell is between -64 mV (Spruston, Johnston 1992) and -84 mV

(Fricker et al. 1999). These and other electrophysiological features were extracted from experimental voltage traces using the eFEL library (see Methods). With the exception of the CP15, a total 232 features were extracted and evaluated in all models. The CP15 model was weakly excitable, which means that at the current amplitude of 0.8 nA it fired only one spike and at the current amplitude of 1.0 nA it only fired three spikes. Therefore, it was not possible to extract all features.

As expected, the M18 model, which has been tuned for selected somatic features before¹⁷ and our newly tuned model, performed best in this test. The M18 model has reached errors lower than 1 in 58 features. Errors lower than 2 in all 61 features were reached by the M18 model and our model (**Figure 5.1**).

The voltage base is the average voltage during the last 10% of time before the stimulus (Geit et al. 2016). The experimentally measured value of voltage base varies between -69.2 ± 4.5 mV (input current amplitude 0.2 nA) to -69.9 ± 4.6 mV (input current amplitude 1.0 nA) (Migliore et al. 2018). The models do not capture differences in voltage base across steps and therefore have fixed voltage base values corresponding to their resting potentials (Table S3): C10 (-63.8 mV), CP15 (-66.3 mV), Tu19 (-65 mV), To21 (-72.7 mV), and M18 (-69.6 mV). The M18 model was the best in this feature with an average error of 0.0459. The remaining models displayed average errors below the maximum error accepted.

The voltage deflection reflects a hyperpolarized state that is revealed at negative input currents (Geit et al. 2016). An average error lower than 1 was reached by models of CP15, To21, and M18. The remaining models had an average error greater than 2 (**Figure 5.1**).

The spike count reflects the number of spikes fired during the stimulus (Geit et al. 2016). **Figure 5.1** plots the spike numbers against the injected current for all tested models together with experimental data. The C10 and Tu19 models were too excitable, resulting in a high average error (**Figure 5.1**). The experimental data were fitted best by the M18 model (**Figure 5.1**), as confirmed by the lowest average error (**Figure 5.1**). CP15 and To21 models also achieved relatively low errors of 1.4 and 1, respectively.

Time to the first (or last) spike is the time from the start of stimulus to the maximum of the first (or last) peak (Geit et al. 2016). These were measured for currents of 0.8 nA and 1.0 nA. All models produced realistic spike times with an error of less than 2 (**Figure 5.1**). Time to the first spike was also expressed as the inverse value – inv_time_to_first_spike, calculated

as 1 over time to the first spike. Models of CP15, To21, and M18 achieved score less than 2 and models of C10 and Tu19 achieved scores greater than 2.

Other spike event features include inverted interspike intervals, namely inv_first_ISI, inv_second_ISI, inv_third_ISI, inv_fourth_ISI, inv_fifth_ISI and inv_last_ISI. The error of the first ISI was less than 2 in all models. For the remaining ISI intervals, errors of models of CP15, To21, and M18 were still below 2. However, errors of models of C10 and Tu19 increased with each next interspike interval.

The final score of this test for each model is compared in **Figure 5.6**. The CP15 model's performance was surprisingly good considering the fact that it was not tuned for this test. The M18 and To21 performed best.

5.3.2 Depolarization block test

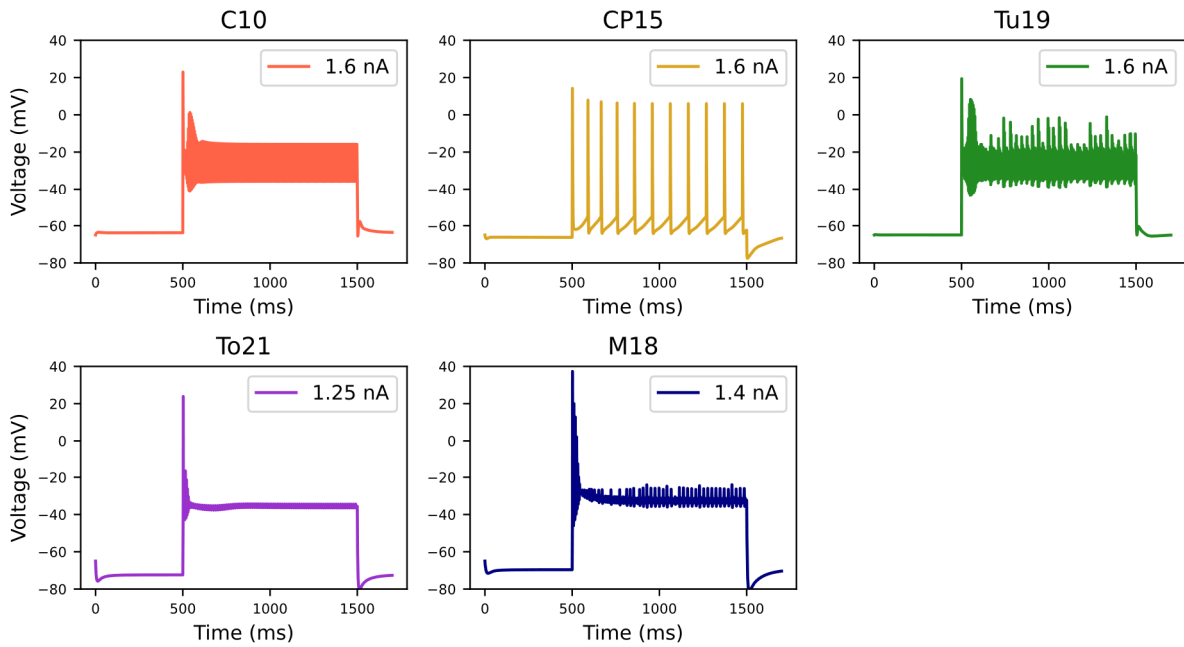
Next, we tested the readiness of the models to enter depolarization block. For this we performed several somatic current injections for each tested model. We started with an initial amplitude of 0.05 nA and gradually increased it by 0.05 nA up to a final amplitude of 1.6 nA. We measured the current threshold needed for the models to enter depolarization block. Below a threshold value, the models fire a regular, weakly adapting, train of APs for the entire duration of the current step. If the models are capable of entering depolarization block (**Figure 5.2**), above the threshold value and during the current step, the AP amplitude decreases to zero and the membrane potential reaches an equilibrium point (V_{eq}) (Bianchi et al. 2012).

Only M18 and To21 models entered depolarization block. For models that did not enter depolarization block, we plotted the somatic response to the highest current intensity of 1.6 nA (**Figure 5.2**). The equilibrium (steady state) value of the membrane potential during the depolarization block was experimentally determined to be -40.1 ± 3.4 mV (Bianchi et al. 2012). For the To21 the value of V_{eq} was -35.9 mV, which corresponds to an error of 1.2.

The M18 displayed slightly more depolarized equilibrium values ($V_{eq} = -32.52$ mV, *error* = 2.2) (**Figure 5.2**). Both models had a higher current threshold for entering depolarization block than the experimental value of 0.6 ± 0.3 nA¹². For the To21 model it was 1.2 nA (*error* = 1.8) and for the M18 model it was 1.4 nA (*error* = 2.5) (**Figure 5.2**). The final score in this test was calculated only for the models that entered depolarization block. The To21 model achieved a score of 1.6 and the M18 model reached a score of 2.4 (**Figure 5.6**).



a



b

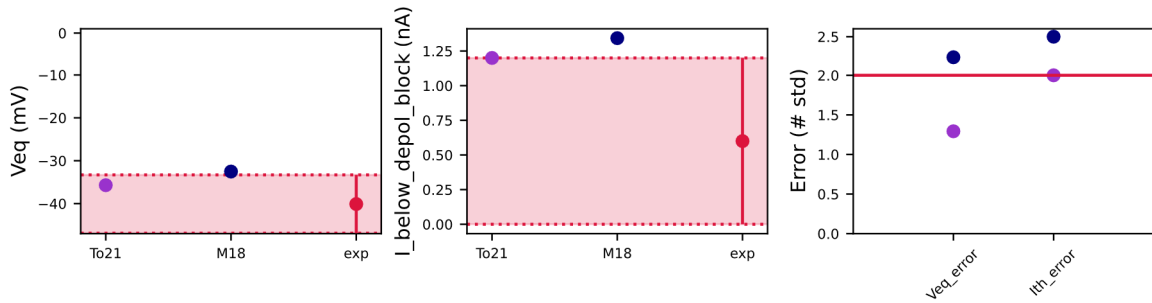


Figure 5.2: The Depolarization Block Test expressed the ability of models to enter depolarization block under sustained input current. (a) Somatic voltage response of models to the current at which the models entered depolarization block. If the model did not enter depolarization block, the somatic voltage response is the response to the maximum current intensity. (b) The values of the equilibrium voltage during depolarization block, the current intensity before the model enters depolarization block, and associated errors in these features expressed by the number of standard deviations for models that have entered depolarization block. Experimental values with the double standard deviations were obtained from the paper of Bianchi et al. (Bianchi et al. 2012). The red horizontal line represents $sd = 2$ and determines the maximum error accepted.

5.3.3 Postsynaptic attenuation test

To test the models for their ability to replicate the attenuation of EPSPs, we applied several stimuli using a double exponential synapse at various distances from the soma on the apical trunk. At the same time, we recorded the amplitudes of the EPSP at the stimulus site and at the soma. Finally, we calculated EPSP attenuation value for a given distance. The attenuation value expresses the ratio between the EPSP amplitude evoked at the dendrite and the EPSP amplitude

measured at the soma, quantifying how much of the dendritically evoked EPSP amplitude is retained at the soma. For model validation, we calculated the errors between model EPSP attenuation values and experimental EPSP attenuation values at a distance of about 100 μm , 200 μm , and 300 μm from the soma.

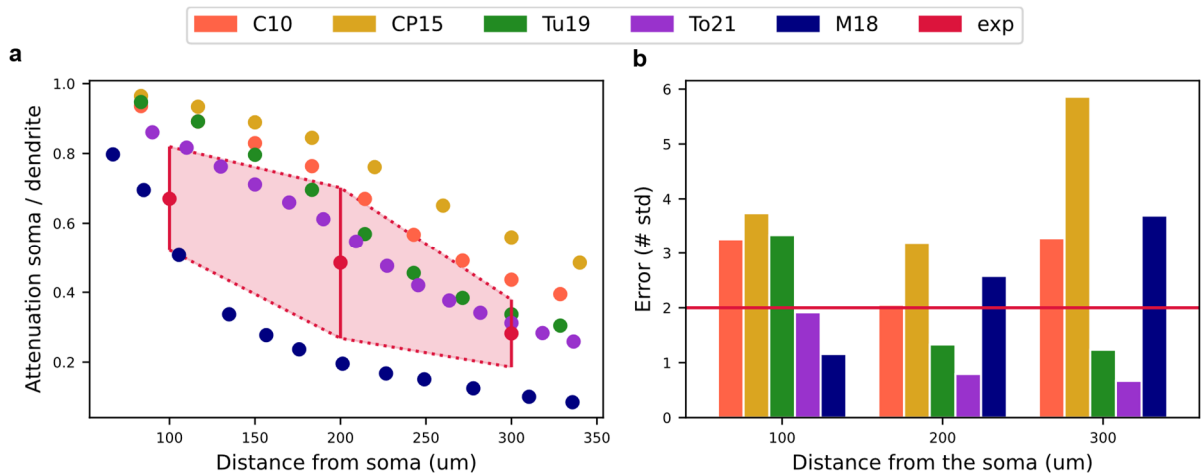


Figure 5.3: The Postsynaptic Potential Attenuation Test evaluated the rate of attenuation of excitatory postsynaptic potentials (EPSPs) during their propagation along the apical trunk of the tested models. (a) The rate of attenuation of postsynaptic potential calculated as $EPSP_{soma}/EPSP_{dend}$ at different distances from the soma on the apical trunk. Experimental values with the double standard deviations are obtained from the paper of Magee and Cook (Magee, Cook 2000). **(b)** Model errors in the EPSP attenuation expressed by the number of standard deviations at different distances from the soma. The red horizontal line represents $sd = 2$ and determines the maximum error accepted.

For all tested models, the postsynaptic EPSP attenuation was enhanced with increasing distance from the soma. This was reflected in the decreasing $EPSP_{soma}/EPSP_{dend}$ ratio with increasing distance from the soma (Figure 5.3). These simulations were qualitatively consistent with the experimental data from Magee and Cook (Magee, Cook 2000).

In general, the M18 model showed the strongest attenuation. In contrast, the CP15 model showed the weakest attenuation (Figure 5.3). We compared the attenuation errors of the models at different distances from the soma. At the distance of 100 μm , the models that had acceptable error less than 2 were the M18 ($error = 1.15$) and our model ($error = 1.92$). In the middle of the apical trunk, at 200 μm from the soma, the To21 and the Tu19 models had the smallest error (1.08 and 1.86 respectively). Also, at the distance of 300 μm from the soma, the two latter models had the lowest error (1.07 and 1.82, respectively) (Figure 5.3). The final score of this test for each model is compared in Figure 5.6.

5.3.4 Backpropagating action potential test

Next, we compared the models with respect to the attenuation of bAPs, which represent plasticity-relevant depolarization events. In CA1 pyramidal cells, the AP is typically initiated in the axon hillock and propagated forward to the axon and backward to the dendritic tree as a bAP. The bAP amplitude attenuates with increasing distance from the soma. At a distance of 280 μm from the soma, the attenuation is less than 50%. However, at a distance beyond 300 μm from the soma, there is a dichotomy of bAP spreading, with either strong bAP attenuation of 70–85% (i.e. weak backpropagation) or weak bAP attenuation of 25–45% (i.e. strong backpropagation), respectively (Golding et al. 2001). This dichotomy was observed only for the first spike in a train of APs, whereas the attenuation of the last spike was similar to the attenuation of the first spike in weakly-propagating cells. This can be explained by the difference in the degree of amplification of the AP by voltage-gated channels in the distal dendrites (Golding et al. 2001).

In the tested models we compared the effectiveness and the mode of backpropagation of APs. To do this, the bAP Test uses somatic current injection to generate a train of APs at a frequency of about 15 Hz and measures the amplitudes of the first AP and the last AP in the train at various positions on the apical trunk. However, the CP15 model did not reach a firing frequency of about 15 Hz and thus the test failed. For this reason, we wrote our own implementation of the bAP test for this model. We plotted the voltage trace of the first and last AP at the proximal and distal locations on the apical trunk (**Figure 5.4**). It is clear from these figures that our model is weakly-propagating and the remaining models are strongly-propagating.

Here, however, it is important to note that in all tested simplified models, the distal 200 μm of the apical trunk are modeled as a single NEURON section with a low number of compartments and therefore larger bAP-related errors may occur in this region due to the low spatial resolution. This should be taken into account when interpreting the bAP test results.

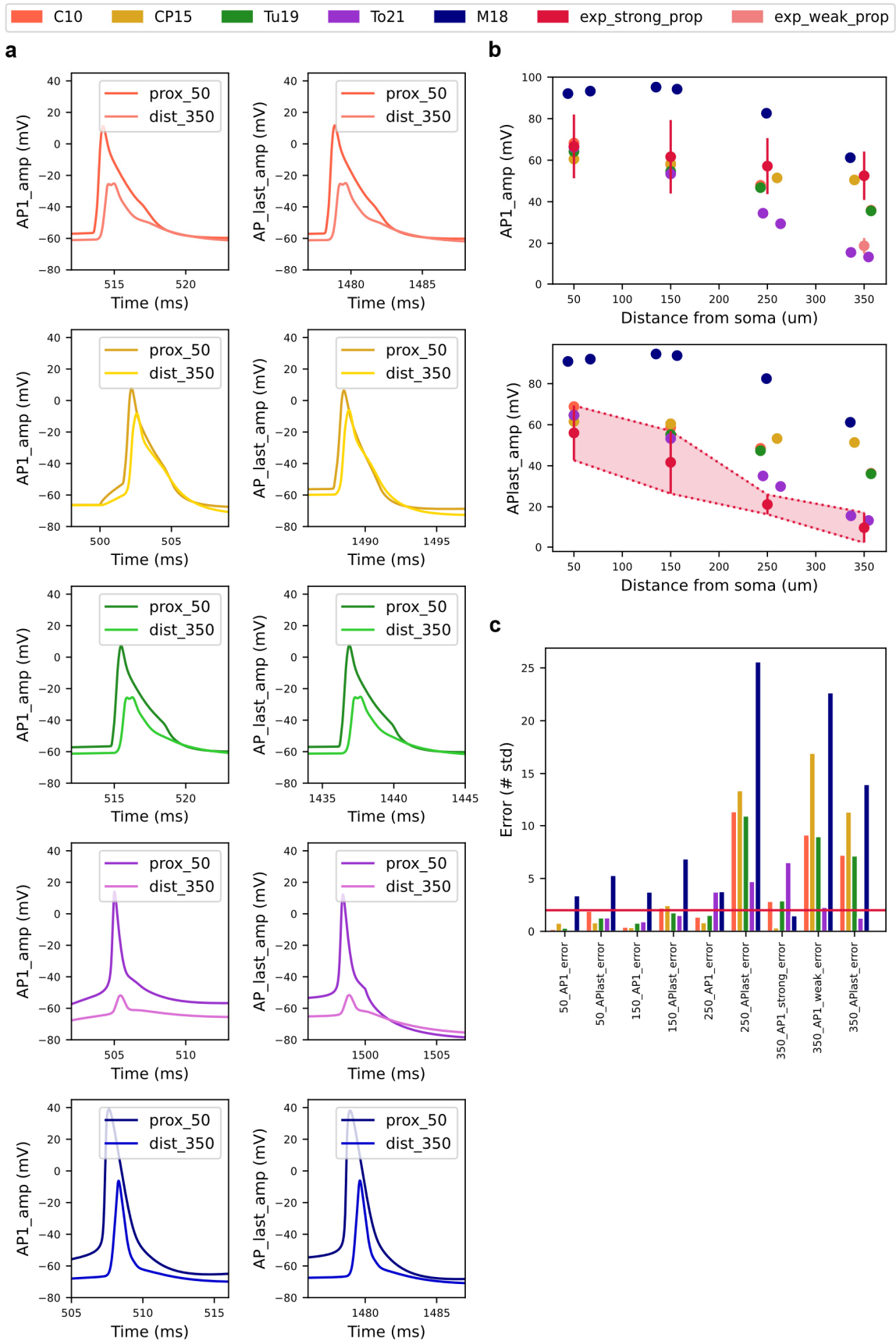


Figure 5.4: The Backpropagating Action Potential (bAP) Test evaluates the models' ability to reproduce experimentally determined bAP attenuation. (a) The first and last AP from the AP train recorded at distances

of 50 μm and 350 μm from the soma. **(b)** The amplitude of the first AP (top) and the amplitude of the last AP (bottom) from the AP train decreased with increasing distance from the soma. Experimental values with the double standard deviations for bAPs are obtained from measurements of Golding et al. (Golding et al. 2001). Based on the first bAP, CA1 pyramidal cells can be divided into two groups – weakly-propagating and strongly-propagating (top) (Golding et al. 2001). **(c)** Model errors in the back-propagation of APs expressed by the number of standard deviations at different distances from the soma. The red horizontal line represents $sd = 2$ and determines the maximum error accepted.

In the case of the first AP, the C10, CP15, Tu19, and To21 models obtained similar amplitude values in the proximal parts of the apical trunk ($< 200 \mu\text{m}$) as compared to experimental data. In the distal part of the apical trunk, C10, CP15, and Tu19 models reproduced qualitatively the bAP values of strongly-propagating cells. In contrast, our model reproduced the bAP values of weakly-propagating cells. At most distances from soma, M18 model generated bAPs with markedly higher amplitudes than observed in the experiments (**Figure 5.4**). At a distance of 350 μm from the soma, it reached similar values to those measured in the experiment (**Figure 5.4**). Based on the weak bAP attenuation, we can classify it as a strongly-propagating model. Based on the results, we can conclude that the CP15 model best captured the observed data for the first AP in strongly-propagating cells.

The amplitude of the last AP of the spike train diminished in all models as the distance from the soma increased. Experimental data were best fit by our model. For the C10, CP15, and Tu19 models, the backpropagation was slightly stronger than experimental values. Similarly to the first amplitude, the M18 model had higher values of the last AP in the AP train than the observed data in all parts of the apical trunk (**Figure 5.4**).

Model errors for the first and last AP amplitudes at each measurement site on the apical trunk are shown as a bar plot (**Figure 5.4**). The graph shows that errors greater than 2 occurred predominantly in bAP measurements in the distal parts of the apical trunk. One of the factors that could have caused the strong backpropagation was that only one longer NEURON section with a relatively low spatial resolution (i.e., with a low number of compartments) was used to model this part of the apical trunk in published reduced models, but not in our model.

In calculating the final test score, we took into account that the bAP in CA1 cells was propagating in two modes. Therefore, each model had a calculated score for strong and weak bAP propagation data, respectively. In this test our model performed best. The total score of the models is shown in **Figure 5.6**.

5.3.5 Oblique integration test

For testing the dendritic integration properties of CA1 models, we used the Oblique Integration Test. The test was applied to three models, namely Tu19, To21 and M18. The C10 model was not tested because this model had no explicitly modelled oblique dendrites. The CP15 model was also not tested because no appropriate dendrites which met the two conditions for testing (see Methods) were found in this model.

To investigate how tested dendrites integrate incoming synaptic inputs, we measured dendritic EPSPs at the stimulation location. Evoked EPSPs could be detected as an increase in the somatic voltage and for this reason we also measured the somatic response to synaptic stimulation. EPSPs evoked by an asynchronous input pattern (2 ms interval between inputs) were summed in a sublinear manner in all models. However, the Tu19 model generated a dendritic spike when a stimulation pattern consisted of 10 inputs (**Figure 5.5**). In the case of a synchronous input pattern (0.2 ms interval between inputs), all models summed EPSPs supralinearly, resulting in the generation of a dendritic spike (**Figure 5.5**). In the case of the M18 and To21 models, five synchronous inputs were required to evoke a dendritic spike. In the case of the Tu19 model, up to nine synchronous inputs were required. From the experimental data it is known that higher levels of synchronous input (five to seven spines at 0.1 ms interval) lead to dendritic spike generation (Losonczy, Magee 2006).

Dendritic spikes were detected at the soma as a sharp increase in the somatic voltage. This increase in the somatic voltage consisted of a fast and a slow phase. We calculated the peak temporal derivative of the somatic voltage (dV/dt) for each number of inputs. Based on this, we could determine the voltage threshold for generating a dendritic spike. We determined the threshold separately for proximal and distal locations and from these values we calculated a mean threshold (**Figure 5.5**). The peak (dV/dt) values at a threshold for each model are shown in Fig. 5d. The amplitude at the threshold (**Figure 5.5**) was calculated as a mean of measured EPSP amplitudes at the threshold for each tested location. We characterized a slow phase of the somatic voltage increase using a mean time to peak, during which somatic EPSP reached its peak amplitude (**Figure 5.5**). All tested models had a markedly lower values than observed in experiments.

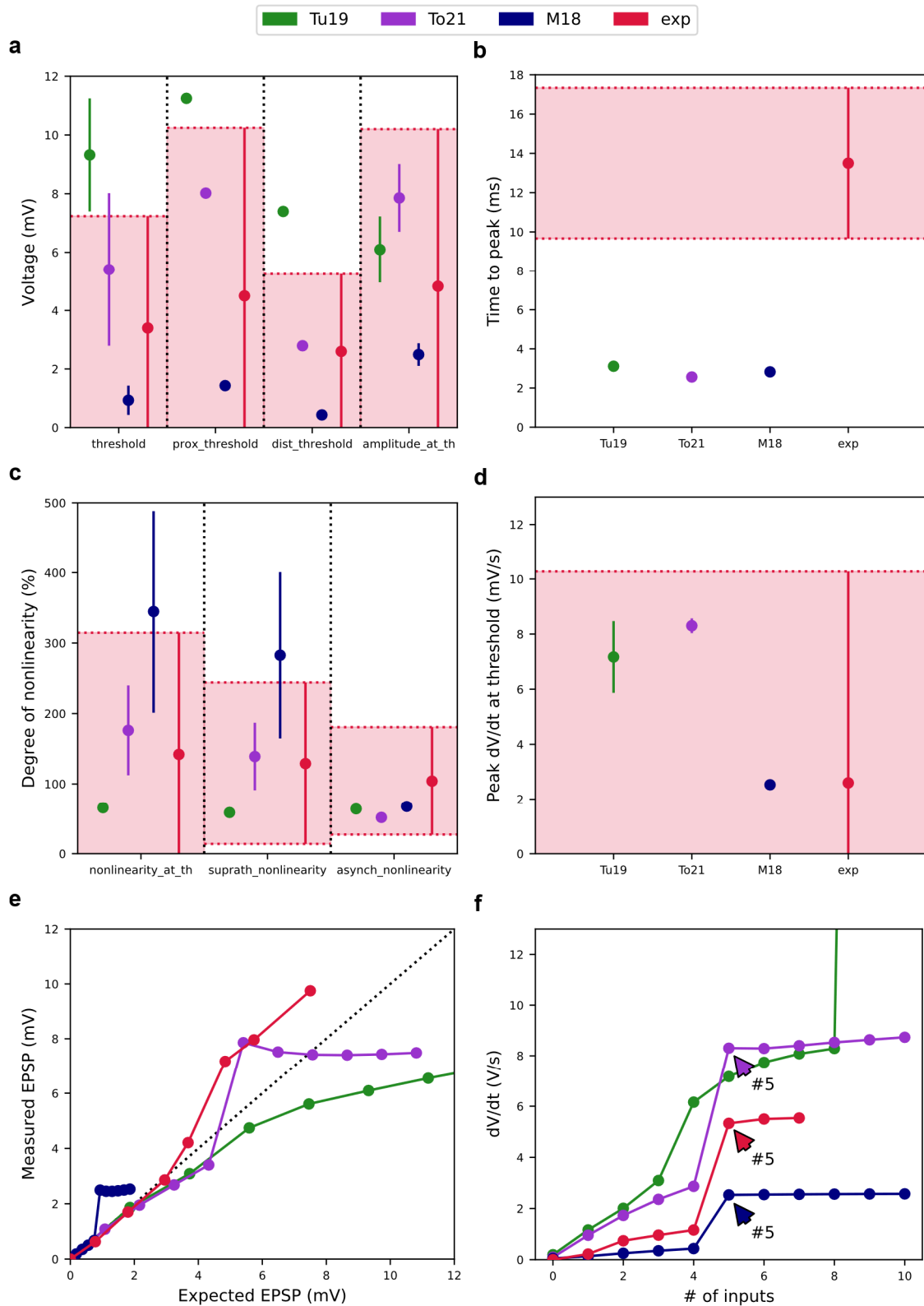


Figure 5.5: The Oblique Integration Test evaluated nonlinear dendritic integration of asynchronous and synchronous synaptic inputs in the oblique dendrites of the tested models. (a) The mean threshold for a dendritic spike initiation, the proximal threshold for a dendritic spike initiation, and the distal threshold for a dendritic spike initiation, and the amplitude at the threshold measured at the soma with a dendritic spike present.

(b) The increase in the somatic voltage upon a dendritic spike can be characterized by the time in which the maximum amplitude is reached (time to peak). All models had this value significantly lower than experimental data. **(c)** The mean threshold nonlinearity associated with a dendritic spike, suprathreshold nonlinearity and the degree of nonlinearity for asynchronous input patterns calculated for each tested model. **(d)** The peak temporal derivative of somatic voltage response at the threshold for dendritic spike initiation. **(e)** Averaged input – output curves for synchronous inputs of all tested models. A sharp increase in the curve indicates a dendritic spike. Dashed line represents linear summation. **(f)** Plot of dV/dt versus number of inputs. Arrows indicate the number of synchronous inputs required to induce a dendritic spike. Note a sharp increase in the somatic voltage during the dendritic spike initiation. All experimental values with the double standard deviations were obtained from the paper of Losonczy and Magee (Losonczy, Magee 2006).

To quantify the degree of nonlinearity, we calculated the mean nonlinearity at the threshold, the suprathreshold nonlinearity and the asynchronous nonlinearity using formulas in Losonczy and Magee (Losonczy, Magee 2006). The M18 and To21 models reached higher mean degree of nonlinearity at the threshold and the suprathreshold nonlinearity than experimental values but mean values of our model remained in the experimental range (**Figure 5.5**). The Tu19 model had values slightly below 100%. All models were in the experimental range for the asynchronous nonlinearity (**Figure 5.5**).

In terms of the overall score, the To21 and M18 models scored below 2. The Tu19 model achieved an overall score of 2.14 in this test (**Figure 5.6**). **Figure 5.6** shows all final scores of the models achieved in each test as the number of standard deviations. We can see that our CA1 pyramidal cell model reached the average lowest error when taking into account all of the tests.

5.3.6 Model runtimes and the importance of biophysical mechanisms for the performance of reduced-morphology models

To estimate the computational speed of the models, we measured runtimes for each model and each test. The runtimes are shown in **Figure 5.7**. As expected, testing took the longest for the M18 model, as it is a full-morphology model. It contains the largest number of compartments for which calculations need to be performed. Testing on reduced models was 2–7 times faster, depending on the test performed. In the case of network models, this time saving could be even higher. The most significant factor in reducing the runtimes is the smaller number of compartments as compared to the full-morphology M18 model.

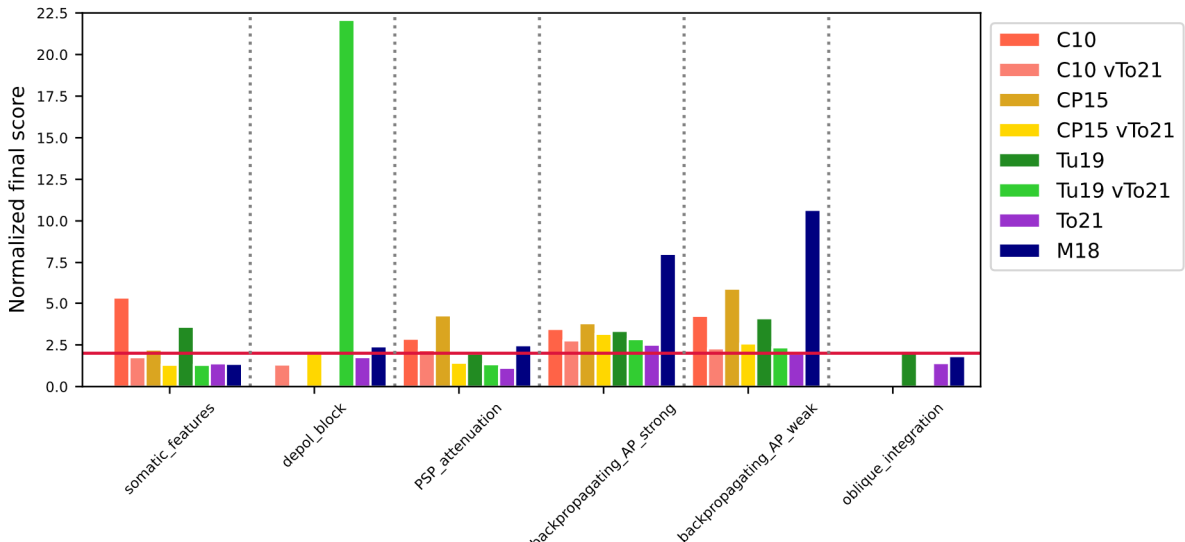


Figure 5.6: The final error score of all models achieved for each test. The final error score for a given test is expressed as the average of the errors of all tested features (see Methods). If the model does not pass the test, it is indicated by a blank space. The figure also contains the final scores from the modified reduced morphology models labeled as vTo21 at the end of the model's name in the legend (see text for more details). The red horizontal line represents $sd = 2$.

In the case of reduced models, the number of compartments and branch points is similar. The C10, CP15, Tu19 models have similar ion channel content whereas the To21 model has similar channels to the M18 model. Both groups have similar channel types with some exceptions: (1) The K_M channel in the To21 and M18 models is adapted for CA1 cells (Shah et al. 2008) and plays an important role in the cell's entry into the depolarization block (see **Error! Reference source not found.**). (2) The C10, CP15, Tu19 models contain Ca_L , Ca_R , Ca_T calcium channels and To21 and M18 contain Ca_L , Ca_N , Ca_T calcium channels. The difference is also in the implementation of the calcium accumulation mechanism. (3) The C10, CP15, Tu19 models have a complete channel content inserted only in the soma and in a subset of sections forming the apical trunk and basal dendrites. On the other hand, the To21 and M18 models have a complete set of channels in each section.

It follows from the above that the C10, CP15 and Tu19 models should have similar runtimes. This was confirmed by our runtime measurements (**Figure 5.7**). The runtimes for the To21 model were higher as compared to the other reduced-morphology models, which could be due to the differences mentioned in the point (3) in the previous paragraph. In line with this, a slight increase in runtimes for modified reduced-morphology models (vTo21) may be explained by the insertion of all channels into all sections in these models. In the case of the bAP test, a significant proportion of the total runtime is the first step of the test, which is to

find a suitable current intensity at which the model fires around 15 Hz. This search can significantly extend the total runtime. Examples are the Tu19 and Tu19_vTo21 models, where twice as many simulations (IClamps) were required for the Tu19 model as for the Tu19_vTo21 model.

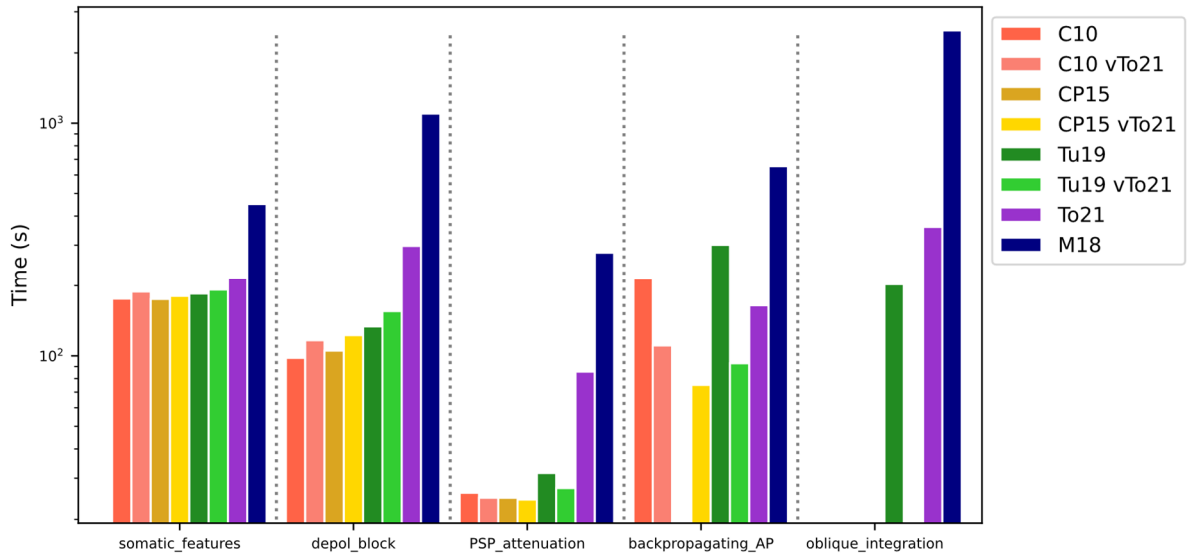


Figure 5.7: The runtimes of all models for each test. If the model does not pass the test, it is indicated by a blank space. The figure also contains the runtimes of the modified reduced morphology models, which is indicated as vTo21 at the end of the model's name in the legend (see text for more details). The bAP Test for the CP15 model was implemented by us and therefore we did not measure the runtime.

Importantly, the final error scores of the modified reduced-morphology models in the tests improved markedly (Fig. 6). These results show, first, that ion channel biophysics is the key property important for the successful performance in the standardized HippoUnit tests and, second, that the performance of available reduced-morphology models can be easily improved by implementing biophysics from the realistic (To21 and M18) models. For discussion, see Chapter 10.

Chapter 6

6 Meta-STDP rule stabilizes synaptic weights under *in vivo*-like ongoing spontaneous activity in a computational model of CA1 pyramidal cell (Tomko et al. 2020)

6.1 Introduction

It is widely accepted that in the brain processes related to learning and memory there are changes at the level of synapses. Synapses have the ability to change their strength depending on the stimuli, which is called activity-dependent synaptic plasticity. To date, many mathematical models describing activity-dependent synaptic plasticity have been introduced. However, the remaining question is whether these rules apply in general to the whole brain or only to individual areas or even just to individual types of cells. Here, we decided to test whether the well-known rule of STDP extended by metaplasticity (meta-STDP) supports long-term stability of major synaptic inputs to hippocampal CA1 pyramidal neurons. For this reason, we have coupled synaptic models equipped with a previously established meta-STDP rule to a biophysically realistic computational model of the hippocampal CA1 pyramidal cell with a simplified dendritic tree. Our simulations show that the meta-STDP rule is able to keep synaptic weights stable during ongoing spontaneous input activity as it happens in the hippocampus *in vivo*. This is functionally advantageous as neurons should not change their weights during the ongoing activity of neural circuits *in vivo*. However, they should maintain their ability to display plastic changes in the case of significantly different or “meaningful” inputs. Thus, our study is the first step before we attempt to simulate different stimulation protocols which induce changes in synaptic weights *in vivo*.

6.2 Methods

6.2.1 Computational model of CA1 pyramidal cell

In creating of our model, we were inspired by a previously published model (Cutsuridis, Graham, et al. 2010), which is available online in the ModeDB database under accession No. 123815, and which we used in our previous study (Tomko et al. 2019). However, we have

extended the morphology since this model did not contain the side dendritic branches where the majority of excitatory inputs is located in the real cell especially in the proximal and medial parts of the dendritic tree (Megías et al. 2001). Basal dendrites in the stratum oriens (SO) were modeled by two thicker proximal sections, followed by 2 thinner distal sections. We added another 2 distal sections while maintaining the same parameters as the original distal sections. An apical trunk 400 μm long in the stratum radiatum (SR) consisted of 3 interconnected sections, which decreased in thickness with increasing distance from the soma. We attached one section to the center of each section of the apical trunk, representing thin oblique dendrites. A dendritic tuft in the stratum lacunosum-moleculare (SLM) was represented by two dendrites, each consisting of 3 sections with gradually decreasing thickness. We have kept this part unchanged (Cutsuridis, Graham, et al. 2010). The original model also contained an axon, which we also preserved. The structure of the model and typical somatic responses are shown in

Figure 6.1.

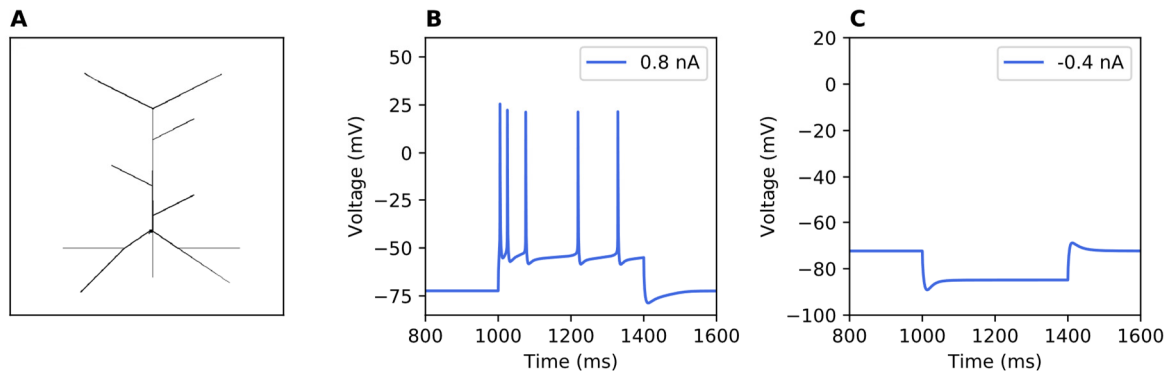


Figure 6.1: Morphology and typical somatic responses of the model. (A) The reduced morphology of the model captures all essential parts of the dendritic tree of CA1 neurons. (B), (C) The typical somatic responses of the model to the positive and negative somatic current injections.

Passive and active properties of our model were adapted from the full-morphology model of CA1 pyramidal cell presented in the paper of the Migliore et al. (2018) which is accessible in the ModelDB database (accession No. 244688). All apical and basal sections have uniformly distributed sodium current, a delayed rectifier K⁺ current (Kdr), a dendritic A-Type K⁺ current (KA), a hyperpolarization-activated cation current (I_h), three types of Ca²⁺ currents (CaL, CaN, CaT), and two types of calcium-activated K⁺ currents (KCa and Cagk). The somatic section has the same set of currents. However, a dendritic A-Type K⁺ current is exchanged for a somatic A-Type K⁺ current and a somatic M-Type K⁺ current (KM) is included. The axonal section contains a sodium current, a delayed rectifier K⁺ current, and M-Type and A-Type K⁺

currents. Each section containing calcium current contains a simple calcium extrusion mechanism. The peak conductivity of I_h and KA were calculated separately for each section according to its distance from the soma. Similarly, the equilibrium potential of the passive current (e_{pas}) was calculated for each section (Migliore et al. 2018). Kinetics of inserted ionic channels are described in **Appendix A** and used parameters are in **Table 0.1** and **Table 0.2**.

6.2.2 Model synaptic inputs

Excitatory synapses are modeled using NEURON (Hines, Carnevale 1997) built-in synapse class *Exp2Syn*. Synaptic conductivity is expressed using a two-state kinetic scheme described by two exponential functions (4.1), where w is the synaptic weight, $\tau_1 = 0.5$ ms is the rise time constant, and $\tau_2 = 3$ ms is the decay time constant (Cutsuridis, Graham, et al. 2010). The synaptic weight is modified according to the meta-STDP plasticity rule (see below).

Each synapse received a train of presynaptic spikes that were generated by independent spikes generators. In NEURON it is taken care of by the built-in process *NetStim*. Presynaptic spikes sequence delivered to one synapse consisted of a combination of random and periodic spike trains. We have chosen this strategy because we can thus simulate the theta activity that is a prominent state of the hippocampal network (Buzsáki 2002), plus the random spikes.

6.2.3 Synaptic plasticity rule

To model synaptic plasticity, we used the meta-STDP rule with the nearest neighbor implementation. In this implementation, each presynaptic spike is paired with two time-closest postsynaptic spikes. One occurring before the presynaptic spike and the other occurring after the presynaptic spike. The choice of this pairing scheme is related to the fact that it is biologically relevant, as it agrees with the BCM theory (Bienenstock et al. 1982) as shown by Izhikevich and Desai (Izhikevich, Desai 2003). The weight change is calculated as (4.2).

The positive weight change (potentiation) occurs when the presynaptic spike precedes the postsynaptic spike. On the other hand, weakening of the weight (depression) occurs when the postsynaptic spike precedes the presynaptic spike. It is calculated using (3.47) and (3.48), where $\Delta t = t_{post} - t_{pre}$, A_p and A_d are potentiation and depression amplitudes, respectively, τ_p and τ_d are decay constants for the time windows over which synaptic change can occur. Parameter t_{post} represents the instant of time at which the local voltage on the postsynaptic dendrite, where a synapse is located, exceeds the threshold of -30 mV.

Amplitudes of LTP/LTD in the meta-STDP are dynamically changed as a function of a previous temporal average of soma spiking θ_M , which is calculated using (3.46), (3.51), and (3.52), where $A_p(t)$ and $A_d(t)$ are amplitudes for potentiation and depression at time t , and α is a scaling constant. $A_p(0)$ and $A_d(0)$ are initial values at time 0. The term $\langle c_\tau \rangle$ expresses the weighted temporal average of the postsynaptic spike count, with the most recent spikes entering the sum with bigger weight than the previous ones (Benuskova, Abraham 2007). The source code of *Exp2Syn* endowed with the meta-STDP rule is available on ModelDB database under accession number 185350. The simulations were performed with the NEURON simulation environment (version 7.7.2) (Hines, Carnevale 1997) embedded in Python 2.7.16.

6.3 Results

When stabilizing the model, we worked with parameters from two groups. On the one hand, it was the number of synapses, the distribution of synapses on the dendrites and their initial weight values. The second group were the parameters of synaptic plasticity and metaplasticity. We analyzed the simulation results from both perspectives at the same time, but we always modified only one selected parameter. All these parameters were optimized by trial and error.

6.3.1 Number of synapses, distribution of synapses and initial weights

We started with an initial number of synapses of 600, which we uniformly randomly distributed to the dendritic tree, maintaining the ratio of synapses on the individual branch parts according to Table 3 from the paper of Megías et al. (2001). The total number of excitatory synapses impinging on a single CA1 neuron was estimated to be about 30 000. Their relative representation on individual parts of the dendritic tree is as follows: 38.3% on the stratum oriens distal dendrites, 0.8% on the stratum oriens proximal dendrites, 0.9% on the stratum radiatum thick medial dendrites, 7.1% on the stratum radiatum thick distal dendrites, 47.1% on the stratum radiatum thin dendrites, 1.6% on the stratum lacunosum-moleculare thick dendrites, 1.4% on the stratum lacunosum-moleculare medial dendrites, and 2.8% on the stratum lacunosum-moleculare thin dendrites (Megías et al. 2001). The number of synapses in individual layers were: SO – 240 (40%), SR – 330 (55%), and SLM – 30 (5%).

The meta-STDP synaptic plasticity rule requires the model cell to fire as is the case *in vivo*. Our goal was to achieve an output firing frequency of about 2 Hz, which was also observed *in vivo* (Mizuseki, Buzsáki 2013). We decided to generate the initial synaptic weights

from the normal distribution, while we experimentally found suitable parameters of the normal distribution, namely $\mu = 0.000165$ and $\sigma = 0.000015$. For any randomly generated initial synaptic weights from the normal distribution thus defined, the meta-STDP rule ensured that the synaptic weights were dynamically stable during ongoing spontaneous activity and at the same time the output frequency was around 2 Hz. This result is important because even in *in vivo* experiments, the stable baseline is measured for some time before applying the stimulation protocol (Abraham et al. 2007). We also experimented with the lognormal distribution of initial weights, which was observed in several *in vitro*, *ex vivo*, and *in vivo* studies (Buzsáki, Mizuseki 2014). Our unpublished results suggest that the meta-STDP rule is able to maintain dynamically stable weights generated from the lognormal distribution.

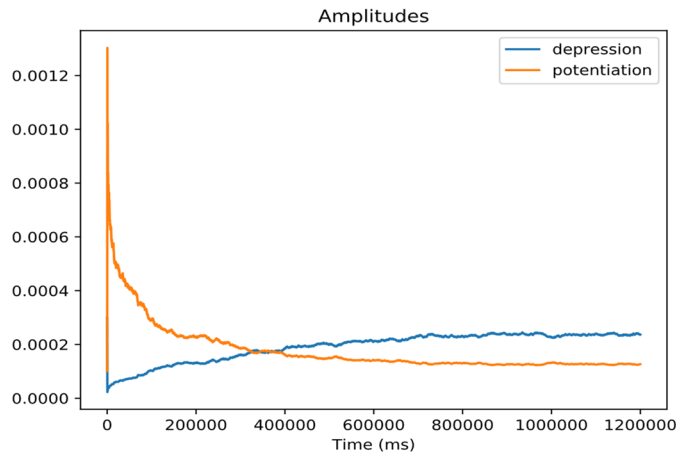


Figure 6.2: The CA1 pyramidal cell model depression and potentiation amplitudes were stabilized after a short transitory period with employed meta-STDP rule.

When generating weights from the normal distribution with the indicated parameters and simulating spontaneous activity for 20 min, 3 groups of synapses were formed at the end of the simulation. The first group consisted of synapses, the final weights of which were more or less the same as the initial ones (change in weights $\pm 5\%$). The second group consisted of synapses that were attenuated, and their final weights were approximately 50% lower than the initial ones. The last group consisted of synapses with weight changes between 5–50%. It should be noted here that in each group there were synapses with different initial weights and from different parts of the dendritic tree. At this point, we asked ourselves the question of whether synapses, whose weights have significantly decreased as a result of spontaneous activity, are necessary to stabilize the entire system. We decided to remove them, reducing the total number of synapses to 391. Thus, the resulting number of synapses in individual layers is as follows: SO – 158 (40.4%), SR – 203 (51.9%), and SLM – 30 (7.6%) As we can see from

the results, the percentage of synapses within each layer was maintained as in (Megías et al. 2001). Due to the removal of synapses, we increased all initial weights by 20% in order to maintain cell firing which is necessary to activate synaptic plasticity and metaplasticity in our meta-STDP rule.

6.3.2 Synaptic plasticity parameters

In evaluating the stability of synaptic plasticity and metaplasticity parameters, we monitor the evolution of depression and potentiation amplitudes and the evolution of the integrated spike count scaled by alpha over time (3.46). The integrated spike count is important because the amplitudes are adjusted based on it. This mechanism represents metaplasticity. In simulations, it is crucial that its value oscillates around the value 1. Values higher than one results in increased depression and weakened potentiation. Conversely, values less than one yield potentiation to be attenuated and depression enhanced. Slight oscillations around 1 will ensure dynamically stable amplitudes and thus the entire system. The free parameters are mainly α and the average time constant τ for the postsynaptic spike count (3.46). The following proved to be the most suitable parameter values: $A_p(0) = 0.0001$, $A_d(0) = 0.0003$, $\tau_p = 20$ ms, $\tau_d = 20$ ms, $\tau = 100000$ ms, and $\alpha = 500$. The following figures show the results of potentiation and depression amplitudes (**Figure 6.2**) and integrated spike count θ_M scaled by α (**Figure 6.3**) for any typical simulation.

6.3.3 Results of simulations

After simulating spontaneous activity for 20min, we achieved dynamically stable synaptic weights in all layers. **Figure 6.3**, **Figure 6.4**, **Figure 6.5**, **Figure 6.6**, and **Figure 6.7** show the results for any simulation with the best parameters of the meta-STDP plasticity rule for the period of 20 min. For discussion, see Chapter 10.

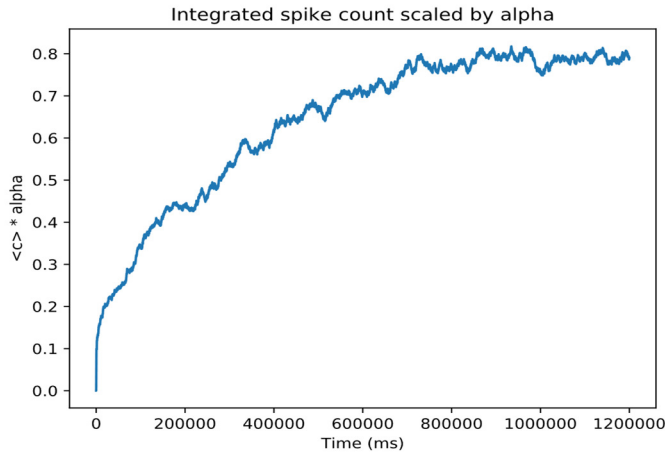


Figure 6.3: Evolution of the integrated spike count scaled by alpha with employed meta-STDP rule applied to the synapses of the CA1 pyramidal cell model.

The results document that the weights are stable on average in all layers of the dendritic tree of the CA1 pyramidal cell model endowed with the meta-STDP synaptic plasticity rule. For discussion, see Chapter 10.

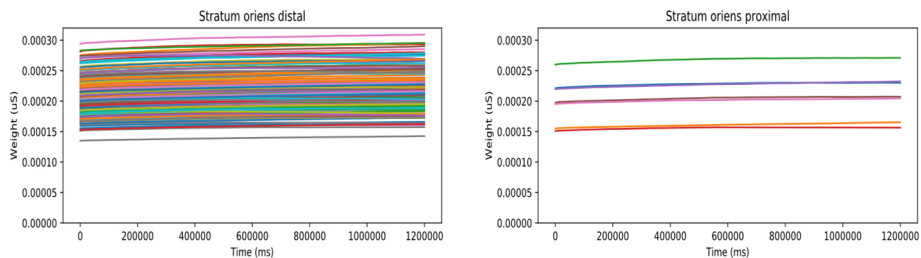


Figure 6.4: Evolution of synaptic weights in the distal SO (left) and the proximal SO (right) of the CA1 pyramidal cell model. The x-axis denotes time in ms and the y-axis denotes values of synaptic weights.

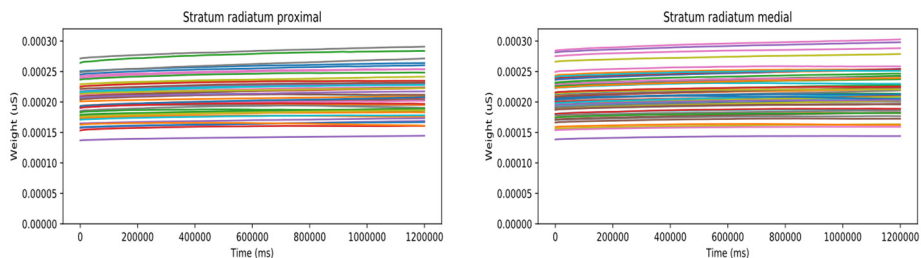


Figure 6.5: Evolution of synaptic weights in the proximal SR (left) and the medial SR (right) of the CA1 pyramidal cell model. The x-axis denotes time in ms and the y-axis denotes values of synaptic weights.

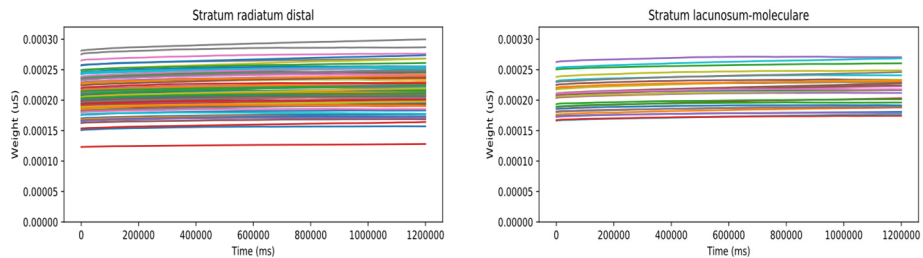


Figure 6.6: Evolution of synaptic weights in the distal SR (left) and the SLM (right) of the CA1 pyramidal cell model. The x-axis denotes time in ms and the y-axis denotes values of synaptic weights.

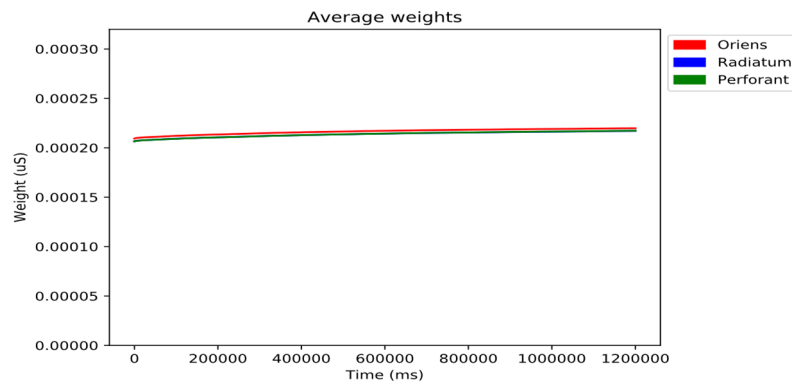


Figure 6.7: Evolution of synaptic weights average in the stratum oriens, radiatum, and lacunosum-moleculare of the CA1 pyramidal cell model. The x-axis denotes time in ms and the y-axis denotes values of average synaptic weights.

Chapter 7

7 Coincident activity of Schaffer and commissural pathways enables simultaneous LTP and LTD

7.1 Introduction

A balance between LTP and LTD is essential for stability of neuronal network. In addition, the stability is required for retaining acquired information as well as the flexibility for learning new information (Abraham, Robins 2005). In an experimental study, that motivated our modeling, authors have addressed whether and how LTP and LTD are induced simultaneously *in vivo*, and whether and how the state of the hippocampal network itself affects the induction of LTP and LTD. They have proposed a stability hypothesis that coincident Schaffer and commissural activity could cause LTP and LTD simultaneously in both pathways converging onto CA1 synapses of the hippocampal network, the state of which could also affect the induction, thereby contributing to memory process of the network. (Dong et al. 2008).

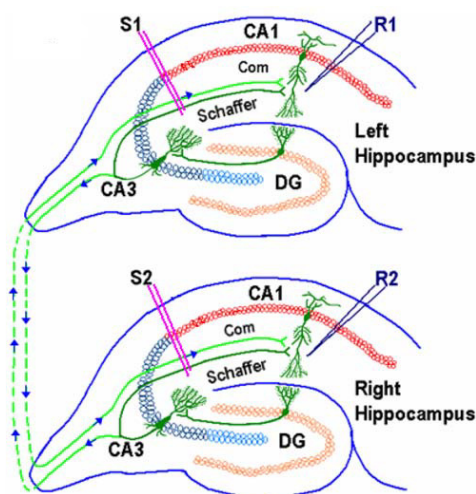


Figure 7.1: Position of stimulation and recording electrodes. S1/2 = stimulation electrode; R1/2 recording electrode; Com = commissural pathway; Schaffer = Schaffer collaterals (Adapted from Dong et al. 2008 with permission).

To test the stability hypothesis, they used a novel strategy to induce LTP and LTD by giving sequential stimulation (SSt) to Schaffer collaterals preceding or following to commissural pathway within a few tens of milliseconds, in pentobarbital-, urethane-anesthetized or freely-moving rats. Using different anesthesia, they simulated different

hippocampal network state (Dong et al. 2008). It is known that pentobarbital decreases spontaneous activity (O’Beirne et al. 1987) which was also observed in this study. The hippocampal EEG power was the lowest under the pentobarbital, higher under the urethan and much higher in awake rats (Dong et al. 2008).

Recordings of the field excitatory postsynaptic potentials (fEPSPs) were made from the CA1 stratum radiatum in response to ipsilateral Schaffer and contralateral commissural stimulation. To induce LTP or LTD, SSt that consisted of 600 pulses at 5 Hz, or at 1 and 10 Hz was delivered to ipsilateral Schaffer and contralateral commissural pathways with stimulation timing between both inputs indicated by the inter-peak intervals (Δt) of the fEPSPs (**Figure 7.1: Position of stimulation and recording electrodes.** S1/2 = stimulation electrode; R1/2 recording electrode; Com = commissural pathway; Schaffer = Schaffer collaterals**Figure 7.1**) (Dong et al. 2008).

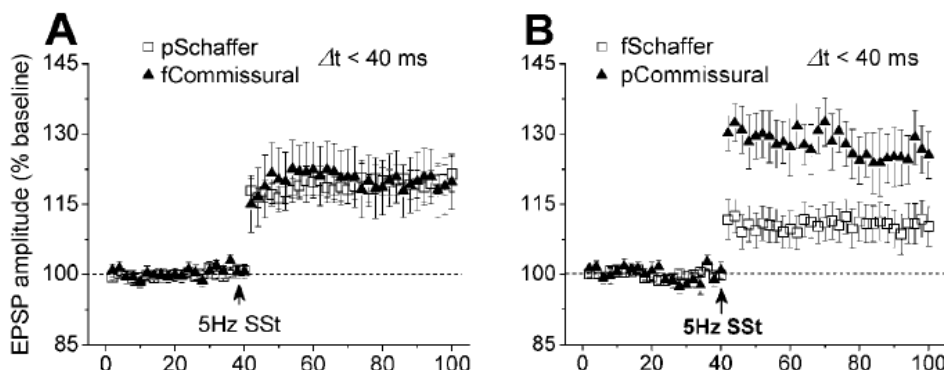
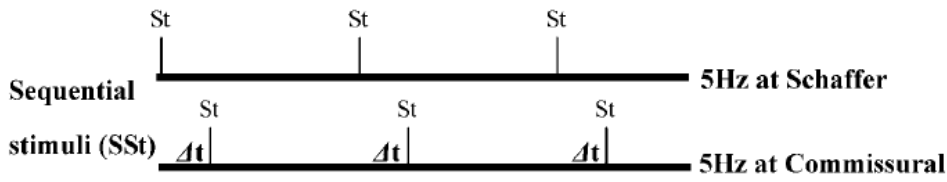


Figure 7.2: Coincident Schaffer/commissural activity induces LTP in both pathways in pentobarbital-anesthetized rats. (A) Sequential stimulation (600 pulses, 5 Hz for 2 min) to Schaffer preceding to commissural pathway within a timing window of 40 ms induced LTP in both. (B) When the activity sequence was reversed and within the timing window of 40 ms, the stimulation induced larger LTP in the commissural and smaller LTP in the Schaffer pathway (Adapted from Dong et al. 2008 with permission).

Using pentobarbital anesthesia (**Figure 7.2**), SSt (600 pulses at 5 Hz) applied to Schaffer preceding to commissural pathway within a 40-ms timing window ($\Delta t < 40ms$) induced similar magnitudes of LTP in both pathways. When the activity sequence was reversed (i.e.,

SSt to Schaffer following to commissural activity), the SSt induced a larger LTP in commissural and a smaller LTP in Schaffer pathway. In addition, the following conditions had to be met for the induction of this type of LTP:

- 40 ms timing window; the timing window longer than 40 ms does not induce LTP in either path,
- coincident activity of both pathways; SSt delivered alone to the one pathway failed to change synaptic efficiencies,
- SSt delivered at 5 Hz; SSt at 1 Hz or 10 Hz failed to change synaptic efficiencies in both pathways (Dong et al. 2008).

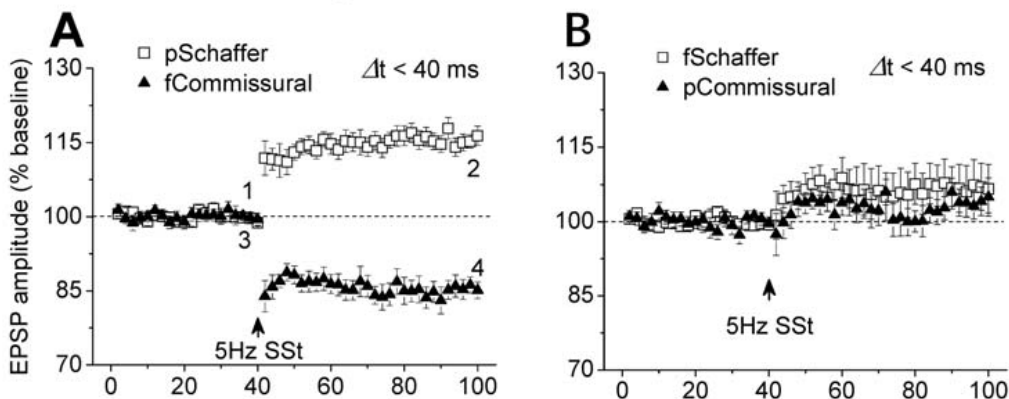


Figure 7.3: Coincident Schaffer/commissural activity induces LTP and LTD in urethane-anesthetized or freely-moving rats. (A) The stimulation to Schaffer preceding to commissural pathway within a timing window of 40 ms induced LTP in the preceding and LTD in the following pathway. (B) However, when the activity sequence was reversed in which Schaffer followed commissural pathway within a window of 40 ms, the stimulation had no significant effect on synaptic efficacy in either pathway (Adapted from Dong et al. 2008 with permission).

Using urethane anesthesia or in freely-moving rats (Figure 7.3), SSt applied to Schaffer preceding to commissural pathway ($\Delta t < 40\text{ms}$) consistently induced LTP in the Schaffer and LTD in the commissural pathway. Furthermore, they tested a SSt protocol that consisted of 600 pulses at 5 Hz with 2 s intervals per 10 pulses, because this theta-like activity possibly occurs in the hippocampal network under physiological conditions. This ‘natural’ SSt to Schaffer preceding to commissural pathways induced Schaffer LTP and commissural LTD simultaneously in both pathways. This demonstrates that coincident Schaffer and commissural activity can induce LTP and LTD in the hippocampal network *in vivo*, simultaneously. However, SSt applied to Schaffer following to commissural pathway had no significant effect

on synaptic efficacy in either pathway. In addition, both LTP and LTP/LTD were dependent on NMDA receptors (Dong et al. 2008).

The observed Timing of Afferent pathways Dependent Plasticity (TADP) shares some but not all properties with STDP. First, TADP is LTP only or LTP/LTD simultaneously in afferent pathways of a neural network. Second, timing window of TADP is within 40 ms, which is the same for LTP and LTD and thus they are induced simultaneously. Third, TADP is sensitive to the conditions. Fourth, in TADP, LTP only or LTP/LTD are induced in both pathways if Schaffer precedes commissural pathway; the reversed activity sequence produces either varied LTP magnitudes or no synaptic plasticity in both pathways. Nevertheless, TADP could very likely be a network form of STDP because both are determined by precise timing and temporal order (Dong et al. 2008).

The presented TADP findings could be important for memory processes in the hippocampal network depending on LTP only versus LTP/LTD states. A state of the hippocampal network with LTP only could provide flexibility of the system to learn new information; the other state of the network with simultaneous LTP and LTD could endow stability to the system for retaining acquired information (Abraham, Robins 2005; Dong et al. 2008). Authors suggested that the prominent theta state of the hippocampal network may be a powerful mechanism for rapidly switching the flexibility or stability of the network in the memory process (Dong et al. 2008).

To test whether the level of spontaneous activity determines LTP vs. LTP/LTD outcomes of SSt, here we employed the meta-STDP synaptic plasticity rule in our validated CA1 pyramidal cell model. We applied the SSt protocol simultaneously to the Schaffer and commissural synapses. We reproduced experimental data in case of the pentobarbital anesthesia. In addition, we showed how the level of spontaneous activity affects the magnitude and direction of synaptic plasticity at stimulated and unstimulated synapses.

7.2 Methods

We used our compartmental model of CA1 pyramidal cell described in detail in Chapter 5. We employed the meta-STDP rule to simulate synaptic plasticity. The principle of this rule is explained in previous chapters and therefore we do not describe it here. We distributed synapses on dendrites as is shown in Chapter 6. The number of synapses and their initial weights were same as is described in Chapter 6 - Number of synapses, distribution of synapses

and initial weights. The initial synaptic plasticity parameters were chosen as in Chapter 6 - Synaptic plasticity parameters.

The SSt protocol requires the division of excitation synapses into Schaffer and commissural. To solve this issue, we randomly divided synapses whereas we maintained the ratio between Schaffer and commissural synapses in layers. The Schaffer : commissural ration in the SR dendrites was 50% : 50% and in the SO dendrites was 70% : 30% (Shinohara et al. 2012).

The SSt protocol consisted of 600 pulses at 5 Hz for 2 minutes. We varied with value of the parameter Δt . We tested both stimulation scenarios when SSt was applied to Schaffer preceding (following) to commissural synapses. The SSt protocol was implemented using NEURON's *VecStim* class. In the first step, we defined a vector to hold times of stimuli for each stimulated synapse. Next, we used the *play* method of the *VecStim* class to use these times to trigger a synapse. The SSt protocol was applied 5 minutes after the start of simulation and the simulation was terminated 3 minutes after the end of the SSt. During the simulation, ongoing spontaneous activity was simulated at all synapses.

To generate spontaneous activity, we used NEURON's *NetStim* class. The *NetStim* class generates a train of presynaptic stimuli. The interspike interval (*ISI*) of spiking activity is generated according to the equation:

$$ISI = (1 - n)ISI_0 + negexp(-nISI_0) \quad (7.1)$$

where, n is fractional noise function with $0 < n < 1$, *negexp*($-x$) is the negative exponential distribution, which is equal to homogeneous Poisson distribution with probability of the next spike occurring after time *ISI*. When n is zero, the *ISI* is equal to ISI_0 (initial value of *ISI*) and spiking activity is periodic. When n is between zero and one, spiking activity is quasi-periodic. When $n = 1$, then the spike series obeys the homogeneous Poisson distribution. In all simulations, we used $n = 1$ and changed the *ISI* value depending on the level of spontaneous activity. Each synapse was connected to its own independent *NetStim* object.

We used the backward Euler method for numerical integration. The time step was 0.02 ms. We recorded the somatic voltage, input spikes from each synapse, values of potentiation and depression amplitudes, the integrated spike count, and synaptic weights. To record synaptic weights, we used the time step equal to 1 ms. We saved recorded data as binary files (.p).

We calculated the evolution of average weights over time from: (1) Schaffer synapses in SO (ori_SCH), (2) Schaffer synapses in SR (rad_SCH), (3) Schaffer synapses in SO and SR (ori_rad_SCH), (4) commissural synapses in SO (ori_COM), (5) commissural synapses in SR (rad_COM), (6) commissural synapses in SO and SR (ori_rad_COM), (7) perforant synapses in SLM (lm). Similarly, we calculated the percentage change in average weights to evaluate the effect of stimulation protocol on synaptic weights.

7.3 Results

First, we simulated scenario of pentobarbital anesthesia. It is known that a pentobarbital anesthesia decreases a level of spontaneous activity (O’Beirne et al. 1987). To simulate this condition, we set the level of incoming spontaneous activity to 3 Hz or 1 Hz, respectively.

We started with spontaneous activity of 3 Hz. After a stable baseline for 5 min, we applied the SSt protocol to Schaffer preceding commissural pathway within a 20-ms timing window. The sequential stimulation induced LTD of similar magnitude at all stimulated synapses. We also observed heterosynaptic LTD at unstimulated synapses in SLM (Figure 7.4). Parameters of metaplasticity (3.46) were: $\alpha = 400$, $\tau = 40000$ ms.

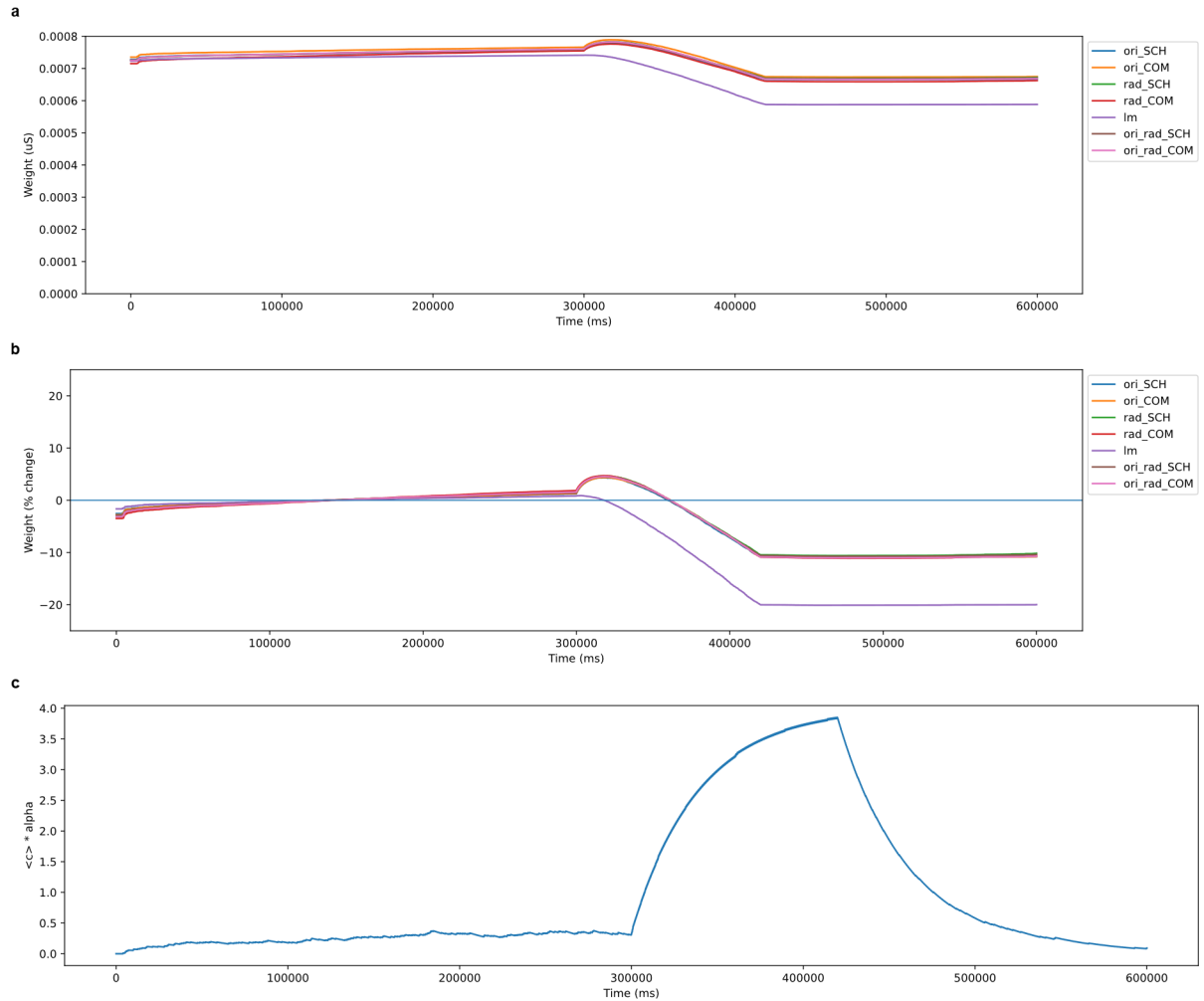


Figure 7.4: Coincident Schaffer/commissural activity induces LTD at both pathways at the 3 Hz level of spontaneous activity. (a) Average weights decrease as a result of sequential stimulation. (b) Sequential stimulation leads to ~10% LTD at stimulated synapses and ~20% heterosynaptic LTD at non-stimulated synapses. (c) Evolution of integrated spike count documents increase somatic spiking during the stimulation protocol.

Here we hypothesized that a decreased level of spontaneous activity could change a direction of synaptic plasticity at stimulated synapses. We set the spontaneous activity level to 1 Hz, which resulted in no somatic spikes outside of the stimulation protocol. After a stable baseline for 5 minutes, we applied the SSt protocol to Schaffer preceding commissural pathway within a 20-ms timing window. This resulted in ~23% LTP at commissural synapses and ~20% LTP at Schaffer synapses. Heterosynaptic LTD at unstimulated perforant synapses was ~5% LTP at commissural synapses (Figure 7.5).

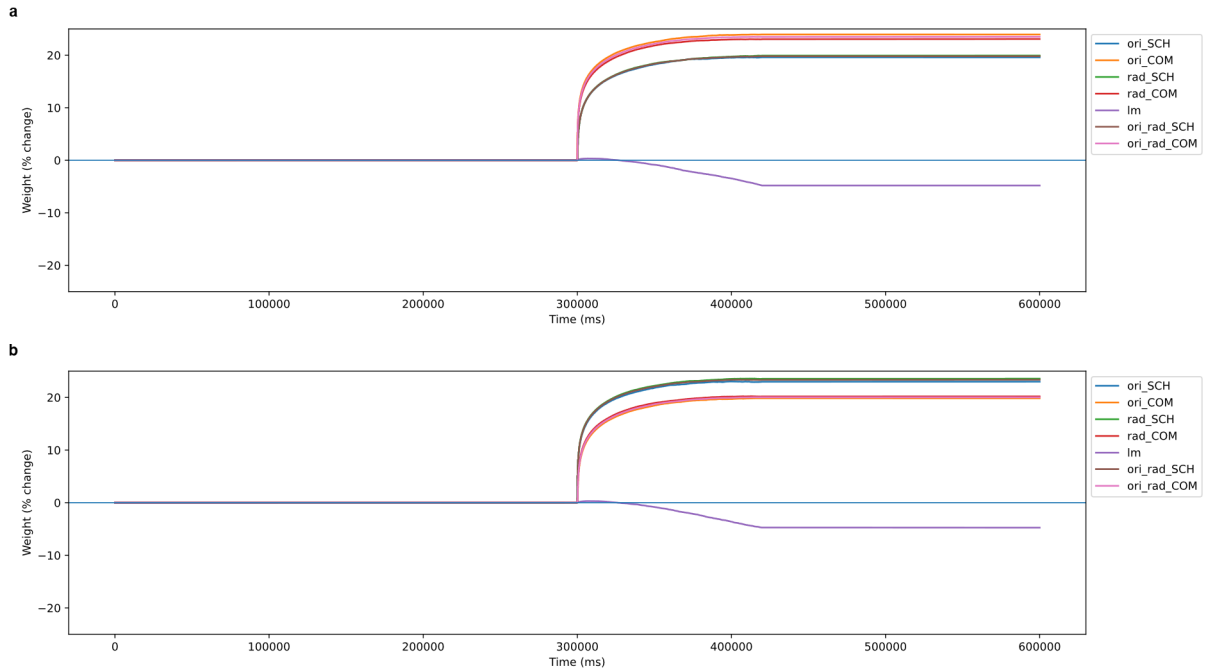


Figure 7.5: Coincident Schaffer/commissural activity induces LTP at both pathways at the 1 Hz level of spontaneous activity. (a) Sequential stimulation applied to Schaffer preceding commissural pathway leads stronger LTP at commissural synapses and weaker LTP at Schaffer synapses. (b) When the order is reversed, the SSt stimulation induces stronger LTP at Schaffer synapses and weaker LTP at commissural synapses.

When the activity sequence was reversed, the SSt protocol applied to Schaffer following commissural pathway induced also LTP at both pathways. However, LTP at Schaffer synapses was stronger (~23%) while LTP at commissural synapses was weaker (~20%). Heterosynaptic LTD at perforant synapses was maintained at a similar level (~5%) (Figure 7.5). Parameters of metaplasticity (3.46) were: $\alpha = 400$, $\tau = 40000$ ms.

In conclusion, we showed that the sequential stimulation (SSt, 600 pulses at 5 Hz) applied to Schaffer and commissural synapses can induce LTP at stimulated synapses. We used the reduced-morphology model of CA1 pyramidal cell and employed the meta-STDP synaptic plasticity rule. We showed that a level of spontaneous activity can change the direction of synaptic plasticity and have impact on the level of heterosynaptic plasticity. For discussion, see Chapter 10.

Chapter 8

8 Long-Term Potentiation and Depression in CA1 synapses

8.1 Introduction

In the CA1 region of hippocampus, the interaction between LTP and LTD can be interfering (Muller et al. 1995; Le Ray et al. 2004) or cooperative (Sajikumar, Frey 2004). In the presented study, authors tested hypothesis of functional compartmentalization by examining the interaction between CA1 synapses expressing LTP and LTD. They characterized the properties of interference and cooperativity between LTP and LTD induced (1) at two separate synaptic inputs located within or across morphologically defined CA1 dendritic compartments (apical and basal dendrites), and (2) with different time intervals between inductions (Pavlovsky, Alarcon 2012).

Published experiments that motivated our modeling were performed on hippocampal slices from adult mice. Field excitatory postsynaptic potentials were recorded from either apical or basal dendritic compartments by placing both stimulating and recording electrodes in the stratum radiatum or stratum oriens of the CA1 area, respectively. The authors used stimulation protocols to induce the late phase of LTP (strong LTP, L-LTP) and late phase of LTD (strong LTD, L-LTD), which are dependent on new protein synthesis. The strong LTD can be induced by delivering one train of paired-pulses low frequency stimulation (PP-1 Hz, 1 train of 50-msec paired-pulses at 1 Hz for 15 min). The strong form of LTP can be induced by delivering four repetitive trains of high frequency stimulation (4 HFS, four trains of 1-sec stimulation at 100 Hz, 5 min intertrain interval). A protein independent form of LTD expressing the early phase of LTD (E-LTD), can be induced by delivering one train of low frequency stimulation (1 Hz, 900 pulses at 1 Hz for 15 min) (**Figure 8.1**) (Pavlovsky, Alarcon 2012).

The main findings of the experimental study were: (1) the interaction between LTP and LTD was much stronger within the same dendritic compartment than across basal and apical compartments, (2) the nature of interaction, interference or cooperation was strongly depended on the time interval between interactions, while interference occurred at shorter and cooperative interactions occurred at longer time intervals. (3) The intracompartamental

interference between LTP and LTD depended on new protein synthesis but not on transcription (Pavlovsky, Alarcon 2012).

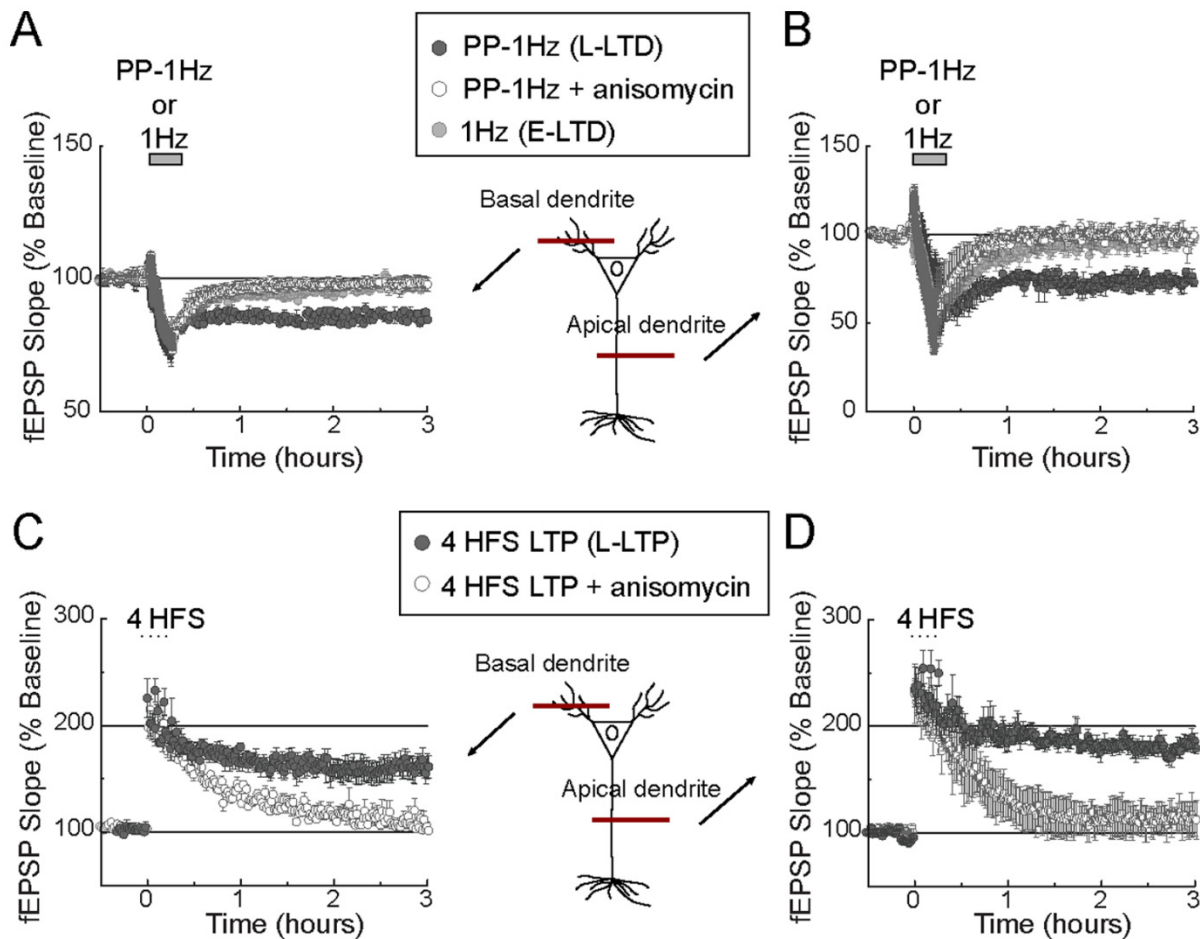


Figure 8.1: Expression of strong and weak forms of LTP and LTD in the basal and apical dendrites of CA1 pyramidal neurons. (A, B) A strong form of LTD (L-LTD) was induced by paired pulses of low frequency in the basal (A, dark gray circles) and apical (B, dark gray circles) dendritic compartments. Conversely, a weak form of LTD (E-LTD) was induced after a single train of low frequency stimulation in the basal (A, light gray circles) and apical (B, light gray circles) dendritic compartments. Blockage of new protein synthesis transformed strong LTD into weak LTD in the basal (A, open circles) and apical (B, open circles) dendritic compartments. (C, D): A strong form of LTP (L-LTP) was induced by 4 trains of high frequency stimulation in the basal (C, dark gray circles) and apical (D, dark gray circles) dendritic compartments. Blockage of new protein synthesis transformed strong LTP into weak LTP that expressed the early phase of LTP in the basal (C, open circles) and apical (D, open circles) dendritic compartments (Adapted from Pavlovsky, Alarcon 2012 with permission).

The findings on the intracompartamental interference between LTP and LTD showed a dependence on *de novo* protein synthesis. This suggests that induction either LTP or LTD might restrict the expression of subsequent synaptic plasticity. In addition, cooperative interactions could only take place when this interfering activity is reduced. On the other side, the intercompartmental interference does not appear to require the synthesis mRNA or protein.

This could be due to synaptically-driven dendritic depolarization and subsequent somatic spiking and bAP, which could invade the opposing dendritic compartment (Pavlovsky, Alarcon 2012).

Spatial and temporal interactions between plastic synapses of a neuron might enable processing of information arriving at its distinct functional compartments from different brain areas, and associate or segregate such information. They propose that this information processing arises from the changes in synaptic weights due to synaptic plasticity interactions (Pavlovsky, Alarcon 2012).

Here we aimed to apply the paired-pulses low-frequency stimulation to induction LTD and the high-frequency stimulation to induction LTP in our model. We applied these protocols to apical and basal synapses, respectively. We showed that our reduce-morphology model endowed with the meta-STDP synaptic plasticity rule is able to induce LTP and LTD on basal and apical synapses. In addition, we observed heterosynaptic depression at unstimulated synapses.

8.2 Methods

We used our compartmental model of CA1 pyramidal cell described in detail in Chapter 5. We employed the meta-STDP rule to simulate synaptic plasticity. The operation principle of this rule is explained in previous chapters and therefore we do not describe it here. We distributed synapses on dendrites as shown in Chapter 6. The number of synapses and their initial weights were same as described in Chapter 6 - Number of synapses, distribution of synapses and initial weights. The initial synaptic plasticity parameters were chosen as in Chapter 6 - Synaptic plasticity parameters.

To induce LTD, we delivered one train of paired-pulses low frequency stimulation (PP-1 Hz, 1 train of 50-msec paired-pulses at 1 Hz for 15 min) to synapses. We induced LTP by delivering four repetitive trains of high frequency stimulation (4 HFS, four trains of 1-sec stimulation at 100 Hz, 3 or 5 min intertrain interval). The protocols were implemented using NEURON's *VecStim* class. We defined a vector to hold times of stimuli for each stimulated synapse. Next, we used the *play* method of the *VecStim* class to use these times to trigger synaptic response. The protocols were applied 3 or 5 minutes after the start of simulation and the simulation was terminated 3 minutes after the end of protocols. During the simulation, ongoing spontaneous activity was simulated at all synapses.

To generate spontaneous activity, we used NEURON's *NetStim* class. The *NetStim* class generates a train of presynaptic stimuli. The interspike interval (*ISI*) of spiking activity is generated according to the equation (7.1). In all simulations, we used $n = 1$ and changed the *ISI* value depending on the level of spontaneous activity. Each synapse was connected to its own independent *NetStim* object.

We used the backward Euler method for numerical integration. The time step was 0.02 ms. We recorded the somatic voltage, input spikes from each synapse, values of potentiation and depression amplitudes, the integrated spike count, and synaptic weights. To record synaptic weights, we used the time step equal to 1 ms. We saved recorded data as binary files (.p).

We calculated the evolution of average weights over time from: (1) stimulated synapses in SO (ori_stim), (2) unstimulated synapses in SO (ori_unstim), (3) stimulated synapses in SR (rad_stim), (4) unstimulated synapses in SR (rad_unstim), (5) unstimulated synapses in SLM (lm_unstim). Similarly, we calculated the percentage change in average weights to evaluate the effect of stimulation protocol on synaptic weights.

8.3 Results

In one simulation, one protocol (HFS or PP) was applied to synapses within one dendritic compartment (SO or SR). Each combination of parameters was tested for both protocols and both dendritic compartments. For the HFS stimulation protocol, we used the intertrain interval of either 3 or 5 minutes. The shorter 3-minute interval had no effect on the magnitude of the subsequent LTP compared to the longer 5-minute interval. Our goal was to find a combination of parameters to induce LTP/LTD at SO/SR synapses.

8.3.1 LTP and LTD are induced at apical and basal synapses

The HFS stimulation protocol (4 HFS, four trains of 1-sec stimulation at 100 Hz, 3 or 5 min intertrain interval) was used to stimulate synapses in SO and SR, separately (**Figure 8.2**). We stimulated 80% of synapses in the SO or SR. During each simulation, all synapses were also activated by a background spontaneous activity at level 2 Hz. HFS protocol applied in SO synapses induced ~15% LTP. Unstimulated synapses in all dendritic compartments showed ~2 % heterosynaptic LTD. Similarly, in the case of SR synapses, the application of HFS protocol resulted in ~15% LTP and ~2 % heterosynaptic LTD at unstimulated synapses (**Figure 8.3**).

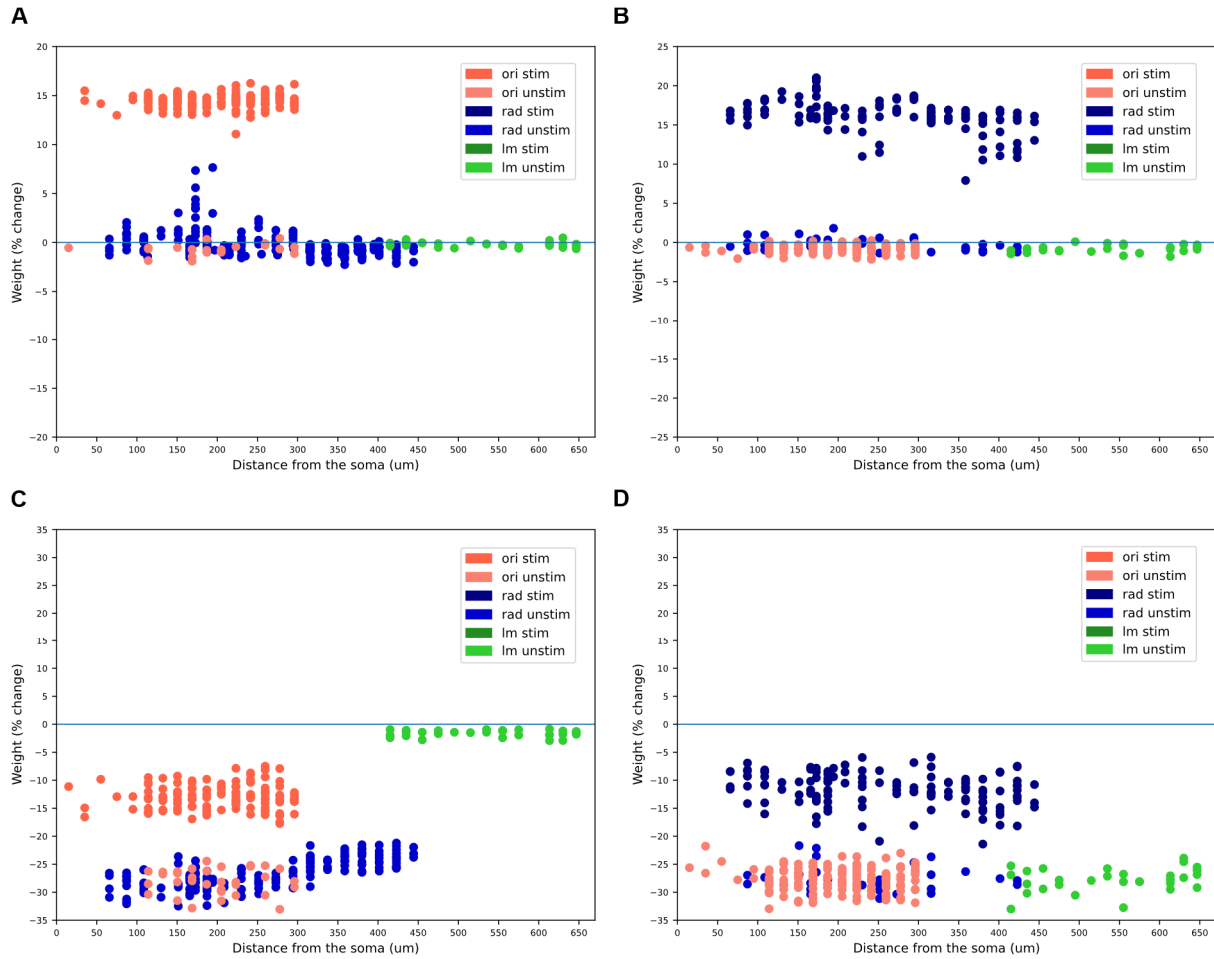


Figure 8.2: HFS induces LTP, and PP induces LTD at synapses in the basal and apical dendritic compartments of the CA1 pyramidal cell model. Each dot represents an individual synapse. The weight change was calculated from the initial and final weight for each synapse. **(A)** HFS applied to synapses in SO leads to ~15% LTP on stimulated synapses and no heterosynaptic plasticity. **(B)** HFS applied to synapses in SR leads to ~15% LTP on stimulated synapses and no heterosynaptic plasticity. **(C)** PP applied to synapses in SO leads to ~13% LTD on stimulated synapses and ~25% het-LTD on unstimulated synapses in SO, SR and no change in weights of synapses in SLM. **(D)** PP applied to synapses in SR leads to ~10% LTD on stimulated synapses and ~30% het-LTD on unstimulated synapses in all layers.

Application of the PP stimulation protocol (PP-1 Hz, 1 train of 50-msec paired-pulses at 1 Hz for 15 min) results in LTD at stimulated synapses (**Figure 8.2**). In the case of SO synapses, the magnitude of LTD was ~13%. However, the magnitude of heterosynaptic plasticity depended on dendritic compartment. The strongest het-LTD was observed at SO synapses (~30%). At SR synapses ~20% het-LTD was observed. The weakest, ~2% het-LTD was observed at synapses in SLM dendrites.

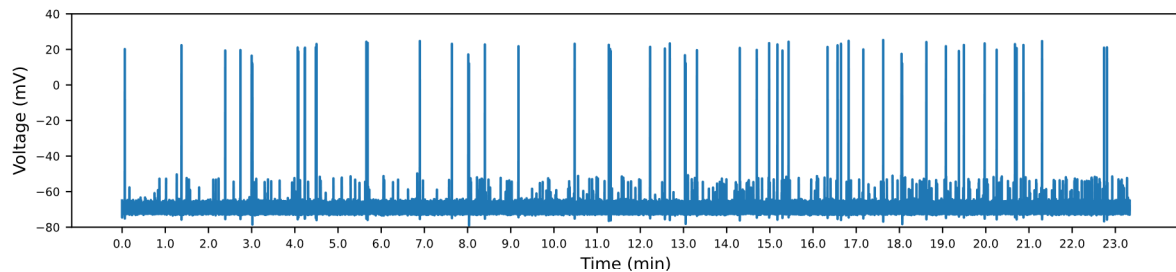
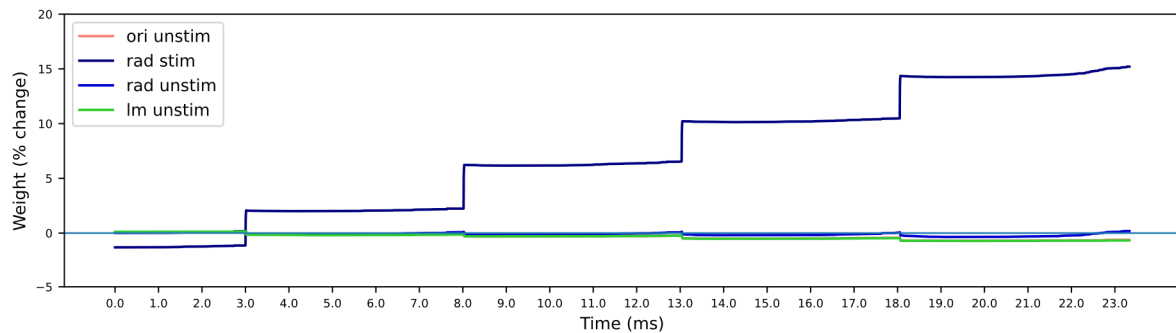
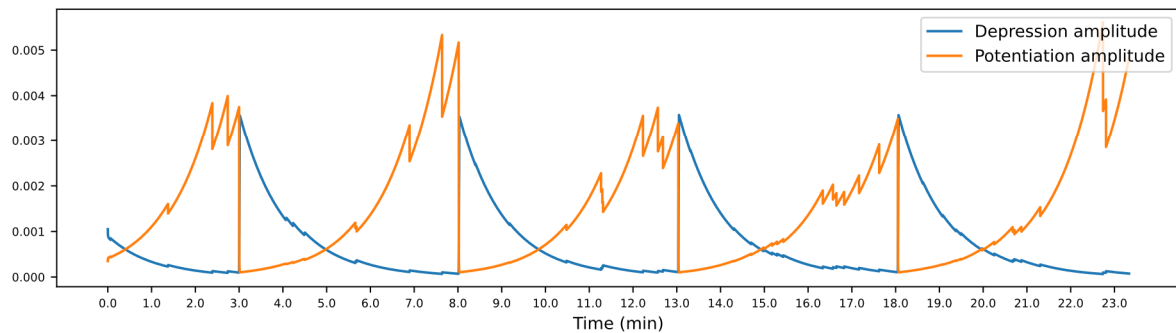
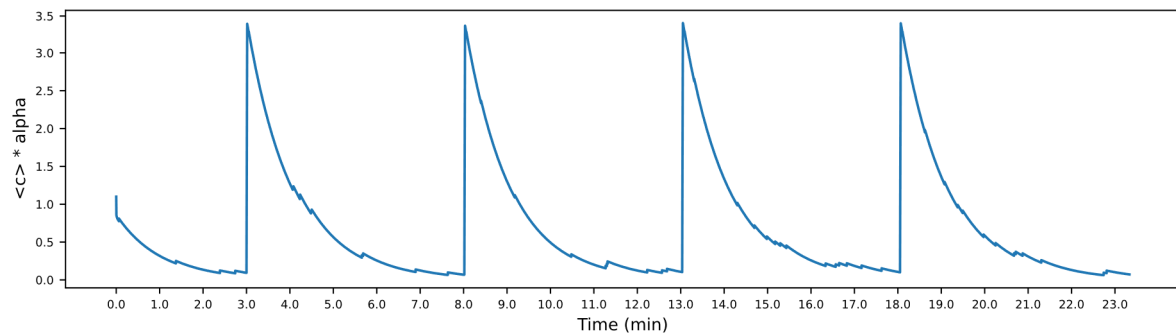
A**B****C****D**

Figure 8.3: HFS stimulation of synapses in SR results in LTP. (A) Voltage recorded at the soma shows spikes due to HFS and ongoing spontaneous activity. (B) Evolution of average synaptic weights form all dendritic compartments expressed as % change with respect to their baseline value. Baseline value was calculated as the average weight from the first 3 minutes of simulation. (C) Evolution of potentiation, A_p , and depression, A_d ,

amplitudes during the simulation. (D) Evolution of the integrated spike count during the simulation. Peaks demonstrate higher somatic activity due to the application of HFS.

When we applied the PP protocol in SR synapses, we observed $\sim 10\%$ LTD. In contrast to SO synapses, PP protocol applied in SR synapses induced $\sim 30\%$ heterosynaptic LTD at all unstimulated synapses. In this case, the magnitude of het-LTD was independent on dendritic compartment (**Figure 8.4**).

Presented results were achieved using these synaptic plasticity parameters: $\alpha = 2000$, $\tau = 60000$ ms, $\tau_d = 25$ ms, $\tau_p = 25$ ms.

8.3.2 Effect of α and τ on the magnitude and direction of synaptic plasticity

During the process of fitting the parameters, we systematically manipulated the parameter α . For $\alpha \leq 1600$, we used $\tau = 40000$ and for $\alpha \geq 1800$, we used $\tau = 60000$. In the case of LTP, the higher α results in weaker LTP. The decrease in LTP size was most visible in LTP at SR synapses. Unstimulated synapses showed minimal changes in their weights. When we stimulated SR synapses, weak (max. $\sim 5\%$) het-LTP occurred at unstimulated synapses for smaller α or het-LTD for bigger α .

However, in the case of PP protocol, we observed the change in direction of homosynaptic plasticity due to a higher α . At both SO and SR synapses, $\alpha < 1600$ resulted in LTP at stimulated synapses where the magnitude of LTP decreased with increasing of α . For $\alpha \geq 1600$, the magnitude of LTD at stimulated synapses increased with increasing of α . Using the PP protocol, we observed only a heterosynaptic LTD or no change in synaptic weights at unstimulated synapses. The magnitude of het-LTD increased with increasing of α . These results show that the parameters α and τ have a significant effect on synaptic plasticity. For discussion, see Chapter 10.

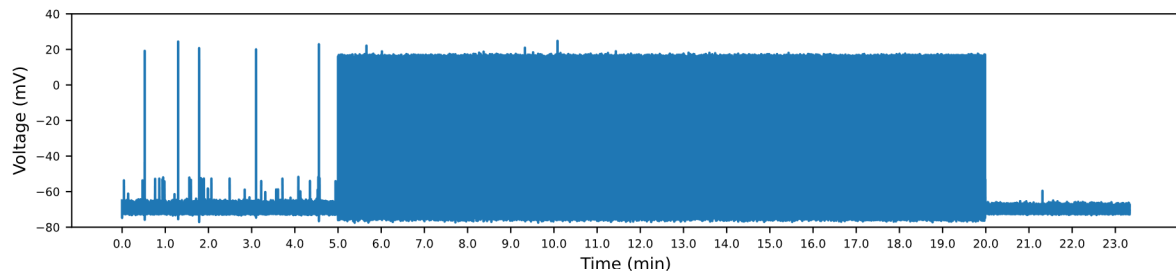
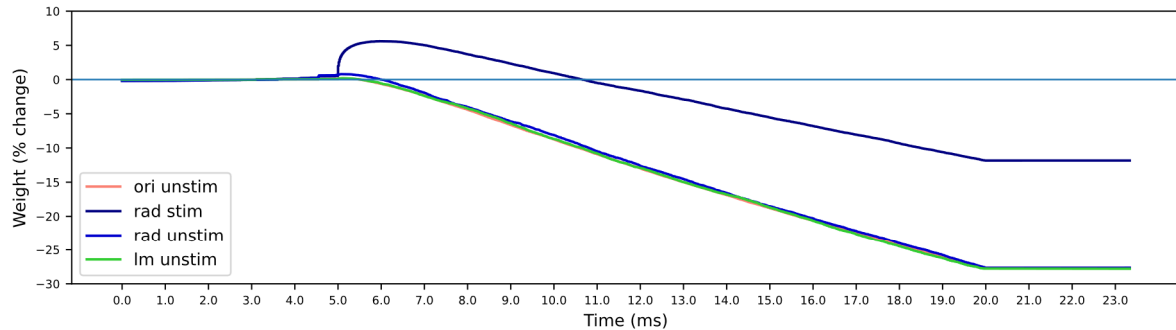
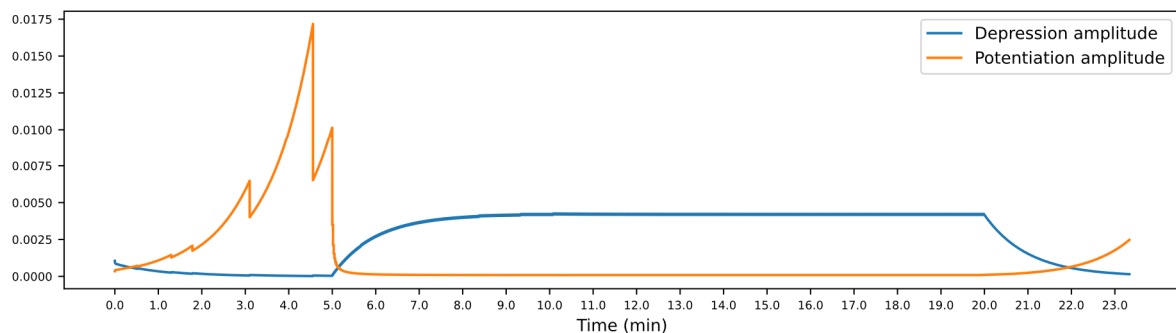
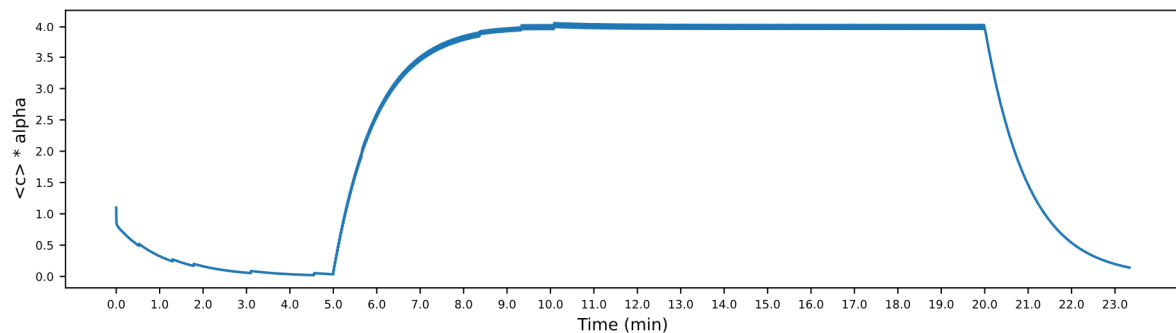
A**B****C****D**

Figure 8.4: PP stimulation of synapses in SR results in LTD. (A) Voltage recorded at the soma shows spikes due to PP and ongoing spontaneous activity. (B) Evolution of average synaptic weights form all dendritic compartments expressed as % change with respect to their baseline value. Baseline value was calculated as the average weight from the first 5 minutes of simulation. (C) Evolution of potentiation, A_p , and depression, A_d ,

amplitudes during the simulation. **(D)** Evolution of the integrated spike count during the simulation. The increase in the integrated spike count demonstrates higher somatic activity due to the application of PP.

Chapter 9

9 Dendritic sodium spikes are required for long-term potentiation at distal synapses on hippocampal pyramidal neurons

9.1 Introduction

The perforant path (PP) carries predominantly spatial information from the entorhinal cortex terminates at synapses in the apical tuft of CA1 pyramidal cells. LTP at these synapses requires strong synaptic activation, and LTP induction can have a significant impact on the output from CA1 neurons (Colbert, Levy 1993; Ahmed, Siegelbaum 2009; Takahashi, Magee 2009; Kim et al. 2015). LTP at these synapses does not require bAP; rather, LTP is correlated with the initiation of dSpikes, which often do not trigger action potential firing and bAPs (Golding, Spruston 1998; Golding et al. 2002). NMDAR and voltage-gated calcium channels are known to contribute to the induction of LTP at PP-synapses (Golding et al. 2002; Takahashi, Magee 2009). However, the importance of dendritic sodium channels and Na-dSpikes has not been addressed until 2015, mostly because these channels are essential for action potential firing in presynaptic axons and terminals, thus making it difficult to block them without inhibiting synaptic transmission. Kim et al. (2015) used a relatively low concentration of bath-applied tetrodotoxin (TTX; 20 nM) to achieve a partial block of the sodium channel without blocking presynaptic action potential firing or synaptic transmission, which allowed them to study dendritic sodium spikes (Kim et al. 2015).

All their recordings were performed using rat hippocampal slices. GABA_A and GABA_B receptors were blocked. Recordings were obtained from the soma and from the dendrites (200–320 µm away from the soma). For LTP induction, stimulus intensities were set to give EPSP amplitudes of 2–5 mV in somatic recordings and 4–10 mV in dendritic recordings. To induce PP → CA1tuft LTP, they used theta-burst stimulation (TBS), which consisted of five burst stimuli grouped at 5 Hz, with each consisting of 5 synaptic stimuli at 100 Hz. This stimulus was repeated three times (TBSx3), at 30-s intervals. Each TBS was delivered under one of the following three conditions: (1) paired with brief (2 ms) somatic current injections at 50 Hz to evoke 3 action potentials during each burst (TBSx3+Current), (2) with the soma voltage-

clamped at -68 to -70 mV (TBSx3+SomaticVC), or (3) alone (5-stim TBSx3). The study was supported by computational modeling using a morphologically realistic compartmental model of rat CA1 pyramidal cell. To simulate bath application of 20 nM TTX, they reduced the conductance of Na_v channels to 50% of control; to simulate bath application of 50 μM AP5 or 10 μM nimodipine, they reduced the NMDAR or L- Ca_v channel conductance to zero. For all simulations, either a somatic voltage clamp at -70 mV was simulated or $g_{\text{Na,soma}}$ and $g_{\text{Na,axon}}$ were set to be zero in order to mimic the experimental paradigm in which axo-somatic action potential firing was prevented (Kim et al. 2015).

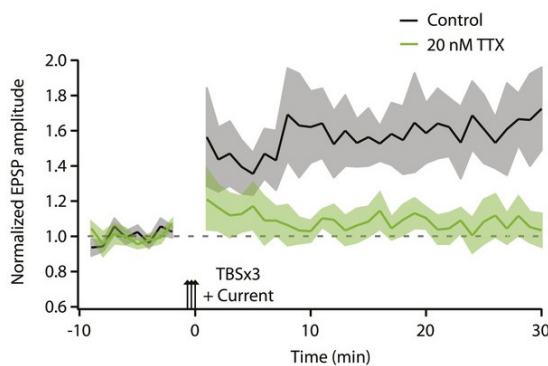


Figure 9.1: Application of 20 nM TTX blocks LTP induction at PP synapses (Adapted from Kim et al. 2015 with permission).

The study has shown three key findings. First, the study supports a more direct causal link between the occurrence of dSpikes and induction of LTP at PP synapses than previous studies which showed only a correlative link between dSpikes and PP LTP. Second, the results from the study suggest that Na-dSpikes are the major contributors, and slow NMDAR-dependent synaptic depolarization is neither sufficient nor necessary for LTP at these synapses (**Figure 9.1**). Third, the results provide insight into the mechanisms by which Na-dSpikes are coupled to the induction of LTP through calcium influx at PP \rightarrow CA1tuft synapses. The block of LTP only by the fast calcium chelator BAPTA strongly supports the hypothesis that the large, localized increases in intracellular calcium concentration are necessary for the induction of PP \rightarrow CA1tuft LTP (Kim et al. 2015).

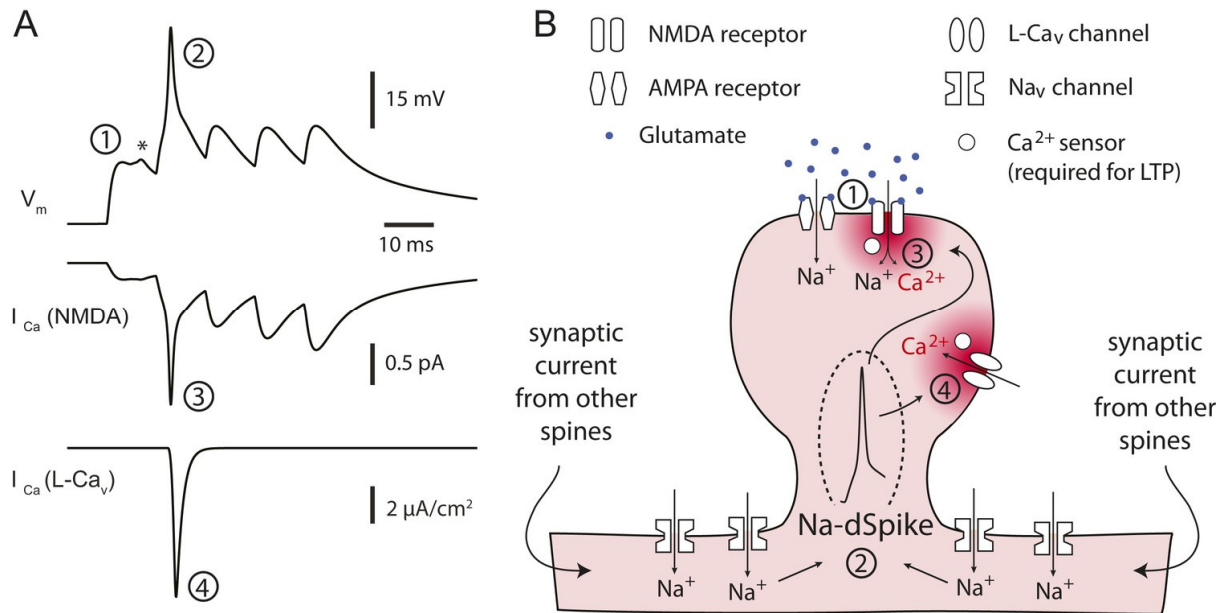


Figure 9.2: Proposed conceptual model for the critical role of Na-dSpikes in the induction of PP → CA1tuft LTP. (A) Synaptic membrane potential and calcium currents in response to a high-frequency burst activation of glutamatergic synapses. (B) Schematic illustration of the events leading to the induction of PP → CA1tuft LTP (Adapted from Kim et al. 2015 with permission).

They proposed a conceptual model for the critical role of Na-dSpikes in the induction of LTP at PP synapses (Figure 9.2). Strong activation of PP synapses results in EPSPs (1) and, on some trials, subsequently leads to initiation of Na-dSpikes (2). The locally generated Na-dSpike mediates the largest I_{Ca} through both NMDAR channels (3) and L-Cav channels (4), thus resulting in a high, localized calcium concentration near the mouth of the channels, which activates a series of biochemical events necessary for the induction of LTP. This intracellular calcium diffuses away, contributing only modestly to the ‘bulk’ calcium concentration throughout the dendritic spine and shaft, which is eventually removed from the cytoplasm by pumps in the plasma membrane and in organelles such as the endoplasmic reticulum. In contrast, the smaller, longer-lasting I_{Ca} through NMDAR channels generated during the slow synaptic depolarization produces a lower localized calcium concentration near the channel pore, but contributes more to the bulk calcium concentration (Kim et al. 2015).

For further validation of our morphologically reduced compartmental CA1 PC model, here we employed it to performed similar simulations as in Kim et al. (2015). We applied TBS stimulation to induce a dendritic spike at apical tuft dendrites. We showed that dendritic sodium channels are required for triggering dSpikes. In addition, we employed the meta-STDP synaptic plasticity rule. We showed that dendritic spikes are required for simulated LTP due to voltage-based meta-STDP.

9.2 Methods

We used our compartmental model of CA1 pyramidal cell described in detail in Chapter 5. However, for software-related reasons (possibility of multiplying the number of segments without changing essential model properties) we modified the apical trunk. In the original model, oblique dendrites (`rad_t1`, `rad_t2`, `rad_t3`) are connected to the center of sections forming the apical trunk (`radTprox`, `radTmed`, `radTdist`). Here, we divided each of the apical trunk sections into two half-length sections (for example, `radTprox` → `radTprox1 + radTprox2`) and connected the oblique dendrites to the “1” end of the new sections (for example, connect `rad_t1(0)`, `radTprox(1)`). In this modification, the oblique dendrites are connected at the same distance from the soma as in the original model, but they are connected to the ends of the sections. We can now guarantee that these points will exist if the number of segments changes. We employed the meta-STDP rule to simulate synaptic plasticity. The operation principle of this rule has been explained in previous chapters and therefore we do not describe it here.

We inserted one synapse in each segment of apical tuft sections. Every synapse was considered to have AMPA and NMDA receptors ($g_{AMPA} = g_{NMDA} = 0.18 \text{ nS}$), and both were modelled as a difference of two exponentially decaying functions with rise and decay time constants of 0.2 and 2 ms for AMPARs and 1 and 50 ms for NMDARs (Kim et al. 2015).

We used a model configuration of ionic channels and their conductances as in our model (Appendix B). The L-Cav density was uniform, $g_{CaL} = 0.00803 \text{ mS/cm}^2$. The Nav density in the apical tuft dendrites was uniform, $g_{Na} = 38.28 \text{ mS/cm}^2$. To simulate bath application of 20 nM TTX, we reduced the conductance of Nav channels to 50% of control. To simulate bath application of 50 μM AP5 or 10 μM nimodipine, we reduced the NMDAR or L-Cav channel conductance to zero. (Kim et al. 2015).

The TBS stimulation consisted of five burst stimuli grouped at 5 Hz, with each consisting of 5 synaptic stimuli at 100 Hz. This stimulus was repeated one or three times (TBSx3), at 30-s intervals. TBS was implemented using NEURON’s *VecStim* class. We defined a vector to hold times of stimuli for each stimulated synapse. Next, we used the *play* method of the *VecStim* class to use these times to activate a synapse. The protocol was applied 20 ms after the start of simulation. Alternatively, we used *SpikeGenerator*.

We used the backward Euler method for numerical integration. The time step was 0.02 ms. We recorded the somatic voltage, dendritic voltage, I_{Na} , I_{Ca} (L-Ca_v), and I_{Ca} (NMDA) from each segment of apical tuft sections. We saved recorded data as binary files (.p).

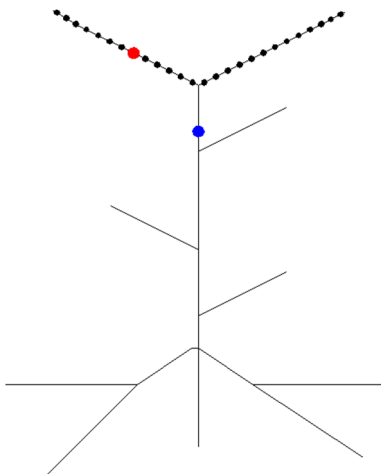


Figure 9.3: Model configuration. The black dots represent synapses, the red dot is the recording site in the apical tuft dendrite ($lm_medium1(0.1)$), and the blue dot is the recording site in the apical trunk ($radTdist2(0.1)$).

9.3 Results

We employed our reduced-morphology model of CA1 pyramidal cell to test the effect of Na-dSpikes on LTP at PP synapses, as shown previously by Kim et al. (2015). The model contained a sodium channel, three types of potassium channels (K_{DR} , K_A , K_M), a non-specific I_h channel, three types of calcium channels (C_{AL} , C_{AN} , C_{AT}), two types of calcium activated potassium channels (K_{Ca} , K_{Cagk}), and a calcium accumulation mechanism. In contrast, in Kim et al. (2015) study, a full-morphology compartmental model of CA1 pyramidal cell containing Na_v , K_v (K_{DR} , K_A), L- Ca_v channels, and simple models of calcium buffers, calcium diffusion, and calcium extrusion was used (Kim et al. 2015). We distributed excitatory synapses in each compartment of the apical tuft dendrites i.e., each segment of each section forming the apical tuft dendrites contained one synapse. Each synapse consisted of fast AMPA and slow NMDA components. Synaptic weights of AMPA and NMDA were identical. In addition, we endowed AMPA synapse with the meta-STDP synaptic plasticity rule.

9.3.1 Setting the synaptic weights

First, we needed to adjust synaptic weights to induce a dendritic spike. To evaluate this, we recorded dendritic and somatic voltages. We selected two different sites on the apical dendrites as representative. The first of them was located on the apical trunk at a distance of $315\ \mu m$ from the soma - $radTdist2(0.1)$. The second was located on the apical tuft dendrite at a distance of $515\ \mu m$ from the soma – $lm_medium1(0.1)$ (Figure 9.3). We calculated the EPSP amplitude as the difference between the voltage base and the maximum voltage at each recorded site for

each value of synaptic weights, which is documented in **Table 9.1**. We systematically increased synaptic weights from 0.18 nS to 0.62 nS.

Table 9.1: Dependence of EPSP amplitude on stimulus intensity. (*) – occurrence of a dendritic spike

	soma(0.5)		radTdist2(0.1)		lm_medium1(0.1)	
voltage base (mV)	-75.37		-74.25		-73.74	
Weight (nS)	Maximum voltage (mV)	EPSP amplitude (mV)	Maximum voltage (mV)	EPSP amplitude (mV)	Maximum voltage (mV)	EPSP amplitude (mV)
0.18	-72.42	2.95	-69.26	4.99	-64.91	8.33
0.38	-71.53	3.84	-65.97	8.28	-58.94	14.8
0.58	-70.73	4.64	-63.94	10.31	-53.34	20.4
0.62	-62.08	13.29*	-20.07*	54.18	-5.92*	67.82

We used 1x TBS (5 stimuli, 100 Hz) to induce dendritic EPSPs. For synaptic weights of 0.18 nS, 1x TBS induced 8.33 mV EPSP on apical tuft dendrites, 4.99 mV EPSP on the distal end of the apical trunk, and 2.95 somatic EPSP (**Table 9.1**, **Figure 9.4**). This value of synaptic weights was not sufficient to elicit a dendritic spike. The first dendritic spike was triggered when we set the synaptic weights to 0.62 nS (**Figure 9.4**). In this case, the dendritic spike occurred in response to the last TBS stimulus. The gradual increasing in the weights elicited dendritic spikes for each TBS stimulus: 0.65 nS – 2 dSpikes, 0.68 nS – 3 dSpikes, 0.70 nS – 4 dSpikes, and 0.72 – 5 dSpikes (**Figure 9.4**).

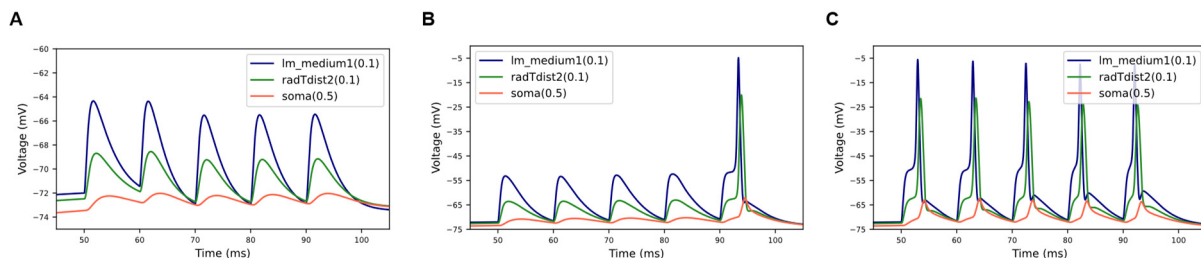


Figure 9.4: Voltage recordings in response to different TBS intensities. Note the EPSPs attenuation between the dendrites and the soma. (A) TBS with an intensity of 0.18 nS is not sufficient to induce a dendritic spike. (B) TBS with an intensity of 0.62 nS leads to one dendritic spike. (C) TBS with an intensity of 0.72 nS triggers a dendritic spike for each stimulus.

In experiments, Kim et al. (2015) set stimulus intensities to give EPSP amplitudes of 2-5 mV in somatic recordings and 4-10 mV in dendritic recordings (Kim et al. 2015). This is

consistent with approximately 50% attenuation of EPSPs between the dendrite (200–300 μm from the soma) and the soma (Golding et al. 2005). We calculated the attenuation of EPSPs between the dendrite (315 μm from the soma) and the soma from data in **Table 9.1**. In the absence of dSpike, the EPSPs attenuation is 50.17%, while in the presence of dSpike, the EPSPs attenuation is 43.76%. This shows that our model realistically models the EPSP attenuation.

9.3.2 Effect of TTX on dendritic spikes

We next examined the effect of TTX on triggering of dendritic spikes in the apical tuft dendrites. We simulated the application of 20 nM TTX as reducing of dendritic Na_v channels conductance to 50% of control.

Under the control condition, a single TBS stimulus leads to massive influx of sodium ions and calcium ions through the L- Ca_v channels and NMDAR channels which results in dendritic spikes. Recording of calcium currents showed that a primary source of calcium is through the NMDAR channels in our model. When we partially blocked the sodium channels reducing their conductance to 50% of control, we observed effect consistent with the results of Kim et al. (2015). Application of low TTX inhibited dendritically initiated spikes. At the same time, calcium influx through the L- Ca_v channels and NMDAR channels was inhibited, which is evidenced by both lower calcium currents and lower intracellular calcium concentration (**Figure 9.5**). These results suggest that the large calcium currents through the L- Ca_v channels and NMDAR channels were mediated by locally generated Na-dSpikes.

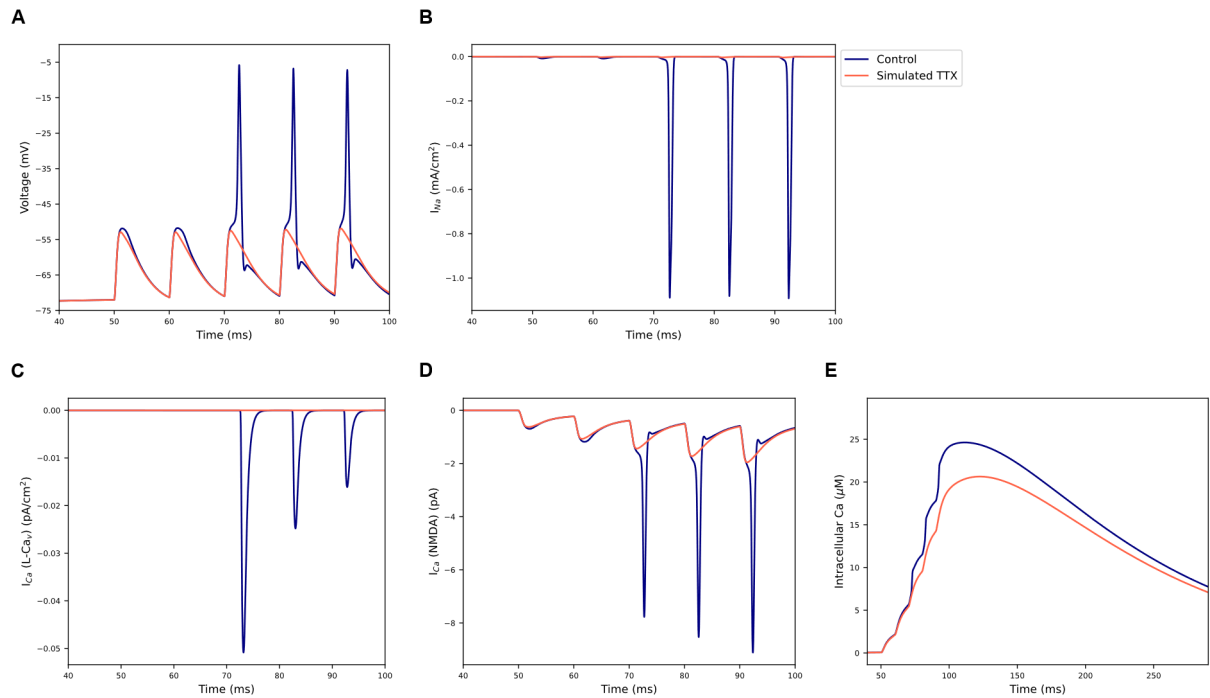


Figure 9.5: The effect of simulated TTX application on dendritic spikes. Application of 20 nM TTX blocks dendritic spike induction. **(A)** Representative trace of simulated dendritic voltage shows no dendritic spike after application of TTX. **(B)** Representative trace of simulated sodium current shows no Na-dSpike after application of TTX. **(C)** Representative trace of simulated calcium current mediated by the L- Ca_v channels. Application of TTX leads to decrease in influx of Ca^{2+} ions. **(D)** Representative trace of calcium current mediated by the NMDAR channels. Application of TTX leads to decrease in influx of Ca^{2+} ions. **(E)** Representative trace of intracellular calcium concentration. Simulated application of TTX decreases intracellular calcium concentration.

9.3.3 Effect of AP5 and nimodipine on dendritic spikes

To further investigate the effect of the L- Ca_v and NMDAR channels on dendritic spikes, we tested two scenarios. We first simulated application of 10 μM nimodipine, which is known as a calcium channels blocker, as reduction of the L- Ca_v channel conductance to zero. This resulted in a minimal reduction in intracellular calcium concentration compared to control conditions (**Figure 9.6**). This result is consistent with result of Kim et al. (2015), where they found that 10 μM nimodipine did not have a significant effect on dendritic calcium responses during burst stimulation of the PP (Kim et al. 2015). The minimal effect of the L- Ca_v channel on intracellular calcium concentration can be explained by the very low conductivity of the L- Ca_v channel in our model (8e^{-6} mho/ cm^2) compared to the model (125e^{-3} mho/ cm^2) used by Kim et al. (2015).

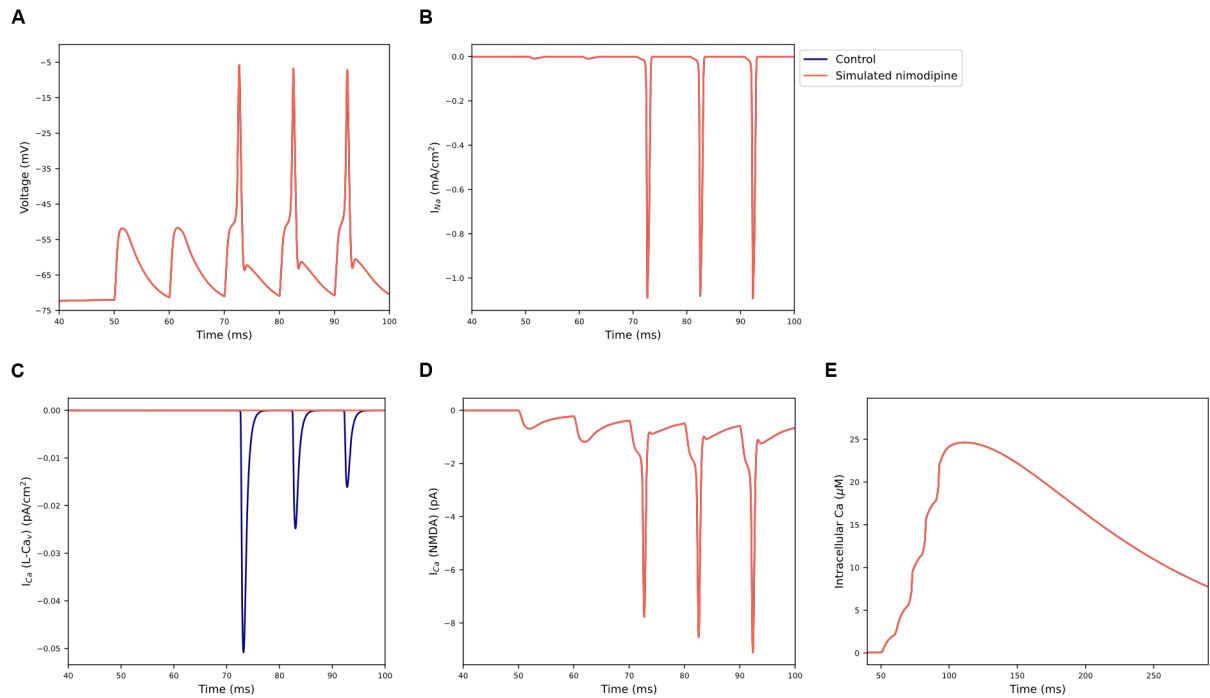


Figure 9.6: The effect of simulated nimodipine application on dendritic spikes. Blocking of the L- Ca_v channels has minimal effect on intracellular calcium concentration and dendritic spikes induction. (A) Representative trace of simulated dendritic voltage shows presence of dSpikes after application of nimodipine. (B) Representative trace of simulated sodium current shows no change in sodium current due to application of nimodipine. (C) Representative trace of simulated calcium current through the L- Ca_v channels which is blocked by application of numodipine. (D) Representative trace of simulated calcium current through NMDAR channels shows no change in calcium current due to application of nimodipine. (E) The minimal change in intracellular calcium concentration due to application of nimodipine.

Next, we simulated application of 50 μM AP5 as a reduction of the NMDAR channel conductance to zero. This results in suppression of dSpikes. At the same time, we did not observe large sodium influx and increase in intracellular calcium concentration was minimal (**Figure 9.7**). We can conclude that the large, transient, localized increase in intracellular calcium concentration mediated by Na-dSpikes is critical for the induction of PP-dSpikes.

9.3.4 The role of dSpikes in LTP induction at PP synapses

We employed meta-STDP synaptic plasticity rule to examine LTP induction at PP synapses using the TBS stimulation protocol. Note, we did not observe any somatic spike using the PP-TBS stimulation protocol. Therefore, metaplasticity rule was not activated and the meta-STDP rule behaved as classical non-metaplastic STDP rule. In our simulations, only AMPAR synapses were subject to synaptic plasticity changes. We used these synaptic plasticity parameters: $\tau_d = 50$ ms, $\tau_p = 16.8$ ms, $A_+ = A_- = \text{synaptic weight}$.

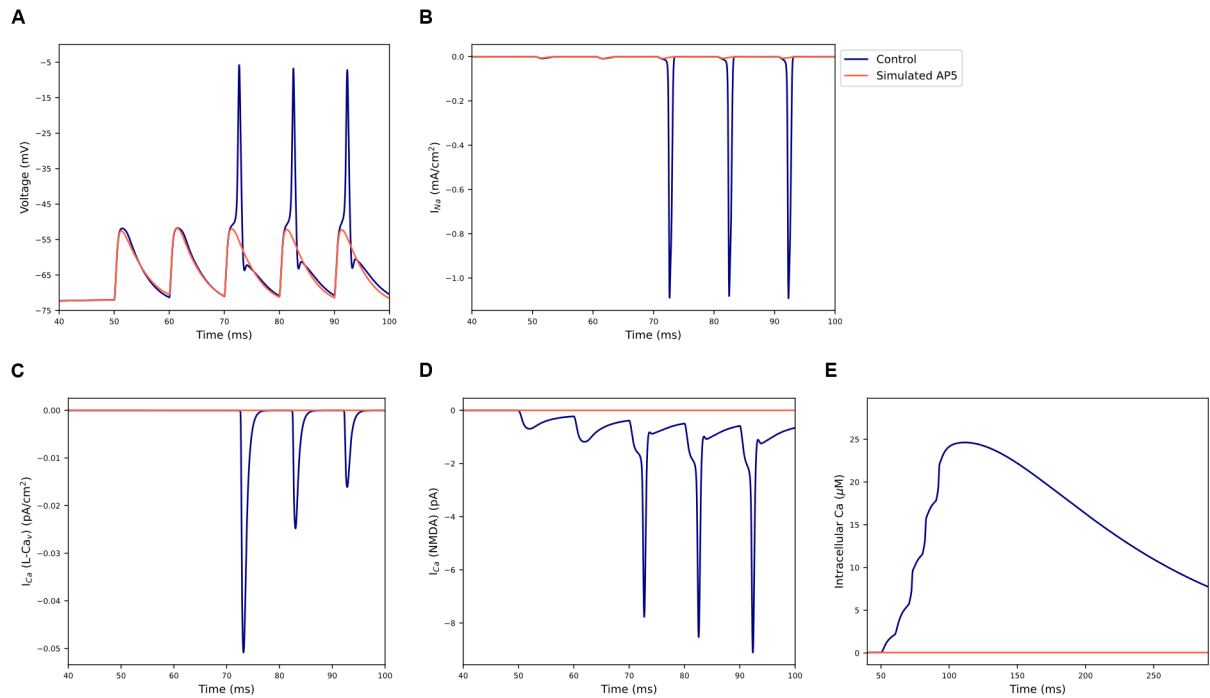


Figure 9.7: The effect of simulated AP5 application on dendritic spikes. Blockade of NMDAR channels has a significant effect on intracellular calcium concentration, leading to failure to induce dendritic spikes. **(A)** Representative trace of simulated dendritic voltage shows no dSpikes after application of AP5. **(B)** Representative trace of simulated sodium current shows no Na-dSpikes due to application of AP5. **(C)** Representative trace of simulated calcium current through the L-Ca_V channels shows reduction in the calcium current due to application of AP5. **(D)** Representative trace of simulated calcium current through NMDAR channels shows no calcium current when the AP5 was applied. **(E)** The significant effect of blocked NMDAR channels on intracellular calcium concentration.

LTP was induced only in the presence of dendritic spikes (**Figure 9.8**). This is due to the voltage-based implementation of STDP where a postsynaptic event is registered when the membrane potential at synaptic place reaches the threshold value. In our case it is -37 mV. This threshold value is higher than a dSpike threshold (**Figure 9.4**) and therefore a dSpike is considered as a postsynaptic event. For discussion, see Chapter 10.

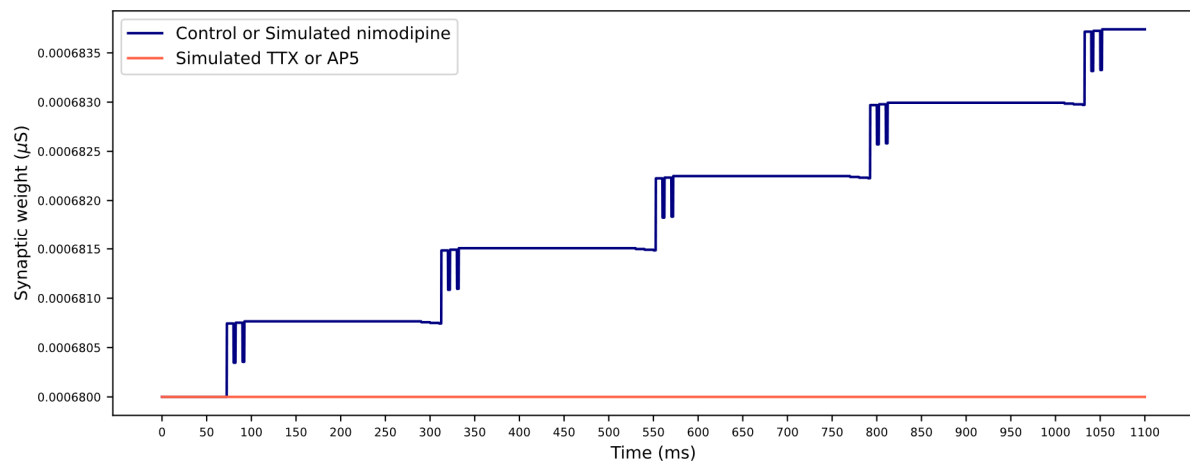


Figure 9.8: TBS stimulation protocol induces LTP at PP synapses in the presence of dendritic spikes. When dendritic spikes did not occur, LTP was not induced.

Chapter 10

10 Discussion

The main results of this work can be summarized as follows: (1) We developed a new model with reduced morphology for the CA1 pyramidal cell. The model was tested and validated using HippoUnit tests and shows sufficient biological plausibility (Tomko et al. 2021). (2) We distributed excitation synapses endowed with the meta-STDP synaptic plasticity rule on the dendrites of the model. During ongoing spontaneous activity, synaptic weights were dynamically stable, consistent with experimental *in vivo* observations (Tomko et al. 2020). (3) We presented the ability of the model to induce synaptic plasticity using different stimulation protocols. We observed the induction of both homosynaptic and heterosynaptic plasticity and proposed a relationship between the magnitude and direction of homo- and heterosynaptic plasticity and the location of dendritic compartments and the meta-STDP parameters. (4) We showed that sodium dendritic spikes and calcium influx through the NMDAR channels are required for dendritic spike and LTP induction at distal synapses in our model. This is consistent with the experimental results. Here we discuss the individual points with regard to the limitations and future work.

10.1 Validation of our model using HippoUnit

The model preserves canonical electrophysiological features defined by HippoUnit while decreasing computational time due to its low morphological complexity. The model successfully reproduces somatic, dendritic, and synaptic electrophysiological features of CA1 pyramidal neurons. These include somatic voltage and spiking responses, bAP and EPSP attenuation as well as nonlinear synaptic integration triggering dendritic spikes. The performance of the model was similar to a published full-morphology model that had been previously tuned to simulate some of these features (Migliore et al. 2018). When comparing the final error score for all the tests combined, our model performed better than the three other reduced-morphology models, and even slightly better than the full-morphology model. The benefit of our validated model for the neuroscientific community is that it can be used as a replacement for full-morphology models for faster simulations of single cell behavior. Furthermore, although we did not test it explicitly, we expect it to help significantly reduce runtimes for network simulations.

The HippoUnit test suite is a Python-based tool for systematic testing of CA1 pyramidal cells models. So far, this tool has only been used to test complex full-morphology models (Sáray et al. 2021). Here, for the first time we used it to test simplified reduced-morphology models. For a comparison with a full-morphology model, we included also the M18 model. The reason for this was that it has been previously tuned for some of the HippoUnit features and therefore it can be viewed as a reference model. Moreover, its biophysics provided the basis for active mechanisms (including their parameters) implemented in our model.

The better performance of our model as compared to the three other reduced-morphology models is not surprising, as they were created to capture specific CA1 pyramidal cell behavior (see Introduction and Methods) and not tuned for HippoUnit tests. Importantly, our purpose was not to criticize the validity of these models in biology but rather to use them as controls for the improvement and validation of our model. The models remain valid for the cell behavior they were tuned for. Moreover, by changing their biophysical mechanisms (see **Figure 5.6**, **Figure 5.7**), we showed that they can be easily adjusted to perform well in the HippoUnit tests (see the “vTo21” models in Results). Thus, using our or similar approaches, future users of reduced-morphology ModelDB models can extend their validity beyond phenomena they were tuned for by adapting them with the standardized HippoUnit tests.

10.1.1 Somatic voltage response

The Somatic Features Test revealed that the M18 model reached the best score. This was not unexpected, as this model has been previously optimized for some of the somatic features (Migliore et al. 2018). The results show that the C10 and Tu19 models are highly excitable, which is manifested by high spike counts, firing rates and low interspike intervals. In contrast, the CP15 model was weakly excitable. The somatic properties of the models depend strongly on their perisomatic ion channel content. The models differed in their maximum channel conductance values and this accounts for their different test performance. This interpretation is supported also by the observation that inserting M18/To21 ion channels into the three untuned reduced-morphology models significantly decreased their error score for somatic features (see the “vTo21” models in **Figure 5.6**, **Figure 5.7**).

10.1.2 Depolarization block

CA1 pyramidal neurons respond to a strong current injection with a depolarization block. When the current intensity exceeds a certain threshold, neurons stop firing while maintaining the membrane potential at a constant level throughout the stimulation period. Sodium (NaT) and

potassium (K_{DR}) channels, which underlie the basic spiking mechanism, play a major role in this response of neurons. In particular, the interaction between their activating and inactivating properties is of key importance (Bianchi et al. 2012; Tucker et al. 2012). The depolarization block emerges when, during an interval between subsequent APs, the NaT channel does not deinactivate completely and K_{DR} does not activate sufficiently to repolarize the neuron. Both conditions are met in I_{Na} and I_{KDR} models by Shah et al. (Shah et al. 2008) that were used also in the benchmark M18 model and our To21 model. Whereas NaT and K_{DR} are sufficient for the depolarization block, K_M and K_{mAHP} channels determine the equilibrium voltage during the block (Bianchi et al. 2012). Previous simulations have shown that the steady-state activation and inactivation of I_{Na} and I_{KDR} currents from Poirazi et al. (Poirazi et al. 2003a; 2003b) prevents reaching depolarization block (Bianchi et al. 2012). This is relevant since the C10, CP15, and Tu19 models use the I_{Na} and I_{KDR} models from Poirazi et al. (Poirazi et al. 2003a; 2003b). Taken together, this explains why the M18 and To21 models successfully enter depolarization block whereas the untuned control models do not. The To21 model reached the best score because we adjusted the maximal conductance of I_{Na} , I_{KDR} , I_{KM} , I_{CaL} , and I_{CaT} to the same values as reported in Table 1 in Bianchi et al. (Bianchi et al. 2012) who focused on reproducing the depolarization block.

10.1.3 Postsynaptic potential attenuation

CA1 pyramidal cells display a characteristic strong dendrosomatic attenuation of excitatory postsynaptic potentials (Magee, Cook 2000; Golding et al. 2005). Local injections of EPSC-shaped currents into different sites of the dendritic tree induce location-dependent EPSPs. As the distance between the stimulated site and the soma increases, the amplitude of these locally evoked EPSPs increases, but at the same time, the EPSP amplitudes recorded at the soma decrease. However, for Schaffer collateral inputs, the amplitude of synaptically evoked somatic EPSPs is independent of synapse location (Magee, Cook 2000) due to a distance-dependent increase in postsynaptic AMPA conductance and AMPA receptor content (Andrásfalvy, Magee 2001; Andrásfalvy et al. 2003).

Such experimentally observed EPSP attenuation was better captured by our model than by the reference M18 model or the three other reduced-morphology models. In our model, the recorded peaks of the amplitudes of local and somatic EPSPs were similar to those in figure 2B in Magee and Cook (Magee, Cook 2000). In the case of the M18 model, the local EPSPs were larger and their dendrosomatic attenuation was stronger than indicated by the range of

experimental values. Also, the remaining C10 and CP15 models captured the EPSP attenuation only qualitatively. Only the Tu19 model showed attenuation values similar to the experimental data. Overall, the dendritic filtering was too strong in the reference full-morphology M18 model and too weak in the C10 and CP15 models. Thus, the interplay between dendritic geometry and biophysical cable properties (especially the axial and membrane resistivity, and the distribution of I_h , see (Golding et al. 2005)) would require further fine tuning in these models to reproduce the EPSP attenuation data not only qualitatively but also quantitatively.

10.1.4 Backpropagation of action potentials

APs backpropagate into the apical trunk and basal dendrites of the CA1 pyramidal cell becoming weaker with increasing distance from the soma. Regarding the backpropagation of APs, the CA1 pyramidal cells can be distinguished as strongly- and weakly-propagating. When comparing the bAP amplitude in the proximal and distal parts of the apical trunk, strongly-propagating cells lose approximately 25–45% of the AP amplitude, while weakly-propagating cells lose up to 70–85% (Golding et al. 2001). Different distributions of sodium and A-type potassium channels are sufficient to account for the bAP dichotomy (Golding et al. 2001). In agreement with this, the maximum conductance of the I_{KA} had an increasing gradient in the C10, CP15, and Tu19 models with increasing distance from the soma, leading to a regime between weak and strong backpropagation. An adjustment of the conductances would move these models closer to weak or strong backpropagation experimental results. The relatively high error of the benchmark M18 model was due to high somatic AP amplitude caused by strong axonal sodium conductance. In contrast, our model used a slightly reduced sodium conductance. The result was a somatic AP with similar characteristics to those in Golding et al. (Golding et al. 2001) (see their figure 3). At the same time, following Golding et al., we used an increasing gradient of I_{KA} in the apical trunk which resulted in weak AP backpropagation. In summary, the good performance of our model in the bAP Test can be explained by the fine-tuning of I_{Na} and I_{KA} based on bAP simulations and experiments of Golding et al. (Golding et al. 2001).

10.1.5 Synaptic integration in dendrites

Most excitatory synaptic inputs of CA1 pyramidal cells are located on thin radial oblique dendrites in the stratum radiatum. Signals from these inputs are integrated linearly or supralinearly depending on the degree of their synchronization. Asynchronous inputs exhibit linear summation while synchronous inputs are summed supralinearly, both in the case of

clustered and distributed configurations (Gasparini et al. 2004; Losonczy, Magee 2006). The result of such supralinear summation is a dendritic spike. This supports the idea that a single radial oblique dendrite of the CA1 pyramidal cell serves as a single integrative compartment or subunit (Poirazi et al. 2003b; Losonczy, Magee 2006).

The Oblique Integration Test evaluated how the models integrated synchronous and asynchronous synaptic inputs. Since synapses had to be placed on oblique branches, the test was run only on three models, M18, Tu19, and our model. In the case of synchronized inputs, dendritic spikes were generated in line with data. It is known that at least five synchronized inputs are required to generate a dendritic spike (Gasparini et al. 2004; Losonczy, Magee 2006). In agreement with these experiments, such low number of activated inputs was needed for the M18 and To21 models. The Tu19 model required nine synchronous inputs to generate the dendritic spike. A putative dendritic spike can be detected on the soma as a rapid increase in the somatic voltage (Losonczy, Magee 2006). We saw a similar increase in all the models. In addition, we observed that the level of non-linearity was in the experimental range for all models. On the other hand, asynchronous inputs are known to sum up linearly at the lateral branches of CA1 neurons (Losonczy, Magee 2006). In the three models, the synaptic integration of asynchronous inputs was slightly sublinear but still in the experimental range. The time to peak for corresponding somatic events was faster than in experiments and would require tuning of dendritic filtering or possibly implementing synaptic inhibition. Taken together, the models were able to generate realistic synaptically driven dendritic spikes. These results indicate that the presence of dendritic sodium and calcium channels are sufficient for mimicking nonlinear integration of dendritic synaptic events.

10.1.6 Limitation of the model

In our model, we used a set of channels from the M18 model. Subsequently, we used a "one-size-fits-all" approach (Marder, Taylor 2011) to manually adjust the conductances of sodium, potassium, and calcium channels. However, neurons exhibit high (~ 2 - 6-fold) variability of ion currents and ion channel expression (Liss et al. 2001; Swensen, Bean 2005; Schulz et al. 2006; Goaillard et al. 2009). Computational modeling suggests that this is the case also for CA1 pyramidal cells (Migliore et al. 2018). Therefore, it is important to emphasize that the final ion channel composition of our model represents only one possible realistic solution in the parameter space. In the future, we would like to use population-based (also called ensemble or database) modeling (Günay et al. 2008; Marder, Taylor 2011; Britton et al. 2013; Sekulic et

al. 2014; Iavarone et al. 2019) to generate populations of realistic reduced-morphology models that would reflect the variability of experimental data. For this purpose, an update for the distribution of CA1 pyramidal cell ion channels based on available literature would be desirable as recently done for hippocampal dentate granule cells (Beining et al. 2017). By studying such a population of models, it is possible to reveal various mechanisms and correlations that play important roles in the function of the neuron as such and the whole network of neurons (Marder, Taylor 2011).

10.2 Stabilization of synaptic weights during ongoing spontaneous activity

Computational studies that model synaptic plasticity *in vivo* neglect the fact that *in vivo* neurons exhibit an ongoing spontaneous spiking in the neural circuits (Deshmukh et al. 2010). The first synaptic plasticity theory that explicitly took into account ongoing neuronal activity was the BCM theory (Bienenstock et al. 1982). A key element of this BCM theory is a whole-cell variable termed the modification threshold, the tipping point at which the presynaptic activity either leads to long-term depression (LTD) or long-term potentiation (LTP) of synaptic efficacy. A second key element is the theory's postulate that the average ongoing level of spontaneous activity dynamically sets the position of the LTD/LTP tipping point in such a way that potentiation is favored when the postsynaptic cell firing is low on average and, vice versa, depression is favored when the postsynaptic activity is high on average. The proposal of a modifiable plasticity threshold foreshadowed the concept of metaplasticity (Abraham 2008), developed to account for the abundant experimental evidence that prior neural activity can change the state of neurons and synapses such that the outcome of future synaptic plasticity protocols is altered.

Here we study how key components of learning mechanisms in the brain, namely spike timing-dependent plasticity and metaplasticity, interact with spontaneous activity in the input pathways of the CA1 neuron model. We optimized the synaptic model parameters to achieve the long-term stability of synaptic weights under *in vivo*-like conditions mimicking ongoing spontaneous activity as recorded in neuronal circuits (Buzsáki 2002). Each synapse received an independent spike train input consisting of periodic spikes corresponding to theta activity and random spikes corresponding to random background activity. Average frequency of spikes in the one spike train was ~8 Hz. During the 20-min simulation of spontaneous activity, the individual synaptic weights and synaptic plasticity parameters are dynamically stable. These

results provide a good basis for experimenting with synaptic plasticity stimulation protocols and ultimately for modeling the synaptic plasticity observed in CA1 pyramidal cells *in vivo*.

In our previous study (Tomko et al. 2019), we used a model from Cutsuridis et al. (2010). Using HippoUnit tests (Sáray et al. 2021), we tested and compared the latter model and our currently used model (see Chapter 5). As a result, our model achieved better results than the Cutsuridis model (Cutsuridis, Graham, et al. 2010), which is more excitable (see Chapter 5). The consequence of the higher excitability of the Cutsuridis model was that at the beginning of each simulation there was a significant increase in the integrated spike count function θ_M and at the same time a decrease in the weights (**Figure 4.5**, **Figure 4.7**) (Tomko et al. 2019). In our current model, the weights are dynamically stable from the beginning of the simulation (**Figure 6.4**, **Figure 6.5**, **Figure 6.6**, and **Figure 6.7**) and the integrated spike count function θ_M saturation occurs gradually (**Figure 6.3**). By adding side branches, we have ensured that experimentally observed non-linear summation of synaptic inputs occurs on these branches, resulting in dendritic spikes (see Chapter 5).

10.3 Simulations of synaptic plasticity

To study the ability of our model to induce synaptic plasticity, we used four stimulation protocols: (1) sequential stimulation, (2) high-frequency stimulation, (3) paired-pulses stimulation, and (4) theta-burst stimulation. In all simulations, we employed meta-STDP as a synaptic plasticity rule.

10.3.1 Sequential stimulation protocol

The sequential stimulation protocol is used to simultaneously stimulate the Schaffer and commissural pathways. Key aspects that play an important role in the induction of synaptic plasticity using this protocol are the order of stimulation (Schaffer precedes commissural or Schaffer follows commissural), the state of the hippocampal network, and the time window between stimuli (Dong et al. 2008).

We simulated a case of pentobarbital anesthesia in which we obtained LTP simultaneously at Schaffer and commissural synapses. When Schaffer's stimulation preceded the commissural stimulation, LTP at the commissural synapses were stronger. In the experimental data, the authors observed a similar magnitude of LTP at both synapses (Dong et al. 2008). When Schaffer's stimulation followed the commissural stimulation, LTP at the Schaffer synapses was stronger in our simulations. In contrast, in the experimental data (Dong

et al. 2008) LTP at the Schaffer synapses was weaker than at commissural synapses. This effect can be explained by metaplasticity and weight change due to the first pair of stimuli.

Consider the case when stimulation of Schaffer synapses precedes commissural synapses and consider only the first pair of stimuli. Let t_1 be the stimulation time of Schaffer synapses and t_2 be the stimulation time of commissural synapses. Then $t_2 - t_1 = 20$ ms. Before stimulation, $\theta_M = 0$. The first stimulus at time t_1 induces a somatic spike. This in turn activates metaplasticity to favor potentiation. θ_M increases but is still less than 1. The amplitude of the potentiation increases rapidly and reaches its peak. $A_+(t_1) < A_+(t_2)$ and $\theta_M(t_1) < \theta_M(t_2)$. According to Equation (3.51), therefore, the weights of the commissural synapses are strengthened more than the Schaffer synapses weights. These initial stimuli cause the observed difference between LTP at Schaffer and commissural synapses. The same situation occurs in the reverse order of stimulation.

The effect of spontaneous activity on homosynaptic and heterosynaptic activity was shown experimentally (Abraham et al. 2007) as well as using computational modeling (Benuskova, Jedlicka 2012; Jedlicka et al. 2015). Thus, we implemented background ongoing spontaneous activity. We showed that direction of synaptic plasticity induced by the sequential stimulation depends on a level of spontaneous activity. The lower level of spontaneous activity changed LTD to LTP at stimulated synapses. This could be due to absence of somatic spikes caused by 1 Hz spontaneous activity. In this case, each pair of Schaffer and commissural stimulation results in two somatic spikes. They are detected as postsynaptic events at synapses. The nearest-neighbor pairing scheme of STDP causes a potentiation due to SSt protocol. In the case of 3 Hz spontaneous activity, spontaneous spikes can occur between spikes induced by the SSt and metaplasticity switches the modification threshold towards LTD. Therefore, LTD can occur at stimulated synapses.

In our model, we added excitatory synapses to dendrites in SLM. This allowed us to observe heterosynaptic plasticity because these synapses are activated only by spontaneous activity. Heterosynaptic LTD at these synapses was a result of spontaneous activity and dSpikes propagated to the SLM dendrites. As the level of spontaneous activity is lowered, low number of presynaptic spikes activates the synapses. Spontaneous activity only is not sufficient to evoke postsynaptic spikes and due to STDP pairing scheme, LTD occurs on these synapses.

10.3.2 High-frequency stimulation and paired-pulses stimulation protocols

High-frequency stimulation and paired-pulses stimulation protocols are typically used to induce LTP and LTD, respectively (Pavlowsky, Alarcon 2012). We implemented these protocols and showed that we can induce LTP and LTD on synapses using our model. Since we did not stimulate all synapses, we observed the phenomenon of heterosynaptic plasticity at unstimulated synapses. In addition, we observed the influence of the α parameter on the magnitude and direction of synaptic plasticity. These results should be considered as preliminary and further simulations are required to confirm the observed effects.

The effect of α on the magnitude and direction of synaptic plasticity can be explained by equations (3.46) and (3.52). From (3.52), the depression amplitude in time t , $A_d(t)$, is a product of $A_d(0)$ and $\theta_M(t)$. From (3.46), θ_M which is defined as the time average of the square of postsynaptic activity and is scaled by α . In general, postsynaptic activity is high during the duration of the stimulation protocol. This manifested as an increase in θ_M . When we increase α , θ_M increases even more, making the depression effect stronger and changing LTP to LTD.

We observed heterosynaptic depression at unstimulated synapses. This arises from an ongoing spontaneous activity because the meta-STDP rule implements the nearest-neighbor pairing scheme. To change a synaptic weight, synapse must receive a presynaptic spike and detect a postsynaptic event. The postsynaptic event is detected, when the membrane voltage reaches a threshold value (-37 mV) at a place of synapse. In the case of synapses in SLM dendrites, they can detect a postsynaptic event due to bAP. However, bAP attenuates when propagating along the apical trunk. When a stimulation protocol is applied to SR synapses, bAP or EPSP can reach the apical dendrites in SLM and these synapses can modify their weights. However, when a stimulation protocol is applied to SO synapses, bAP or EPSP attenuates before they reach the distal apical dendrites because the spontaneous activity of 2 Hz is not sufficient to support propagation of bAP and EPSP. Therefore, we do not observe heterosynaptic depression at SLM synapses when we stimulated synapses in SO.

Another case is the induction of heterosynaptic plasticity using HFS and PP protocols. In the case of HFS, we observed almost no heterosynaptic plasticity. On the other hand, in the PP protocol, we observed strong heterosynaptic depression mainly at synapses within the same dendritic compartment as the synapses were stimulated. These differences can be explained by the length of stimulation protocols and the level of spontaneous activity. With 2 Hz

spontaneous activity, a presynaptic spike occurs approximately every 500 ms. The HFS protocol consists of 4 trains of 1-sec stimulation at 100 Hz, i.e., 100 spikes with an interspike interval of 10 ms arrive within one train. Therefore, due to 2 Hz spontaneous activity, approximately two pairings occur during one HFS train at unstimulated synapses resulting in weak observed plasticity.

On the other hand, the PP protocol lasts 15 minutes. Every second, synapses are stimulated by one pair of stimuli with an interspike interval of 50 ms. Each pair of stimuli induces 2 somatic spikes, which are backpropagated to the dendrites and unstimulated synapses detect them as postsynaptic events. Therefore, stronger heterosynaptic depression may occur at unstimulated synapses due to PP protocol.

When interpreting the results, we must take into account the simplifications of the model. The main simplification is its reduced morphology. We used only fast excitatory AMPAR synapses (Chapters 4, 6, 7, 8). Synapses were placed randomly on the dendrites but maintaining the ratio between the individual dendritic compartments (Megías et al. 2001). Initial weights were generated from the normal distribution. The first improvement could be a real distribution of synapses taking into account dendritic filtering, as discussed in Chapter 2.5.2 (Jarsky et al. 2005; Nicholson et al. 2006; Katz et al. 2009; Menon et al. 2013). In Chapter 9, we showed the importance of NMDAR channels in synaptic plasticity. Therefore, we need to add NMDAR channels so that we can more realistically simulate synaptic plasticity. Last but not least, our model lacks inhibitory inputs. Inhibition plays a key role in dendritic integration (Müller et al. 2012; Müller, Remy 2014; Bloss et al. 2016) as well as synaptic plasticity (Saudargienė, Graham 2015). Therefore, we should implement simple inhibition.

10.3.3 Theta-burst stimulation

Theta-burst stimulation is a typical stimulation protocol to induction of LTP (Kim et al. 2015). We used this protocol to study a role of Na-dSpikes in induction of LTP at PP synapses. Dendritic spikes at apical tuft dendrites are triggered by a massive influx of sodium ions which in turn open NMDAR channels and increase in intracellular calcium concentration. This together results in induction of dSpike which is registered as a postsynaptic event by STDP rule and LTP is induced.

Dendritic spikes in distal apical dendrites play major role in synaptic integration and relaying synaptic signals from stratum lacunosum-moleculare to the soma. In absence of dSpikes, inputs from these regions have a minimal effect on the soma (Golding, Spruston 1998;

Jarsky et al. 2005). In comparison to SR synapses, PP synapses cause the large local depolarization which results in dSpike before the somatic action potential (Nicholson et al. 2006). The forward propagation of dSpikes along the apical trunk to the soma typically failed and do not trigger somatic action potential. This was also observed in our simulations (**Figure 9.4**). However, the effectiveness at driving somatic action potential can be facilitated by very modest synaptic activity in SR (Jarsky et al. 2005). We need to perform further simulations to test this effect in our model.

NMDA-dependent LTP requires activation of NMDA receptors. This can be achieved with repeated strong tetanus such as TBS. Activated NMDA receptors mediate a strong calcium influx and an increase in intracellular calcium concentration. This in turn activates the biochemical reactions that lead to the induction of LTP (Citri, Malenka 2008; Baltaci et al. 2019). Na-dSpikes play a critical role in this process. They contribute to LTP induction by promoting large, transient, localized increases in intracellular calcium concentration near the calcium-conducting pores of NMDAR and L-type Ca_v channels (Kim et al. 2015). We investigated the role of Na-dSpikes in LTP induction using our model with reduced morphology. We have shown that Na channels as well as NMDAR channels are necessary for LTP induction (Kim et al. 2015). Their separate blocking did not sufficiently depolarize the membrane and did not result in dSpikes. Thus, the voltage-based STDP did not detect any postsynaptic event and there was no change in synaptic weights.

NMDA-dependent LTD can be induced by a low-frequency stimulation. Modest and repeated activation of NMDAR leads to a modest increase in the intracellular calcium which is a signal to LTD induction (Dudek, Bear 1992; Citri, Malenka 2008; Lüscher, Malenka 2012). Kim et al. (2015) observed LTD in neurons buffered with 10 mM BAPTA which is used to chelating the intracellular calcium (Kim et al. 2015). This suggests that LTD can be induced by activation of NMDARs in absence of calcium influx (Nabavi et al. 2013). On the other hand, the recent study has shown that the induction of LTD in the hippocampal CA1 region is dependent on ionotropic, rather than metabotropic, NMDA signaling (Babiec et al. 2014). We observed LTD, which was induced by a paired-pulses stimulation protocol. We also observed heterosynaptic LTD at unstimulated synapses (see Chapter 8). Our results were obtained in the absence of NMDAR. The question is how LTD and het-LTD will be affected after the addition of NMDAR channels. Additional simulations could answer this question.

10.4 Synaptic plasticity rule

In this thesis, we used the voltage-based STDP synaptic plasticity rule combined with fast BCM-like metaplasticity. This rule of synaptic plasticity considers exceeding the local voltage threshold at the site of synapse to be a postsynaptic event (Jedlicka et al. 2015). In our case, it was always associated with the occurrence of a dendritic spike. It is known and in Chapter 9 we showed that calcium signals are important in synaptic plasticity. We could implement calcium detection in this rule of synaptic plasticity. Another possibility is to use the synaptic plasticity rule, which already includes calcium signals (Ebner et al. 2019).

The meta-STDP rule includes fast BCM-like metaplasticity implemented as an integrated spike count, which is a form of global metaplasticity (Benuskova, Abraham 2007; Jedlicka et al. 2015). In this case, the rule can only detect somatic spikes. However, dendritic spikes can also be detected at the soma as a sharp increase in somatic voltage (Losonczy, Magee 2006; Sáray et al. 2021). When modifying the rule to integrate somatic voltage we could also include the detection of dendritic spikes in metaplasticity. Furthermore, we could implement local metaplasticity for each dendritic branch. This idea comes from a two-stage dendritic integration model, where each dendrite can serve as a separate computational unit and inputs from individual branches are integrated at the soma (Poirazi et al. 2003a; Katz et al. 2009; Gidon et al. 2020). Last but not least, experimental verification of model predictions of heterosynaptic plasticity is needed.

Another way is to use an energy-based model of synaptic plasticity in which synaptic plasticity is associated with the degree of deviation of energy states. Metabolic energy is calculated based on the postsynaptic membrane potential and the membrane current density. If the firing energy state is less (larger) than the resting energy state, potentiation (depression) in synaptic weights occurs, respectively. If the firing energy state is relatively close to the resting energy state, synaptic weights remain unchanged. This model unifies homo- and heterosynaptic plasticity and authors were able to reproduce spike-timing dependent plasticity as well as cooperative plasticity (Chen et al. 2020). Using this model, we could calculate the energy efficiency of synaptic plasticity observed in our model and compare the energy consumption of synaptic plasticity using different plasticity stimulation protocols.

11 References

ABRAHAM, Wickliffe C, 2008. Metaplasticity: Tuning synapses and networks for plasticity. *Nature Reviews Neuroscience* [online]. 2008. Vol. 9, no. 5, p. 387–399. DOI 10.1038/nrn2356. Available from: <https://doi.org/10.1038/nrn2356>

ABRAHAM, Wickliffe C and BEAR, M F, 1996. Metaplasticity: the plasticity of synaptic plasticity. *Trends in Neurosciences* [online]. 1996. Vol. 19, no. 4, p. 126–130. DOI [https://doi.org/10.1016/S0166-2236\(96\)80018-X](https://doi.org/10.1016/S0166-2236(96)80018-X). Available from: <https://www.sciencedirect.com/science/article/pii/S016622369680018X>

ABRAHAM, Wickliffe C, LOGAN, Barbara, WOLFF, Amy and BENUSKOVA, Lubica, 2007. “Heterosynaptic” LTD in the dentate gyrus of anesthetized rat requires homosynaptic activity. *Journal of Neurophysiology* [online]. 1 August 2007. Vol. 98, no. 2, p. 1048–1051. DOI 10.1152/jn.00250.2007. Available from: <https://doi.org/10.1152/jn.00250.2007>

ABRAHAM, Wickliffe C, MASON-PARKER, S E, BEAR, M F, WEBB, S and TATE, W P, 2001. Heterosynaptic metaplasticity in the hippocampus *in vivo*: a BCM-like modifiable threshold for LTP. *Proceedings of the National Academy of Sciences of the United States of America* [online]. 2001/08/21. 11 September 2001. Vol. 98, no. 19, p. 10924–10929. DOI 10.1073/pnas.181342098. Available from: <https://pubmed.ncbi.nlm.nih.gov/11517323>

ABRAHAM, Wickliffe C and ROBINS, Anthony, 2005. Memory retention – the synaptic stability versus plasticity dilemma. *Trends in Neurosciences* [online]. 2005. Vol. 28, no. 2, p. 73–78. DOI <https://doi.org/10.1016/j.tins.2004.12.003>. Available from: <https://www.sciencedirect.com/science/article/pii/S0166223604003704>

Action potential schematic, 2017. [online]. [Accessed 14 May 2021]. Available from: https://commons.wikimedia.org/wiki/File:Action_potential_schematic.png

AHMED, Mohsin S and SIEGELBAUM, Steven A, 2009. Recruitment of N-Type Ca²⁺ Channels during LTP Enhances Low Release Efficacy of Hippocampal CA1 Perforant Path Synapses. *Neuron* [online]. 13 August 2009. Vol. 63, no. 3, p. 372–385. DOI 10.1016/j.neuron.2009.07.013. Available from: <https://doi.org/10.1016/j.neuron.2009.07.013>

ALBERTS, B, JOHNSON, A, WILSON, J H, LEWIS, J, HUNT, T, ROBERTS, K, RAFF, M and WALTER, P, 2008. *Molecular Biology of the Cell* [online]. Garland Science. ISBN 9780815341116. Available from: <https://books.google.sk/books?id=iepjmRfP3ZoC>

ALI, Afia B and NELSON, Charmaine, 2006. Distinct Ca²⁺ Channels Mediate Transmitter Release at Excitatory Synapses Displaying Different Dynamic Properties in Rat Neocortex. *Cerebral Cortex* [online]. 1 March 2006. Vol. 16, no. 3, p. 386–393. DOI 10.1093/cercor/bhi117. Available from: <https://doi.org/10.1093/cercor/bhi117>

ALMOG, Mara and KORNGREEN, Alon, 2016. Is realistic neuronal modeling realistic? *Journal of Neurophysiology* [online]. 2016. Vol. 116, no. 5, p. 2180–2209. DOI 10.1152/jn.00360.2016. Available from: www.jn.org

AMARAL, D. G., DOLORFO, Cynthia and ALVAREZ-ROYO, Pablo, 1991. Organization of CA1 projections to the subiculum: A PHA-L analysis in the rat. *Hippocampus*. 1991. DOI 10.1002/hipo.450010410.

AMARAL, D. G. and WITTER, M. P., 1989. The three-dimensional organization of the hippocampal formation: A review of anatomical data. *Neuroscience*. 1989. DOI 10.1016/0306-4522(89)90424-7.

ANDRÁSFALVY, Bertalan K and MAGEE, J C, 2001. Distance-dependent increase in AMPA receptor number in the dendrites of adult hippocampal CA1 pyramidal neurons. *Journal of Neuroscience* [online]. 1 December 2001. Vol. 21, no. 23, p. 9151–9159. DOI 10.1523/jneurosci.21-23-09151.2001. Available from: <http://www.jneurosci.org/content/21/23/9151.abstract>

ANDRÁSFALVY, Bertalan K, SMITH, Mark A, BORCHARDT, Thilo, SPRENGEL, Rolf and MAGEE, J C, 2003. Impaired regulation of synaptic strength in hippocampal neurons from GluR1-deficient mice. *Journal of Physiology* [online]. 1 October 2003. Vol. 552, no. 1, p. 35–45. DOI 10.1113/jphysiol.2003.045575. Available from: <https://doi.org/10.1113/jphysiol.2003.045575>

ANGGONO, Victor and HUGANIR, Richard L, 2012. Regulation of AMPA receptor trafficking and synaptic plasticity. *Current opinion in neurobiology* [online]. 2012/01/02. June 2012. Vol. 22, no. 3, p. 461–469. DOI 10.1016/j.conb.2011.12.006. Available from: <https://pubmed.ncbi.nlm.nih.gov/22217700>

ANTUNES, G and SIMOES-DE-SOUZA, F M, 2018. AMPA receptor trafficking and its role in heterosynaptic plasticity. *Scientific reports* [online]. 9 July 2018. Vol. 8, no. 1, p. 10349. DOI 10.1038/s41598-018-28581-w. Available from: <https://pubmed.ncbi.nlm.nih.gov/29985438>

BABIEC, Walter E, GUGLIETTA, Ryan, JAMI, Shekib A, MORISHITA, Wade, MALENKA, Robert C and O'DELL, Thomas J, 2014. Ionotropic NMDA receptor signaling is required for the induction of long-term depression in the mouse hippocampal CA1 region. *The Journal of neuroscience : the official journal of the Society for Neuroscience* [online]. 9 April 2014. Vol. 34, no. 15, p. 5285–5290. DOI 10.1523/JNEUROSCI.5419-13.2014. Available from: <https://pubmed.ncbi.nlm.nih.gov/24719106>

BALTACI, Saltuk Bugra, MOGULKOC, Rasim and BALTACI, Abdulkerim Kasim, 2019. Molecular Mechanisms of Early and Late LTP. *Neurochemical Research* [online]. 2019. Vol. 44, no. 2, p. 281–296. DOI 10.1007/s11064-018-2695-4. Available from:

<https://doi.org/10.1007/s11064-018-2695-4>

BANNISTER, N J and LARKMAN, A U, 1995. Dendritic morphology of CA1 pyramidal neurones from the rat hippocampus: I. Branching patterns. *Journal of Comparative Neurology* [online]. 11 September 1995. Vol. 360, no. 1, p. 150–160. DOI <https://doi.org/10.1002/cne.903600111>. Available from: <https://doi.org/10.1002/cne.903600111>

BEINING, Marcel, MONGIAT, Lucas Alberto, SCHWARZACHER, Stephan Wolfgang, CUNTZ, Hermann and JEDLICKA, Peter, 2017. T2N as a new tool for robust electrophysiological modeling demonstrated for mature and adult-born dentate granule cells. *eLife* [online]. 22 November 2017. Vol. 6. DOI 10.7554/elife.26517. Available from: <https://elifesciences.org/articles/26517>

BENUSKOVA, Lubica and ABRAHAM, Wickliffe C, 2007. STDP rule endowed with the BCM sliding threshold accounts for hippocampal heterosynaptic plasticity. *Journal of Computational Neuroscience* [online]. 2007. Vol. 22, no. 2, p. 129–133. DOI 10.1007/s10827-006-0002-x. Available from: <https://doi.org/10.1007/s10827-006-0002-x>

BENUSKOVA, Lubica, DIAMOND, Mathew E and EBNER, Ford F, 1994. Dynamic synaptic modification threshold: Computational model of experience-dependent plasticity in adult rat barrel cortex. *Proceedings of the National Academy of Sciences of the United States of America* [online]. 24 May 1994. Vol. 91, no. 11, p. 4791–4795. DOI 10.1073/pnas.91.11.4791. Available from: <https://pubmed.ncbi.nlm.nih.gov/8197136>

BENUSKOVA, Lubica and JEDLICKA, Peter, 2012. Computational modeling of long-term depression of synaptic weights: Insights from stdp, metaplasticity and spontaneous activity. *Neural Network World*. 2012. Vol. 22, no. 2, p. 161–180. DOI 10.14311/NNW.2012.22.010.

BENUSKOVA, Lubica, REMA, Velayudhan, ARMSTRONG-JAMES, Michael and EBNER, Ford F, 2001. Theory for normal and impaired experience-dependent plasticity in neocortex of adult rats. *Proceedings of the National Academy of Sciences* [online]. 27 February 2001. Vol. 98, no. 5, p. 2797 LP – 2802. DOI 10.1073/pnas.051346398. Available from: <http://www.pnas.org/content/98/5/2797.abstract>

BI, Guo-qiang and POO, Mu-ming, 2001. Synaptic Modification by Correlated Activity: Hebb's Postulate Revisited. *Annual Review of Neuroscience* [online]. 1 March 2001. Vol. 24, no. 1, p. 139–166. DOI 10.1146/annurev.neuro.24.1.139. Available from: <https://doi.org/10.1146/annurev.neuro.24.1.139>

BIANCHI, Daniela, MARASCO, Addolorata, LIMONGIELLO, Alessandro, MARCHETTI, Cristina, MARIE, Helene, TIROZZI, Brunello and MIGLIORE, M, 2012. On the mechanisms underlying the depolarization block in the spiking dynamics of CA1 pyramidal neurons. *Journal of Computational Neuroscience*. October 2012. Vol. 33, no. 2, p. 207–225. DOI 10.1007/s10827-012-0383-y.

BIENENSTOCK, E L, COOPER, L N and MUNRO, P W, 1982. Theory for the development of neuron selectivity: Orientation specificity and binocular interaction in visual cortex. *Journal of Neuroscience* [online]. January 1982. Vol. 2, no. 1, p. 32–48. DOI 10.1523/jneurosci.02-01-00032.1982. Available from: <https://pubmed.ncbi.nlm.nih.gov/7054394>

BILLEH, Yazan N, CAI, Binghuang, GRATIY, Sergey L, DAI, Kael, IYER, Ramakrishnan, GOUWENS, Nathan W, ABBASI-ASL, Reza, JIA, Xiaoxuan, SIEGLE, Joshua H, OLSEN, Shawn R, KOCH, Christof, MIHALAS, Stefan and ARKHIPOV, Anton, 2020. Systematic Integration of Structural and Functional Data into Multi-scale Models of Mouse Primary Visual Cortex. *Neuron* [online]. 6 May 2020. Vol. 106, no. 3, p. 388- 403.e18. [Accessed 4 November 2020]. DOI 10.1016/j.neuron.2020.01.040. Available from: <http://www.ncbi.nlm.nih.gov/pubmed/32142648>

BLISS, T V P and LØMO, T, 1973. Long-lasting potentiation of synaptic transmission in the dentate area of the anaesthetized rabbit following stimulation of the perforant path. *The Journal of Physiology* [online]. 1 July 1973. Vol. 232, no. 2, p. 331–356. DOI <https://doi.org/10.1113/jphysiol.1973.sp010273>. Available from: <https://doi.org/10.1113/jphysiol.1973.sp010273>

BLOSS, Erik B., CEMBROWSKI, Mark S, KARSH, Bill, COLONELL, Jennifer, FETTER, Richard D. and SPRUSTON, Nelson, 2016. Structured Dendritic Inhibition Supports Branch-Selective Integration in CA1 Pyramidal Cells. *Neuron* [online]. 2016. Vol. 89, no. 5, p. 1016–1030. DOI <https://doi.org/10.1016/j.neuron.2016.01.029>. Available from: <https://www.sciencedirect.com/science/article/pii/S0896627316000544>

BREM, Anna-Katharine, RAN, Kathy and PASCUAL-LEONE, Alvaro, 2013. Learning and memory. *Handbook of clinical neurology* [online]. 2013. Vol. 116, p. 693–737. DOI 10.1016/B978-0-444-53497-2.00055-3. Available from: <https://pubmed.ncbi.nlm.nih.gov/24112934>

BRITTON, Oliver J., BUENO-OROVIO, Alfonso, VAN AMMEL, Karel, LU, Hua Rong, TOWART, Rob, GALLACHER, David J. and RODRIGUEZ, Blanca, 2013. Experimentally calibrated population of models predicts and explains intersubject variability in cardiac cellular electrophysiology. *Proceedings of the National Academy of Sciences of the United States of America* [online]. 4 June 2013. Vol. 110, no. 23, p. E2098–E2105. [Accessed 22 June 2020]. DOI 10.1073/pnas.1304382110. Available from: <https://www.pnas.org/content/110/23/E2098>

BRZOSKO, Zuzanna, MIERAU, Susanna B and PAULSEN, Ole, 2019. Neuromodulation of Spike-Timing-Dependent Plasticity: Past, Present, and Future. *Neuron* [online]. 21 August 2019. Vol. 103, no. 4, p. 563–581. DOI 10.1016/j.neuron.2019.05.041. Available from: <https://doi.org/10.1016/j.neuron.2019.05.041>

BUZSÁKI, György, 2002. *Theta oscillations in the hippocampus* [online]. 31 January 2002. Elsevier. Available from: [https://doi.org/10.1016/S0896-6273\(02\)00586-X](https://doi.org/10.1016/S0896-6273(02)00586-X)

BUZSÁKI, György and MIZUSEKI, Kenji, 2014. *The log-dynamic brain: How skewed distributions affect network operations* [online]. 2014. Available from: <https://doi.org/10.1038/nrn3687>

CAI, Xiang, LIANG, Conrad W, MURALIDHARAN, Sukuman, KAO, Joseph P Y, TANG, Cha-Min and THOMPSON, Scott M, 2004. Unique Roles of SK and Kv4.2 Potassium Channels in Dendritic Integration. *Neuron* [online]. 14 October 2004. Vol. 44, no. 2, p. 351–364. DOI 10.1016/j.neuron.2004.09.026. Available from: <https://doi.org/10.1016/j.neuron.2004.09.026>

CAPORALE, Natalia and DAN, Yang, 2008. Spike Timing–Dependent Plasticity: A Hebbian Learning Rule. *Annual Review of Neuroscience* [online]. 17 June 2008. Vol. 31, no. 1, p. 25–46. DOI 10.1146/annurev.neuro.31.060407.125639. Available from: <https://doi.org/10.1146/annurev.neuro.31.060407.125639>

CHATER, Thomas E and GODA, Yukiko, 2014. The role of AMPA receptors in postsynaptic mechanisms of synaptic plasticity. *Frontiers in cellular neuroscience* [online]. 27 November 2014. Vol. 8, p. 401. DOI 10.3389/fncel.2014.00401. Available from: <https://pubmed.ncbi.nlm.nih.gov/25505875>

CHATER, Thomas E and GODA, Yukiko, 2021. My Neighbour Hetero — deconstructing the mechanisms underlying heterosynaptic plasticity. *Current Opinion in Neurobiology* [online]. 2021. Vol. 67, p. 106–114. DOI 10.1016/j.conb.2020.10.007. Available from: <https://doi.org/10.1016/j.conb.2020.10.007>

Chemical synapse, 2015. [online]. [Accessed 14 May 2021]. Available from: https://commons.wikimedia.org/wiki/File:SynapseSchematic_en.svg

CHEN, Chien-Chang, SHEN, Jhe-Wei, CHUNG, Ni-Chun, MIN, Ming-Yuan, CHENG, Sin-Jong and LIU, Ingrid Y, 2012. Retrieval of Context-Associated Memory is Dependent on the Cav3.2 T-Type Calcium Channel. *PLOS ONE* [online]. 3 January 2012. Vol. 7, no. 1, p. e29384. Available from: <https://doi.org/10.1371/journal.pone.0029384>

CHEN, Huanwen, XIE, Lijuan, WANG, Yijun and ZHANG, Hang, 2020. Memory retention in pyramidal neurons: a unified model of energy-based homo and heterosynaptic plasticity with homeostasis. *Cognitive Neurodynamics*. 2020. DOI 10.1007/s11571-020-09652-z.

CHEN, Shmuel, BENNINGER, Felix and YAARI, Yoel, 2014. Role of Small Conductance Ca²⁺-Activated K⁺ Channels in Controlling CA1 Pyramidal Cell Excitability. *The Journal of Neuroscience* [online]. 11 June 2014. Vol. 34, no. 24, p. 8219 LP – 8230. DOI 10.1523/JNEUROSCI.0936-14.2014. Available from: <http://www.jneurosci.org/content/34/24/8219.abstract>

CHEN, Xixi and JOHNSTON, Daniel, 2004. Properties of single voltage-dependent K⁺

channels in dendrites of CA1 pyramidal neurones of rat hippocampus. *The Journal of physiology* [online]. 2004/06/24. 15 August 2004. Vol. 559, no. Pt 1, p. 187–203. DOI 10.1113/jphysiol.2004.068114. Available from: <https://pubmed.ncbi.nlm.nih.gov/15218076>

CHEVALEYRE, Vivien and CASTILLO, Pablo E., 2004. Endocannabinoid-mediated metaplasticity in the hippocampus. *Neuron*. 2004. Vol. 43, no. 6, p. 871–881. DOI 10.1016/j.neuron.2004.08.036.

CHISTIAKOVA, Marina, BANNON, Nicholas M, BAZHENOV, Maxim and VOLGUSHEV, Maxim, 2014. Heterosynaptic plasticity: multiple mechanisms and multiple roles. *The Neuroscientist: a review journal bringing neurobiology, neurology and psychiatry* [online]. 2014/04/11. October 2014. Vol. 20, no. 5, p. 483–498. DOI 10.1177/1073858414529829. Available from: <https://pubmed.ncbi.nlm.nih.gov/24727248>

CHISTIAKOVA, Marina, BANNON, Nicholas M, CHEN, Jen-Yung, BAZHENOV, Maxim and VOLGUSHEV, Maxim, 2015. *Homeostatic role of heterosynaptic plasticity: models and experiments* [online]. 2015. ISBN 1662-5188. Available from: <https://www.frontiersin.org/article/10.3389/fncom.2015.00089>

CHOWDHURY, Dhrubajyoti and HELL, Johannes W, 2018. Homeostatic synaptic scaling: molecular regulators of synaptic AMPA-type glutamate receptors. *F1000Research* [online]. 28 February 2018. Vol. 7, p. 234. DOI 10.12688/f1000research.13561.1. Available from: <https://pubmed.ncbi.nlm.nih.gov/29560257>

CHUA, John J E, KINDLER, Stefan, BOYKEN, Janina and JAHN, Reinhard, 2010. The architecture of an excitatory synapse. *Journal of Cell Science* [online]. 15 March 2010. Vol. 123, no. 6, p. 819 LP – 823. DOI 10.1242/jcs.052696. Available from: <http://jcs.biologists.org/content/123/6/819.abstract>

CITRI, Ami and MALENKA, Robert C, 2008. Synaptic Plasticity: Multiple Forms, Functions, and Mechanisms. *Neuropsychopharmacology* [online]. 2008. Vol. 33, no. 1, p. 18–41. DOI 10.1038/sj.npp.1301559. Available from: <https://doi.org/10.1038/sj.npp.1301559>

COHEN, N J and SQUIRE, L R, 1980. Preserved learning and retention of pattern-analyzing skill in amnesia: dissociation of knowing how and knowing that. *Science* [online]. 10 October 1980. Vol. 210, no. 4466, p. 207 LP – 210. DOI 10.1126/science.7414331. Available from: <http://science.sciencemag.org/content/210/4466/207.abstract>

COLBERT, C M and JOHNSTON, Daniel, 1996. Axonal Action-Potential Initiation and Na⁺ Channel Densities in the Soma and Axon Initial Segment of Subiculum Pyramidal Neurons. *The Journal of Neuroscience* [online]. 1 November 1996. Vol. 16, no. 21, p. 6676 LP – 6686. DOI 10.1523/JNEUROSCI.16-21-06676.1996. Available from: <http://www.jneurosci.org/content/16/21/6676.abstract>

COLBERT, C M and LEVY, W B, 1993. Long-term potentiation of perforant path synapses in hippocampal CA1 in vitro. *Brain Research* [online]. 1993. Vol. 606, no. 1, p. 87–91. DOI [https://doi.org/10.1016/0006-8993\(93\)91573-B](https://doi.org/10.1016/0006-8993(93)91573-B). Available from: <https://www.sciencedirect.com/science/article/pii/000689939391573B>

COLBERT, C M, MAGEE, J C, HOFFMAN, D A and JOHNSTON, Daniel, 1997. Slow Recovery from Inactivation of Na⁺ Channels Underlies the Activity-Dependent Attenuation of Dendritic Action Potentials in Hippocampal CA1 Pyramidal Neurons. *The Journal of Neuroscience* [online]. 1 September 1997. Vol. 17, no. 17, p. 6512 LP – 6521. DOI 10.1523/JNEUROSCI.17-17-06512.1997. Available from: <http://www.jneurosci.org/content/17/17/6512.abstract>

COON, D and MITTERER, J O, 2008. *Introduction to Psychology: Gateways to Mind and Behavior* [online]. Cengage Learning. Available Titles CengageNOW Series. ISBN 9780495599111. Available from: <https://books.google.sk/books?id=vw20LEaJe10C>

COOPER, L N and BEAR, M F, 2012. The BCM theory of synapse modification at 30: interaction of theory with experiment. *Nature Reviews Neuroscience* [online]. 2012. Vol. 13, no. 11, p. 798–810. DOI 10.1038/nrn3353. Available from: <https://doi.org/10.1038/nrn3353>

CRANK, J and NICOLSON, P, 1947. A practical method for numerical evaluation of solutions of partial differential equations of the heat-conduction type. *Mathematical Proceedings of the Cambridge Philosophical Society* [online]. 2008/10/24. 1947. Vol. 43, no. 1, p. 50–67. DOI DOI: 10.1017/S0305004100023197. Available from: <https://www.cambridge.org/core/article/practical-method-for-numerical-evaluation-of-solutions-of-partial-differential-equations-of-the-heatconduction-type/B3230893A53384D418228AB39D41A451>

CRILL, W E, 1996. Persistent Sodium Current in Mammalian Central Neurons. *Annual Review of Physiology* [online]. 1 October 1996. Vol. 58, no. 1, p. 349–362. DOI 10.1146/annurev.ph.58.030196.002025. Available from: <https://doi.org/10.1146/annurev.ph.58.030196.002025>

CUI, Yihui, PROKIN, Ilya, MENDES, Alexandre, BERRY, Hugues and VENANCE, Laurent, 2018. Robustness of STDP to spike timing jitter. *Scientific reports* [online]. 25 May 2018. Vol. 8, no. 1, p. 8139. DOI 10.1038/s41598-018-26436-y. Available from: <https://pubmed.ncbi.nlm.nih.gov/29802357>

CUTSURIDIS, Vassilis, COBB, Stuart and GRAHAM, Bruce P, 2010. Encoding and retrieval in a model of the hippocampal CA1 microcircuit. *Hippocampus* [online]. 1 March 2010. Vol. 20, no. 3, p. 423–446. DOI 10.1002/hipo.20661. Available from: <https://doi.org/10.1002/hipo.20661>

CUTSURIDIS, Vassilis, GRAHAM, Bruce P, COBB, S and VIDA, Imre, 2010. *Hippocampal Microcircuits: A Computational Modeler's Resource Book* [online]. Springer New York.

Springer Series in Computational Neuroscience. ISBN 9781441909961. Available from: https://books.google.sk/books?id=cmT6_LxO69wC

CUTSURIDIS, Vassilis and POIRAZI, Panayiota, 2015. A computational study on how theta modulated inhibition can account for the long temporal windows in the entorhinal-hippocampal loop. *Neurobiology of Learning and Memory* [online]. 2015. Vol. 120, p. 69–83. DOI 10.1016/j.nlm.2015.02.002. Available from: <http://www.sciencedirect.com/science/article/pii/S1074742715000234>

DE LERA RUIZ, Manuel and KRAUS, Richard L, 2015. Voltage-Gated Sodium Channels: Structure, Function, Pharmacology, and Clinical Indications. *Journal of Medicinal Chemistry* [online]. 24 September 2015. Vol. 58, no. 18, p. 7093–7118. DOI 10.1021/jm501981g. Available from: <https://doi.org/10.1021/jm501981g>

Dendritic spike, 2013. [online]. [Accessed 14 May 2021]. Available from: https://commons.wikimedia.org/wiki/File:Dendritic_spike.png

DERKACH, Victor A, OH, Michael C, GUIRE, Eric S and SODERLING, Thomas R, 2007. Regulatory mechanisms of AMPA receptors in synaptic plasticity. *Nature Reviews Neuroscience* [online]. 2007. Vol. 8, no. 2, p. 101–113. DOI 10.1038/nrn2055. Available from: <https://doi.org/10.1038/nrn2055>

DESHMUKH, Sachin S, YOGANARASIMHA, D, VOICU, Horatiu and KNIERIM, James J, 2010. Theta modulation in the medial and the lateral entorhinal cortices. *Journal of Neurophysiology* [online]. 2010/05/26. August 2010. Vol. 104, no. 2, p. 994–1006. DOI 10.1152/jn.01141.2009. Available from: <https://pubmed.ncbi.nlm.nih.gov/20505130>

DESTEXHE, Alain, CONTRERAS, D, SEJNOWSKI, T J and STERIADE, M, 1994. A model of spindle rhythmicity in the isolated thalamic reticular nucleus. *Journal of Neurophysiology* [online]. 1 August 1994. Vol. 72, no. 2, p. 803–818. DOI 10.1152/jn.1994.72.2.803. Available from: <https://doi.org/10.1152/jn.1994.72.2.803>

DINGLEDINE, Raymond, BORGES, Karin, BOWIE, Derek and TRAYNELIS, Stephen F, 1999. The Glutamate Receptor Ion Channels. *Pharmacological Reviews* [online]. 1 March 1999. Vol. 51, no. 1, p. 7 LP – 62. Available from: <http://pharmrev.aspetjournals.org/content/51/1/7.abstract>

DONG, Zhi Fang, HAN, Hui Li, CAO, Jun, ZHANG, Xia and XU, Lin, 2008. Coincident activity of converging pathways enables simultaneous long-term potentiation and long-term depression in hippocampal CA1 network In Vivo. *PLoS ONE*. 6 August 2008. Vol. 3, no. 8. DOI 10.1371/journal.pone.0002848.

DRUCKMANN, Shaul, BANITT, Yoav, GIDON, Albert, SCHÜRMANN, Felix, MARKRAM, Henry and SEGEV, Idan, 2007. A Novel Multiple Objective Optimization Framework for Constraining Conductance-Based Neuron Models by Experimental Data.

Frontiers in Neuroscience [online]. 15 October 2007. Vol. 1, no. 1, p. 7–18.
DOI 10.3389/neuro.01.1.1.001.2007. Available from:
<https://pubmed.ncbi.nlm.nih.gov/18982116>

DUDEK, Serena M and BEAR, M F, 1992. Homosynaptic long-term depression in area CA1 of hippocampus and effects of N-methyl-D-aspartate receptor blockade. *Proceedings of the National Academy of Sciences of the United States of America*. 1992. Vol. 89, no. 10, p. 4363–4367. DOI 10.1073/pnas.89.10.4363.

EBNER, Christian, CLOPATH, Claudia, JEDLICKA, Peter and CUNTZ, Hermann, 2019. Unifying Long-Term Plasticity Rules for Excitatory Synapses by Modeling Dendrites of Cortical Pyramidal Neurons. *Cell Reports*. 24 December 2019. Vol. 29, no. 13, p. 4295–4307.e6. DOI 10.1016/j.celrep.2019.11.068.

EINEVOLL, Garte T, DESTEXHE, Alain, DIESMANN, Markus, GRÜN, Sonja, JIRSA, Viktor, DE KAMPS, Marc, MIGLIORE, M, NESS, Torbjørn V, PLESSER, Hans E and SCHÜRMANN, Felix, 2019. *The Scientific Case for Brain Simulations* [online]. 22 May 2019. Elsevier. [Accessed 4 November 2020]. Available from: <http://www.ncbi.nlm.nih.gov/pubmed/31121126>

ETHERINGTON, Sarah J, ATKINSON, Susan E, STUART, Greg J and WILLIAMS, Stephen R, 2010. *Synaptic Integration* [online]. 19 May 2010. Major Reference Works. ISBN 9780470015902. Available from: <https://doi.org/10.1002/9780470015902.a0000208.pub2>

FABER, E S Louise and SAH, Pankaj, 2003. Calcium-Activated Potassium Channels: Multiple Contributions to Neuronal Function. *The Neuroscientist* [online]. 1 June 2003. Vol. 9, no. 3, p. 181–194. DOI 10.1177/1073858403009003011. Available from: <https://doi.org/10.1177/1073858403009003011>

FICKER, E and HEINEMANN, U, 1992. Slow and fast transient potassium currents in cultured rat hippocampal cells. *The Journal of physiology* [online]. January 1992. Vol. 445, p. 431–455. DOI 10.1113/jphysiol.1992.sp018932. Available from: <https://pubmed.ncbi.nlm.nih.gov/1501141>

FREIR, Darragh B and HERRON, Caroline E, 2003. Inhibition of L-type voltage dependent calcium channels causes impairment of long-term potentiation in the hippocampal CA1 region in vivo. *Brain Research* [online]. 2003. Vol. 967, no. 1, p. 27–36. DOI [https://doi.org/10.1016/S0006-8993\(02\)04190-2](https://doi.org/10.1016/S0006-8993(02)04190-2). Available from: <https://www.sciencedirect.com/science/article/pii/S0006899302041902>

FRICK, Andreas, MAGEE, J C, KOESTER, Helmut J, MIGLIORE, M and JOHNSTON, Daniel, 2003. Normalization of Ca²⁺ Signals by Small Oblique Dendrites of CA1 Pyramidal Neurons. *The Journal of Neuroscience* [online]. 15 April 2003. Vol. 23, no. 8, p. 3243 LP – 3250. DOI 10.1523/JNEUROSCI.23-08-03243.2003. Available from:

<http://www.jneurosci.org/content/23/8/3243.abstract>

FRICKER, Desdemona, VERHEUGEN, Jos A.H. and MILES, Richard, 1999. Cell-attached measurements of the firing threshold of rat hippocampal neurones. *Journal of Physiology* [online]. 15 June 1999. Vol. 517, no. 3, p. 791–804. DOI 10.1111/j.1469-7793.1999.0791s.x. Available from: <https://pubmed.ncbi.nlm.nih.gov/10358119>

GASPARINI, Sonia and MAGEE, J C, 2006. State-dependent dendritic computation in hippocampal CA1 pyramidal neurons. *Journal of Neuroscience*. 15 February 2006. Vol. 26, no. 7, p. 2088–2100. DOI 10.1523/JNEUROSCI.4428-05.2006.

GASPARINI, Sonia, MIGLIORE, M and MAGEE, J C, 2004. On the initiation and propagation of dendritic spikes in CA1 pyramidal neurons. *Journal of Neuroscience* [online]. 8 December 2004. Vol. 24, no. 49, p. 11046–11056. DOI 10.1523/JNEUROSCI.2520-04.2004. Available from: <http://www.jneurosci.org/content/24/49/11046.abstract>

GEIT, Werner Van, MOOR, Ruben, RANJAN, Rajnish, RIQUELME, Luis and ROESSERT, Christian, 2016. BlueBrain/eFEL. [online]. 2016. [Accessed 22 June 2020]. Available from: <https://github.com/BlueBrain/eFEL>

GENTET, Luc J, STUART, Greg J and CLEMENTS, John D, 2000. Direct Measurement of Specific Membrane Capacitance in Neurons. *Biophysical Journal* [online]. 2000. Vol. 79, no. 1, p. 314–320. DOI [https://doi.org/10.1016/S0006-3495\(00\)76293-X](https://doi.org/10.1016/S0006-3495(00)76293-X). Available from: <https://www.sciencedirect.com/science/article/pii/S000634950076293X>

GERKIN, Richard C, BIRGIOLAS, Justas, JARVIS, Russell J, OMAR, Cyrus and CROOK, Sharon M, 2019. *NeuronUnit: A package for data-driven validation of neuron models using SciUnit* [online]. 1 January 2019. Available from: <http://biorxiv.org/content/early/2019/06/09/665331.abstract>

GIDON, Albert, ZOLNIK, Timothy Adam, FIDZINSKI, Pawel, BOLDUAN, Felix, PAPOUTSI, Athanasia, POIRAZI, Panayiota, HOLT Kamp, Martin, VIDA, Imre and LARKUM, Matthew Evan, 2020. Dendritic action potentials and computation in human layer 2/3 cortical neurons. *Science* [online]. 3 January 2020. Vol. 367, no. 6473, p. 83 LP – 87. DOI 10.1126/science.aax6239. Available from: <http://science.sciencemag.org/content/367/6473/83.abstract>

GOAILLARD, Jean Marc, TAYLOR, Adam L, SCHULZ, David J and MAR DER, Eve, 2009. Functional consequences of animal-to-animal variation in circuit parameters. *Nature Neuroscience* [online]. 2009. Vol. 12, no. 11, p. 1424–1430. DOI 10.1038/nn.2404. Available from: <https://doi.org/10.1038/nn.2404>

GOLDING, N L, JUNG, H Y, MICKUS, T and SPRUSTON, Nelson, 1999. Dendritic calcium spike initiation and repolarization are controlled by distinct potassium channel subtypes in CA1 pyramidal neurons. *The Journal of neuroscience : the official journal of the Society for*

Neuroscience [online]. 15 October 1999. Vol. 19, no. 20, p. 8789–8798.
DOI 10.1523/JNEUROSCI.19-20-08789.1999. Available from:
<https://pubmed.ncbi.nlm.nih.gov/10516298>

GOLDING, N L, KATH, William L and SPRUSTON, Nelson, 2001. Dichotomy of action-potential backpropagation in CA1 pyramidal neuron dendrites. *Journal of Neurophysiology* [online]. 1 December 2001. Vol. 86, no. 6, p. 2998–3010. DOI 10.1152/jn.2001.86.6.2998. Available from: <https://doi.org/10.1152/jn.2001.86.6.2998>From Duplicate 1 (Dichotomy of action-potential backpropagation in CA1 pyramidal neuron dendrites - Golding, Nace L.; Kath, William L.; Spruston, Nelson)From Duplicate 1 (Dichotomy of action-potential backpropagation in CA1 pyramidal neuron dendrites - Golding, Nace L; Kath, William L; Spruston, Nelson)doi: 10.1152/jn.2001.86.6.2998From Duplicate 2 (Dichotomy of action-potential backpropagation in CA1 pyramidal neuron dendrites - Golding, Nace L; Kath, William L; Spruston, Nelson)doi: 10.1152/jn.2001.86.6.2998

GOLDING, N L, MICKUS, T, KATZ, Yael, KATH, William L and SPRUSTON, Nelson, 2005. Factors mediating powerful voltage attenuation along CA1 pyramidal neuron dendrites. *Journal of Physiology* [online]. 1 October 2005. Vol. 568, no. 1, p. 69–82. DOI 10.1113/jphysiol.2005.086793. Available from: <https://doi.org/10.1113/jphysiol.2005.086793>

GOLDING, N L and SPRUSTON, Nelson, 1998. Dendritic Sodium Spikes Are Variable Triggers of Axonal Action Potentials in Hippocampal CA1 Pyramidal Neurons. *Neuron* [online]. 1 November 1998. Vol. 21, no. 5, p. 1189–1200. DOI 10.1016/S0896-6273(00)80635-2. Available from: [https://doi.org/10.1016/S0896-6273\(00\)80635-2](https://doi.org/10.1016/S0896-6273(00)80635-2)

GOLDING, N L, STAFF, Nathan P and SPRUSTON, Nelson, 2002. Dendritic spikes as a mechanism for cooperative long-term potentiation. *Nature* [online]. 2002. Vol. 418, no. 6895, p. 326–331. DOI 10.1038/nature00854. Available from: <https://doi.org/10.1038/nature00854>

GOLOMB, David, YUE, Cuiyong and YAARI, Yoel, 2006. Contribution of Persistent Na⁺ Current and M-Type K⁺ Current to Somatic Bursting in CA1 Pyramidal Cells: Combined Experimental and Modeling Study. *Journal of Neurophysiology* [online]. 1 October 2006. Vol. 96, no. 4, p. 1912–1926. DOI 10.1152/jn.00205.2006. Available from: <https://doi.org/10.1152/jn.00205.2006>

GU, Ning, VERVAEKE, Koen and STORM, Johan F, 2007. BK potassium channels facilitate high-frequency firing and cause early spike frequency adaptation in rat CA1 hippocampal pyramidal cells. *The Journal of Physiology* [online]. 1 May 2007. Vol. 580, no. 3, p. 859–882. DOI <https://doi.org/10.1113/jphysiol.2006.126367>. Available from: <https://doi.org/10.1113/jphysiol.2006.126367>

GÜNEY, Cengiz, EDGERTON, Jeremy R and JAEGER, Dieter, 2008. Channel density distributions explain spiking variability in the globus pallidus: A combined physiology and computer simulation database approach. *Journal of Neuroscience* [online]. 23 July 2008. Vol. 28, no. 30, p. 7476–7491. DOI 10.1523/JNEUROSCI.4198-07.2008. Available from:

<http://www.jneurosci.org/content/28/30/7476.abstract>

GUTZMANN, Jakob J, LIN, Lin and HOFFMAN, D A, 2019. *Functional Coupling of Cav2.3 and BK Potassium Channels Regulates Action Potential Repolarization and Short-Term Plasticity in the Mouse Hippocampus* [online]. 2019. ISBN 1662-5102. Available from: <https://www.frontiersin.org/article/10.3389/fncel.2019.00027>

HARDINGHAM, Neil, WRIGHT, Nick, DACHTLER, James and FOX, Kevin, 2008. Sensory Deprivation Unmasks a PKA-Dependent Synaptic Plasticity Mechanism that Operates in Parallel with CaMKII. *Neuron* [online]. 2008. Vol. 60, no. 5, p. 861–874. DOI <https://doi.org/10.1016/j.neuron.2008.10.018>. Available from: <https://www.sciencedirect.com/science/article/pii/S089662730800891X>

HARRIS, Charles R., MILLMAN, K. Jarrod, VAN DER WALT, Stéfan J., GOMMERS, Ralf, VIRTANEN, Pauli, COURNAPEAU, David, WIESER, Eric, TAYLOR, Julian, BERG, Sebastian, SMITH, Nathaniel J., KERN, Robert, PICUS, Matti, HOYER, Stephan, VAN KERKWIJK, Marten H., BRETT, Matthew, HALDANE, Allan, DEL RÍO, Jaime Fernández, WIEBE, Mark, PETERSON, Pearu, GÉRARD-MARCHANT, Pierre, SHEPPARD, Kevin, REDDY, Tyler, WECKESSER, Warren, ABBASI, Hameer, GOHLKE, Christoph and OLIPHANT, Travis E., 2020. *Array programming with NumPy*. 17 September 2020. Nature Research.

HÄUSSER, Michael, 2001. *Synaptic function: Dendritic democracy*. 2001.

HEBB, D O, 1949. *The organization of behavior; a neuropsychological theory*. Oxford, England: Wiley.

HERZ, Andreas V.M., GOLLISCH, Tim, MACHENS, Christian K and JAEGER, Dieter, 2006. *Modeling single-neuron dynamics and computations: A balance of detail and abstraction* [online]. 6 October 2006. Available from: <http://science.sciencemag.org/content/314/5796/80.abstract>

HH circuit, 2011. [online]. [Accessed 19 May 2021]. Available from: <https://commons.wikimedia.org/wiki/File:MembraneCircuit.svg>

HILLE, Bertil, 2001. *Ion Channels of Excitable Membranes*. 3rd editio. Sunderland: Sinauer Associates.

HINES, M L and CARNEVALE, N T, 1997. *The NEURON Simulation Environment* [online]. 1 August 1997. MIT Press. Available from: <https://doi.org/10.1162/neco.1997.9.6.1179>

HINES, M L and CARNEVALE, N T, 2000. Expanding NEURON's Repertoire of Mechanisms with NMODL. *Neural Computation* [online]. 1 May 2000. Vol. 12, no. 5, p. 995–1007. DOI [10.1162/089976600300015475](https://doi.org/10.1162/089976600300015475). Available from:

<https://doi.org/10.1162/089976600300015475>

HINES, M L, DAVISON, Andrew and MULLER, Eilif, 2009. *NEURON and Python* [online]. 2009. ISBN 1662-5196. Available from: <https://www.frontiersin.org/article/10.3389/neuro.11.001.2009>

HINES, M L, MARKRAM, Henry and SCHÜRMANN, Felix, 2008. Fully implicit parallel simulation of single neurons. *Journal of Computational Neuroscience*. 2008. Vol. 25, no. 3, p. 439–448. DOI 10.1007/s10827-008-0087-5.

Hippocampal formation, 2008. [online]. [Accessed 14 May 2021]. Available from: [https://commons.wikimedia.org/wiki/File:CajalHippocampus_\(modified\).png](https://commons.wikimedia.org/wiki/File:CajalHippocampus_(modified).png)

HIRATANI, Naoki and FUKAI, Tomoki, 2017. Detailed dendritic excitatory/inhibitory balance through heterosynaptic spike-timing-dependent plasticity. *Journal of Neuroscience*. 13 December 2017. Vol. 37, no. 50, p. 12106–12122. DOI 10.1523/JNEUROSCI.0027-17.2017.

HODGKIN, A L and HUXLEY, A F, 1952. A quantitative description of membrane current and its application to conduction and excitation in nerve. *The Journal of physiology* [online]. August 1952. Vol. 117, no. 4, p. 500–544. DOI 10.1113/jphysiol.1952.sp004764. Available from: <https://pubmed.ncbi.nlm.nih.gov/12991237>

HOFFMAN, D A, MAGEE, J C, COLBERT, C M and JOHNSTON, Daniel, 1997. K⁺ channel regulation of signal propagation in dendrites of hippocampal pyramidal neurons. *Nature* [online]. 1997. Vol. 387, no. 6636, p. 869–875. DOI 10.1038/43119. Available from: <https://doi.org/10.1038/43119>

HSU, Ching Lung, ZHAO, Xinyu, MILSTEIN, Aaron D. and SPRUSTON, Nelson, 2018. Persistent Sodium Current Mediates the Steep Voltage Dependence of Spatial Coding in Hippocampal Pyramidal Neurons. *Neuron* [online]. 11 July 2018. Vol. 99, no. 1, p. 147-162.e8. DOI 10.1016/j.neuron.2018.05.025. Available from: <https://doi.org/10.1016/j.neuron.2018.05.025>From Duplicate 1 (Persistent Sodium Current Mediates the Steep Voltage Dependence of Spatial Coding in Hippocampal Pyramidal Neurons - Hsu, Ching Lung; Zhao, Xinyu; Milstein, Aaron D; Spruston, Nelson)

HU, Wenqin, TIAN, Cuiping, LI, Tun, YANG, Mingpo, HOU, Han and SHU, Yousheng, 2009. Distinct contributions of Nav1.6 and Nav1.2 in action potential initiation and backpropagation. *Nature Neuroscience* [online]. 2009. Vol. 12, no. 8, p. 996–1002. DOI 10.1038/nn.2359. Available from: <https://doi.org/10.1038/nn.2359>

HUANG, ShiYong, TREVIÑO, Mario, HE, Kaiwen, ARDILES, Alvaro, PASQUALE, Roberto de, GUO, Yatu, PALACIOS, Adrian, HUGANIR, Richard and KIRKWOOD, Alfredo, 2012. Pull-push neuromodulation of LTP and LTD enables bidirectional experience-induced synaptic scaling in visual cortex. *Neuron* [online]. 9 February 2012. Vol. 73, no. 3, p. 497–510. DOI 10.1016/j.neuron.2011.11.023. Available from:

<https://pubmed.ncbi.nlm.nih.gov/22325202>

HULME, Sarah R, JONES, Owen D, IRELAND, David R and ABRAHAM, Wickliffe C, 2012. Calcium-dependent but action potential-independent BCM-like metaplasticity in the hippocampus. *The Journal of neuroscience : the official journal of the Society for Neuroscience* [online]. 16 May 2012. Vol. 32, no. 20, p. 6785–6794. DOI 10.1523/JNEUROSCI.0634-12.2012. Available from: <https://pubmed.ncbi.nlm.nih.gov/22593048>

HULME, Sarah R, JONES, Owen D, RAYMOND, Clarke R, SAH, Pankaj and ABRAHAM, Wickliffe C, 2013. Mechanisms of heterosynaptic metaplasticity. *Philosophical transactions of the Royal Society of London. Series B, Biological sciences* [online]. 2 December 2013. Vol. 369, no. 1633, p. 20130148. DOI 10.1098/rstb.2013.0148. Available from: <https://pubmed.ncbi.nlm.nih.gov/24298150>

HUNTER, John D., 2007. Matplotlib: A 2D graphics environment. *Computing in Science and Engineering*. 2007. Vol. 9, no. 3, p. 90–95. DOI 10.1109/MCSE.2007.55.

IAVARONE, Elisabetta, YI, Jane, SHI, Ying, ZANDT, Bas Jan, O'REILLY, Christian, VAN GEIT, Werner, ROESSERT, Christian, MARKRAM, Henry and HILL, Sean L, 2019. Experimentally-constrained biophysical models of tonic and burst firing modes in thalamocortical neurons. *PLoS Computational Biology* [online]. 16 May 2019. Vol. 15, no. 5, p. e1006753–e1006753. DOI 10.1371/journal.pcbi.1006753. Available from: <https://pubmed.ncbi.nlm.nih.gov/31095552>

Inactivation diagram, 2015. [online]. [Accessed 14 May 2021]. Available from: https://en.wikipedia.org/wiki/File:Inactivation_diagram.jpg

IZHIKEVICH, Eugene M and DESAI, Niraj S, 2003. Relating STDP to BCM. *Neural Computation* [online]. 1 July 2003. Vol. 15, no. 7, p. 1511–1523. DOI 10.1162/089976603321891783. Available from: <https://doi.org/10.1162/089976603321891783>

JAHR, Craig E and STEVENS, Charles F, 1990. Voltage dependence of NMDA-activated macroscopic conductances predicted by single-channel kinetics. *Journal of Neuroscience* [online]. 1 September 1990. Vol. 10, no. 9, p. 3178–3182. DOI 10.1523/jneurosci.10-09-03178.1990. Available from: <http://www.jneurosci.org/content/10/9/3178.abstract>

JARSKY, Tim, ROXIN, Alex, KATH, William L and SPRUSTON, Nelson, 2005. Conditional dendritic spike propagation following distal synaptic activation of hippocampal CA1 pyramidal neurons. *Nature Neuroscience* [online]. 2005. Vol. 8, no. 12, p. 1667–1676. DOI 10.1038/nn1599. Available from: <https://doi.org/10.1038/nn1599>

JEDLICKA, Peter, 2002. Synaptic plasticity, metaplasticity and BCM theory. *Bratislavské lekárske listy*. 2002. Vol. 103, no. 4–5, p. 137–143.

JEDLICKA, Peter, BENUSKOVA, Lubica and ABRAHAM, Wickliffe C, 2015. A Voltage-Based STDP Rule Combined with Fast BCM-Like Metaplasticity Accounts for LTP and Concurrent “Heterosynaptic” LTD in the Dentate Gyrus In Vivo. *PLoS Computational Biology* [online]. 6 November 2015. Vol. 11, no. 11, p. e1004588–e1004588. DOI 10.1371/journal.pcbi.1004588. Available from: <https://pubmed.ncbi.nlm.nih.gov/26544038>

JOHNSTON, Daniel, HOFFMAN, D A, MAGEE, J C, POOLOS, N P, WATANABE, S, COLBERT, C M and MIGLIORE, M, 2000. Dendritic potassium channels in hippocampal pyramidal neurons. *The Journal of physiology* [online]. 15 May 2000. Vol. 525 Pt 1, no. Pt 1, p. 75–81. DOI 10.1111/j.1469-7793.2000.00075.x. Available from: <https://pubmed.ncbi.nlm.nih.gov/10811726>

JONES, Scott L, TO, Minh-Son and STUART, Greg J, 2017. Dendritic small conductance calcium-activated potassium channels activated by action potentials suppress EPSPs and gate spike-timing dependent synaptic plasticity. BARTOS, Marlene (ed.), *eLife* [online]. 2017. Vol. 6, p. e30333. DOI 10.7554/eLife.30333. Available from: <https://doi.org/10.7554/eLife.30333>

JUNG, H Y, MICKUS, T and SPRUSTON, Nelson, 1997. Prolonged Sodium Channel Inactivation Contributes to Dendritic Action Potential Attenuation in Hippocampal Pyramidal Neurons. *The Journal of Neuroscience* [online]. 1 September 1997. Vol. 17, no. 17, p. 6639 LP – 6646. DOI 10.1523/JNEUROSCI.17-17-06639.1997. Available from: <http://www.jneurosci.org/content/17/17/6639.abstract>

KANG, Young-Jin, CLEMENT, Ethan M, SUMSKY, Stefan L, XIANG, Yangfei, PARK, In-Hyun, SANTANELLO, Sabato, GREENFIELD, Lazar John, GARCIA-RILL, Edgar, SMITH, Bret N and LEE, Sang-Hun, 2020. The critical role of persistent sodium current in hippocampal gamma oscillations. *Neuropharmacology* [online]. 2020. Vol. 162, p. 107787. DOI <https://doi.org/10.1016/j.neuropharm.2019.107787>. Available from: <https://www.sciencedirect.com/science/article/pii/S0028390819303454>

CASTELLAKIS, George and POIRAZI, Panayiota, 2019. *Synaptic Clustering and Memory Formation*. 6 December 2019. Frontiers Media S.A.

KATONA, István, SPERLÁGH, Beáta, SÍK, Attila, KÄFALVI, Attila, VIZI, E. Sylvester, MACKIE, Ken and FREUND, T. F., 1999. Presynaptically located CB1 cannabinoid receptors regulate GABA release from axon terminals of specific hippocampal interneurons. *Journal of Neuroscience*. 1999. Vol. 19, no. 11, p. 4544–4558. DOI 10.1523/jneurosci.19-11-04544.1999.

KATZ, Yael, MENON, Vilas, NICHOLSON, Daniel A., GEINISMAN, Yuri, KATH, William L and SPRUSTON, Nelson, 2009. Synapse Distribution Suggests a Two-Stage Model of Dendritic Integration in CA1 Pyramidal Neurons. *Neuron*. 30 July 2009. Vol. 63, no. 2, p. 171–177. DOI 10.1016/j.neuron.2009.06.023.

KERNIGHAN, Brian W and PIKE, Rob, 1983. *The UNIX Programming Environment*. Prentice Hall Professional Technical Reference. ISBN 0139376992.

KIM, Jinyun, WEI, Dong-Sheng and HOFFMAN, D A, 2005. Kv4 potassium channel subunits control action potential repolarization and frequency-dependent broadening in rat hippocampal CA1 pyramidal neurones. *The Journal of Physiology* [online]. 1 November 2005. Vol. 569, no. 1, p. 41–57. DOI <https://doi.org/10.1113/jphysiol.2005.095042>. Available from: <https://doi.org/10.1113/jphysiol.2005.095042>

KIM, Yujin, HSU, Ching Lung, CEMBROWSKI, Mark S, MENSH, Brett D and SPRUSTON, Nelson, 2015. Dendritic sodium spikes are required for long-term potentiation at distal synapses on hippocampal pyramidal neurons. *eLife*. 2015. Vol. 4, no. AUGUST2015. DOI 10.7554/eLife.06414.

KIRKWOOD, Alfredo, RIOULT, Marc G and BEAR, M F, 1996. Experience-dependent modification of synaptic plasticity in visual cortex. *Nature* [online]. 1996. Vol. 381, no. 6582, p. 526–528. DOI 10.1038/381526a0. Available from: <https://doi.org/10.1038/381526a0>

KNAUER, Beate and YOSHIDA, Motoharu, 2019. Switching between persistent firing and depolarization block in individual rat CA1 pyramidal neurons. *Hippocampus* [online]. 1 September 2019. Vol. 29, no. 9, p. 817–835. DOI <https://doi.org/10.1002/hipo.23078>. Available from: <https://doi.org/10.1002/hipo.23078>

KOCH, Christof, 1999. *Biophysics of Computation: Information Processing in Single Neurons*. Oxford: Oxford University Press. ISBN 978-0195181999.

KOLE, Maarten H.P., ILSCHNER, Susanne U., KAMPA, Björn M., WILLIAMS, Stephen R, RUBEN, Peter C. and STUART, Greg J, 2008. Action potential generation requires a high sodium channel density in the axon initial segment. *Nature Neuroscience*. 2008. DOI 10.1038/nn2040.

KSHATRI, Aravind S, GONZALEZ-HERNANDEZ, Alberto and GIRALDEZ, Teresa, 2018. *Physiological Roles and Therapeutic Potential of Ca²⁺ Activated Potassium Channels in the Nervous System* [online]. 2018. ISBN 1662-5099. Available from: <https://www.frontiersin.org/article/10.3389/fnmol.2018.00258>

LACINOVÁ, L, 2005. Voltage-dependent calcium channels. *General physiology and biophysics* [online]. 2005. Vol. 24 Suppl 1, p. 1–78. Available from: <http://europepmc.org/abstract/MED/16096350>

LARSON, John and MUNKÁCSY, Erin, 2015. Theta-burst LTP. *Brain research* [online]. 2014/10/27. 24 September 2015. Vol. 1621, p. 38–50. DOI 10.1016/j.brainres.2014.10.034. Available from: <https://pubmed.ncbi.nlm.nih.gov/25452022>

LE RAY, Didier, FERNÁNDEZ DE SEVILLA, David, BELÉN PORTO, Ana, FUENZALIDA, Marco and BUÑO, Washington, 2004. Heterosynaptic metaplastic regulation of synaptic efficacy in CA1 pyramidal neurons of rat hippocampus. *Hippocampus* [online]. 1 January 2004. Vol. 14, no. 8, p. 1011–1025. DOI <https://doi.org/10.1002/hipo.20021>. Available from: <https://doi.org/10.1002/hipo.20021>

LEE, Hey-Kyoung and KIRKWOOD, Alfredo, 2019. Mechanisms of Homeostatic Synaptic Plasticity in vivo. *Frontiers in cellular neuroscience* [online]. 3 December 2019. Vol. 13, p. 520. DOI 10.3389/fncel.2019.00520. Available from: <https://pubmed.ncbi.nlm.nih.gov/31849610>

LEITCH, B, SZOSTEK, A, LIN, R and SHEVTSOVA, O, 2009. Subcellular distribution of L-type calcium channel subtypes in rat hippocampal neurons. *Neuroscience* [online]. 2009. Vol. 164, no. 2, p. 641–657. DOI <https://doi.org/10.1016/j.neuroscience.2009.08.006>. Available from: <https://www.sciencedirect.com/science/article/pii/S0306452209013001>

LEVY, Aaron D, OMAR, Mitchell H and KOLESKE, Anthony J, 2014. Extracellular matrix control of dendritic spine and synapse structure and plasticity in adulthood. *Frontiers in neuroanatomy* [online]. 20 October 2014. Vol. 8, p. 116. DOI 10.3389/fnana.2014.00116. Available from: <https://pubmed.ncbi.nlm.nih.gov/25368556>

LEVY, W B and STEWARD, O, 1983. Temporal contiguity requirements for long-term associative potentiation/depression in the hippocampus. *Neuroscience* [online]. 1983. Vol. 8, no. 4, p. 791–797. DOI [https://doi.org/10.1016/0306-4522\(83\)90010-6](https://doi.org/10.1016/0306-4522(83)90010-6). Available from: <https://www.sciencedirect.com/science/article/pii/0306452283900106>

LISMAN, John E and SPRUSTON, Nelson, 2005. Postsynaptic depolarization requirements for LTP and LTD: a critique of spike timing-dependent plasticity. *Nature Neuroscience* [online]. 2005. Vol. 8, no. 7, p. 839–841. DOI 10.1038/nn0705-839. Available from: <https://doi.org/10.1038/nn0705-839>

LISS, Birgit, FRANZ, Oliver, SEWING, Sabine, BRUNS, Ralf, NEUHOFF, Henrike and ROEPER, Jochen, 2001. Tuning pacemaker frequency of individual dopaminergic neurons by Kv4.3L and KChip3.1 transcription. *EMBO Journal* [online]. 15 October 2001. Vol. 20, no. 20, p. 5715–5724. DOI 10.1093/emboj/20.20.5715. Available from: <https://doi.org/10.1093/emboj/20.20.5715>

LIU, Pin W and BEAN, Bruce P, 2014. Kv2 Channel Regulation of Action Potential Repolarization and Firing Patterns in Superior Cervical Ganglion Neurons and Hippocampal CA1 Pyramidal Neurons. *The Journal of Neuroscience* [online]. 2 April 2014. Vol. 34, no. 14, p. 4991 LP – 5002. DOI 10.1523/JNEUROSCI.1925-13.2014. Available from: <http://www.jneurosci.org/content/34/14/4991.abstract>

LORINCZ, Andrea and NUSSER, Zoltan, 2010. Molecular Identity of Dendritic Voltage-

Gated Sodium Channels. *Science* [online]. 14 May 2010. Vol. 328, no. 5980, p. 906 LP – 909. DOI 10.1126/science.1187958. Available from: <http://science.sciencemag.org/content/328/5980/906.abstract>

LOSONCZY, Attila and MAGEE, J C, 2006. Integrative Properties of Radial Oblique Dendrites in Hippocampal CA1 Pyramidal Neurons. *Neuron*. 20 April 2006. Vol. 50, no. 2, p. 291–307. DOI 10.1016/j.neuron.2006.03.016.

LÜSCHER, Christian and MALENKA, Robert C, 2012. NMDA receptor-dependent long-term potentiation and long-term depression (LTP/LTD). *Cold Spring Harbor perspectives in biology* [online]. 1 June 2012. Vol. 4, no. 6, p. a005710. DOI 10.1101/cshperspect.a005710. Available from: <https://pubmed.ncbi.nlm.nih.gov/22510460>

MACCAFERRI, G, DAVID, J., ROBERTS, B., SZUCS, Peter, COTTINGHAM, Carol A. and SOMOGYI, Peter, 2000. Cell surface domain specific postsynaptic currents evoked by identified GABAergic neurones in rat hippocampus in vitro. *Journal of Physiology*. 2000. Vol. 524, no. 1, p. 91–116. DOI 10.1111/j.1469-7793.2000.t01-3-00091.x.

MACCAFERRI, G, MANGONI, M, LAZZARI, A and DIFRANCESCO, D, 1993. Properties of the hyperpolarization-activated current in rat hippocampal CA1 pyramidal cells. *Journal of Neurophysiology* [online]. 1 June 1993. Vol. 69, no. 6, p. 2129–2136. DOI 10.1152/jn.1993.69.6.2129. Available from: <https://doi.org/10.1152/jn.1993.69.6.2129>

MAGEE, J C, 1998. Dendritic Hyperpolarization-Activated Currents Modify the Integrative Properties of Hippocampal CA1 Pyramidal Neurons. *The Journal of Neuroscience* [online]. 1 October 1998. Vol. 18, no. 19, p. 7613 LP – 7624. DOI 10.1523/JNEUROSCI.18-19-07613.1998. Available from: <http://www.jneurosci.org/content/18/19/7613.abstract>

MAGEE, J C, AVERY, R B, CHRISTIE, B R and JOHNSTON, Daniel, 1996. Dihydropyridine-sensitive, voltage-gated Ca²⁺ channels contribute to the resting intracellular Ca²⁺ concentration of hippocampal CA1 pyramidal neurons. *Journal of Neurophysiology* [online]. 1 November 1996. Vol. 76, no. 5, p. 3460–3470. DOI 10.1152/jn.1996.76.5.3460. Available from: <https://doi.org/10.1152/jn.1996.76.5.3460>

MAGEE, J C and CARRUTH, Michael, 1999. Dendritic Voltage-Gated Ion Channels Regulate the Action Potential Firing Mode of Hippocampal CA1 Pyramidal Neurons. *Journal of Neurophysiology* [online]. 1 October 1999. Vol. 82, no. 4, p. 1895–1901. DOI 10.1152/jn.1999.82.4.1895. Available from: <https://doi.org/10.1152/jn.1999.82.4.1895>

MAGEE, J C and COOK, Erik P, 2000. Somatic EPSP amplitude is independent of synapse location in hippocampal pyramidal neurons. *Nature Neuroscience* [online]. 2000. Vol. 3, no. 9, p. 895–903. DOI 10.1038/78800. Available from: <https://doi.org/10.1038/78800>

MAGÓ, Ádám, WEBER, Jens P., UJFALUSSY, Balázs B. and MAKARA, Judit K., 2020. Synaptic plasticity depends on the fine-scale input pattern in thin dendrites of CA1 pyramidal

neurons. *Journal of Neuroscience*. 25 March 2020. Vol. 40, no. 13, p. 2593–2605. DOI 10.1523/JNEUROSCI.2071-19.2020.

MÄKI-MARTTUNEN, Tuomo, KAUFMANN, Tobias, ELVSÅSHAGEN, Torbjørn, DEVOR, Anna, DJUROVIC, Srdjan, WESTLYE, Lars T, LINNE, Marja-Leena, RIETSCHEL, Marcella, SCHUBERT, Dirk, BORGWARDT, Stefan, EFRIM-BUDISTEANU, Magdalena, BETTELLA, Francesco, HALNES, Geir, HAGEN, Espen, NÆSS, Solveig, NESS, Torbjørn V, MOBERGET, Torgeir, METZNER, Christoph, EDWARDS, Andrew G, FYHN, Marianne, DALE, Anders M, EINEVOLL, Gaute T and ANDREASSEN, Ole A, 2019. Biophysical Psychiatry—How Computational Neuroscience Can Help to Understand the Complex Mechanisms of Mental Disorders. *Frontiers in Psychiatry* [online]. 2019. Vol. 10, p. 534. DOI 10.3389/fpsyg.2019.00534. Available from: <https://www.frontiersin.org/article/10.3389/fpsyg.2019.00534>

MALENKA, Robert C and NICOLL, Roger A, 1993. NMDA-receptor-dependent synaptic plasticity: multiple forms and mechanisms. *Trends in Neurosciences* [online]. 1993. Vol. 16, no. 12, p. 521–527. DOI [https://doi.org/10.1016/0166-2236\(93\)90197-T](https://doi.org/10.1016/0166-2236(93)90197-T). Available from: <https://www.sciencedirect.com/science/article/pii/016622369390197T>

MARDER, Eve and TAYLOR, Adam L, 2011. Multiple models to capture the variability in biological neurons and networks. In: *Nature Neuroscience* [online]. February 2011. p. 133–138. Available from: <https://pubmed.ncbi.nlm.nih.gov/21270780>

MARKRAM, Henry, LÜBKE, Joachim, FROTSCHER, Michael and SAKMANN, Bert, 1997. Regulation of synaptic efficacy by coincidence of postsynaptic APs and EPSPs. *Science* [online]. 10 January 1997. Vol. 275, no. 5297, p. 213–215. DOI 10.1126/science.275.5297.213. Available from: <http://science.sciencemag.org/content/275/5297/213.abstract>

MAROSO, Mattia, SZABO, Gergely G, KIM, Hannah K., ALEXANDER, Allyson, BUI, Anh D., LEE, Sang-Hun, LUTZ, Beat and SOLTESZ, Ivan, 2016. Cannabinoid Control of Learning and Memory through HCN Channels. *Neuron* [online]. 2 March 2016. Vol. 89, no. 5, p. 1059–1073. DOI 10.1016/j.neuron.2016.01.023. Available from: <https://doi.org/10.1016/j.neuron.2016.01.023>

MARTIN, S J, GRIMWOOD, P D and MORRIS, R. G.M., 2000. *Synaptic plasticity and memory: An evaluation of the hypothesis* [online]. 1 March 2000. Annual Reviews. Available from: <https://doi.org/10.1146/annurev.neuro.23.1.649>

MARTINA, M, SCHULTZ, J H, EHMKÉ, H, MONYER, H and JONAS, P, 1998. Functional and molecular differences between voltage-gated K⁺ channels of fast-spiking interneurons and pyramidal neurons of rat hippocampus. *The Journal of neuroscience : the official journal of the Society for Neuroscience* [online]. 15 October 1998. Vol. 18, no. 20, p. 8111–8125. DOI 10.1523/JNEUROSCI.18-20-08111.1998. Available from: <https://pubmed.ncbi.nlm.nih.gov/9763458>

MCBAIN, C J and MAYER, M L, 1994. N-methyl-D-aspartic acid receptor structure and function. *Physiological Reviews* [online]. 1 July 1994. Vol. 74, no. 3, p. 723–760. DOI 10.1152/physrev.1994.74.3.723. Available from: <https://doi.org/10.1152/physrev.1994.74.3.723>

MEGÍAS, M., EMRI, Zs, FREUND, T. F. and GULYÁS, A. I., 2001. Total number and distribution of inhibitory and excitatory synapses on hippocampal CA1 pyramidal cells. *Neuroscience* [online]. 5 February 2001. Vol. 102, no. 3, p. 527–540. [Accessed 29 April 2020]. DOI 10.1016/S0306-4522(00)00496-6. Available from: <https://www.sciencedirect.com/science/article/abs/pii/S0306452200004966?via%3Dihub>

MELTON, Arthur W, 1963. Implications of short-term memory for a general theory of memory. *Journal of Verbal Learning and Verbal Behavior* [online]. 1963. Vol. 2, no. 1, p. 1–21. DOI [https://doi.org/10.1016/S0022-5371\(63\)80063-8](https://doi.org/10.1016/S0022-5371(63)80063-8). Available from: <https://www.sciencedirect.com/science/article/pii/S0022537163800638>

MENON, Vilas, MUSIAL, Timothy F., LIU, Annie, KATZ, Yael, KATH, William L, SPRUSTON, Nelson and NICHOLSON, Daniel A., 2013. Balanced synaptic impact via distance-dependent synapse distribution and complementary expression of AMPARs and NMDARs in hippocampal dendrites. *Neuron*. 18 December 2013. Vol. 80, no. 6, p. 1451–1463. DOI 10.1016/j.neuron.2013.09.027.

METZ, Alexia E, JARSKY, Tim, MARTINA, M and SPRUSTON, Nelson, 2005. R-type calcium channels contribute to afterdepolarization and bursting in hippocampal CA1 pyramidal neurons. *Journal of Neuroscience* [online]. 15 June 2005. Vol. 25, no. 24, p. 5763–5773. DOI 10.1523/JNEUROSCI.0624-05.2005. Available from: <https://pubmed.ncbi.nlm.nih.gov/15958743>

METZ, Alexia E, SPRUSTON, Nelson and MARTINA, M, 2007. Dendritic D-type potassium currents inhibit the spike afterdepolarization in rat hippocampal CA1 pyramidal neurons. *The Journal of physiology* [online]. 2007/02/22. 15 May 2007. Vol. 581, no. Pt 1, p. 175–187. DOI 10.1113/jphysiol.2006.127068. Available from: <https://pubmed.ncbi.nlm.nih.gov/17317746>

MICKUS, T, JUNG, H Y and SPRUSTON, Nelson, 1999. Properties of Slow, Cumulative Sodium Channel Inactivation in Rat Hippocampal CA1 Pyramidal Neurons. *Biophysical Journal* [online]. 1999. Vol. 76, no. 2, p. 846–860. DOI [https://doi.org/10.1016/S0006-3495\(99\)77248-6](https://doi.org/10.1016/S0006-3495(99)77248-6). Available from: <https://www.sciencedirect.com/science/article/abs/pii/S0006349599772486>

MIGLIORE, M, CANNIA, C., LYTTON, W. W., MARKRAM, Henry and HINES, M L, 2006. Parallel network simulations with NEURON. *Journal of Computational Neuroscience*. 2006. Vol. 21, no. 2, p. 119–129. DOI 10.1007/s10827-006-7949-5.

MIGLIORE, M, COOK, Erik P, JAFFE, D B, TURNER, D A and JOHNSTON, Daniel, 1995. Computer simulations of morphologically reconstructed CA3 hippocampal neurons. *Journal of Neurophysiology* [online]. 1 March 1995. Vol. 73, no. 3, p. 1157–1168. DOI 10.1152/jn.1995.73.3.1157. Available from: <https://doi.org/10.1152/jn.1995.73.3.1157>

MIGLIORE, M and SHEPHERD, Gordon M, 2002. Emerging rules for the distributions of active dendritic conductances. *Nature Reviews Neuroscience* [online]. 2002. Vol. 3, no. 5, p. 362–370. DOI 10.1038/nrn810. Available from: <https://doi.org/10.1038/nrn810>

MIGLIORE, Rosanna, LUPASCU, Carmen A, BOLOGNA, Luca L, ROMANI, Armando, COURCOL, Jean Denis, ANTONEI, Stefano, VAN GEIT, Werner, THOMSON, Alex M., MERCER, Audrey, LANGE, Sigrun, FALCK, Joanne, ROESSERT, Christian, SHI, Ying, HAGENS, Olivier, PEZZOLI, Maurizio, FREUND, T. F., KALI, Szabolcs, MULLER, Eilif, SCHÜRMANN, Felix, MARKRAM, Henry and MIGLIORE, M, 2018. The physiological variability of channel density in hippocampal CA1 pyramidal cells and interneurons explored using a unified data-driven modeling workflow. *PLoS Computational Biology*. 1 September 2018. Vol. 14, no. 9. DOI 10.1371/journal.pcbi.1006423.

MILLS, L R, NIESEN, C E, SO, A P, CARLEN, P L, SPIGELMAN, I and JONES, O T, 1994. N-type Ca₂₊ channels are located on somata, dendrites, and a subpopulation of dendritic spines on live hippocampal pyramidal neurons. *The Journal of neuroscience : the official journal of the Society for Neuroscience* [online]. November 1994. Vol. 14, no. 11 Pt 2, p. 6815–6824. DOI 10.1523/JNEUROSCI.14-11-06815.1994. Available from: <https://pubmed.ncbi.nlm.nih.gov/7525892>

MIZUSEKI, Kenji and BUZSÁKI, György, 2013. Preconfigured, skewed distribution of firing rates in the hippocampus and entorhinal cortex. *Cell Reports* [online]. 2013. Vol. 4, no. 5, p. 1010–1021. DOI 10.1016/j.celrep.2013.07.039. Available from: <http://www.sciencedirect.com/science/article/pii/S221124713004014>

MOCZYDŁOWSKI, E and LATORRE, R, 1983. Gating kinetics of Ca₂₊-activated K⁺ channels from rat muscle incorporated into planar lipid bilayers. Evidence for two voltage-dependent Ca₂₊ binding reactions. *Journal of General Physiology* [online]. 1 October 1983. Vol. 82, no. 4, p. 511–542. DOI 10.1085/jgp.82.4.511. Available from: <https://doi.org/10.1085/jgp.82.4.511>

MORRISON, Abigail, DIESMANN, Markus and GERSTNER, Wulfram, 2008. Phenomenological models of synaptic plasticity based on spike timing. *Biological cybernetics* [online]. 2008/05/20. June 2008. Vol. 98, no. 6, p. 459–478. DOI 10.1007/s00422-008-0233-1. Available from: <https://pubmed.ncbi.nlm.nih.gov/18491160>

MOSCOVITCH, Morris, CABEZA, Roberto, WINOCUR, Gordon and NADEL, Lynn, 2016. Episodic Memory and Beyond: The Hippocampus and Neocortex in Transformation. *Annual review of psychology* [online]. 2016. Vol. 67, p. 105–134. DOI 10.1146/annurev-psych-113011-143733. Available from: <https://pubmed.ncbi.nlm.nih.gov/26726963>

MOSER, Edvard I, MOSER, May-Britt and MCNAUGHTON, Bruce L, 2017. Spatial representation in the hippocampal formation: a history. *Nature Neuroscience* [online]. 2017. Vol. 20, no. 11, p. 1448–1464. DOI 10.1038/nn.4653. Available from: <https://doi.org/10.1038/nn.4653>

MÜLLER, Christina, BECK, Heinz, COULTER, Douglas and REMY, Stefan, 2012. Inhibitory Control of Linear and Supralinear Dendritic Excitation in CA1 Pyramidal Neurons. *Neuron* [online]. 2012. Vol. 75, no. 5, p. 851–864. DOI <https://doi.org/10.1016/j.neuron.2012.06.025>. Available from: <https://www.sciencedirect.com/science/article/pii/S0896627312005879>

MÜLLER, Christina and REMY, Stefan, 2014. Dendritic inhibition mediated by O-LM and bistratified interneurons in the hippocampus. *Frontiers in Synaptic Neuroscience*. 2014. Vol. 6, no. SEP, p. 1–15. DOI 10.3389/fnsyn.2014.00023.

MULLER, D., HEFFT, S. and FIGUROV, A., 1995. Heterosynaptic interactions between UP and LTD in CA1 hippocampal slices. *Neuron*. 1995. Vol. 14, no. 3, p. 599–605. DOI 10.1016/0896-6273(95)90316-X.

MÜLLER, Peter, DRAGUHN, Andreas and EGOROV, Alexei V, 2018. Persistent sodium current modulates axonal excitability in CA1 pyramidal neurons. *Journal of Neurochemistry* [online]. 1 August 2018. Vol. 146, no. 4, p. 446–458. DOI <https://doi.org/10.1111/jnc.14479>. Available from: <https://doi.org/10.1111/jnc.14479>

NABAVI, Sadegh, KESSELS, Helmut W, ALFONSO, Stephanie, AOW, Jonathan, FOX, Rocky and MALINOW, Roberto, 2013. Metabotropic NMDA receptor function is required for NMDA receptor-dependent long-term depression. *Proceedings of the National Academy of Sciences* [online]. 5 March 2013. Vol. 110, no. 10, p. 4027 LP – 4032. DOI 10.1073/pnas.1219454110. Available from: <http://www.pnas.org/content/110/10/4027.abstract>

NARAYANAN, Rishikesh and JOHNSTON, Daniel, 2010. The h current is a candidate mechanism for regulating the sliding modification threshold in a BCM-like synaptic learning rule. *Journal of Neurophysiology* [online]. 16 June 2010. Vol. 104, no. 2, p. 1020–1033. DOI 10.1152/jn.01129.2009. Available from: <https://doi.org/10.1152/jn.01129.2009>

NEVIAN, Thomas, LARKUM, Matthew Evan, POLSKY, Alon and SCHILLER, Jackie, 2007. Properties of basal dendrites of layer 5 pyramidal neurons: a direct patch-clamp recording study. *Nature Neuroscience* [online]. 2007. Vol. 10, no. 2, p. 206–214. DOI 10.1038/nn1826. Available from: <https://doi.org/10.1038/nn1826>

NGO-ANH, Thu Jennifer, BLOODGOOD, Brenda L, LIN, Michael, SABATINI, Bernardo L, MAYLIE, James and ADELMAN, John P, 2005. SK channels and NMDA receptors form a Ca²⁺-mediated feedback loop in dendritic spines. *Nature Neuroscience* [online]. 2005. Vol. 8, no. 5, p. 642–649. DOI 10.1038/nn1449. Available from: <https://doi.org/10.1038/nn1449>

NICHOLSON, Daniel A., TRANA, Rachel, KATZ, Yael, KATH, William L, SPRUSTON, Nelson and GEINISMAN, Yuri, 2006. Distance-Dependent Differences in Synapse Number and AMPA Receptor Expression in Hippocampal CA1 Pyramidal Neurons. *Neuron*. 4 May 2006. Vol. 50, no. 3, p. 431–442. DOI 10.1016/j.neuron.2006.03.022.

NORMANN, Claus, PECKYS, Diana, SCHULZE, Christian H, WALDEN, Jörg, JONAS, P and BISCHOFBERGER, Josef, 2000. Associative Long-Term Depression in the Hippocampus Is Dependent on Postsynaptic N-Type Ca²⁺ Channels. *The Journal of Neuroscience* [online]. 15 November 2000. Vol. 20, no. 22, p. 8290 LP – 8297. DOI 10.1523/JNEUROSCI.20-22-08290.2000. Available from: <http://www.jneurosci.org/content/20/22/8290.abstract>

O'BEIRNE, M., GUREVICH, N. and CARLEN, P L, 1987. Pentobarbital inhibits hippocampal neurons by increasing potassium conductance. *Canadian Journal of Physiology and Pharmacology* [online]. 1 January 1987. Vol. 65, no. 1, p. 36–41. DOI 10.1139/y87-007. Available from: <https://doi.org/10.1139/y87-007>From Duplicate 1 (Pentobarbital inhibits hippocampal neurons by increasing potassium conductance - O'Beirne, M; Gurevich, N; Carlen, P L)

OH, Won Chan, PARAJULI, Laxmi Kumar and ZITO, Karen, 2015. Heterosynaptic Structural Plasticity on Local Dendritic Segments of Hippocampal CA1 Neurons. *Cell Reports* [online]. 2015. Vol. 10, no. 2, p. 162–169. DOI <https://doi.org/10.1016/j.celrep.2014.12.016>. Available from: <https://www.sciencedirect.com/science/article/pii/S2211124714010456>

OLIPHANT, Travis E., 2007. Python for scientific computing. *Computing in Science and Engineering*. May 2007. Vol. 9, no. 3, p. 10–20. DOI 10.1109/MCSE.2007.58.

OMORI, Toshiaki, AONISHI, Toru, MIYAKAWA, Hiroyoshi, INOUE, Masashi and OKADA, Masato, 2006. Estimated distribution of specific membrane resistance in hippocampal CA1 pyramidal neuron. *Brain Research* [online]. 2006. Vol. 1125, no. 1, p. 199–208. DOI <https://doi.org/10.1016/j.brainres.2006.09.095>. Available from: <https://www.sciencedirect.com/science/article/pii/S000689930602926X>

OMORI, Toshiaki, AONISHI, Toru, MIYAKAWA, Hiroyoshi, INOUE, Masashi and OKADA, Masato, 2009. Steep decrease in the specific membrane resistance in the apical dendrites of hippocampal CA1 pyramidal neurons. *Neuroscience Research* [online]. 2009. Vol. 64, no. 1, p. 83–95. DOI <https://doi.org/10.1016/j.neures.2009.01.012>. Available from: <https://www.sciencedirect.com/science/article/pii/S016801020900039X>

OTMAKHOVA, Nonna A, OTMAKHOV, Nikolai and LISMAN, John E, 2002. Pathway-specific properties of AMPA and NMDA-mediated transmission in CA1 hippocampal pyramidal cells. *Journal of Neuroscience*. 2002. Vol. 22, no. 4, p. 1199–1207. DOI 10.1523/jneurosci.22-04-01199.2002.

PALACIO, Stephanie, CHEVALEYRE, Vivien, BRANN, David H, MURRAY, Karl D,

PISKOROWSKI, Rebecca A and TRIMMER, James S, 2017. Heterogeneity in Kv2 Channel Expression Shapes Action Potential Characteristics and Firing Patterns in CA1 versus CA2 Hippocampal Pyramidal Neurons. *eNeuro* [online]. 24 August 2017. Vol. 4, no. 4, p. ENEURO.0267-17.2017. DOI 10.1523/ENEURO.0267-17.2017. Available from: <https://pubmed.ncbi.nlm.nih.gov/28856240>

PAVLOWSKY, Alice and ALARCON, Juan Marcos, 2012. Interaction between long-term potentiation and depression in CA1 synapses: Temporal constraints, functional compartmentalization and protein synthesis. HENDRICKS, Michael (ed.), *PLoS ONE* [online]. 17 January 2012. Vol. 7, no. 1, p. e29865. [Accessed 10 November 2020]. DOI 10.1371/journal.pone.0029865. Available from: <https://dx.plos.org/10.1371/journal.pone.0029865>

PHILPOT, Benjamin D, CHO, Kathleen K A and BEAR, M F, 2007. Obligatory role of NR2A for metaplasticity in visual cortex. *Neuron* [online]. 15 February 2007. Vol. 53, no. 4, p. 495–502. DOI 10.1016/j.neuron.2007.01.027. Available from: <https://pubmed.ncbi.nlm.nih.gov/17296552>

POIRAZI, Panayiota, BRANNON, Terrence and MEL, Bartlett W, 2003a. Pyramidal neuron as two-layer neural network. *Neuron* [online]. 27 March 2003. Vol. 37, no. 6, p. 989–999. [Accessed 22 June 2020]. DOI 10.1016/S0896-6273(03)00149-1. Available from: <http://www.ncbi.nlm.nih.gov/pubmed/12670427>

POIRAZI, Panayiota, BRANNON, Terrence and MEL, Bartlett W, 2003b. Arithmetic of subthreshold synaptic summation in a model CA1 pyramidal cell. *Neuron* [online]. 27 March 2003. Vol. 37, no. 6, p. 977–987. [Accessed 11 November 2020]. DOI 10.1016/S0896-6273(03)00148-X. Available from: <http://www.ncbi.nlm.nih.gov/pubmed/12670426>

POLSKY, Alon, MEL, Bartlett W and SCHILLER, Jackie, 2004. Computational subunits in thin dendrites of pyramidal cells. *Nature Neuroscience* [online]. 2004. Vol. 7, no. 6, p. 621–627. DOI 10.1038/nn1253. Available from: <https://doi.org/10.1038/nn1253>

RALL, Wilfrid, 1962. Theory of Physiological Properties of Dendrites. *Annals of the New York Academy of Sciences* [online]. 1 March 1962. Vol. 96, no. 4, p. 1071–1092. DOI <https://doi.org/10.1111/j.1749-6632.1962.tb54120.x>. Available from: <https://doi.org/10.1111/j.1749-6632.1962.tb54120.x>

RAMIREZ, Alejandro and ARBUCKLE, Melissa R, 2016. Synaptic Plasticity: The Role of Learning and Unlearning in Addiction and Beyond. *Biological psychiatry* [online]. 2016/09/08. 1 November 2016. Vol. 80, no. 9, p. e73–e75. DOI 10.1016/j.biopsych.2016.09.002. Available from: <https://pubmed.ncbi.nlm.nih.gov/27697156>

RAMON Y CAJAL, Santiago, 1894. The Croonian lecture.—La fine structure des centres nerveux. *Proceedings of the Royal Society of London* [online]. 1 January 1894. Vol. 55, no. 331–335, p. 444–468. DOI 10.1098/rspl.1894.0063. Available from: <https://doi.org/10.1098/rspl.1894.0063>

<https://doi.org/10.1098/rspl.1894.0063>

RAMON Y CAJAL, Santiago, 1995. *Histology of the nervous system of man and vertebrates*. Oxford: Oxford University Press. ISBN 9780195074017.

ROYECK, Michel, HORSTMANN, Marie Therese, REMY, Stefan, REITZE, Margit, YAARI, Yoel and BECK, Heinz, 2008. Role of Axonal NaV1.6 Sodium Channels in Action Potential Initiation of CA1 Pyramidal Neurons. *Journal of Neurophysiology* [online]. 1 October 2008. Vol. 100, no. 4, p. 2361–2380. DOI 10.1152/jn.90332.2008. Available from: <https://doi.org/10.1152/jn.90332.2008>

SAILER, Claudia A, KAUFMANN, Walter A, KOGLER, Michaela, CHEN, Lie, SAUSBIER, Ulrike, OTTERSEN, Ole Petter, RUTH, Peter, SHIPSTON, Michael J and KNAUS, Hans-Günther, 2006. Immunolocalization of BK channels in hippocampal pyramidal neurons. *European Journal of Neuroscience* [online]. 1 July 2006. Vol. 24, no. 2, p. 442–454. DOI <https://doi.org/10.1111/j.1460-9568.2006.04936.x>. Available from: <https://doi.org/10.1111/j.1460-9568.2006.04936.x>

SAJIKUMAR, Sreedharan and FREY, Julietta U, 2004. Late-associativity, synaptic tagging, and the role of dopamine during LTP and LTD. *Neurobiology of Learning and Memory* [online]. 2004. Vol. 82, no. 1, p. 12–25. DOI <https://doi.org/10.1016/j.nlm.2004.03.003>. Available from: <https://www.sciencedirect.com/science/article/pii/S1074742704000255>

SÁRAY, Sára, ROESSERT, Christian, APPUKUTTAN, Shailesh, MIGLIORE, Rosanna, VITALE, Paola, LUPASCU, Carmen A, BOLOGNA, Luca L, VAN GEIT, Werner, ROMANI, Armando, DAVISON, Andrew, MULLER, Eilif, FREUND, T. F. and KÁLI, Szabolcs, 2021. HippoUnit: A software tool for the automated testing and systematic comparison of detailed models of hippocampal neurons based on electrophysiological data. *PLOS Computational Biology* [online]. 29 January 2021. Vol. 17, no. 1, p. e1008114. DOI 10.1371/journal.pcbi.1008114. Available from: <https://doi.org/10.1371/journal.pcbi.1008114>

SAUDARGIENĖ, Aušra and GRAHAM, Bruce P, 2015. Inhibitory control of site-specific synaptic plasticity in a model CA1 pyramidal neuron. *Biosystems* [online]. 2015. Vol. 130, p. 37–50. DOI <https://doi.org/10.1016/j.biosystems.2015.03.001>. Available from: <https://www.sciencedirect.com/science/article/pii/S0303264715000349>

SCHULZ, David J, GOAILLARD, Jean Marc and MARDER, Eve, 2006. Variable channel expression in identified single and electrically coupled neurons in different animals. *Nature Neuroscience* [online]. 2006. Vol. 9, no. 3, p. 356–362. DOI 10.1038/nn1639. Available from: <https://doi.org/10.1038/nn1639>

SEKULIC, Vladislav, LAWRENCE, J Josh and SKINNER, Frances K, 2014. Using multi-compartment ensemble modeling as an investigative tool of spatially distributed biophysical balances: Application to hippocampal oriens-lacunosum/moleculare (O-LM) cells. *PLoS ONE*

[online]. 31 October 2014. Vol. 9, no. 10, p. e106567-. DOI 10.1371/journal.pone.0106567. Available from: <https://doi.org/10.1371/journal.pone.0106567>

SHAH, Mala M., MIGLIORE, M, VALENCIA, Ignacio, COOPER, Edward C. and BROWN, David A., 2008. Functional significance of axonal Kv7 channels in hippocampal pyramidal neurons. *Proceedings of the National Academy of Sciences of the United States of America* [online]. 3 June 2008. Vol. 105, no. 22, p. 7869–7874. [Accessed 12 November 2020]. DOI 10.1073/pnas.0802805105. Available from: <https://www.pnas.org/content/105/22/7869>

SHEN, Hongmei, ZHU, Huiwen, PANJA, Debabrata, GU, Qinhua and LI, Zheng, 2020. Autophagy controls the induction and developmental decline of NMDAR-LTD through endocytic recycling. *Nature communications* [online]. 12 June 2020. Vol. 11, no. 1, p. 2979. DOI 10.1038/s41467-020-16794-5. Available from: <https://pubmed.ncbi.nlm.nih.gov/32532981>

SHI, Song-Hai, HAYASHI, Yasunori, ESTEBAN, José A and MALINOW, Roberto, 2001. Subunit-Specific Rules Governing AMPA Receptor Trafficking to Synapses in Hippocampal Pyramidal Neurons. *Cell* [online]. 2001. Vol. 105, no. 3, p. 331–343. DOI [https://doi.org/10.1016/S0092-8674\(01\)00321-X](https://doi.org/10.1016/S0092-8674(01)00321-X). Available from: <https://www.sciencedirect.com/science/article/pii/S009286740100321X>

SHINOHARA, Yoshiaki, HOSOYA, Aki, YAHAGI, Kazuko, FERECSKÓ, Alex S, YAGUCHI, Kunio, SÍK, Attila, ITAKURA, Makoto, TAKAHASHI, Masami and HIRASE, Hajime, 2012. Hippocampal CA3 and CA2 have distinct bilateral innervation patterns to CA1 in rodents. *The European journal of neuroscience* [online]. 2012. Vol. 35, no. 5, p. 702–710. DOI 10.1111/j.1460-9568.2012.07993.x. Available from: <http://europepmc.org/abstract/MED/22339771>

SMITH, Mark A, ELLIS-DAVIES, Graham C R and MAGEE, J C, 2003. Mechanism of the distance-dependent scaling of Schaffer collateral synapses in rat CA1 pyramidal neurons. *The Journal of physiology* [online]. 2003/02/21. 1 April 2003. Vol. 548, no. Pt 1, p. 245–258. DOI 10.1113/jphysiol.2002.036376. Available from: <https://pubmed.ncbi.nlm.nih.gov/12598591>

SPRUSTON, Nelson and JOHNSTON, Daniel, 1992. Perforated patch-clamp analysis of the passive membrane properties of three classes of hippocampal neurons. *Journal of Neurophysiology* [online]. 1 March 1992. Vol. 67, no. 3, p. 508–529. DOI 10.1152/jn.1992.67.3.508. Available from: <https://doi.org/10.1152/jn.1992.67.3.508>

SPRUSTON, Nelson, SCHILLER, Y, STUART, Greg J and SAKMANN, Bert, 1995. Activity-dependent action potential invasion and calcium influx into hippocampal CA1 dendrites. *Science* [online]. 14 April 1995. Vol. 268, no. 5208, p. 297 LP – 300. DOI 10.1126/science.7716524. Available from: <http://science.sciencemag.org/content/268/5208/297.abstract>

SPRUSTON, Nelson, STUART, Greg J and HÄUSSER, Michael, 2016. Principles of dendritic integration. In: *Dendrites*. 3rd. Oxford University Press. p. 351–398.

STERRATT, David, GRAHAM, Bruce P, GILLIES, Andrew and WILLSHAW, David, 2011. *Principles of Computational Modelling in Neuroscience* [online]. Cambridge: Cambridge University Press. ISBN 9780521877954. Available from: <https://www.cambridge.org/core/books/principles-of-computational-modelling-in-neuroscience/9E360450B94A386051003D763A287CF0>

STORM, Johan F, 1990. Chapter 12 Potassium currents in hippocampal pyramidal cells. In: STORM-MATHISEN, J, ZIMMER, J and OTTERSEN, O P B T - Progress in Brain Research (eds.), *Understanding the Brain Through the Hippocampus the Hippocampal Region as a Model for Studying Brain Structure and Function* [online]. Elsevier. p. 161–187. ISBN 0079-6123. Available from: <https://www.sciencedirect.com/science/article/pii/S0079612308612480>

STUART, Greg J, SPRUSTON, Nelson, SAKMANN, Bert and HÄUSSER, Michael, 1997. Action potential initiation and backpropagation in neurons of the mammalian CNS. *Trends in Neurosciences* [online]. 1 March 1997. Vol. 20, no. 3, p. 125–131. DOI 10.1016/S0166-2236(96)10075-8. Available from: [https://doi.org/10.1016/S0166-2236\(96\)10075-8](https://doi.org/10.1016/S0166-2236(96)10075-8)

SURGES, Rainer, FREIMAN, Thomas M and FEUERSTEIN, Thomas J, 2004. Input resistance is voltage dependent due to activation of Ih channels in rat CA1 pyramidal cells. *Journal of Neuroscience Research* [online]. 15 May 2004. Vol. 76, no. 4, p. 475–480. DOI <https://doi.org/10.1002/jnr.20075>. Available from: <https://doi.org/10.1002/jnr.20075>

SWENSEN, Andrew M and BEAN, Bruce P, 2005. Robustness of burst firing in dissociated Purkinje neurons with acute or long-term reductions in sodium conductance. *Journal of Neuroscience* [online]. 6 April 2005. Vol. 25, no. 14, p. 3509–3520. DOI 10.1523/JNEUROSCI.3929-04.2005. Available from: <http://www.jneurosci.org/content/25/14/3509.abstract>

TAKAHASHI, Hiroto and MAGEE, J C, 2009. Pathway Interactions and Synaptic Plasticity in the Dendritic Tuft Regions of CA1 Pyramidal Neurons. *Neuron*. 16 April 2009. Vol. 62, no. 1, p. 102–111. DOI 10.1016/j.neuron.2009.03.007.

TAKEUCHI, Tomonori, DUSZKIEWICZ, Adrian J and MORRIS, R. G.M., 2013. The synaptic plasticity and memory hypothesis: encoding, storage and persistence. *Philosophical transactions of the Royal Society of London. Series B, Biological sciences* [online]. 2 December 2013. Vol. 369, no. 1633, p. 20130288. DOI 10.1098/rstb.2013.0288. Available from: <https://pubmed.ncbi.nlm.nih.gov/24298167>

TOMKO, Matus, BENUSKOVA, Lubica and JEDLICKA, Peter, 2021. A new reduced-morphology model for CA1 pyramidal cells and its validation and comparison with other models using HippoUnit. *Scientific Reports* [online]. 2021. Vol. 11, no. 1, p. 7615. DOI 10.1038/s41598-021-87002-7. Available from: <https://doi.org/10.1038/s41598-021-87002-7>

TOMKO, Matus, JEDLICKA, Peter and BENUSKOVA, Lubica, 2019. Computational model of CA1 pyramidal cell with meta-STDP stabilizes under ongoing spontaneous activity as in vivo. In: *Kognícia a umelý život 2019* [online]. Bratislava: Vydavateľstvo Univerzity Komenského. 2019. p. 118–123. Available from: <http://cogsci.fmph.uniba.sk/kuz2019/files/zbornik.KUZ2019.pdf>

TOMKO, Matus, JEDLICKA, Peter and BENUSKOVA, Lubica, 2020. Meta-STDP Rule Stabilizes Synaptic Weights Under in Vivo-like Ongoing Spontaneous Activity in a Computational Model of CA1 Pyramidal Cell. In: *Lecture Notes in Computer Science (including subseries Lecture Notes in Artificial Intelligence and Lecture Notes in Bioinformatics)*. Springer Science and Business Media Deutschland GmbH. 2020. p. 670–680. ISBN 9783030616151.

TONG, Rudi, CHATER, Thomas E, EMPTAGE, Nigel John and GODA, Yukiko, 2021. Heterosynaptic cross-talk of pre- and postsynaptic strengths along segments of dendrites. *Cell Reports* [online]. 2021. Vol. 34, no. 4, p. 108693. DOI 10.1016/j.celrep.2021.108693. Available from: <https://doi.org/10.1016/j.celrep.2021.108693>

TRIESCH, Jochen, VO, Anh Duong and HAFNER, Anne-Sophie, 2018. Competition for synaptic building blocks shapes synaptic plasticity. *eLife* [online]. 2018. Vol. 7, p. e37836. DOI 10.7554/eLife.37836. Available from: <https://doi.org/10.7554/eLife.37836>

TSIEN, Joe Z, HUERTA, Patricio T and TONEGAWA, Susumu, 1996. The Essential Role of Hippocampal CA1 NMDA Receptor-Dependent Synaptic Plasticity in Spatial Memory. *Cell* [online]. 27 December 1996. Vol. 87, no. 7, p. 1327–1338. DOI 10.1016/S0092-8674(00)81827-9. Available from: [https://doi.org/10.1016/S0092-8674\(00\)81827-9](https://doi.org/10.1016/S0092-8674(00)81827-9)

TSUBOKAWA, H and ROSS, W N, 1996. IPSPs modulate spike backpropagation and associated $[Ca^{2+}]_i$ changes in the dendrites of hippocampal CA1 pyramidal neurons. *Journal of Neurophysiology* [online]. 1 November 1996. Vol. 76, no. 5, p. 2896–2906. DOI 10.1152/jn.1996.76.5.2896. Available from: <https://doi.org/10.1152/jn.1996.76.5.2896>

TUCKER, Kristal R, HUERTAS, Marco A, HORN, John P, CANAVIER, Carmen C and LEVITAN, Edwin S, 2012. Pacemaker rate and depolarization block in nigral dopamine neurons: A somatic sodium channel balancing act. *Journal of Neuroscience* [online]. 17 October 2012. Vol. 32, no. 42, p. 14519–14531. DOI 10.1523/JNEUROSCI.1251-12.2012. Available from: <http://www.jneurosci.org/content/32/42/14519.abstract>

TURI, Gergely Farkas, LI, Wen Ke, CHAVLIS, Spyridon, PANDI, Ioanna, O'HARE, Justin, PRIESTLEY, James Benjamin, GROSMARK, Andres Daniel, LIAO, Zhenrui, LADOW, Max, ZHANG, Jeff Fang, ZEMELMAN, Boris V., POIRAZI, Panayiota and LOSONCZY, Attila, 2019. Vasoactive Intestinal Polypeptide-Expressing Interneurons in the Hippocampus Support Goal-Oriented Spatial Learning. *Neuron* [online]. 2019/01/31. 20 March 2019.

Vol. 101, no. 6, p. 1150- 1165.e8. DOI 10.1016/j.neuron.2019.01.009. Available from: <https://pubmed.ncbi.nlm.nih.gov/30713030>

TURRIGIANO, Gina G, 2008. The self-tuning neuron: synaptic scaling of excitatory synapses. *Cell* [online]. 31 October 2008. Vol. 135, no. 3, p. 422–435. DOI 10.1016/j.cell.2008.10.008. Available from: <https://pubmed.ncbi.nlm.nih.gov/18984155>

TURRIGIANO, Gina G, LESLIE, Kenneth R, DESAI, Niraj S, RUTHERFORD, Lana C and NELSON, Sacha B, 1998. Activity-dependent scaling of quantal amplitude in neocortical neurons. *Nature* [online]. 1998. Vol. 391, no. 6670, p. 892–896. DOI 10.1038/36103. Available from: <https://doi.org/10.1038/36103>

UDAGAWA, Rie, NAKANO, Makoto and KATO, Nobuo, 2006. Blocking L-type calcium channels enhances long-term depression induced by low-frequency stimulation at hippocampal CA1 synapses. *Brain Research* [online]. 2006. Vol. 1124, no. 1, p. 28–36. DOI <https://doi.org/10.1016/j.brainres.2006.09.051>. Available from: <https://www.sciencedirect.com/science/article/pii/S0006899306027934>

UEBACHS, Mischa, OPITZ, Thoralf, ROYECK, Michel, DICKHOF, Gesa, HORSTMANN, Marie Therese, ISOM, Lori L and BECK, Heinz, 2010. Efficacy loss of the anticonvulsant carbamazepine in mice lacking sodium channel beta subunits via paradoxical effects on persistent sodium currents. *The Journal of neuroscience : the official journal of the Society for Neuroscience* [online]. 23 June 2010. Vol. 30, no. 25, p. 8489–8501. DOI 10.1523/JNEUROSCI.1534-10.2010. Available from: <http://www.jneurosci.org/content/30/25/8489.abstract>

VIRTANEN, Pauli, GOMMERS, Ralf, OLIPHANT, Travis E., HABERLAND, Matt, REDDY, Tyler, COURNAPEAU, David, BUROVSKI, Evgeni, PETERSON, Pearu, WECKESSER, Warren, BRIGHT, Jonathan, VAN DER WALT, Stéfan J., BRETT, Matthew, WILSON, Joshua, MILLMAN, K. Jarrod, MAYOROV, Nikolay, NELSON, Andrew R.J., JONES, Eric, KERN, Robert, LARSON, Eric, CAREY, C. J., POLAT, İlhan, FENG, Yu, MOORE, Eric W., VANDERPLAS, Jake, LAXALDE, Denis, PERKTOLD, Josef, CIMRMAN, Robert, HENRIKSEN, Ian, QUINTERO, E. A., HARRIS, Charles R., ARCHIBALD, Anne M., RIBEIRO, Antônio H., PEDREGOSA, Fabian, VAN MULBREGT, Paul, VIJAYKUMAR, Aditya, BARDELLI, Alessandro Pietro, ROTHBERG, Alex, HILBOLL, Andreas, KLOECKNER, Andreas, SCOPATZ, Anthony, LEE, Antony, ROKEM, Ariel, WOODS, C. Nathan, FULTON, Chad, MASSON, Charles, HÄGGSTRÖM, Christian, FITZGERALD, Clark, NICHOLSON, David A., HAGEN, David R., PASECHNIK, Dmitrii V., OLIVETTI, Emanuele, MARTIN, Eric, WIESER, Eric, SILVA, Fabrice, LENDERS, Felix, WILHELM, Florian, YOUNG, G., PRICE, Gavin A., INGOLD, Gert Ludwig, ALLEN, Gregory E., LEE, Gregory R., AUDREN, Hervé, PROBST, Irvin, DIETRICH, Jörg P., SILTERRA, Jacob, WEBBER, James T., SLAVIĆ, Janko, NOTHMAN, Joel, BUCHNER, Johannes, KULICK, Johannes, SCHÖNBERGER, Johannes L., DE MIRANDA CARDOSO, José Vinícius, REIMER, Joscha, HARRINGTON, Joseph, RODRÍGUEZ, Juan Luis Cano, NUNEZ-IGLESIAS, Juan, KUCZYNSKI, Justin, TRITZ, Kevin, THOMA, Martin, NEWVILLE, Matthew, KÜMMERER, Matthias, BOLINGBROKE, Maximilian, TARTRE, Michael, PAK, Mikhail, SMITH, Nathaniel J., NOWACZYK, Nikolai, SHEBANOV, Nikolay,

PAVLYK, Oleksandr, BRODTKORB, Per A., LEE, Perry, MCGIBBON, Robert T., FELDBAUER, Roman, LEWIS, Sam, TYGIER, Sam, SIEVERT, Scott, VIGNA, Sebastiano, PETERSON, Stefan, MORE, Surhud, PUDLIK, Tadeusz, OSHIMA, Takuya, PINGEL, Thomas J., ROBITAILLE, Thomas P., SPURA, Thomas, JONES, Thouis R., CERA, Tim, LESLIE, Tim, ZITO, Tiziano, KRAUSS, Tom, UPADHYAY, Utkarsh, HALCHENKO, Yaroslav O. and VÁZQUEZ-BAEZA, Yoshiki, 2020. SciPy 1.0: fundamental algorithms for scientific computing in Python. *Nature Methods* [online]. 1 March 2020. Vol. 17, no. 3, p. 261–272. [Accessed 18 May 2021]. DOI 10.1038/s41592-019-0686-2. Available from: <https://doi.org/10.1038/s41592-019-0686-2>

VOLIANSKIS, Arturas, FRANCE, Grace, JENSEN, Morten S, BORTOLOTTO, Zuner A, JANE, David E and COLLINGRIDGE, Graham L, 2015. Long-term potentiation and the role of N-methyl-D-aspartate receptors. *Brain research* [online]. 2015/01/22. 24 September 2015. Vol. 1621, p. 5–16. DOI 10.1016/j.brainres.2015.01.016. Available from: <https://pubmed.ncbi.nlm.nih.gov/25619552>

VOSE, Linnea R and STANTON, Patric K, 2017. Synaptic Plasticity, Metaplasticity and Depression. *Current neuropharmacology* [online]. 2017. Vol. 15, no. 1, p. 71–86. DOI 10.2174/1570159x14666160202121111. Available from: <https://pubmed.ncbi.nlm.nih.gov/26830964>

WANG, Hongyan and WAGNER, John J, 1999. Priming-Induced Shift in Synaptic Plasticity in the Rat Hippocampus. *Journal of Neurophysiology* [online]. 1 October 1999. Vol. 82, no. 4, p. 2024–2028. DOI 10.1152/jn.1999.82.4.2024. Available from: <https://doi.org/10.1152/jn.1999.82.4.2024>

WANG, Kang, LIN, Mike T, ADELMAN, John P and MAYLIE, James, 2014. Distinct Ca²⁺ sources in dendritic spines of hippocampal CA1 neurons couple to SK and Kv4 channels. *Neuron* [online]. 22 January 2014. Vol. 81, no. 2, p. 379–387. DOI 10.1016/j.neuron.2013.11.004. Available from: <https://pubmed.ncbi.nlm.nih.gov/24462100>

WANG, Sheng-Zhi and TAO, Huizhong Whit, 2009. History matters: illuminating metaplasticity in the developing brain. *Neuron* [online]. 29 October 2009. Vol. 64, no. 2, p. 155–157. DOI 10.1016/j.neuron.2009.10.012. Available from: <https://pubmed.ncbi.nlm.nih.gov/19874782>

WANG, Xiao-Jing, HU, Hailan, HUANG, Chengcheng, KENNEDY, Henry, LI, Chengyu Tony, LOGOTHEΤΙΣ, Nikos, LU, Zhong-Lin, LUO, Qingming, POO, Mu-ming, TSAO, Doris, WU, Si, WU, Zhaohui, ZHANG, Xu and ZHOU, Douglas, 2020. Computational neuroscience: a frontier of the 21st century. *National Science Review* [online]. 12 September 2020. Vol. 7, no. 9, p. 1418–1422. DOI 10.1093/nsr/nwaa129. Available from: <https://doi.org/10.1093/nsr/nwaa129>

WATANABE, S, HOFFMAN, D A, MIGLIORE, M and JOHNSTON, Daniel, 2002. Dendritic K⁺ channels contribute to spike-timing dependent long-term potentiation in hippocampal

pyramidal neurons. *Proceedings of the National Academy of Sciences* [online]. 11 June 2002. Vol. 99, no. 12, p. 8366 LP – 8371. DOI 10.1073/pnas.122210599. Available from: <http://www.pnas.org/content/99/12/8366.abstract>

WENTHOLD, R J, PETRALIA, R S, BLAHOS J, I I and NIEDZIELSKI, A S, 1996. Evidence for multiple AMPA receptor complexes in hippocampal CA1/CA2 neurons. *The Journal of Neuroscience* [online]. 15 March 1996. Vol. 16, no. 6, p. 1982 LP – 1989. DOI 10.1523/JNEUROSCI.16-06-01982.1996. Available from: <http://www.jneurosci.org/content/16/6/1982.abstract>

WIERA, Grzegorz, NOWAK, Daria, VAN HOVE, Inge, DZIEGIEL, Piotr, MOONS, Lieve and MOZRZYMAS, Jerzy W, 2017. Mechanisms of NMDA Receptor- and Voltage-Gated L-Type Calcium Channel-Dependent Hippocampal LTP Critically Rely on Proteolysis That Is Mediated by Distinct Metalloproteinases. *The Journal of Neuroscience* [online]. 1 February 2017. Vol. 37, no. 5, p. 1240 LP – 1256. DOI 10.1523/JNEUROSCI.2170-16.2016. Available from: <http://www.jneurosci.org/content/37/5/1240.abstract>

XU, Jian, ANTION, Marcia D, NOMURA, Toshihiro, KRANIOTIS, Stephen, ZHU, Yongling and CONTRACTOR, Anis, 2014. Hippocampal metaplasticity is required for the formation of temporal associative memories. *The Journal of neuroscience : the official journal of the Society for Neuroscience* [online]. 10 December 2014. Vol. 34, no. 50, p. 16762–16773. DOI 10.1523/JNEUROSCI.2869-13.2014. Available from: <https://pubmed.ncbi.nlm.nih.gov/25505329>

YAMADA-HANFF, Jason and BEAN, Bruce P, 2015. Activation of Ih and TTX-sensitive sodium current at subthreshold voltages during CA1 pyramidal neuron firing. *Journal of Neurophysiology* [online]. 19 August 2015. Vol. 114, no. 4, p. 2376–2389. DOI 10.1152/jn.00489.2015. Available from: <https://doi.org/10.1152/jn.00489.2015>

ZENKE, Friedemann and GERSTNER, Wulfram, 2017. Hebbian plasticity requires compensatory processes on multiple timescales. *Philosophical Transactions of the Royal Society B: Biological Sciences* [online]. 5 March 2017. Vol. 372, no. 1715, p. 20160259. DOI 10.1098/rstb.2016.0259. Available from: <https://doi.org/10.1098/rstb.2016.0259>

ZHANG, Jiyuan, GUAN, Xin, LI, Qin, MEREDITH, Andrea L, PAN, Hui-Lin and YAN, Jiusheng, 2018. Glutamate-activated BK channel complexes formed with NMDA receptors. *Proceedings of the National Academy of Sciences* [online]. 18 September 2018. Vol. 115, no. 38, p. E9006 LP-E9014. DOI 10.1073/pnas.1802567115. Available from: <http://www.pnas.org/content/115/38/E9006.abstract>

Appendix A

The following equations describe the kinetics of the ion channels used in our CA1 pyramidal cell model.

two types of calcium activated potassium channels (K_{Ca} , K_{Cagk}), and a calcium accumulation mechanism

Sodium channel

The model of sodium channel (*naxn.mod*) was described by Migliore et al. (1997). The channel was uniformly distributed throughout the soma, basal dendrites, apical dendrites, and apical tuft. The channel kinetics are:

$$\begin{aligned}
 I_{Na} &= g_{Na}(V - E_{Na}) & g_{Na} &= \overline{g_{Na}} * m^3 * h \\
 m' &= (m_\infty - m)/\tau_m & h' &= (h_\infty - h)/\tau_h \\
 m_\infty &= a_1/(a_1 + b_1) & h_\infty &= 1/(1 + \exp((V + 50)/4)) \\
 q_t &= 2^{((C-24)/10)} \\
 \tau_m(V) &= \begin{cases} 1/(a_1 + b_1)/q_t, & \tau_m(V) \geq 0.02 \\ 0.02, & \tau_m(V) < 0.02 \end{cases} \\
 \tau_m(V) &= \begin{cases} 1/(a_2 + b_2)/q_t, & \tau_h(V) \geq 0.5 \\ 0.5, & \tau_h(V) < 0.5 \end{cases} \\
 a_1(V) &= trap_0(V, -30, 0.4, 7.2) & a_2(V) &= trap_0(V, -45, 0.03, 1.5) \\
 b_1(V) &= trap_0(-V, 30, 0.124, 7.2) & b_2(V) &= trap_0(-V, 45, 0.01, 1.5)
 \end{aligned} \tag{Appendix A.1}$$

where, $\overline{g_{Na}}$ is the maximum sodium conductance in mho/cm², V is the voltage in mV, C is the temperature in Celsius and $trap_0$ is a function defined as:

```

FUNCTION trap0(v, th, a, q) {
    if (fabs(v-th) > 1e-6) {
        trap0 = a * (v - th) / (1 - exp(-(v - th)/q))
    } else {
        trap0 = a * q
    }
}.

```

Delayed rectifier K+ channel

The model of delayed rectifier K+ channel (*kdrca1.mod*) was described by Ficker and Heinemann (Ficker, Heinemann 1992). The channel was uniformly distributed throughout the soma, basal dendrites, apical dendrites, and apical tuft. The channel kinetics are:

$$\begin{aligned}
 I_{K(DR)} &= g_{K(DR)}(V - E_{K(DR)}) & g_{K(DR)} &= \overline{g_{K(DR)}} * n \\
 \tau_n(V) &= \begin{cases} \beta_n(V)/(0.02 * (1/\alpha_n(V))), & \tau_n(V) \geq 2 \\ 2, & \tau_n(V) < 2 \end{cases} \\
 n' &= (n_\infty - n)/\tau_n & \alpha_n(V) &= \exp(-0.003 * (V - V_{1/2}) * F)/(RT) \\
 n_\infty(V) &= 1/(1 + \alpha_n(V)) & \beta_n(V) &= \exp(-0.00021 * (V - V_{1/2}) * F)/(RT)
 \end{aligned} \tag{Appendix A.2}$$

where $\overline{g_{K(DR)}}$ is the maximum potassium conductance in mho/cm², V is the voltage in mV, $V_{1/2}$ is the half-activation voltage, F is the Faraday constant, R is the ideal gas constant and T is the temperature in Kelvin.

K_A channel

The K_A channel models and distributions were based on previous study (Migliore et al. 2018) and adjusted during the optimization process (see Our new reduced-morphology model). Along the apical and basal dendrites, the maximal channel conductance, $\overline{g_{K(A)}}$, was distributed with increasing exponential gradient:

$$\begin{aligned}
 \overline{g_{K(A)}} &= (15.0 / (1.0 + \exp((300 - d) / 50))) \\
 &\quad * 0.012921529390557651
 \end{aligned} \tag{Appendix A.3}$$

where d is distance in μm from the soma (Migliore et al. 2018).

We used two different K_A channel models to differentiate between proximal and distal K_A channels. A proximal K_A channel model (*kaprox.mod*) was used for the soma and axon. The model was originally described by Ficker and Heinemann (Ficker, Heinemann 1992) and later modified by M. Migliore. The channel kinetics are:

$$\begin{aligned}
 I_{K(A)} &= g_{K(A)}(V - E_{K(A)}) & g_{K(A)} &= \overline{g_{K(A)}} * n * l \\
 n' &= (n_\infty - n)/\tau_n & l' &= (l_\infty - l)/\tau_l \\
 n_\infty(V) &= 1/(1 + \alpha_n(V)) & l_\infty(V) &= 1/(1 + \alpha_l(V))
 \end{aligned}$$

$$\begin{aligned}
\tau_n(V) &= \begin{cases} \beta_n(V)/(q_t * 0.05 * (1 + \alpha_n(V))), & \tau_n(V) \geq 0.1 \\ 0.1, & \tau_n(V) < 0.1 \end{cases} \\
\tau_l(V) &= \begin{cases} 0.26 * (V + 50)/1, & \tau_l(V) \geq 2/1 \\ 2/1, & \tau_l(V) < 2/1 \end{cases} \\
q_t &= 5^{((C-24)/10)} \\
\alpha_n(V) &= \exp(0.003 * \zeta_n(V) * (V - V_{1/2}) * F / (R * (273.16 + C))) \\
\beta_n(V) &= \exp(0.003 * \zeta_n(V) * 0.55 * (V - V_{1/2}) * F / (R * (273.16 + C))) \\
\zeta_n(V) &= -1.5 - 1/(1 + \exp((V + 40)/5)) \\
\alpha_l(V) &= \exp(0.003 * 3 * (V - V_{1/2}) * F / (R * (273.16 + C))) \\
\beta_l(V) &= \exp(0.003 * 3 * 1 * (V - V_{1/2}) * F / (R * (273.16 + C)))
\end{aligned}$$

(Appendix A.4)

where, $\overline{g_{K(A)}}$ is the maximum potassium conductance in mho/cm², V is the voltage in mV, $V_{1/2}$ is the half-activation voltage, F is the Faraday constant, R is the ideal gas constant and C is the temperature in Celsius.

A distal K_A channel model (*kad.mod*) was used for the apical and basal dendrites. The model was originally described by Ficker and Heinemann (Ficker, Heinemann 1992) and later modified by M. Migliore. The channel kinetics are:

$$\begin{aligned}
I_{K(A)} &= g_{K(A)}(V - E_{K(A)}) & g_{K(A)} &= \overline{g_{K(A)}} * n * l \\
n' &= (n_\infty - n)/\tau_n & l' &= (l_\infty - l)/\tau_l \\
n_\infty(V) &= 1/(1 + \alpha_n(V)) & l_\infty(V) &= 1/(1 + \alpha_l(V)) \\
\tau_n(V) &= \begin{cases} \beta_n(V)/(q_t * 0.1 * (1 + \alpha_n(V))), & \tau_n(V) \geq 0.2 \\ 0.2, & \tau_n(V) < 0.2 \end{cases} \\
\tau_l(V) &= \begin{cases} 0.26 * (V + 50)/1, & \tau_l(V) \geq 2/1 \\ 2/1, & \tau_l(V) < 2/1 \end{cases} \\
q_t &= 5^{((C-24)/10)} \\
\alpha_n(V) &= \exp(0.003 * \zeta_n(V) * (V - V_{1/2}) * F / (R * (273.16 + C))) \\
\beta_n(V) &= \exp(0.003 * \zeta_n(V) * 0.39 * (V - V_{1/2}) * F / (R * (273.16 + C))) \\
\zeta_n(V) &= -1.8 - 1/(1 + \exp((V + 40)/5)) \\
\alpha_l(V) &= \exp(0.003 * 3 * (V - V_{1/2}) * F / (R * (273.16 + C))) \\
\beta_l(V) &= \exp(0.003 * 3 * 1 * (V - V_{1/2}) * F / (R * (273.16 + C)))
\end{aligned}$$

(Appendix A.5)

where $\overline{g_{K(A)}}$ is the maximum potassium conductance in mho/cm², V is the voltage in mV, $V_{1/2}$ is the half-activation voltage, F is the Faraday constant, R is the ideal gas constant and C is the temperature in Celsius.

K_M channel

The K_M channel model (*kmb.mod*) was described by Mala Shah (Shah et al. 2008). The channel was uniformly distributed throughout the soma, apical dendrites, and basal dendrites. The channel kinetics are:

$$\begin{aligned}
 I_{K(M)} &= g_{K(M)}(V - E_{K(M)}) & g_{K(M)} &= \overline{g_{K(M)}} * m^1 \\
 m' &= (m_\infty - m)/\tau_m \\
 m_\infty(V) &= \left(1/\left(1 + \exp \left(((V - V_{1/2} - 0))/-10 \right) \right) \right) \\
 \tau_m(V) &= 60 + \beta_m(V)/\left(0.003 * (1 + \alpha_m(V)) \right) \\
 \alpha_m(V) &= \exp \left(0.0378 * 7 * (V - V_{1/2} - 0) \right) \\
 \beta_m(V) &= \exp \left(0.0378 * 7 * 0.4 * (V - V_{1/2} - 0) \right)
 \end{aligned}
 \tag{Appendix A.6}$$

where, $\overline{g_{K(M)}}$ is the maximum potassium conductance in mho/cm², V is the voltage in mV, $V_{1/2}$ is the half-activation voltage, F is the Faraday constant, R is the ideal gas constant and C is the temperature in Celsius.

Non-specific I_h channel

The non-specific I_h channel model (*h.mod*) was described by Magee (Magee 1998). The channel was inserted into the soma, apical dendrites, and basal dendrites. The maximal channel conductance, $\overline{g_h}$, was distributed with increasing linear gradient:

$$\overline{g_h} = (1.03 * d) * 1.9042409723832741e^{-05} \tag{Appendix A.7}$$

where d is distance in μm from the soma (Migliore et al. 2018). The channel kinetics are:

$$I_h = g_h(V - E_h) \quad g_h = \overline{g_h} * l$$

$$\begin{aligned}
l' &= (l_\infty - l)/\tau_l \\
l_\infty(V) &= 1/\left(1 + \exp(- (V - V_{1/2} - 0)/(-8))\right) \\
\tau_l(V) &= \beta_l(V)/\left(1 * q_t * 0.011 * (1 + \alpha_l(V))\right) \\
q_t &= 4.5^{((C-24)/10)} \\
\alpha_l(V) &= \exp\left(0.0378 * 2.2 * (V - V_{1/2})\right) \\
\beta_l(V) &= \exp\left(0.0378 * 2.2 * 0.4 * (V - V_{1/2})\right)
\end{aligned}
\tag{Appendix A.8}$$

where, $\overline{g_h}$ is the maximum potassium conductance in mho/cm², V is the voltage in mV, $V_{1/2}$ is the half-activation voltage, and C is the temperature in Celsius.

L-type calcium channel

The Ca_L channel model (*cal2.mod*) was originally described by M. Migliore (Migliore et al. 1995) with later modifications. The channel was uniformly distributed throughout the soma, apical dendrites, and basal dendrites. The channel kinetics are:

$$\begin{aligned}
I_{CaL} &= g_{CaL} * ghk(V, cai, cao) \\
g_{CaL} &= \overline{g_{CaL}} * m^2 * (0.001/(0.001 + cai)) \\
m' &= (m_\infty - m)/\tau_m \\
m_\infty(V) &= \alpha_m(V) * (1/(\alpha_m(V) + \beta_m(V))) \\
\tau_m(V) &= \begin{cases} \beta_{mt}(V)/\left(q_t * 0.1 * (1 + \alpha_{mt}(V))\right), & \tau_m(V) \geq 0.2/q_t \\ 0.2/q_t, & \tau_m(V) < 0.2/q_t \end{cases} \\
q_t &= 5^{((C-25)/10)} \\
\alpha_m(V) &= 15.69 * (-1.0 * V + 81.5)/(exp((-1.0 * V + 81.5)/10.0) - 1.0) \\
\beta_m(V) &= 0.29 * exp(-V/10.86) \\
\alpha_{mt}(V) &= \exp\left(0.0378 * 2 * (V - V_{1/2})\right) \\
\beta_{mt}(V) &= \exp\left(0.0378 * 2 * 0.1 * (V - V_{1/2})\right)
\end{aligned}
\tag{Appendix A.9}$$

where, $\overline{g_{CaL}}$ is the maximum calcium conductance in mho/cm², cai is the intracellular calcium concentration in mM, cao is the extracellular calcium concentration in mM, V is the voltage in

mV, $V_{1/2}$ is the half-activation voltage, and C is the temperature in Celsius. There are some additional functions that are described here:

```

FUNCTION ghk(v(mV), ci(mM), co(mM)) (mV) {
    LOCAL nu, f
    f = KTF(celsius)/2
    nu = v/f
    ghk=-f*(1. - (ci/co)*exp(nu))*efun(nu)
}

FUNCTION KTF(celsius (DegC)) (mV) {
    KTF = ((25./293.15)*(celsius + 273.15))
}

FUNCTION efun(z) {
    if (fabs(z) < 1e-4) {
        efun = 1 - z/2
    } else {
        efun = z/(exp(z) - 1)
    }
}

```

N-type calcium channel

The Ca_N channel model (*can2.mod*) was originally described by M. Migliore (Migliore et al. 1995) with later modifications. The channel was uniformly distributed throughout the soma, apical dendrites, and basal dendrites. The channel kinetics are:

$$\begin{aligned}
I_{CaN} &= g_{CaN} * ghk(V, cai, cao) \\
g_{CaN} &= \overline{g_{CaN}} * m^2 * h * (0.001/(0.001 + cai)) \\
m' &= (m_\infty - m)/\tau_m & h' &= (h_\infty - h)/\tau_h \\
m_\infty(V) &= \alpha_m(V) * (1/(\alpha_m(V) + \beta_m(V))) \\
h_\infty(V) &= \alpha_h(V) * (1/(\alpha_h(V) + \beta_h(V)))
\end{aligned}$$

$$\begin{aligned}
\tau_m(V) &= \begin{cases} \beta_{mt}(V)/\left(q_t * 0.03 * (1 + \alpha_{mt}(V))\right), & \tau_m(V) \geq 0.2/q_t \\ 0.2/q_t, & \tau_m(V) < 0.2/q_t \end{cases} \\
\tau_h(V) &= \begin{cases} 80, & \tau_m(V) \geq 0.2 \\ 0.2, & \tau_m(V) < 0.2 \end{cases} \\
q_t &= 5^{((C-25)/10)} \\
\alpha_h(V) &= 0.00016 * \exp(-V/48.4) \\
\beta_h(V) &= 1/(\exp((-V/39.0)/10.0) + 1.0) \\
\alpha_m(V) &= 0.1967 * (-1.0 * V + 19.88)/(\exp((-1.0 * V + 19.88)/10.0) - 1.0) \\
\beta_m(V) &= 0.046 * \exp(-V/20.73) \\
\alpha_{mt}(V) &= \exp(0.0378 * 2 * (V - V_{1/2})) \\
\beta_{mt}(V) &= \exp(0.0378 * 2 * 0.1 * (V - V_{1/2}))
\end{aligned}$$

(Appendix A.10)

where, $\overline{g_{CaN}}$ is the maximum calcium conductance in mho/cm², cai is the intracellular calcium concentration in mM, cao is the extracellular calcium concentration in mM, V is the voltage in mV, $V_{1/2}$ is the half-activation voltage, and C is the temperature in Celsius. There are same additional functions as in the case of Ca_L channel model (see above).

T-type calcium channel

The Ca_T channel model (*cat.mod*) was originally described by M. Migliore (Migliore et al. 1995) with later modifications. The channel was uniformly distributed throughout the soma, apical dendrites, and basal dendrites. The channel kinetics are:

$$\begin{aligned}
I_{CaT} &= g_{CaT} * g h k(V, cai, cao) \\
g_{CaT} &= \overline{g_{CaT}} * m^2 * h \\
m' &= (m_\infty - m)/\tau_m & h' &= (h_\infty - h)/\tau_h \\
a_1 &= 0.2 * (-1.0 * V + 19.26)/(\exp((-1.0 * V + 19.26)/10.0) - 1.0) \\
b_1 &= 0.009 * \exp(-V/22.03) \\
m_\infty(V) &= a_1/(a_1 + b_1) \\
\tau_m(V) &= \begin{cases} \beta_{mt}(V)/\left(q_t * 0.04 * (1 + \alpha_{mt}(V))\right), & \tau_m(V) \geq 0.2 \\ 0.2, & \tau_m(V) < 0.2 \end{cases} \\
a_2 &= 1e^{-6} * \exp(-V/16.26) \\
b_2 &= 1/(\exp((-V + 29.79)/10.0) + 1.0)
\end{aligned}$$

$$\begin{aligned}
h_\infty(V) &= a_2/(a_2 + b_2) \\
\tau_h(V) &= \begin{cases} \beta_h(V)/\left(0.015 * (1 + \alpha_h(V))\right), & \tau_h(V) \geq 10 \\ 10, & \tau_h(V) < 10 \end{cases} \\
q_t &= 5^{((C-25)/10)} \\
\alpha_h(V) &= \exp\left(0.0378 * 3.5 * (V - V_{1/2})\right) \\
\beta_h(V) &= \exp\left(0.0378 * 3.5 * 0.6 * (V - V_{1/2})\right) \\
\alpha_{mt}(V) &= \exp\left(0.0378 * 2 * (V - V_{1/2})\right) \\
\beta_{mt}(V) &= \exp\left(0.0378 * 2 * 0.1 * (V - V_{1/2})\right)
\end{aligned}$$

(Appendix A.11)

where, $\overline{g_{CaT}}$ is the maximum calcium conductance in mho/cm², cai is the intracellular calcium concentration in mM, cao is the extracellular calcium concentration in mM, V is the voltage in mV, $V_{1/2}$ is the half-activation voltage, and C is the temperature in Celsius. There are same additional functions as in the case of Ca_L channel model (see above).

Slow calcium dependent K⁺ channel

The K_{Ca} channel model (*kca.mod*) was originally described by Destexhe et al. (Destexhe et al. 1994) and modified by Y. Poirazi. This channel is activated by intracellular calcium and is not voltage-dependent. The channel was uniformly distributed throughout the soma, apical dendrites, and basal dendrites. The channel kinetics are:

$$\begin{aligned}
I_K &= g_K(V - E_K) & g_K &= \overline{g_K} * m^3 \\
m' &= (m_\infty - m)/\tau_m & m_\infty &= car/(1 + car) \\
q_t &= 3^{((C-22.0)/10)} & car &= (cai/0.00035)^4 \\
\tau_m &= \begin{cases} 1/0.03/(1 + car)/q_t, & \tau_m \geq 0.5 \\ 0.5, & \tau_m < 0.5 \end{cases}
\end{aligned}$$

(Appendix A.12)

where, $\overline{g_K}$ is the maximum potassium conductance in mho/cm², cai is the intracellular calcium concentration in mM, V is the voltage in mV, and C is the temperature in Celsius.

Calcium activated K⁺ channel

The K_{CaGk} channel model (*cagk.mod*) was originally described by Moczydlowski and Latorre (Moczydlowski, Latorre 1983) and later modified. This channel is activated by intracellular calcium and is voltage-dependent. The channel was uniformly distributed throughout the soma, apical dendrites, and basal dendrites. The channel kinetics are:

$$\begin{aligned}
 I_K &= g_K(V - E_K) & g_K &= \overline{g_K} * o^1 \\
 o' &= (o_\infty - o)/\tau_o & o_\infty(V, c) &= \alpha_o(V, c) * \tau_o(V, c) \\
 \tau_o(V, c) &= 1/(\alpha_o(V, c) + \beta_o(V, c)) \\
 \alpha_o(V, c) &= c * 0.28/(c + 48e^{-3} * \exp(-2 * 0.84 * F * V/R/(273.15 + C))) \\
 \beta_o(V, c) &= 0.48/(1 + c/13e^{-6} * \exp(-2 * 1.0 * F * V/R/(273.15 + C)))
 \end{aligned} \tag{Appendix A.13}$$

where, $\overline{g_K}$ is the maximum potassium conductance in mho/cm², c is the calcium concentration in mM, V is the voltage in mV, C is the temperature in Celsius, F is the Faraday constant, and R is the ideal gas constant.

Calcium accumulation

The calcium accumulation model (*cacum.mod*) was described by Polsky et al. (Polsky et al. 2004). Calcium accumulation into a volume of area * depth next to the membrane with a decay (time constant tau) to resting level given by the global calcium variable *cai0_ca_ion*. The model was modified to include a resting current (*irest*) and peak value (*cmax*). The channel was uniformly distributed throughout the soma, apical dendrites, and basal dendrites. The channel kinetics are:

$$\begin{aligned}
 cmax &= cai = cai_0 = 50e^{-6} & cmax &= \begin{cases} cai, & cai > cmax \\ cmax, & cai \leq cmax \end{cases} \\
 cai' &= (irest - ica)/0.4/F/2 * 1e^4 + (cai_0 - cai)/100
 \end{aligned} \tag{Appendix A.14}$$

Where *cai* is the intracellular calcium concentration, *irest* is the resting current, *ica* is the calcium current, *cmax* is the peak value, and *F* is the Faraday constant.

Appendix B

Table 0.1: Uniformly distributed passive parameters, active ionic conductances and reversal potentials of channels for each section of our model.

Mechanism	Somatic	Axonal	Basal	Apical	Trunk
$C_m (\mu F/cm^2)$	1	1	1	1	1
$R_A (\Omega/cm^2)$	115.3958	85.2024	115.3958	115.3958	115.3958
$g_{Na} (S/cm^2)$	0.035	0.035	0.03828	0.03828	0.025
$g_{Kdr} (S/cm^2)$	0.0015	0.01166	0.004304	0.004304	0.02
$g_{KM} (S/cm^2)$	0.001	0.02647	-	-	-
$g_{KCa} (S/cm^2)$	0.0015	-	9.0311e-05	9.0311e-05	9.0311e-05
$g_{KCagk} (S/cm^2)$	4.4820e-05	-	4.4820e-05	4.4820e-05	4.4820e-05
$g_{CaL} (S/cm^2)$	0.0005	-	8.0325e-06	8.0325e-06	8.0325e-06
$g_{CaN} (S/cm^2)$	2.2619e-06	-	2.2619e-06	2.2619e-06	2.2619e-06
$g_{CaT} (S/cm^2)$	0.00005	-	1.1849e-06	1.1849e-06	1.1849e-06
$g_L (S/cm^2)$	9.03139e-05	0.0001289	9.03139e-05	9.03139e-05	9.03139e-05
$[Ca^{2+}]_o (mM)$	50e-6	-	50e-6	50e-6	50e-6
$\tau_{Ca} (ms)$	100	-	100	100	100
$E_{Na} (mV)$	50	50	50	50	50
$E_K (mV)$	-90	-90	-90	-90	-90

Table 0.2: K_A , I_h conductances and reversal potential of passive current in individual sections of the model

Section / Mechanism	$g_{KA} (S/cm^2)$	$g_{Ih} (S/cm^2)$	$E_L (mV)$
Soma	0.0075	1.9042e-05	-65.7269
Axon	0.1637	-	-79.9171
Proximal SO dendrite	0.001433	5.0462e-05	-67.5602
Distal SO dendrite	0.02522	0.0001361	-72.5602
Thick proximal SR dendrite	0.1	5.04624e-05	-67.5602
Thick medium SR dendrite	0.15	0.0001076	-70.8936
Thick distal SR dendrite	0.2	0.0001933	-75.8936
Thin SR dendrite 1	0.006259	9.3308e-05	-70.06023
Thin SR dendrite 1	0.03834	0.0001504	-73.3936
Thin SR dendrite 1	0.1613	0.0002361	-78.3936
Thick SLM dendrite	0.1855	0.0002789	-80.8936
Medium SLM dendrite	0.1926	0.0003361	-84.2269
Thin SLM dendrite	0.1936	0.0003789	-86.7269